

# Studies in High Energy, Mid-Infrared, Bulk Supercontinuum Generation

Towards Infrared Death Laser Development for Strong Field  
Control of Atoms and Laser Selective Chemistry

Dissertation  
zur Erlangung des Doktorgrades  
an der Fakultät für Mathematik, Informatik und Naturwissenschaften  
Fachbereich Physik  
der Universität Hamburg

vorgelegt von  
Aradhana Choudhuri

Hamburg  
2017

Gutachter/innen der Dissertation:

Prof. Dr. Franz Kaertner  
Prof. Dr. R. J. Dwayne Miller

Zusammensetzung der Prüfungskommission:

Prof. Dr. Robin Santra  
Dr. Christian Kraenkel  
Prof. Dr. Franz Kaertner  
Prof. Dr. R. J. Dwayne Miller  
Dr. Axel Ruehl

Vorsitzende/r der Prüfungskommission:

Prof. Dr. Robin Santra

Datum der Disputation:

**03.11.2017**

Vorsitzender Fach-Promotionsausschusses PHYSIK:

Prof. Dr. Wolfgang Hansen

Leiter des Fachbereichs PHYSIK:

Prof. Dr. Michael Potthoff

Dekan der Fakultät MIN:

Prof. Dr. Heinrich Graener

## Eidesstattliche Versicherung / Declaration on oath

Hiermit versichere ich an Eides statt, die vorliegende Dissertationsschrift selbst verfasst und keine anderen als die angegebenen Hilfsmittel und Quellen benutzt zu haben.

Die eingereichte schriftliche Fassung entspricht der auf dem elektronischen Speichermedium.

Die Dissertation wurde in der vorgelegten oder einer ähnlichen Form nicht schon einmal in einem früheren Promotionsverfahren angenommen oder als ungenügend beurteilt.

Hamburg, den 30.07.2017

A handwritten signature in black ink, appearing to read 'Rhadhuni', written above a horizontal line.

Unterschrift der Doktorandin / des Doktoranden

## Zusammenfassung

Ein Lasersystem, das hochenergetische, breitbandige Strahlung phasenstabil bei verschiedenen Wellenlaengen im sichtbaren, nah- und mittleren Infrarotbereich bereitstellen kann, wuerde aufregende Moeglichkeiten ermoeglichen, um fundamentale Prozesse in der Chemie zu untersuchen. Dies wird unter anderem durch neuartige Pump-Probe Aufbauten und die kohaerente Kontrolle von Licht-Materie-Wechselwirkung im „Starke Feldregime“ ermoeglicht. Im so genannte IR Death Laser (IRDL) Projekte soll ein solches Lasersystem entwickelt werden, wobei das Ausloesen von chemischen Reaktionen durch Laserstrahlung als „heiligen Gral“ gilt.

Da nur wenige laseraktive Materialien fuer den mittleren Infrarotbereich existieren, wird eine alternative, breitbandige und hochenergetische Quelle benoetigt, die in parametrische Prozesse, wie Differenzfrequenzerzeugung und parametrische Verstaerker verstaerkt werden soll. So sollen die Ausgangsspezifikationen des IRDL Projekts – drei phasenstabile Laserpulse mit einer Energie von 1 mJ pro Puls und Pulsdauern unter 100 fs bei 3, 7 und 9  $\mu\text{m}$  Wellenlaenge - realisiert werden. Solche Strahlungsquellen koennen auf Weisslichterzeugung in optischen Fasern und Festkoerpermaterialien oder Differenzfrequenzerzeugung basieren, die typischerweise von fs-Titan Saphir Lasersystemen getrieben werden. Die Grundlage des IRDL ist allerdings ein Lasersystem, das 3 ps Pulse bei 2  $\mu\text{m}$  Wellenlaenge und mehreren mJ Pulsenergie emittiert, so dass nicht alle technologischen Loesungen zur Verfuegung stehen. Die Weisslichterzeugung in Festkoerpermaterialien basiert nicht nur auf einfachen, hochstabilen und kostenguenstigen Aufbauten, sondern kann auch mit Pulsen hoher Pulsenergie realisiert werden, was diese Technologie aeusserst attraktiv fuer das IRDL Projekt macht und sie in den Fokus der vorgelegten Arbeit rueckt.

Die Zielsetzung der vorgelegten Arbeit war die Untersuchung der Weisslichterzeugung und ihrer physikalischen Prozesse im Parameterbereich des IRDL Lasersystems und die Maximierung der spektralen Energie auf der langwelligen (Stokes) Seite des Pumplasers.

Um die benoetigten Parameterbereiche und experimentellen Bedingungen zu untersuchen, wurde eine 3+1 dimensionale Simulation, die auf der „Slowly Varying Envelope Approximation“ basiert, entwickelt und mit gemischtem Erfolg durch experimentelle Daten der Weisslichterzeugung bei 1  $\mu\text{m}$  Pumpwellenlaenge validiert. Der exponentielle Abfall der spektralen Energiedicht auf der langwelligen Seite des optischen Spektrums, der sowohl in Experiment, numerischen Simulation, als auch in der Literatur auftrat, war der Anlass fuer eine experimentelle Studie bei 1  $\mu\text{m}$  Pumpwellenlaenge. Hier wurde die vollstaendigen spektralen und raeumlichen Polarisations-eigenschaften des Weisslichts untersucht und beinhalteten auch die konische Emissionen bei weit von der Pumpquelle liegenden Wellenlaengen, die typischerweise fuer Nachverstaerkung ignoriert werden.

Eine wichtige Schlussfolgerung dieser spektrale raeumlichen Polarisationsstudie beinhaltet die kristallografische Qualitaet der nichtlinbenarem Materialien, die fuer die Weisslichterzeugung verwendet wurden (Calziumfluorid und Ytterbium Aluminium Granat(YAG)) und ihr Einfluss auf sowohl die induzierte Rotation des Polarisationszustand der hochenergetischen Strahlung, als auch den dauerhaften Betrieb bei hohen Energien. Dieses hebt die Notwendigkeit, geeignete nichtlineare Kristalle fuer die Weisslichterzeugung mit hochenergetischen Pumpspulsen bei 2  $\mu\text{m}$  Wellenlaenge, hervor. In Zusammenarbeit mit dem Institute for Photonic Sciences (ICFO) wurde eine Studie ueber YAG, Saphir, ZnSe und Diamant gepumpt mit sub-2-Zyklus Pulsen bei 1,8  $\mu\text{m}$  durchgefuehrt. Diese Studie bestaetigte die

Brauchbarkeit aller vier Kristalle fuer die Weisslichterzeugung, wobei die entgueltige Entscheidung von der konkreten Anwendung und den entstehenden Kosten abhaengt: Diamant fuer hochste Pulsenergie auf Grund der hohen Nichtlinearitaet, des grossen Transparenzfensters und weiterer Eigenschaften (der Einsatz von Diamant ist allerdings auf Grund der hohen Kosten fuer Einzelkristalle laenger als 5 mm auf kurze Pulse unter 200 fs Dauer beschraenkt). YAG ist generell fuer den Einsatz im mittleren infraroten Spektralbereich geeignet waehrend Saphir besonders durch seine exzellenten Eigenschaften im nahen infraroten Spektralbereich und seine spektrale Uniformitaet auffaellt. ZnSe stellt einen guten Kompromiss fuer Systeme dar, die hohe Nichtlinearitaeten bei langen Wellenlaengen, z.B. bei Verwendung von ps Pumppulsen erfordern.

Auf der Basis der am ICFO erarbeiteten Resultate zur Weisslichterzeugung in Diamant, wurde die Rolle der stimulierten Ramanstreuung weiter untersucht. Dabei stellte sich heraus, dass stimulierte Ramanverstaerkung eine brauchbare Methode darstellt, um die spektrale Energiedichte eines Weisslichts zu erhoehen. Weitere experimentelle Untersuchungen wurden mit einer Pumpquelle bei 1  $\mu\text{m}$  Wellenlaenge durchgefuehrt. Schlussendlich wurde mit dem IRDL Lasersystem eine nichtlineare Verbreiterung in ZnSe mit einem Fourierlimit von unter 100 fs bei einer Pulsenergie von 120  $\mu\text{J}$  demonstriert. Dabei wurden auch kaskadierte Weisslichterzeugung und Filamentierung beobachtet, die durch die zweite und dritte Harmonische der Pumpwellenlaenge erzeugt wurden. Dies eroeffnete die Moeglichkeit, Pump-Probe Experimente mit Hilfe einer einzigen Lichtquelle und eines breitbandigen pulsformer .

Basierend auf den, in der vorgelegten Arbeit beschriebenen Experimenten, wurde ein mehrstufiger Aufbau, der ultrabreitbandige Strahlung unterstuetzt, fuer den finale IRDL Aufbau vorgeschlagen. Dieser besteht aus nichtlinearer Verbreiterung in ZnSe, direkter Weisslichterzeugung in YAG, gefolgt einer Verstaerkung der langwelligen spektralen Anteile in Diamant.

## Summary

A laser system that delivers high-energy, broadband radiation at multiple phase-locked frequencies over the visible (VIS), near infrared (NIR) and mid infrared (MIR) wavelength regions opens up the possibility of exciting experiments for studying fundamental chemistry, including novel pump-probe setups and strong field coherent control. The IR Death Laser (IRDL) project is aimed towards developing such a laser, with Laser Selective Chemistry (LSC) as its “holy grail” of applications.

Due to the dearth of active laser materials in the Mid-Infrared (MIR), an ultra-broadband, high-energy laser source is required to seed the parametric processes (Difference Frequency Generation, Optical Parametric Amplification/Optical Parametric Chirped Pulse Amplification (OPA / OPCPA)) that are key to achieving the output pulse requirements of the IRDL project—three phase-locked, sub-100 femtosecond, pulses at 3, 7, and 9 $\mu\text{m}$  wavelengths, with 1mJ of energy per pulse. Ultra-broadband seed sources include supercontinua generated in fibers, bulk materials, and intrapulse DFG processes. However, the conversion efficiency of the OP(CP)A stages into the deep MIR from such a driver laser would be low. Recent developments in laser technologies make 2  $\mu\text{m}$ , high-energy laser driver available, with the drawback of few picosecond long pulses. Operating in this high-energy, picosecond, 2 $\mu\text{m}$  regime constrains the choice of broadband seed technique; the low cost, low complexity, stability and high energy throughput characteristics of bulk supercontinuum generation (SCG) make it a particularly attractive technique.

The objective of this work was to investigate supercontinuum generation characteristics and physical parameters particular to the MIR operating regime, with a view towards maximizing the spectral energy density available on the Stokes (red) side of the pump wavelength.

In order to investigate the parameter space and conditions required for SCG, a (3+1)D Supercontinuum Generation simulation, based on the slowly varying envelope approximation, was developed and benchmarked against SCG experiments at 1 $\mu\text{m}$ . The exponential dropoff of spectral energy density on the Stokes side of the pump in SCG output, seen in literature, experiment and simulations, prompted a further study at 1 $\mu\text{m}$  wavelengths designed to check the full spatio-spectral polarization of the SCG output, including the far-from-pump Conical Emission energies usually discarded for other OPA seeding schemes.

An important conclusion of the spatio-spectral polarization study involved crystallographic quality of the nonlinear material used for SCG (Calcium fluoride vs. Yttrium aluminum garnet), and its effect on the induced polarization rotation of intense pump pulses, as well as sustained operation at high energies. This highlighted the need to analyze suitable nonlinear crystals for bulk SCG at 2 $\mu\text{m}$  wavelengths at high peak energies up to the multi-filamentation regime. A SCG study with YAG, Sapphire, ZnSe, and Diamond, pumped with  $\sim 1.8\mu\text{m}$ , sub-2-cycle pulses was undertaken. This confirmed the viability of all four crystals as MIR bulk SCG candidates, with the final choice depending on the application : Diamond for very high energy, MIR pulses due to its high nonlinearity and transparency window, YAG for overall performance in the MIR, Sapphire for excellent NIR properties and flatness of spectrum on the anti-Stokes side of the pump, and ZnSe as a compromise for systems that demand very high nonlinearity at long wavelengths (i.e. for picosecond pulse durations in the deeper MIR region).

Based on the results of SCG in Diamond, the role of Stimulated Raman Scattering in SCG was investigated. Stimulated Raman Amplification emerged as a viable method to increase the spectral energy density of a SCG output, and further studies were undertaken with the use of a 1 $\mu\text{m}$  laser source. Finally, a few-picosecond, 2  $\mu\text{m}$  pump source was used to generate nonlinear broadening in ZnSe —the spectrally

broadened output supporting a minimum Fourier limit of 100 fs was demonstrated, with an energetic output of  $\sim 120 \mu\text{J}$ . Cascaded supercontinuum and filaments generated via the efficient production of 2<sup>nd</sup> and 3<sup>rd</sup> harmonic lines in the ZnSe rod were also observed, opening up the possibility to conduct single-source pump-probe experiments using a broadband pulse-shaper.

Based on the experiments conducted in this study, a multi-stage ultra broadband seed generation setup was proposed for seeding parallel MIR-OPCPAs channels, comprised of high-energy nonlinear broadening in ZnSe, direct chirped supercontinuum generation in YAG, followed by an amplification of the Stokes-side wavelengths in Diamond.

## List of Related Publications

- [1] Choudhuri, A., Zia, H., Calendron, A-L., Cankaya, H., Kaertner, F.X., Hartl, I., Miller, R.J.D., Ruehl, A.. "Full 3D Simulation of White-Light Generation in Bulk Materials", 6<sup>th</sup> EPS-QEOD Europhoton Conference. European Physical Society.
- [2] Zia, H., Choudhuri, A., Hartl, I., Miller, R. J. D., Ruehl, A. "Full (3+ 1) D split-step technique for spatial mode analysis of white light generation in bulk Kerr-media." *CLEO: Science and Innovations*. Optical Society of America, 2015.
- [3] Choudhuri, A., Ruehl, A., Leon, I., DiPalo, N., Hartl, I., Miller, R.J. Dwayne, Biegert, J. "Multi-octave supercontinuum generation driven by few-cycle mid-IR pulses in YAG, ZnSe and Sapphire." *CLEO: QELS\_Fundamental Science*. Optical Society of America, 2016.
- [4] Choudhuri, A., Chatterjee, G., Zheng, J., Hartl, I., Ruehl, A., Miller, R.J.D. "A Spatio-Spectral Polarization Analysis of 1 $\mu$ m-Pumped bulk Supercontinuum in a Cubic Crystal (YAG)". In review: *Optics Letters* (2017).
- [5] Choudhuri, A.<sup>1</sup>, Kardas, T.<sup>1</sup>, Chatterjee, G., Leon, I., DiPalo, N., Hartl, I., Ruehl, A., Biegert, J., Miller, R.J.D. "Using Stimulated Raman Scattering and Amplification in Diamond to Enhance Spectral Energy Density of Bulk Supercontinuum." In preparation for submission to *Optica* (2018).
- [7] Choudhuri, A., Chatterjee, G., Kroetz, P., Hartl, I., Ruehl, A., Miller, R.J.D "Multi-Octave Spanning Supercontinuum in ZnSe pumped with picosecond pulses." In preparation for submission to *Optics Express* (2017).
- [8] Choudhuri, A., Milian, C., Leon, I., DiPalo, N., Hartl, I., Ruehl, A., Biegert, J. Couairon, A. Miller, R.J. Dwayne. "Cascaded 2<sup>nd</sup> and 3<sup>rd</sup> Harmonic Supercontinuum Filaments in 2 $\mu$ m-pumped ZnSe." In preparation.

---

<sup>1</sup> Shared First-Authorship

*For Aswin & Tom*

Dedicated to my teachers:

*Axel Ruehl*

*Marie-Josée Potvin*

*Galina Okouneva*

*Donald McTavish*

*Krishna Dev Kumar*

*GM Choa Kok Sui*

*Sanjoy Choudhuri*

*Sujata Choudhuri*

with deep gratitude to those without  
whom this work would not have been possible:

*R. J. Dwayne Miller*

*Franz Kaertner*

*Ingmar Hartl*

*Jens Biegert*

*Tomas Kardas*

my colleagues in the IRDL, FS-LA, and 2 $\mu$ m-development group, especially

*Peter Kroetz*

*Anne-Laure Calendron*

*Gourab Chatterjee*

*Huseyin Cayanka*

and the last-minute Search and Rescue Squad

*Thomas Meyer*

*Anne-Laure Calendron*

*Axel Ruehl*

*Gourab Chatterjee*

*Gretchen Baisa*

## Table of Contents

1	Introduction	1
1.1	Scope of Thesis	4
1.2	Brief Introduction to Laser Selective Chemistry	5
1.2.1	Water Vapor Pump-Probe Study (Out of Scope)	10
1.2.2	Dual-Wavelength C-H Overtone & Combination Band Study (Out of Scope)	11
1.3	IRDL System Overview	12
1.4	References	18
2	Bulk Supercontinuum Generation Theory	23
2.1	Introduction	23
2.2	A Simplified deconstruction of dominant mechanisms in Filament Formation	28
2.2.1	Kerr SF	30
2.2.2	Plasma Generation	42
2.2.3	Group Velocity Dispersion (GVD)	54
2.3	Spatio-Temporal Evolution of The SC Pulse	56
2.3.1	The Moving Focus Model	56
2.3.2	Pulse Splitting	57
2.3.3	Conical Emission and X-Waves	60
2.3.4	Self Steepening	62
2.4	Additional Notes on the Origin of Spectral Structure in the SC Pulse	63
2.5	Additional Notes on Pre-Focusing Conditions of the Input Pulse	67
2.6	References	71
3	Experimental Studies in Supercontinuum Generation	77
3.1	(3+1)D Bulk Supercontinuum Generation Simulation Development	78
3.1.1	Numerical Model	79
3.1.2	Implementation	79
3.1.3	FLASH-2 Pump Source	80
3.1.4	FLASH-2 Supercontinuum Setup	83
3.1.5	Pertinent Experimental Results & Discussion	84
3.1.6	Numerical Simulation Results and Discussion	88

3.2	Spatio-Spectral Polarization Analysis in a Cubic Crystal (PHAROS, MPSD)	92
3.2.1	PHAROS Pump Source	93
3.2.2	Experimental Setup	96
3.2.3	Results and Discussion	98
3.3	Crystal Performance Comparison for 2 $\mu$ m, sub-2-cycle SCG (ICFO)	105
3.3.1	Pump Source	108
3.3.2	Experimental Setup	110
3.3.3	Results and Discussion	113
3.4	Stimulated Raman Amplification (SRA) in Diamond of YAG Supercontinuum	121
3.4.1	SRA Setup	122
3.4.2	Results and Discussion	123
3.5	Spectral Broadening and High Harmonic Cascaded Filaments in ZnSe (MPSD)	126
3.5.1	IRDL Pump Source	126
3.5.2	Supercontinuum Setup	128
3.5.3	Nonlinear Broadening of the Fundamental: Results and Discussion	129
3.5.4	Cascaded WL Generation in VIS/NIR region	137
3.6	References	141
4	Conclusion	147
4.1	SCG for Long Pulse, Long Wavelength, High Energy Regions	149
4.2	IRDL Beamline Options	151
4.3	Summary	155
APPENDIX A: Material Parameters of Relevant Crystals		I
APPENDIX B: The Gaeta NLSE		II
Appendix References		IV

# 1 INTRODUCTION

---

The high temporal and spatial coherence of laser radiation makes it possible to selectively excite and study molecular chemical bonds through pump-probe experiments [1.1]. Also, the extremely high field conditions achievable with laser radiation can exceed that of the Coulombic field binding an electron [1.2], and it is relatively straightforward to achieve focused light intensities high enough to reach thresholds for multiphoton ionization of molecules [1.3]. An ultrafast laser system that delivers high-energy (on the order of multiple mJ of energy per pulse), tunable, ultra-broadband radiation over the visible (VIS), near infrared (NIR) and mid infrared (MIR) wavelength regions enables a number of experiments that utilize strong-field control and high-harmonic generation for studying fundamental chemistry. This includes the ability to simultaneously drive multiple, ground-state vibrational modes of molecules—the “holy grail”—Laser Selective Chemistry. This is the primary goal of the IR Death Laser (IRDL) Project.

The lack of broadband laser materials in the MIR makes optical parametric processes (Difference Frequency Generation, DFG, and Optical Parametric Amplification, OPA) the only viable techniques to reach the wavelengths and energies of interest [1.12]. These parametric processes utilize the mixing of an energetic pump source with an ultrabroadband seed-source—using intrapulse mixing from the output of a broadband laser system at short wavelengths [1.61], or nonlinearly broadened pulses obtained via supercontinuum generation in fiber or condensed matter [1.31]—to generate the target wavelengths and energies. However, non-oxide DFG/OPA materials (like ZGP) must be used to access wavelengths above  $\sim 5\mu\text{m}$  using a parametric process. The transparency of these materials, and the energy conversion efficiency, requires pumps at or above  $2\mu\text{m}$  [1.27].

The most viable and therefore most commonly used technique for seed generation in the 2 $\mu$ m region is supercontinuum generation (SCG) [1.62]. And, in order to utilize passive carrier phase envelope stabilization, and overcome timing jitter issues in the setup [1.63], a portion of the output of the pump source used for parametric processes is split off into a parallel arm, and used for the SCG process as well [1.31 – 1.33, 1.63]. However, in terms of the pump source, there is a tradeoff between energy scalability and optical bandwidth—a picosecond working regime is common for very high energy pump sources (regenerative amplifiers and multipass amplifiers) in the MIR region [1.27, 1.29], with shorter pulses reported for lower-energy operation [1.64]. The (relatively) long pulses of the pump source, coupled with the wavelength regime, impose certain restrictions on supercontinuum generation process; coherence and compressibility of the seed (and therefore its usability) over the entire generated bandwidth become an issue due to picosecond nonlinear dynamics in the MIR.

Multi-octave supercontinua, pumped by MIR pulses, are routinely generated in highly nonlinear fibers like ZBLAN [1.39] and Tellurite [1.40]. But the fiber approach is limited to, at most, a few hundred nJ of input energy [1.41] due to damage thresholds of the fiber. And even when they are pumped by femtosecond pulses, broadband fiber systems produce a highly structured spectral output that contains distinct regions with varying levels of coherence—though the spectrum may span multiple octaves, wavelengths generated far from the zero dispersion wavelength of the fiber are incoherent, especially for picosecond pulses [1.42]. It is possible to generate soliton-like structures with high coherence from extremely short (<100fs) pump pulses in the MIR (often anomalous dispersion) regime [1.43], but longer pulses lead directly to modulational instabilities that damage the fiber at low energies (i.e. the “rogue wave” phenomena [1.44]), and Raman scattering becomes a not-insignificant source of spectral energy density [1.41]. The problem is compounded by the fact that both modulational instabilities and Raman scattering are seeded via noise, leading to a shot-to-shot incoherence with ultra broadband supercontinua [1.43].

The most promising fiber-based solution is supercontinuum generated via hollow-core fibers [1.45] and Kagome fibers [1.46], which have been shown to be coherent, compressible, and broadband. But their output is both wavelength and pulse-duration dependant. A recent study [1.47] uses a Kagome-fiber for high-energy nonlinear broadening at  $2\mu\text{m}$ , but supercontinuum self-compression within the fiber was not possible due to modulational instabilities; an external, prism-based compression scheme was used after the fiber broadening stage.

On the other hand, generating high-energy supercontinua in bulk materials is, in practice, a very simple and inexpensive process that requires nothing more than an input focusing lens and nonlinear material (lengths ranging from 2mm to 20mm, based on the system). Bulk SCG is highly robust, and produces multi-octave broadband radiation in the MIR with high spectral energy densities of  $\sim 10 \text{ pJ/nm}$  [1.48, 1.49]. Bulk SC output has high temporal coherence [1.50] and spatial coherence as good as, or better than, the input pump source [1.51, 1.52]. Bulk SCG also shows good compressibility [1.53] and maintains the polarization state of the input, even at very high powers (given a suitable choice of bulk material)—see Chapter 3. Low pulse-to-pulse fluctuations and noise stability comparable to the input pump have been demonstrated [1.48, 1.54]. Most importantly, SC pulses in bulk preserve the carrier envelope phase of the input pulse [1.55], phase-lock in independently generated bulk-SC pulses have been demonstrated [1.56], as has phase-locked parametric amplification of portions of the spectral output of bulk SCG [1.57]. Given that SCG in bulk crystals with sub-picosecond [1.58] and picosecond pulses [1.59] has also been demonstrated, bulk supercontinuum generation is a viable solution for the IRDL project.

Nevertheless, despite its potential viability, SCG from a pump-source similar to the IRDL system's (3.2 picosecond Fourier-limited temporal width,  $2\mu\text{m}$  central wavelength,  $>100\mu\text{J}$  pulse energies) has never been reported in literature. The problem of generating sufficient spectral energy density at the target wavelengths in order to avoid parametric superfluorescence in the DFG/OPA stage [1.61] still remains. Studies are required to determine whether a multi-octave SC can be supported by this input pulse with

the same desirable characteristics reported by literature. Therefore, within the context of the overall IRDL project, this work focuses on various SCG experiments undertaken in the MIR, high-energy, and picosecond pulse-width regimes (with particular emphasis on enhancing spectral energy density on the Stokes side of the pump-pulse).

## 1.1 SCOPE OF THESIS

Chapter 1 provides an introduction to this work, brief background on the scientific objective of the IRDL system—Laser Selective Chemistry, and a summary of the IRDL system designed to meet this challenge. The author's contributions include the use of overtone/composition bands to study ground-states as a precursor to the final strong-field control experiments for Laser Selective Chemistry, conceptual design of proof-of-concept experiments, and inputs to the overall design of the IRDL system as well as the design of the pulse-shaping setup.

Chapter 2 provides theoretical background, and uses (or derives) analytical models to illustrate the bulk SCG process, with a focus on the MIR, high-energy, and long-pulse regimes. The author's contribution is the derivation of a combined Kerr Self-Focusing/Plasma Generation analytic model as a "poor-man's estimation tool" for SCG in bulk materials.

Chapter 3 provides an overview of the multiple SCG experiments conducted by the author, namely studies in supercontinuum generation at  $1\mu\text{m}$  wavelengths, induced polarization rotation/depolarization of supercontinuum generation in cubic crystals under intense input beams, experimental comparisons of supercontinuum generation in Diamond, Zinc Selenide (ZnSe), Yttrium-Aluminum Garnet (YAG) and Sapphire in the sub-2-cycle, MIR pulse regime, Stimulated Raman Amplification of supercontinuum spectra, and numerical analyses.

Finally, Chapter 4 summarizes the outcome and conclusions of this work: (a) a “recipe” for high-energy, long-pulse, MIR SCG, and (b) three feasible beamline designs for seed generation depending on the requirements and results of the subsequent parametric colour conversion/amplification stage. The chapter concludes with the outlook for the IRDL system, and further research inputs that are required (particularly temporal and phase characterization of the SC output) for using the seed light generated for a parametric amplification setup.

## 1.2 BRIEF INTRODUCTION TO LASER SELECTIVE CHEMISTRY

The output pulse requirements of the IRDL project (three phase-locked, sub-100 femtosecond, pulses at 3, 7, and 8 $\mu\text{m}$  wavelengths, with 1mJ of energy per pulse) are born out the long-held dream of Laser Selective Chemistry (LSC) [1.4]—the ability to tune the laser wavelength to a molecule’s specific ground-state bond excitation frequency and drive the bond to its dissociation limit.

Since the 1980s, groups have focused significant research efforts towards the creation of a generally applicable Laser Selective Chemistry scheme [1.13], but have been unsuccessful due to various factors including the low maturity of key laser technologies (2 $\mu\text{m}$  lasers, phase-control of femtosecond pulses [1.65]) and limitations in approach. The problem, however, is far from intractable; LSC-like phenomena have been reported in literature recently, albeit only for small molecular systems with bonds of uncommonly low activation energies [1.14 – 1.15] and anomalously sparse vibrational density of states.

At low excitation energy for a given mode, the potential defining a molecular vibration is well approximated as a harmonic oscillator (Figure 1.1, left). At higher excitation energies, the system is driven to higher quantized energy levels that become increasing closer in energy spacing or higher density of states—the states come to resemble a “continuum”. But, realistically, the molecule’s motion begins to exhibit strong anharmonicity through which vibrational modes are coupled to one another (Figure 1.1, right). It is the far-from-equilibrium motions that ultimately sample the strongly anharmonic

potential in the barrier region that mix modes and lead to highly localized motions in the superposition state that ultimately give rise to the chemistry [1.10].

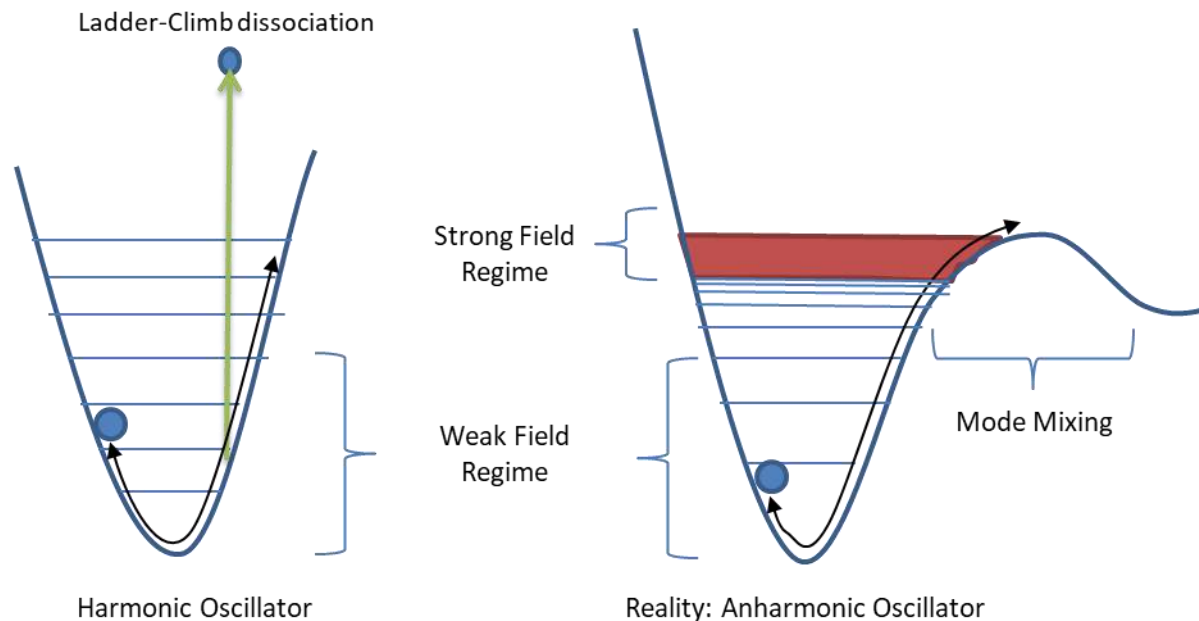


Figure 1.1: Potential Energy Surface characterizing molecular vibration—harmonic oscillator idealization (left) and anharmonic oscillator (right).

There is some debate as to whether LSC is, in fact, possible at all [1.4]: the anharmonic coupling of bonds at high vibrational excitation leads to rapid Intramolecular Vibrational energy Redistribution (IVR), and the sample is simply heated, much as it would be via a Bunsen burner—any question of bond-selective chemistry is rendered moot. However, progress has been made via various coherent control strategies [1.5, 1.11, 1.21] to optimize the production of a target state, and it has recently been shown that there are only a few key modes driving chemistry [1.8-1.10], even for complex systems. For LSC to be possible, not one mode, but several, must be driven (or suppressed) at a timescale faster than the action of IVR [1.11]. Bloembergen et al. [1.16] discuss how IVR can affect the reactivity of a polyatomic system such as  $\text{CF}_3\text{Br}$  when tuning the laser frequency close to the C—F stretch vibration. IVR leads to an ergodic ensemble within a few picoseconds, resulting in the breaking of the weakest bond—the C-Br

bond. In other words, bond-selective multiphoton excitation of a polyatomic molecule in the ground electronic state is restricted by IVR.

There has been success in targeting specific bonds for small molecular systems in which the density of vibrational states are sparse. For example, nonstatistical behavior of fragmentation due to ultrafast electronic activation has been reported, but this was accomplished through the limited vibrational states accessible from the Franck-Condon region [1.18]. Higher levels of control have been demonstrated by Windhorn et al. [1.14], in which they reported nonstatistical dissociation of bonds in diazomethane and metal carbonyls in the gas phase by resonant multiphoton excitation of vibrations using femtosecond IR laser pulses. However, these two molecular systems have anomalously low activation energies - 35–40 kcal/mol (12 000–14 000  $\text{cm}^{-1}$ ); at low energies, vibrational energy-levels are widely spaced and do not couple, providing a special case based on the particular configuration of the selected molecules. The Windhorn study [1.14] concluded that only a few vibrational degrees of freedom were involved in their specific excitation process. They also reported that the  $\text{CH}_2$  group bends significantly out of the molecular plane prior to the dissociation, demonstrating coupling of bending and stretching vibrational modes even at these low energies. Again, the approach was single modal control (irrespective of the observation of multimode character of energy distribution) is far from optimal and cannot be exported to other systems.

There are other systems with unusual IVR characteristics that make LSC more feasible. Stromberg et al. [1.19] studied the vibrational dynamics induced in free  $\text{W}(\text{CO})_6$  molecules in gas-phase as a result of the one-photon excitation of the C-O bond vibration. For this specific molecule, the IVR occurs with a characteristic time of 1.3 ns, and a study by Chekalin et al. [1.20] states that the slow rate of IVR from vibrational modes of the C—O bond is characteristic for all metal carbonyl molecules of this timescale, creating precisely the circumstances under which mode-selective excitation by Windhorn et al. [1.14] took place to the dissociation limit.

LSC for molecular systems with stable covalent bonds and activation energies higher than 50 kcal/mole has, so far, failed [1.21]. Kompanets et al. [1.22] also reported selective multiphoton excitation of the  $\nu_1 = 2194 \text{ cm}^{-1}$  of the asymmetric vibration of the C=C=O bond, noticeable up to the level  $v = 7$ . The study reports the appearance of an instantaneous ( $\tau \ll \tau_{\text{IVR}}$ ) signal of an induced absorption in the nonresonant modes. The authors concluded that the form of the subsequent evolution of this signal and its corresponding characteristic times proved to be different for different modes, which was related to the occurrence of different pathways for the vibrational energy migration in the molecule.

Solving the LSC problem, then, can be seen as a issue of timing and multiplicity of mode; the technical solution is a laser capable of delivering phase-locked pulses at *multiple* selected frequencies, with a shaped pulse temporal profile that is shorter than the IVR timescale for each of the bonds being targeted.

The key objectives required to achieve LSC are multi-mode coherent-control optical drivers operating in a phase-locked manner at a timescale that is shorter than the IVR timescale for each of the bonds being targeted. For example, if we look at selectively breaking bonds within the water molecule—a notoriously difficult system to study due to the very strong coupling between intra and inter molecular bonds that leads to IVR at short timescales—we can see from Table 1 that even in the simplest case to consider, one would have to drive both the stretch and bend modes (approximately 2.7 and 6.5 $\mu\text{m}$ ) at a timescale faster than the shortest IVR (“energy leaking”) timescale, i.e. 270 fs, but with a precise phase relationship between the two driving wavelengths.

Even *if* the control and mode-coupling problem is as simple as outlined above, this form of multi-mode coherent control is not guaranteed to lead to dissociation—as higher and higher states are reached via the applied electric field of the driving laser, the spacing between successively higher states approaches smaller and smaller values, up to the strong-field “continuum”, requiring longer and longer driving

wavelengths at each step. In other words, the IR bandwidth required to support vibrational ladder climbing to dissociation, even with multi-mode control, may be impossible to achieve, and even if a system's bandwidth was realistic (i.e. within the 2 - 20 $\mu$ m window of the IRDL system's targeted capability), at some point the molecule's rotational and librational modes *will* inevitably be activated by the long portions of the driving pulse—mode selectivity will be lost once again, this time due to the broadband nature of the pulse demanded by the strong-field energy spacing.

But what if it *is* possible to pump energy into multiple modes with a single, shorter (IR) wavelength pulse at faster-than-IVR timescales? The potential "well", is a multi-dimensional surface, after all, and a trajectory could, possibly, be found that leads to a conical intersection or dissociation pathway without pushing the system into the extremely high density of states region—not a ladder climb, but an  $n$ -dimensional trek through more favourable (less steep) landscapes (Figure 1.2).

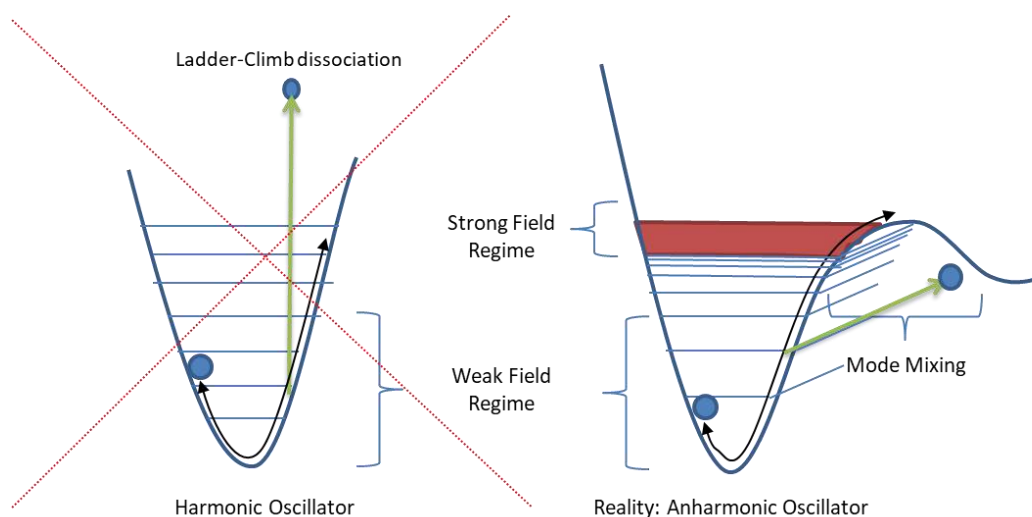


*Figure 1.2: Alternative to Ladder-Climbing (multi-mode vector trajectory with a single pulse)*

While only a thought-experiment at this point, the author proposes the use of a single, shorter-wavelength IR pulse tuned to the overtone and combination vibrational frequencies of a molecular system in order to simultaneously suppress multiple key modes of the molecular system, with a phase-locked, longer-wavelength pulse aimed at the most favourable dissociation mode (C-H stretch, for

example) to provide the “kick” necessary for the system to traverse the energy barrier. Overtone and combination-overtone bands have never previously been used for LSC or other pump-based experiments because of the bands’ relative weakness with respect to the fundamental. However, the IRDL system will have extremely high energies (on the order of mJ) available around the 2 $\mu$ m pump wavelength, and the Anti-Stokes side of the pump (on the order of hundreds of  $\mu$ m) due to the asymmetric spectral broadening of the SCG setup and the very specific higher-harmonic cascaded filament response of ZnSe (See Chapter 5). Instead of discarding this energy in favor of the longer-wavelength-activated fundamental bands, it can be used to drive combination/overtone of the key molecular vibrations. In the worse case, the energy available can be used to map out portions of the multi-dimensional potential energy surface in a manner that may not be possible otherwise (if, say, the fundamental of some mode lies outside the scope of the output parameters of the IRDL system).

The LSC experimental phase of the IRDL project requires significant theoretical inputs regarding specific target wavelengths, pulse durations and pulse shapes. The starting basis for open loop control of the pulse shaping should (ideally) be determined using time dependent DFT calculations and Multiconfigurational Time Dependent Ab Initio methods along with optimal control theory. In the event that theoretical models require experimental data to narrow down the parameter space, two proof-of-concept experiments are proposed; it is hoped that even if theoretical models cannot provide final parameters for pulse shapes and wavelengths, the experimental output of the proof-of-concept studies can be used to coarse-tune parameters as an initial starting point for LSC with the IRDL system.

### 1.2.1 Water Vapor Pump-Probe Study

While experimental applications are out of the scope of this thesis, “way-finding” experiments are proposed. The point of the Water Vapor Pump-Probe study is not to drive the system to dissociation, but to determine whether the IVR timescales for ground-state vibrational modes *can* be mapped using a

multi-frequency setup (Proof of Concept), a first step in demonstrating the potential for controlling the modes with a more advanced system.

Liquid water is one of the most difficult systems to study with respect to IVR—as seen from Table 1, the lower bound for IVR timescales for the Libration modes is 30 fs, and 270 fs for the OH Bend. However, most of the wavelengths of interest fall precisely in the achievable range for the nonlinearly broadened fundamental wavelengths of the IRDL pump source: high-energy, unshaped pulses centered at 2050nm. The  $\sim 100\mu\text{J}$  of broadband energy available from the nonlinearly broadened seed in this region (See Chapter 4) provide an excellent opportunity to contribute to the scientific understanding of water vibrational modes, as well as characterize the IRDL system and diagnostics in preparation for more challenging experiments.

If the IRDL color-generation system can produce a high-energy pulse at  $\sim 1900$  nm targeting the  $av_1 + v_2 + bv_3$  combination band (compressed to sub-200 fs pulse duration), with lower energies available in the 2500 – 2800 nm wavelength region, the precise IVR timescales and response of the symmetric and asymmetric OH stretch bands can be mapped using a pump-probe system, while a Fourier Transform Infrared Spectrometer (FTIR) can be used to monitor energy leakage into the bend mode.

*Table 1: Water Vapor Vibrational Modes and IVR Timescales*

Mode	Name	nm	IVR Timescale Lower Bound (fs)	Bond energy Value
v1	Symmetric OH Stretch	2735	1000	464 kJ
v2	OH Bend	6271	600 [1.36], 270 [1.36, 1.37]	?
v3	Asymmetric OH Stretch	2663	1000	?
L1	Libration 1	25316	30 [1.37]	?
L2	Libration 2	14577	30 [1.37]	?
$v_2(1)$	Bend First Overtone	3174	600 [1.36], 270 [1.36, 1.37]	?
$av_1 + v_2 + bv_3; a+b=1$	<b>Combination Overtone</b>	<b>1901</b>	?	?

### 1.2.2 Dual-Wavelength C-H Overtone & Combination Band Study

The second proposed study involves the C-H bands of an organic molecule, a first step in studying Benzene. Using a setup similar to the water vapor proof-of-concept study, energy-transfer and vibrational activation of a candidate molecule (for example CH<sub>4</sub>) can be studied by driving the fundamental C-H stretch vibrational mode in the ~3000 [nm] regime, and probed using a combination vibrational band in the VIS/NIR regime. Simple phase-delays introduced between each frequency “arm” may be used to study whether the excitation of bend modes has an effect on the energy transfer out of the C-H stretch mode.

## 1.3 IRDL SYSTEM OVERVIEW

The design-to output parameters of the system arise out of the targeted molecular vibrational modes of Benzene [1.23, 1.24] at 3265nm, 6279nm, and 8696nm. A 100fs pulse duration is desired in each wavelength to ensure sub-IVR timescales of the pulses. At the targeted wavelengths, a 100 fs transform-limited pulse has a bandwidth of 157 nm, 666 nm and 1112 nm, respectively. As an aside, note that given the 1 $\mu$ m bandwidth targeting the longest fundamental-mode driving wavelength, it is clear that mode selectivity will be lost entirely in this region; this may necessitate the use of the combination/overtone band approach regardless of whether the fundamental can be activated or not.

The experiment requires molecular fragments to be detected with high precision. A mass-spectrometer, procured by the Miller Mass-Spectrometry subgroup, will be utilized for this purpose. Additionally, the High Energy Mid-IR laser system will be coupled to a state of the art compact DC driven electron diffraction system [1.25]. This Femtosecond Electron Diffraction (FED) subsystem is capable of delivering sub-100 fs electron pulses to the sample system of interest to probe its structure. Such short electron pulses are otherwise only achievable using rf-driven electron accelerators, which are more complicated, more expensive and prone to failure. Using this electron diffraction system in combination with the Mid-

IR laser system, it will be possible to exploit the goals of LSC with probe pulses on the shortest time scales of interest for chemistry and biology. The electron source will be optimized to operate with 300 KV electrons to obtain the highest time resolution for gas phase studies taking into account velocity mismatch time broadening through the sample region. The source opens up the study of systems as thick as 1 micron and bridges the gas phase to solution phase gap in atomically resolved structure dynamics.

Figure 1.3 shows the overall system block diagram for the proposed IRDL and LSC detection setup. Given the challenging performance requirements of the proposed system and the hitherto unexplored territory in terms of both engineering development and scientific inputs, the IRDL system will be developed in phases. Scientific studies, carried out in parallel with subsystem and beamline development were/will be used to inform the design and test parameters of subsequent development (outlined in Table 2, red items highlight the focus of this thesis).

*Table 2: IRDL Project Phases and Experiments*

<i>Phase</i>	<i>Laser Development</i>	<i>Scientific Study</i>
0	System design	MIR high energy amplification, parameter optimization
1	Oscillator & Main Amplifier	<b>Broadband Seed Generation</b>
2	<b>Nonlinear Broadening</b>	Parametric Amplification (DFG & OPA) Parameter Optimization
3	Parametric Color Generation & Amplification	2 $\mu$ m Pump-Probe Spectroscopy of Water Vapor, "Proof of Concept"
4	Diagnostics and Detection Setup	
5	Pulse Shaping	Dual-Wavelength C-H Overtone & Combination Band Study, "Proof of Concept"
6	Beamline Integration with Electron Gun and Mass Spectrometer	
7	Laser Selective Chemistry Experiments: Benzene, the "Holy Grail"	

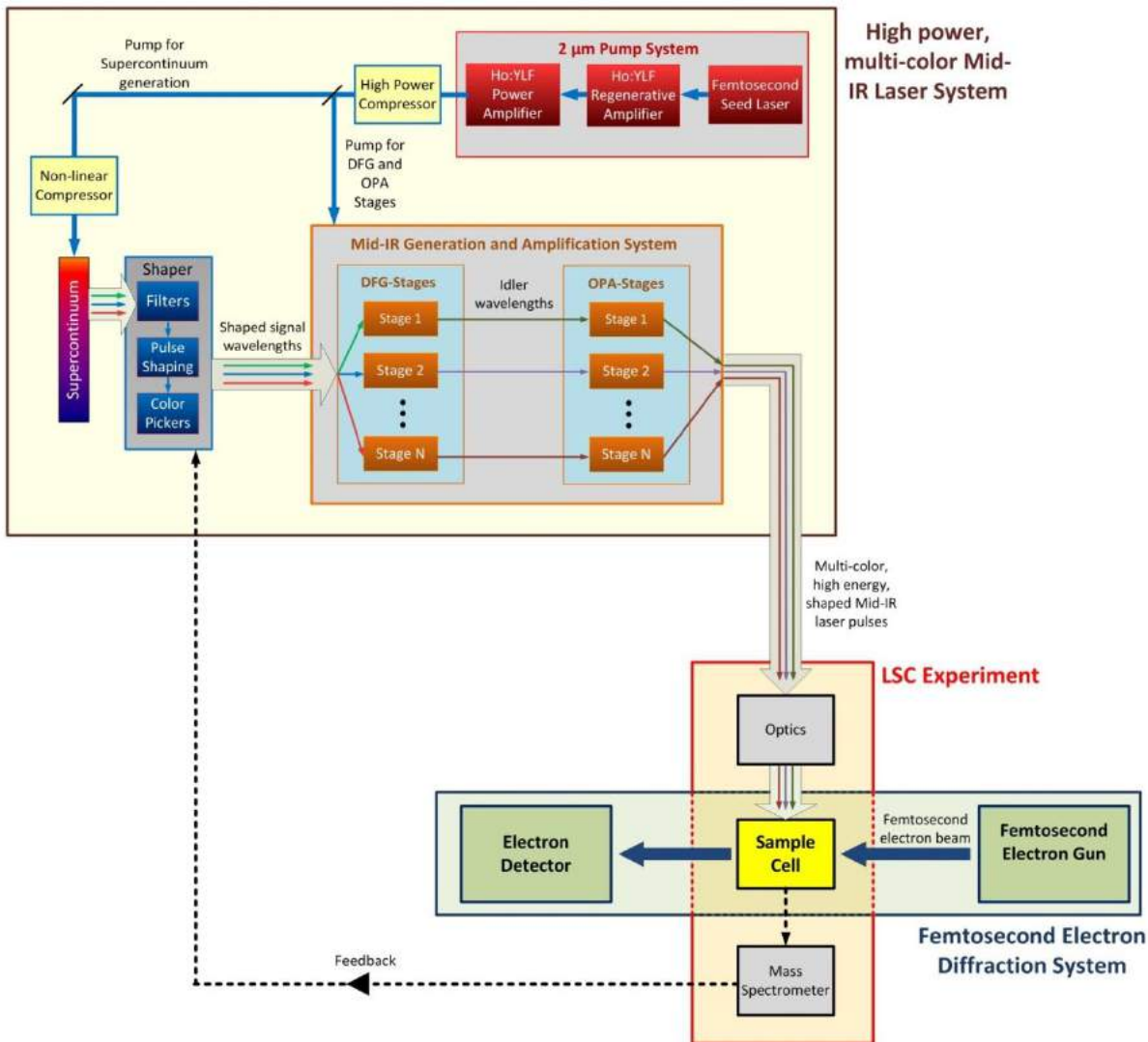


Figure 1.3: Figure 1: System Block Diagram of the IRDL System and LSC Setup

A 2  $\mu\text{m}$  high energy laser serves as the basis of the optical setup. It will be used to generate broadband supercontinuum spectra and to pump the Mid-IR generation and amplification stages via difference frequency generation (DFG) and optical parametric amplification (OPA). As the supercontinuum generation and the DFG+OPA schemes are pumped by a single laser, the generated Mid-IR wavelengths will automatically be passively phase-locked. The IRDL system modules are as follows:

**The Oscillator:** A Ho: fiber oscillator providing nJ, 1ps pulses at 2 $\mu\text{m}$ . This system was developed by the FS-LA group at DESY [1.26]. Further details of the oscillator are provided in Chapter 3.

**The Main Amplifier (pump source):** a Ho:YLF Regenerative Amplifier (RA) developed in-house [1.27]. With a repetition rate of 1 kHz, it amplifies the pulses from the laser oscillator to pulse energies of 10 mJ, which is close to the practical limit due to high depolarization losses of commercial RTP poekels cells. Significant effort has been put into the design of the three laser stages, to guarantee highly stable and low noise laser amplification to high pulse energies. Various laser gain materials provide laser amplification at 2  $\mu\text{m}$ , but Ho:YLF can provide the required properties that are necessary to develop high energy laser amplifiers. These properties include a high damage threshold, negligible thermal lensing, natural birefringence and a small saturation fluence that enables very effective energy transfer from the laser gain media into the laser fields [28, 29]. Further details of the realized RA sub-system are provided in Chapter 3. A multi-pass to boost pulse energies to  $\sim 60$  mJ is a planned addition to the main amplifier sub-system, required to reach the eventual IRDL goal of 1mJ per shaped pulse at each MIR frequency.

**Nonlinear Broadening:** The outcome of this thesis, the nonlinear broadening scheme for the IRDL system is baselined in Chapter 4.

**Parametric Color Generation/Amplification Sub-System:** A highly flexible approach has been chosen to generate tunable broadband laser radiation which will allow a study of a wide range of target molecules in later experimental studies. To cover the wavelength range from 3  $\mu\text{m}$  to 10  $\mu\text{m}$ , a two-crystal approach will be implemented. The CSP and KTA crystals can generate sub-3  $\mu\text{m}$  to 4  $\mu\text{m}$  or to 6.5  $\mu\text{m}$  pulses, respectively [1.30, 1.31]. For longer wavelengths, ZGP is the most promising crystal, which offers a very high nonlinearity of 75 pm/V, high thermal conductivity and hardness [1.32, 1.33]. Both ZGP and CSP provide exceptional phase matching capabilities in the Mid-IR regime, covering their complete transparency range. The type 1 phase matching curves for ZGP and CSP and the corresponding values for their effective nonlinearities  $d_{\text{eff}}$  are shown in figure 2. These curves emphasize the possibility to generate and amplify pulses in a broad Mid-IR regime to high pulse energies while maintaining a large enough bandwidth to support various LSC experiments.

There is some doubt at the moment as to whether (a) the seed needs to be compressed for the parametric amplification stage, or whether the uncompressed seed would be better matched to the 3.2ps pump, and (b) whether the residual pump itself should be compressed for the first color conversion (DFG) stage. The results from simulations out of the parametric amplification group will inform the compression choice.

In the case that only a single DFG stage is baselined (in the case that the physical chemistry theory group determines that the output of the first color conversion stage is energetic enough to begin scientific experiments), a multi-channel, AOM (Acousto-Optic-Modulator) based pulse shaper has been designed, and components obtained such that the system is in a ready-to-assemble state.

**Pulse Shaping:** As phase and amplitude shaping in the mid-IR automatically removes SLMs from consideration, germanium AOMs are the most robust solution available for this regime. The shape of the optical pulse diffracted by the AOM crystal is determined by the phase and amplitude of the acoustic pulse from an arbitrary waveform generator, and the requirement of having the multiple frequencies phase-locked to each other in order to drive multiple modes simultaneously necessitates the use of complex electronics for pulse synchronization. A closed-loop feedback scheme (with output from the mass spectrometer) is envisaged for use in conjunction with a learning algorithm—a standard solution in literature for coherent control [1.34].

The designed shaper is shown in Figure 1.4. An ISOMET Tellurium Oxide AOM will be used for pulses near the 2 $\mu\text{m}$  wavelength, and two ISOMET Germanium High-Energy AOMs (one for the 2.5 $\mu\text{m}$  - 5 $\mu\text{m}$  arm, and one for the 5 $\mu\text{m}$  - 9 $\mu\text{m}$  arm) will be used for the deeper MIR. Matched RF drivers driven by synchronized, phase-locked, 3-channel signals from a signal generator will drive the AOMs, while an RF analyzer will be used as a feedback source to maintain RF drift within parameters and ensure signal

quality. Water-based cooling will be provided to the AOMs and RF drivers using a 2kW Thermotek chiller.

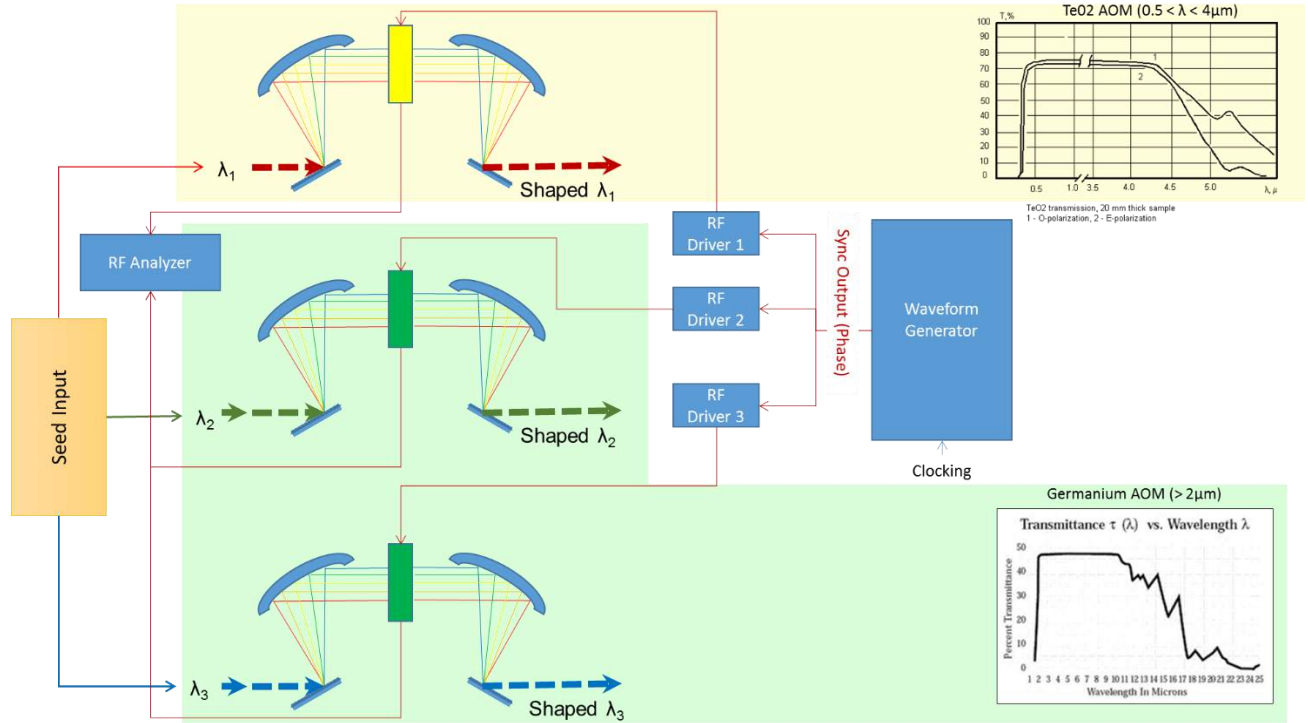


Figure 1.4: Baseline Pulse Shaper

## 1.4 REFERENCES

- [1.1] Allaria, E., et al. "Two-colour pump–probe experiments with a twin-pulse-seed extreme ultraviolet free-electron laser." *Nature communications* 4 (2013).
- [1.2] Miller, David AB, et al. "Band-edge electroabsorption in quantum well structures: The quantum-confined Stark effect." *Physical Review Letters* 53.22 (1984): 2173.
- [1.3] Popov, Vladimir Stepanovich. "Tunnel and multiphoton ionization of atoms and ions in a strong laser field (Keldysh theory)." *Physics-Uspekhi* 47.9 (2004): 855-885.
- [1.4] Zewail, Ahmed H. "Laser selective chemistry—is it possible?." *Physics Today* 33.11 (1980): 27-33.
- [1.5] Armenise, I., and F. Esposito. "N<sub>2</sub>, O<sub>2</sub>, NO state-to-state vibrational kinetics in hypersonic boundary layers: the problem of rescaling rate coefficients to uniform vibrational ladders." *Chemical Physics* 446 (2015): 30-46.
- [1.6] Shen, X. J., et al. "Towards bond selective chemistry from first principles: methane on metal surfaces." *Physical review letters* 112.4 (2014): 046101.
- [1.7] Lisaj, Mateusz, and Oliver Kühn. "Laser-driven localization of collective CO vibrations in metal-carbonyl complexes." *The Journal of chemical physics* 141.20 (2014): 204303.
- [1.8] M. Gao et al. "Mapping Molecular Motions Leading to Charge Delocalization Using Ultrabright Electrons", *Nature* 2013 (496), 343-346.
- [1.9] H. Jean-Ruel et al. "Ring Closing Reaction in Diarylethene Captured by Femtosecond Electron Crystallography", *The Journal of physical chemistry B* 2013, 117 (49) 15894–15902.
- [1.10] R. J. Dwayne Miller. "Atomically Resolved Dynamics: The Chemist's Gedanken Experiment Enters the Lab Frame". *Ann. Rev. Phys.*
- [1.11] Shen, X. J., et al. "Towards bond selective chemistry from first principles: methane on metal surfaces." *Physical review letters* 112.4 (2014): 046101.
- [1.12] Smolski, V. O., et al. "Cr: ZnS laser-pumped subharmonic GaAs optical parametric oscillator with the spectrum spanning 3.6–5.6  $\mu\text{m}$ ." *Optics letters* 40.12 (2015): 2906-2908.
- [1.13] Z. Ahmed. "Laser Selective Chemistry: A New Challenge for Chemists and Physicists." *Engineering and Science* 43.3 (1980): 8-13.
- [1.14] L. Windhorn et al. "Getting ahead of IVR: a demonstration of mid-infrared induced molecular dissociation on a sub-statistical time scale." *The Journal of chemical physics* 119.2 (2003): 641-645.

- [1.15] R. J. D. Miller. "Making the Molecular Movie: Quest for the Structure-Function Correlation of Biology", Lecture: Departments of Chemistry and Physics, University of Toronto, [http://www.mitr.p.lodz.pl/evu/lectures/Miller\\_Lecture.pdf](http://www.mitr.p.lodz.pl/evu/lectures/Miller_Lecture.pdf).
- [1.16] N. Bloembergen, A. H. Zewail. "Energy redistribution in isolated molecules and the question of mode-selective laser chemistry revisited. New experiments on the dynamics of collisionless energy redistribution in molecules possibilities for laser-selective chemistry with subpicosecond pulses." *The Journal of Physical Chemistry* 88.23 (1984): 5459-5465
- [1.17] Song, Di, et al. "Anharmonic Rice-Ramsperger-Kassel-Marcus (RRKM) and product branching ratio calculations for the partially deuterated protonated water dimers: Dissociation and isomerization." *The Journal of chemical physics* 138.10 (2013): 104301.
- [1.18] E. W-G Diau et al. "Femtosecond activation of reactions and the concept of nonergodic molecules." *Science* 279.5352 (1998): 847-851.
- [1.19] C. Stromberg, D. J. Myers, and M. D. Fayer. "Vibrational dynamics of large hot molecules in the collisionless gas phase." *The Journal of chemical physics* 116.9 (2002): 3540-3553.
- [1.20] S. V. Chekalin et al. "Intramolecular Vibrational Dynamics in Free Polyatomic Molecules with C=O Chromophore Bond Excited by Resonant Femtosecond IR Laser Radiation." *The Journal of Physical Chemistry A* (2014).
- [1.21] V. M. Apatin et al. "Excitation and dissociation of polyatomic molecules under the action of femtosecond infrared laser pulses." *Russian Journal of Physical Chemistry B* 1.2 (2007): 113-119.
- [1.22] V. O. Kompanets et al. "Direct observation of the vibrational energy redistribution in (CF<sub>3</sub>)<sub>2</sub>CCO molecules resonantly excited by femtosecond infrared laser radiation." *JETP letters* 92.3 (2010): 135-139.
- [1.23] Wilson Jr, E. Bright. "The normal modes and frequencies of vibration of the regular plane hexagon model of the benzene molecule." *Physical Review* 45.10 (1934): 706.
- [1.24] Wesolowski, Tomasz Adam, et al. "Comparative Study of Benzene- $\pi$ -X (X= O<sub>2</sub>, N<sub>2</sub>, CO) Complexes Using Density Functional Theory: The Importance of an Accurate Exchange-Correlation Energy Density at High Reduced Density Gradients." *The Journal of Physical Chemistry A* 101.42 (1997): 7818-7825.
- [1.25] Daoud, Hazem, Klaus Floettmann, and R. J. Dwayne Miller. "Compression of high-density 0.16 pC electron bunches through high field gradients for ultrafast single shot electron diffraction: The Compact RF Gun." *Structural Dynamics* 4.4 (2017): 044016.
- [1.26] Li, Peng, et al. "Low noise, tunable Ho: fiber soliton oscillator for Ho: YLF amplifier seeding." *Laser Physics Letters* 13.6 (2016): 065104.
- [1.27] Kroetz, Peter, et al. "High energetic and highly stable pulses from a Ho: YLF regenerative amplifier." *Proc. SPIE*. Vol. 9726. 2016.

- [1.28] Kroetz, Peter, et al. "Overcoming bifurcation instability in high-repetition-rate Ho: YLF regenerative amplifiers." *Optics letters* 40.23 (2015): 5427-5430.
- [1.29] Dergachev, A., "High-energy, kHz-rate, picosecond, 2- $\mu$ m laser pump source for mid-IR nonlinear optical devices." *Proc. SPIE 8599*, 85990B (2013).
- [1.30] Chalus, O, et al. "Optical parametric generation in CdSiP<sub>2</sub>." *Optics Letters*, 35.24 (2010).
- [1.31] Malevich, P. et al. "High energy and average power femtosecond laser for driving mid-infrared optical parametric amplifiers." *Optics Letters* 38.15 (2013).
- [1.32] Petrov, V., et al. "Femtosecond parametric generation in ZnGeP<sub>2</sub>." *Optics Letters*, 24.6 (1999).
- [1.33] Dergachev, A., et al. "High-power, high-energy ZGP OPA pumped by a 2.05- $\mu$ m Ho:YLF MOPA system." *Proc. SPIE 6875* (2008).
- [1.34] Levin, Liat, et al. "Coherent control of bond making." *Physical review letters* 114.23 (2015): 233003.
- [1.35] Chaplin, Martin, "Water Structure and Science", [http://www1.lsbu.ac.uk/water/water\\_vibrational\\_spectrum.html](http://www1.lsbu.ac.uk/water/water_vibrational_spectrum.html), created 2000, last-retrieved 12/07/2017.
- [1.36] Deàk, John C., et al. "Vibrational energy relaxation and spectral diffusion in water and deuterated water." *The Journal of Physical Chemistry A* 104.21 (2000): 4866-4875.
- [1.37] Ingrosso, Francesca, et al. "Ultrafast energy transfer from the intramolecular bending vibration to librations in liquid water." *The Journal of Physical Chemistry A* 113.24 (2009): 6657-6665.
- [1.38] Shen, Yuen-Ron. "The principles of nonlinear optics." *New York, Wiley-Interscience, 1984, 575 p.* (1984).
- [1.39] Petersen, Christian Rosenberg, et al. "Mid-infrared supercontinuum covering the 1.4–13.3  $\mu$ m molecular fingerprint region using ultra-high NA chalcogenide step-index fibre." *Nature Photonics* 8.11 (2014): 830-834.
- [1.40] Buccoliero, Daniel, et al. "Thulium pumped high power supercontinuum in loss-determined optimum lengths of tellurite photonic crystal fiber." *Applied Physics Letters* 97.6 (2010): 061106.
- [1.41] Dudley, John M., Goëry Genty, and Stéphane Coen. "Supercontinuum generation in photonic crystal fiber." *Reviews of modern physics* 78.4 (2006): 1135.
- [1.42] Genty, Goëry, John M. Dudley, and Benjamin J. Eggleton. "Modulation control and spectral shaping of optical fiber supercontinuum generation in the picosecond regime." *Applied Physics B: Lasers and Optics* 94.2 (2009): 187-194.

- [1.43] Genty, Goëry, Stéphane Coen, and John M. Dudley. "Fiber supercontinuum sources." *JOSA B* 24.8 (2007): 1771-1785.
- [1.44] Solli, D. R., et al. "Optical rogue waves." *Nature* 450.7172 (2007): 1054.
- [1.45] Faccio, Daniele, et al. "Optical amplification in the near-infrared in gas-filled hollow-core fibers." *Optics letters* 34.19 (2009): 2918-2920.
- [1.46] Debord, Benoît, et al. "Milli-Joule energy-level comb and supercontinuum generation in atmospheric air-filled inhibited coupling Kagome fiber." *Lasers and Electro-Optics (CLEO), 2015 Conference on*. IEEE, 2015.
- [1.47] Murari, Krishna, et al. "Kagome-fiber-based pulse compression of mid-infrared picosecond pulses from a Ho: YLF amplifier." *Optica* 3.8 (2016): 816-822.
- [1.48] Bradler, Maximilian, Peter Baum, and Eberhard Riedle. "Femtosecond continuum generation in bulk laser host materials with sub- $\mu$ J pump pulses." *Applied Physics B* 97.3 (2009): 561.
- [1.49] Silva, F., et al. "Multi-octave supercontinuum generation from mid-infrared filamentation in a bulk crystal." *Nature communications* 3 (2012): 807.
- [1.50] Chin, See Leang, et al. "The white light supercontinuum is indeed an ultrafast white light laser." *Japanese journal of Applied physics* 38.2A (1999): L126.
- [1.51] Watanabe, Wataru, and Kazuyoshi Itoh. "Spatial coherence of supercontinuum emitted from multiple filaments." *Japanese Journal of Applied Physics* 40.2R (2001): 592.
- [1.52] Prade, Bernard, et al. "Spatial mode cleaning by femtosecond filamentation in air." *Optics letters* 31.17 (2006): 2601-2603.
- [1.53] Wegkamp, Daniel, et al. "Phase retrieval and compression of low-power white-light pulses." *Applied Physics Letters* 99.10 (2011): 101101.
- [1.54] Van de Walle, Aymeric, et al. "Spectral and spatial full-bandwidth correlation analysis of bulk-generated supercontinuum in the mid-infrared." *Optics letters* 40.4 (2015): 673-676.
- [1.55] Manzoni, C., et al. "Optical-parametric-generation process driven by femtosecond pulses: Timing and carrier-envelope phase properties." *Physical Review A* 79.3 (2009): 033818.
- [1.56] Bellini, Marco, and Theodor W. Hänsch. "Phase-locked white-light continuum pulses: toward a universal optical frequency-comb synthesizer." *Optics letters* 25.14 (2000): 1049-1051.
- [1.57] Baum, Peter, et al. "Phase-locked ultrashort pulse trains at separate and independently tunable wavelengths." *Optics letters* 30.15 (2005): 2028-2030.
- [1.58] Calendron, Anne-Laure, et al. "White-light generation with sub-ps pulses." *Optics express* 23.11 (2015): 13866-13879.

- [1.59] Indra, Lukáš, et al. "Stable Supercontinuum Generation in YAG with Picosecond Pulses." *CLEO: Applications and Technology*. Optical Society of America, 2017.
- [1.60] Schmidt, Bruno E., et al. "CEP stable 1.6 cycle laser pulses at 1.8  $\mu\text{m}$ ." *Optics express* 19.7 (2011): 6858-6864.
- [1.61] Moses, J., et al. "Highly stable ultrabroadband mid-IR optical parametric chirped-pulse amplifier optimized for superfluorescence suppression." *Optics letters* 34.11 (2009): 1639-1641.
- [1.62] Brida, D., et al. "Few-optical-cycle pulses tunable from the visible to the mid-infrared by optical parametric amplifiers." *Journal of Optics* 12.1 (2009): 013001.
- [1.63] Cerullo, Giulio, et al. "Few-optical-cycle light pulses with passive carrier-envelope phase stabilization." *Laser & Photonics Reviews* 5.3 (2011): 323-351.
- [1.64] Wienke, Andreas, et al. "700 MW peak power of a 380 fs regenerative amplifier with Tm:YAP." *Optics express* 23.13 (2015): 16884-16889.
- [1.65] Xu, Lin, et al. "Route to phase control of ultrashort light pulses." *Optics letters* 21.24 (1996): 2008-2010.

## 2 BULK SUPERCONTINUUM GENERATION THEORY

---

### 2.1 INTRODUCTION

This chapter provides an overview of established theory behind the dynamics of bulk supercontinuum generation (SCG). The dominant nonlinear mechanisms and their interplay is illustrated via analytical models, and a combination of these models is used to derive an estimation tool for parameter and nonlinear media selection in operative regimes where literature may be scarce or starting parameters unknown. All material parameters used for the numerical models illustrated or derived in this chapter are listed in Appendix A.

Supercontinuum (SC) generation is a highly nonlinear frequency conversion phenomena [2.1] observed in nonlinear media—fibers [2.2], gasses [2.3], and condensed media (bulk materials) [2.4]. A relatively narrowband, high peak power laser pulse is broadened via the interaction of hundreds of nonlinear processes [2.1] (including Kerr self-focusing, plasma generation, and group velocity dispersion) as it propagates through the nonlinear medium.

The SC pulse exhibits a (pseudo) self-waveguiding properties—the SC beam remains localized for distances far in excess of the diffraction length of the beam, often in the order of kilometers for SC pulses generated in air [2.1]. SC generation in gasses or condensed media is sometimes also referred to as filamentation, due to the formation of a “filament—a weakly ionized “plasma trail” in the wake of the pulse (Figure 2.1) [2.5]. Note that the formation of plasma and filamentation in a fiber SC process would result in damage to the fiber [2.2].

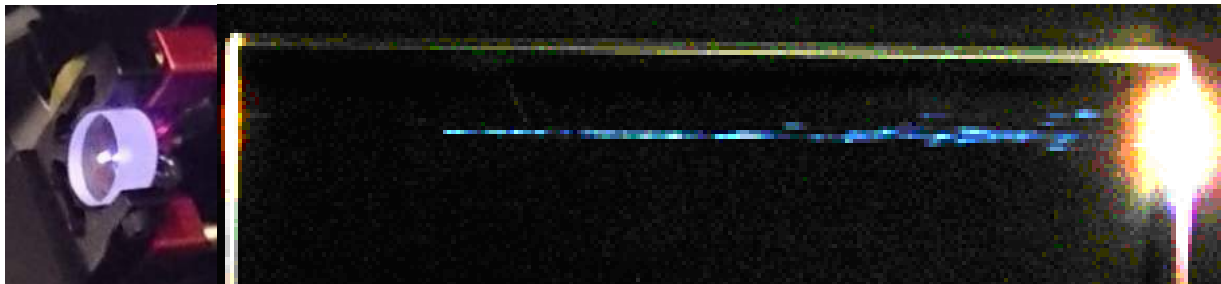


*Figure 2.1: SC Plasma Trail in YAG with the FLASH-2 Facility Laser (left), Plasma filament in bulk glass from Heriot Watt University Non-Linear Optics Group [2.5] (right).*

The SC process produces a very characteristic spatial and spectral output. The transverse spatial output of the SC beam (Figure 2.2) contains a bright White Light (WL) core (that may or may not be bright white in the visible spectral region, depending on the pump wavelength—the most intense part of the core is comprised of wavelengths of the pump region), and Conical Emission (CE)—coloured rings in an anti-diffraction pattern around the core with very large divergence angles.

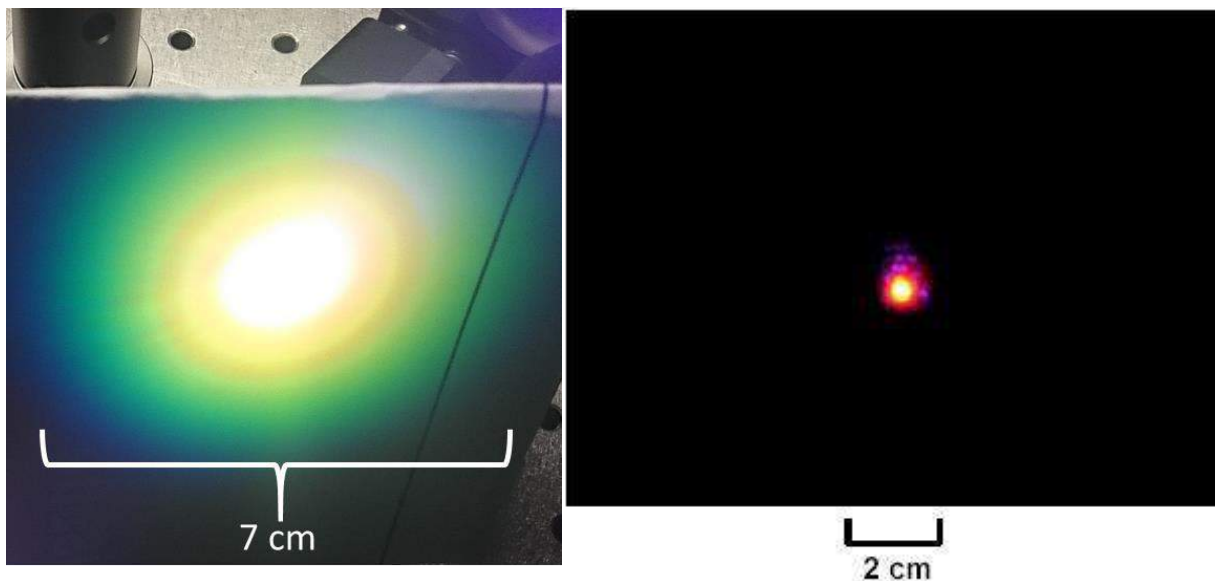


*Figure 2.2: YAG SC beam output at the FLASH Facility Laser (left), Air SC beam output from W. Liu et al. [2.6] (right).*

In a single filament regime, barring any  $\chi^{(2)}$  interactions within the nonlinear crystal that produce beam walkoff, the SC beam is radially symmetric (in both spatial and spectral regimes). In the multi-filament

regime (multiple completing, parallel filaments at high energies), an interference pattern is visible in the output (lines or speckle, Figure 2.3) and can be used to detect the presence of multifilamentation.

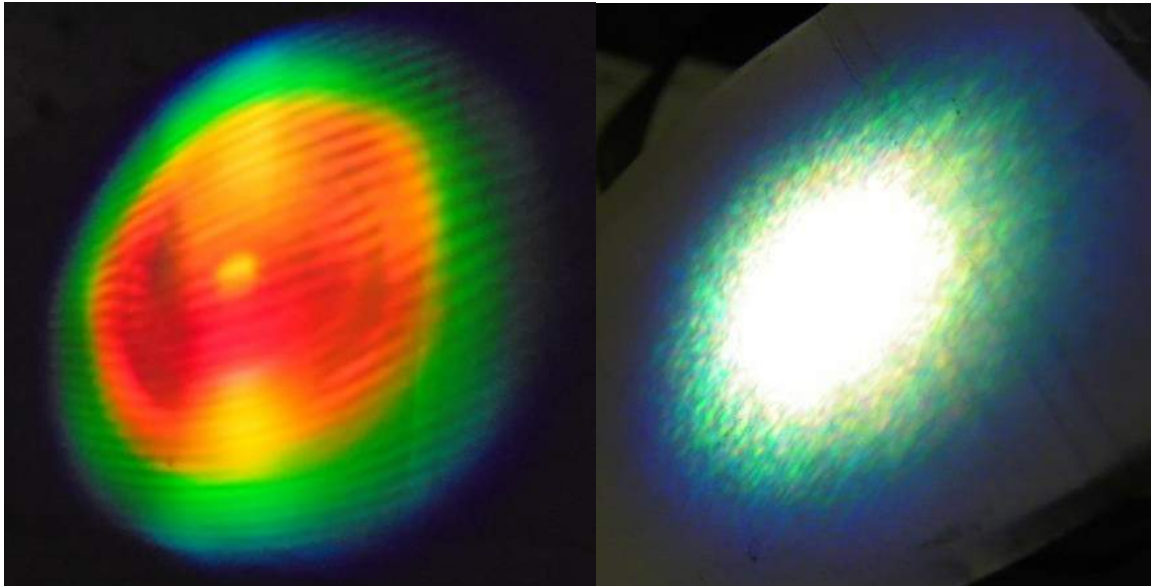


*Figure 2.3: Multifilament SC beam output at the ICFO Laser Facility, interference lines from two filaments in YAG (left), speckle pattern from multiple filaments in Sapphire (right).*

Spectrally, the SC process produces an ultra-broadband, structured spectral output (Figure 2.4 and Figure 2.5) with some (or all) of the following characteristics:

1. A broadened pump region, with exponential dropoff in spectral energy density towards the wings.
2. Asymmetric spectral energy density around the pump wavelength, with higher intensities in the Anti-Stokes (AS) wing [2.4].
3. A peak in the Anti-Stokes region far from the pump wavelength, and a less intense but still noticeable broadband peak region in the Stokes wing.
4. Peaks corresponding to Third Harmonic Generation.
5. Peaks in the spectra corresponding to Raman scattering, parametric frequency generation, etc.

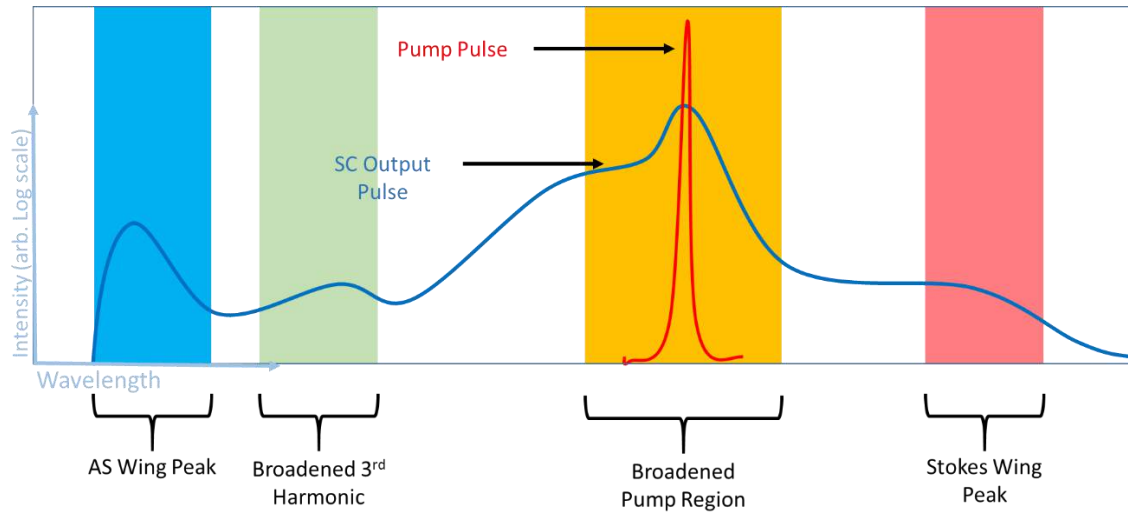


Figure 2.4: Illustration of SC spectral structure

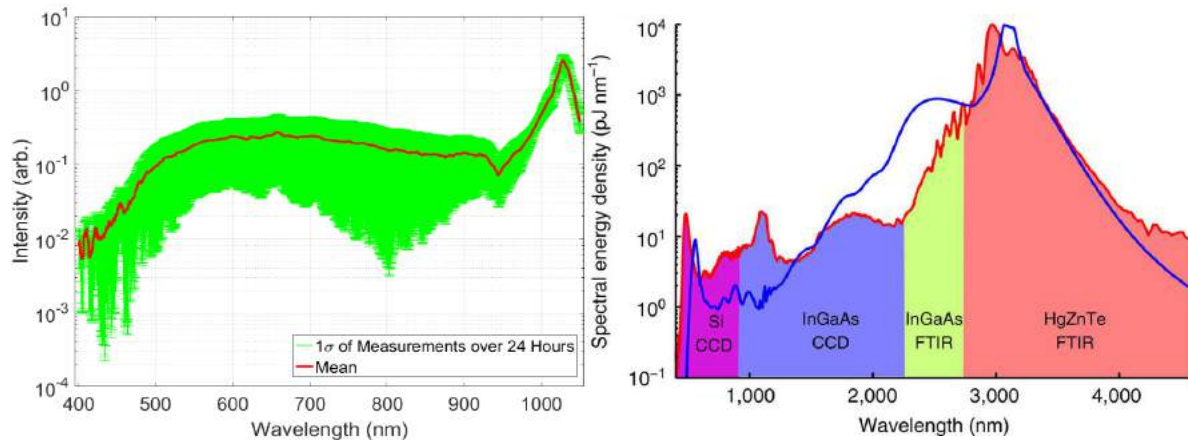


Figure 2.5: Experimental SC spectra, 1 $\mu$ m-pumped YAG from the PHAROS Experiment (left), 3 $\mu$ m-pumped YAG from F. Silva et al. [2.7] (right)

The core of the bulk SC generation setup can be reduced to a pump source, a focusing lens, and a nonlinear material used for SC generation (Figure 2.6). An iris is usually added before the input focusing lens to fine-tune the numerical aperture of the pump beam at the input face of the nonlinear material.

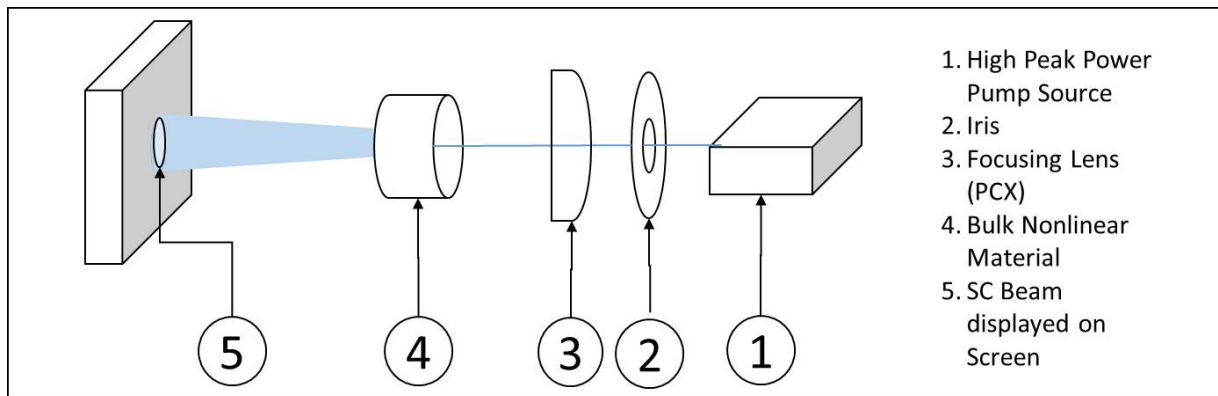


Figure 2.6: Core of Bulk SC generation Setup

Rough alignment for initiating the SC process is often easier to do visually [2.8] than by analyzing spectrometer or power-meter data.

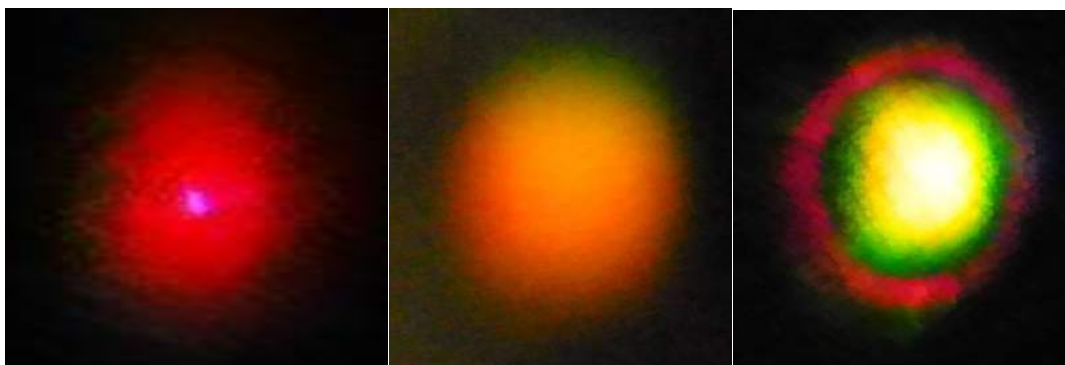


Figure 2.7: Stages of SC development, "first light" Third Harmonic (left), Third Harmonic and AS peak (center), fully broadened SC (right), from the ICFO  $1.8\mu\text{m}$ -pumped experiments in YAG.

As an example, for  $2\mu\text{m}$ -pumped pulses in YAG, the first visual cue for SC generation is a dim reddish glow at the output of the nonlinear crystal (Figure 2.7-left)—the third harmonic of the pump pulse. Next, the most intense Anti-Stokes wavelength present in the CE appears (Figure 2.7-center). Roughly optimizing for visual intensity of output around the setup parameters ( $z$  position, input power, iris diameter) that triggered "first light" in the visible portion of the spectrum most commonly results in a "blooming" of the Conical Emission (Figure 2.7-right) and a full-blown SC. The beam quality and parameters can then be fine-tuned using sensor data.

Multiple Filamentation (MF) is the creation of parallel, competing filaments alongside the primary filament at higher energies [2.8]. Spatio-spectral “hot spots” in the transverse profile of the pulse, diffraction, and any other inhomogeneity in the pulse or the nonlinear medium can create modulational instabilities in the driving pulse that “blow up” at high energies (intensities), creating new loci of SF and filamentation [2.78, 2.79]. Multiple “child” filaments can be created alongside the primary, with filaments competing for energy [2.80] and limiting the length that any one filament may attain. MF is one of the primary processes limiting the total input energy and spectral energy density (conversion) in SCG—additional input energy spawns new filaments instead of extending the length of the primary filament or creating a steeper intensity profile for the primary pulse.

Mutual phase coherence of SC filaments generated from phase-locked pump sources have been verified in spatially separated SC generation processes [2.83, 2.84] and in a single-crystal collinear geometry [2.81]. The phase coherence of multifilament processes have also been demonstrated [2.82].

## 2.2 A SIMPLIFIED DECONSTRUCTION OF DOMINANT MECHANISMS IN FILAMENT FORMATION

The appearance of a filament and the pseudo waveguiding behavior of SC pulses in gasses and bulk materials arises out of the dynamic balance between the dominant mechanisms involved in SC generation: a nonlinear process that increases the intensity gradient of the pulse vs. a nonlinear process that reduces the intensity gradient of the pulse.

It is well-accepted that the primary intensity-gradient increasing process is Kerr Self-Focusing [2.4]. But the intense pump (input) pulse never collapses to the singularity predicted by Kerr theory. Instead, other mechanisms act to arrest the collapse of the pulse. In bulk materials, it is assumed that the dominant arresting mechanism is plasma generation [2.8]—the pulse self focuses only until it reaches to some spot size,  $w_{min}$ , such that the intensity within the pulse is sufficient to trigger plasma generation. At this

point, the focal volume within the nonlinear medium comes to resemble an explosive medium as plasma is generated; the nonlinear medium becomes rapidly ionized and as the electron density exceeds the critical density of the medium, the value of the index of refraction drops below that of the unionized medium [2.9]. This negative change in the index of refraction acts to defocus the pulse, reducing the peak intensity and preventing further self focusing. During this focus/defocus process the pulse is losing energy due to absorption, scattering, etc., as well as losing peak power due to group velocity dispersion and other effects. However, if the pulse retains power in excess of  $P_{cr}$  once it is defocused enough to drop below the intensity threshold for plasma generation, SF dominates yet again, and the pulse begins to re-focus towards the singularity until it reaches  $w_{min}$  and plasma is generated once again. Successive cycles of focusing and de-focusing (also called “filament breathing” [2.4], illustrated in Figure 2.8) can be sustained as long as the pulse remains above  $P_{cr}$ , or transverse modulational instabilities do not trigger a parallel, competing filament that leeches power away from the “primary” filament.

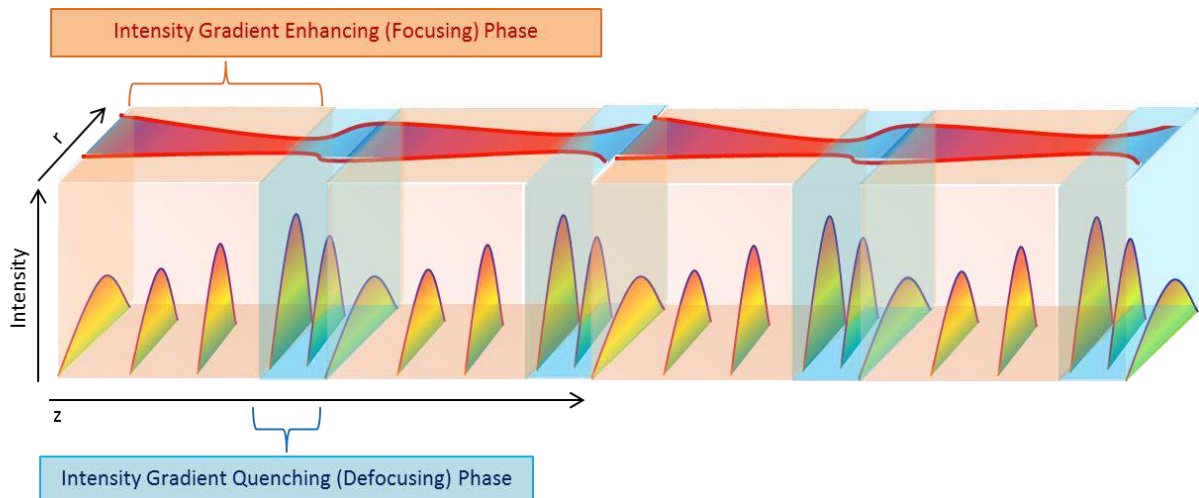


Figure 2.8: Pulse breathing (Focusing/Defocusing Cycles)

A Slowly-Varying-Envelope-Approximation (SVEA) formulation of the Nonlinear Schrodinger Equation [1.1] formulated by Gaeta [2.10] collects the dominant effects involved in bulk supercontinuum generation:

$$\frac{\partial u}{d\zeta} = \frac{i}{4} \left( 1 + \frac{i}{\omega_o \tau_p} \frac{\partial}{\partial \tau} \right)^{-1} \nabla_{\perp}^2 u - i \frac{L_{df}}{L_{ds}} \frac{\partial^2 u}{\partial \tau^2} + i \left( 1 + \frac{i}{\omega_o \tau_p} \frac{\partial}{\partial \tau} \right) \left[ \frac{L_{df}}{L_{nl}} |u|^2 u - \frac{L_{df}}{L_{pl}} \left( 1 - \frac{i}{\omega_o \tau_c} \right) \rho u + i \frac{L_{df}}{L_{mp}} |u|^{2(m-1)} u \right] \quad [1.1]$$

While the equation and terms are fully explained in Appendix B, at this point is sufficient to point out the nonlinear intensity gradient enhancement terms (orange): Kerr Self-Focusing, which results in SPM and Self-Steepening to some extent, and the intensity gradient quenching terms (blue): dispersion and plasma generation.

The complex dynamics involved in the propagation of the pulse result in a high degree of transverse spatial localization and temporal self-compression, resulting in pseudo waveguiding behavior [2.4]. When the dominant self-defocusing mechanism in play is plasma generation, a weakly ionized plasma trail develops in the wake of the pulse; as the relaxation time of the generated electrons is longer than the pulse duration, the plasma trail may continue to radiate incoherent visible and THz radiation [2.4] for longer than the duration of the delay between successive input pulses, influencing subsequent pulses [2.11].

### 2.2.1 Kerr SF

When an electromagnetic wave passes through a material, it interacts with the material's atoms, causing a deformation of the electric field potential proportional to the electric susceptibility of the medium. As the incident wave oscillates, the material's bound electrons emit photons with the same frequency as that of the incident field, but with a difference in phase. The incident wave itself is modified by its transit through the material—it is now a sum of the original wave (minus losses due to the photons absorbed by the material's charges, and scattering) as well as all of the individual waves radiated by the moving charges in the material. The total change in phase (i.e. velocity) of the

constituents of the incident wave is characterized by a dimensionless number—the wavelength-dependent refractive index of a material,  $n$ , under an applied electromagnetic field (light), defined as:

$$n(\lambda) = n_0(\lambda) + n_2(\lambda)I(\lambda) \quad [1.2]$$

Where  $n_0$  is the linear index of refraction,  $n_2$  is the nonlinear index of refraction, and  $I$  is the intensity of the applied field. The linear refractive index for a material can be calculated via the material's Sellmeier (or Cauchy's equation for normal dispersion in the visible wavelength region) once its empirically determined Sellmeier coefficients are known. But the nonlinear index of refraction denotes the anharmonic response of the deformation of the material's electric field potential (nonlinear response) under an applied electromagnetic field. This nonlinear response can be described by a series expansion of the complex polarization vector [2.12],  $\vec{P}$ :

$$\vec{P} = \epsilon_0(\tilde{\chi}^{(1)}\vec{E} + \tilde{\chi}^{(2)}\vec{E}\vec{E} + \tilde{\chi}^{(3)}\vec{E}\vec{E}\vec{E} + \dots) \quad [1.3]$$

Where  $\epsilon_0$  is the permittivity of free space,  $\tilde{\chi}^{(n)}$  is the  $n^{\text{th}}$  order susceptibility tensor of the material, and  $\vec{E}$  is the complex electric field.

Various optical effects arise out of the state of the susceptibility tensor—Second Harmonic Generation (SHG), Sum-Frequency and Difference-Frequency Generation arise out of the second-order susceptibility of the material, while Kerr effects arise out of the third order [2.13].

In crystalline materials, it is the symmetry of the crystal structure that determines the susceptibility terms. In an inversion symmetric medium, the susceptibility tensors of even orders vanish—this means SHG and DFG are not possible in a material like diamond. Of the 32 crystal classes, 11 classes possess inversion symmetry; other symmetries in many of the remaining crystal classes (e.g. cubic crystals like YAG) reduce the non-vanishing tensor elements, leaving the third order nonlinear response of the material—the Kerr nonlinear effect—as the dominant nonlinearity [2.13].

To reiterate, the Kerr nonlinear effect is a change in the refractive index of a material under the application of an electric field. In the case of the optical Kerr effect, the electric field inducing this refractive index change is generated by an intense pulse of light travelling within a nonlinear medium. The time-response of the Kerr effect is given as  $\sim 10^{-16}$  [s] [2.8], far shorter than input pulse durations for supercontinuum generation (SCG).

In the spatio-temporal domain, the intensity-dependant change of the refractive index,  $n(r, z, t) = n_0 + n_2 I(r, z, t)$  due to the Kerr effect leads to the phenomena of self-focusing (SF) where the transverse intensity gradient of the optical pulse creates a transverse refractive index profile similar to that of a lens. For a typical Gaussian pulse, this “Kerr lens” acts as a converging lens, which pushes the off-axis energy of the pulse towards the pulse peak, compressing both the transverse and temporal profile of the pulse [2.14 – 2.17]. The phase-spectral domain analog to SF is Self Phase Modulation (SPM) where the intensity-dependant change of the refractive index produces a shift in the instantaneous phase of the pulse, thereby generating new frequency components. The Kerr lens acts in the temporal domain as well, reducing the on-axis temporal length scale of the pulse [2.19, 2.20]. This space-time focusing effect is accompanied by an increase in the spectral width of the pulse due to SPM.

The critical power required for the onset of the Kerr nonlinear effect is given as [2.21]:

$$P_{cr} = \frac{\alpha \lambda_0^2}{8\pi n_0 n_2} \quad [1.4]$$

where  $\alpha$  is the coefficient corresponding to the pulse shape (3.77 for a Gaussian pulse, 3.72 for a Townes beam),  $\lambda_0$  is the central wavelength of the pulse,  $n_0$  and  $n_2$  are the linear and nonlinear indices of refraction of the material, respectively.

As can be seen from Eq. [1.4], the threshold power for self-focusing does not depend on beam diameter or input intensity (in the spatial *or* temporal domains)—large diameter beams or longer pulses

will create a weaker Kerr lens for self-focusing, and require longer propagation lengths to collapse, but will also be more sensitive to self-focusing. The critical power threshold *does*, however, rely upon the wavelength and the wavelength-dependant indices of refraction--Figure 2.9(a) shows the wavelength dependence of critical power required for self-focusing in Zinc Selenide (ZnSe), YAG (Yttrium-Aluminum-Garnet) and Diamond, while Figure 2.9(b) shows the energies required to reach  $P_{cr}$  for each wavelength at femtosecond and picosecond pulse duration. It should be noted that for shorter femtosecond pulses, the timescale of various nonlinear responses may compete with the sharp and abrupt rise of intensity as the pulse approaches collapse (discussed later in this chapter) and the nonlinear index of refraction may effectively be lower than literature values.

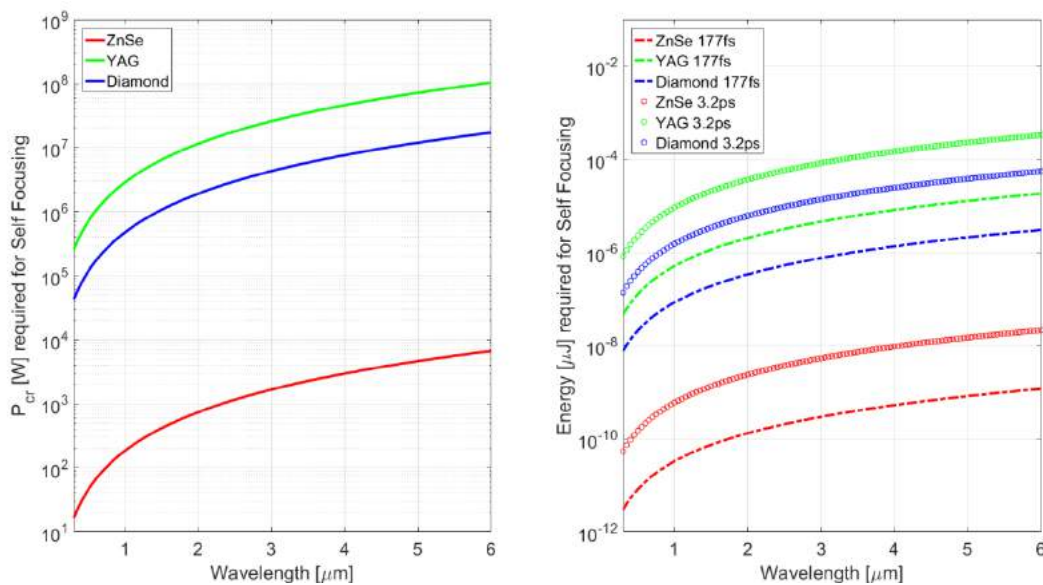


Figure 2.9: Critical power for self-focusing in various materials vs. wavelength (left), energy required for self-focusing in various materials at different pulse-widths vs. wavelength (right).

For a given wavelength in a material, the energy required to reach  $P_{cr}$  rises as the pulse duration is increased (Figure 2.10(a)), and for a given wavelength, the nonlinear index of refraction of a material is what primarily determines the threshold of critical power (Figure 2.10(b)) and the input energy required to reach this threshold at given wavelengths).

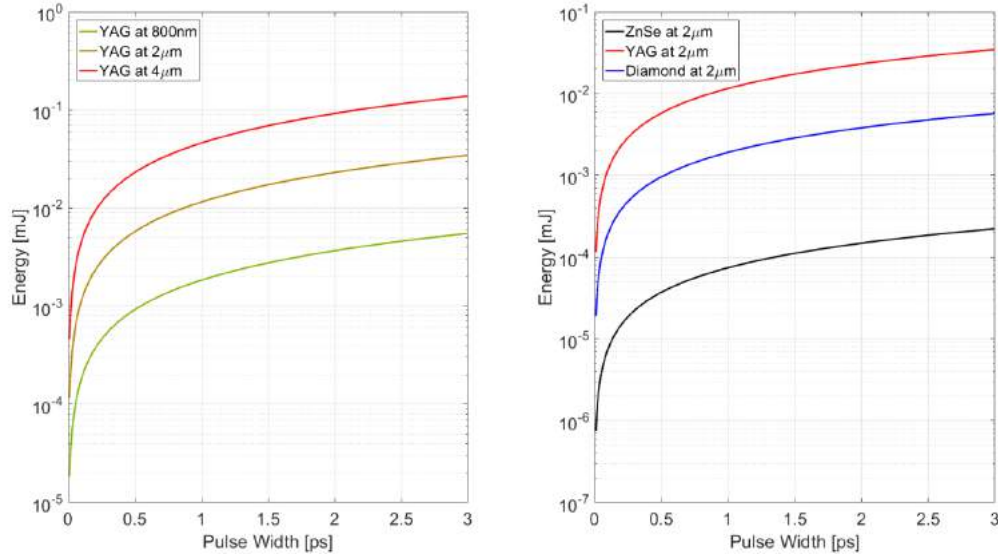


Figure 2.10: Energy required for self-focusing at various wavelengths in YAG (left), Energy required for self-focusing in various materials at 2μm wavelengths (right).

The propagation distance,  $z_f$ , at which this beam would collapse to a singularity (in the absence of other effects) is derived by Marburger [2.21] as:

$$z_f(P) = \frac{0.367ka_0^2}{\sqrt{\left(\sqrt{\frac{P}{P_{cr}} - 0.852}\right)^2 - 0.0219}} \quad [1.5]$$

where  $P$  is the input power,  $k$  is the wavenumber, and  $a_0$  is the radius of the beam at the  $\frac{1}{e}$  intensity.

Values calculated for  $z_f$  for given  $\frac{P}{P_{cr}}$  at various wavelengths are plotted in Figure 2.11. Here it is seen

that the propagation distance for collapse is inversely proportional to the  $\frac{P}{P_{cr}}$  ratio as expected (i.e. with

hither powers, the self-focus forms closer to the entrance face of the nonlinear medium), but *also*

inversely proportional to the wavelength. It should be noted that, as illustrated in Figure 2.12, a given

pulse energy corresponds to a much lower  $\frac{P}{P_{cr}}$  ratio at longer wavelengths—a 10μJ picosecond pulse at

1μm is  $1.0P_{cr}$  and only  $0.2P_{cr}$  at 2μm.

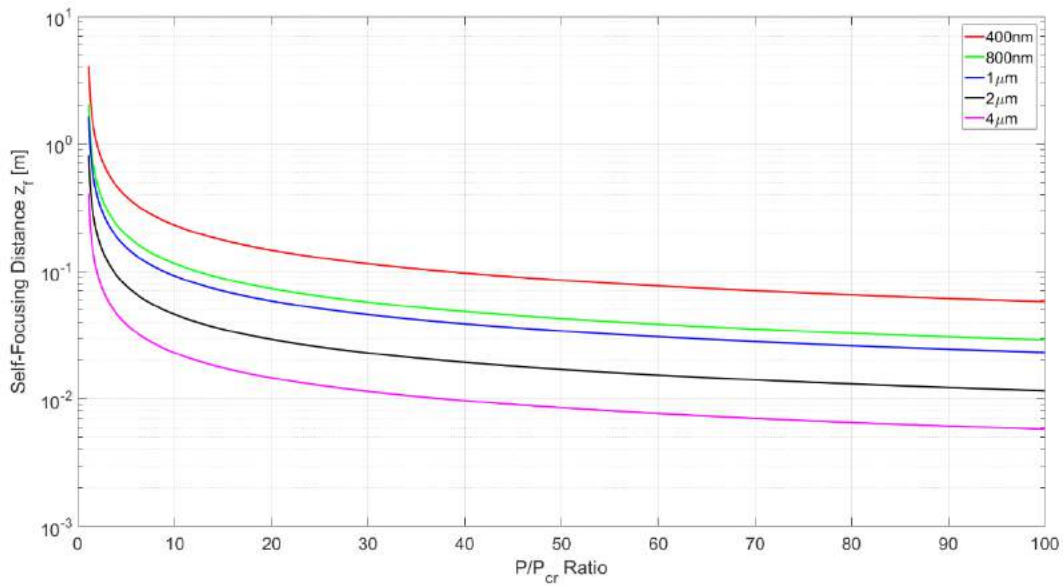


Figure 2.11: Self-focusing distance for YAG vs. input  $\frac{P}{P_{cr}}$  ratios for different wavelengths.

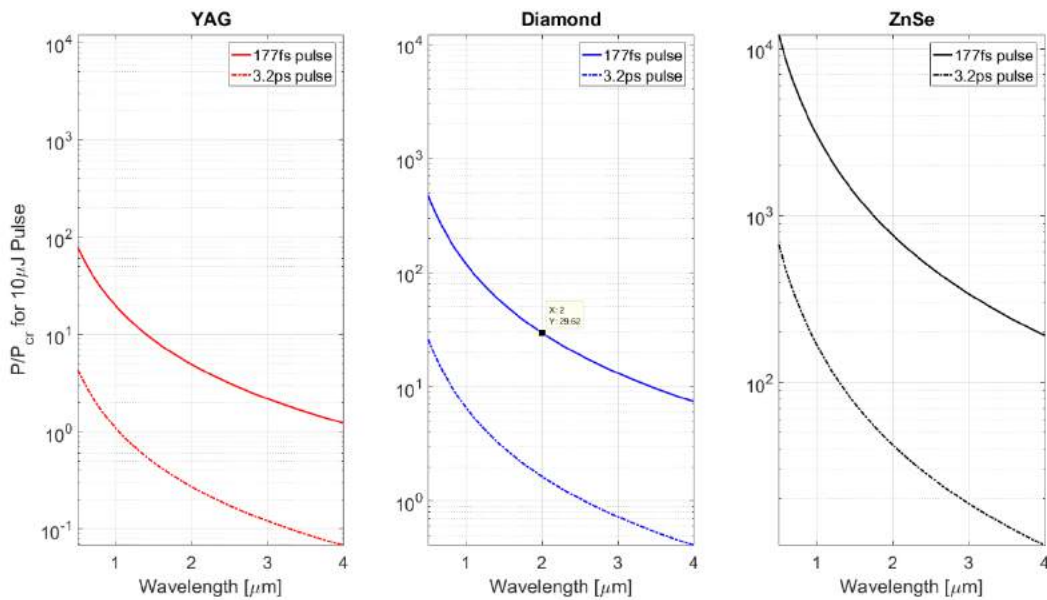


Figure 2.12:  $\frac{P}{P_{cr}}$  values for a  $10\mu\text{J}$  pulse vs. wavelength in YAG (left), Diamond (center) and ZnSe (right).

Using the constant shape approximation for the strong self-focusing case developed by Marburger [2.21], the spot size of the pulse,  $w$ , shrinks as a function of the propagation distance,  $z$ , until it reaches singularity at  $z_f$ :

$$w(z) = 2a_0 \sqrt[4]{1 - \left(\frac{z}{z_f}\right)^2} \quad [1.6]$$

Plotting the output of the above equation for two identical input conditions excepting the pulsewidth, (Figure 2.13) it can be seen that the reduction in  $\frac{P}{P_{cr}}$  for longer wavelengths results in a longer propagation distance before collapse, and that the effect is far more pronounced for a picosecond beam than a femtosecond (partially because a 500 $\mu$ J pulse in the femtosecond regime has a far higher  $\frac{P}{P_{cr}}$  ratio as compared to its energy-equivalent picosecond beam and therefore self-focuses at shorter distances).

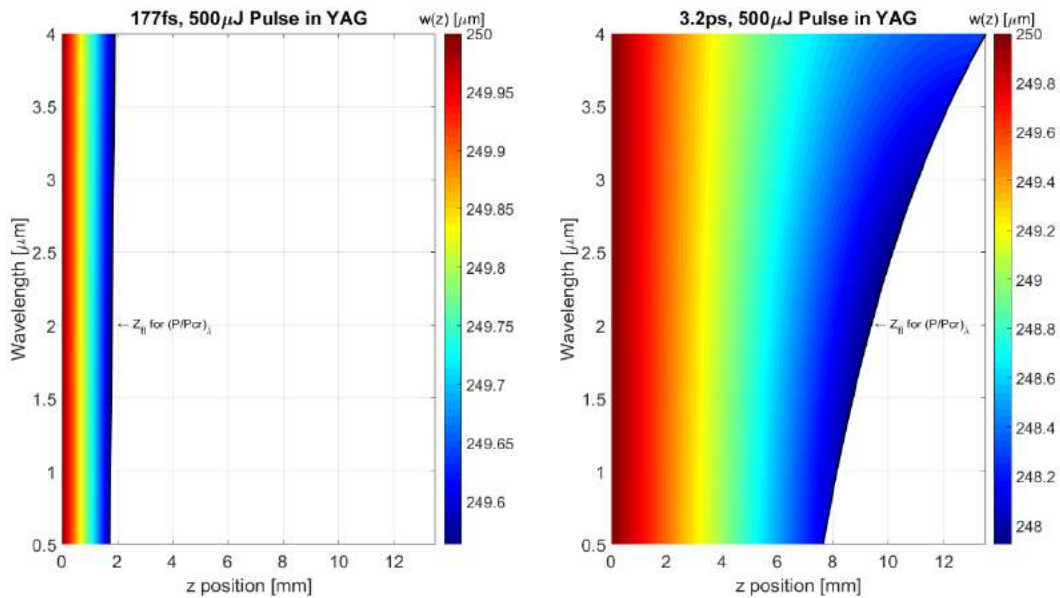


Figure 2.13: Propagation length to reach singularity in YAG for 177fs (left) and 3.2ps (right).

To look more closely at the trends implied by Figure 2.13, in Figure 2.14 illustrates a simplified scenario of a 50 $\mu$ J pulse in YAG with a temporal pulsewidth of 500fs, input collimated to a 200 $\mu$ m spot size.

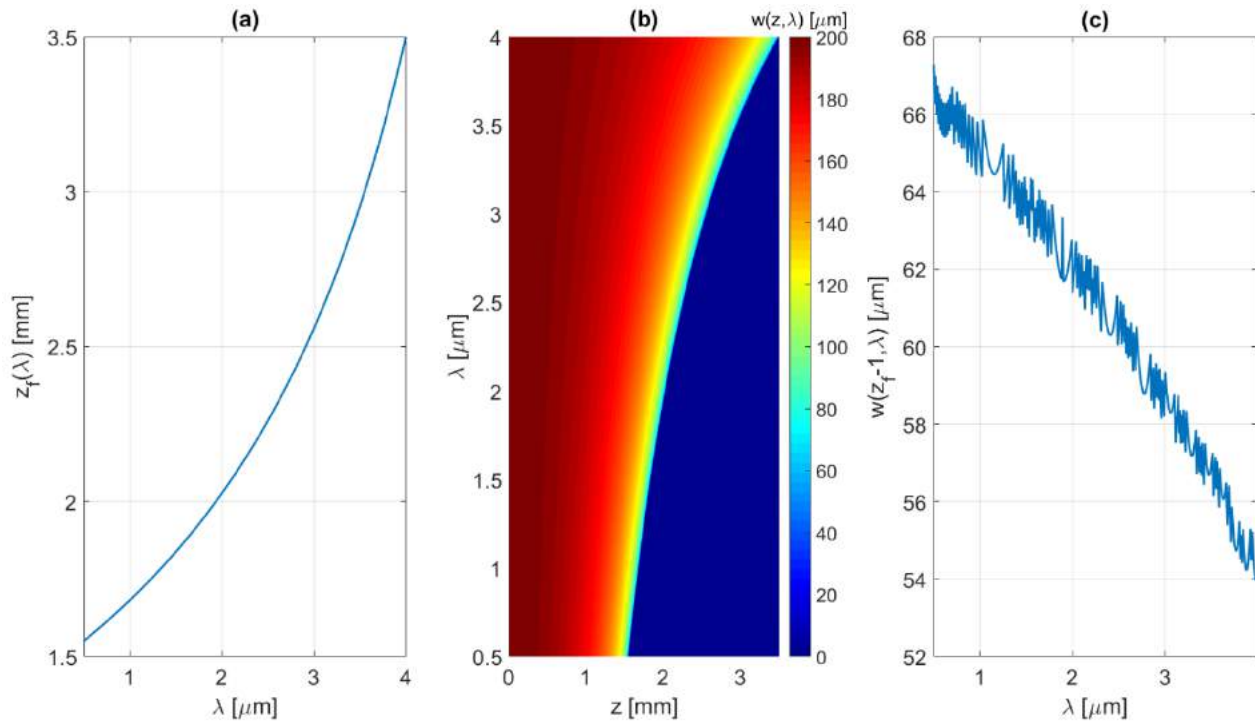


Figure 2.14: SF distance vs.  $\lambda$  (left),  $\lambda$  vs. SF distance (center), and minimum spot size vs  $\lambda$  (right)

Figure 2.14(a) shows that for a given pulse energy, the distance required to reach the focus of the Kerr lens grows with wavelength. In Figure 2.14(b), the diameter of the spot size as a function of wavelength and propagation distance is plotted—pulses with longer wavelengths propagate further in the nonlinear material before reaching singularity, and the development of the intensity gradient is less steep. Finally, in Figure 2.14(c), the evolution of the input spot size diameter of 100 $\mu$ m can be seen before collapse is reached<sup>1</sup>. Pulses at longer wavelengths are reach a smaller transverse diameter (and therefore achieve higher peak intensity) at some specified distance before the theoretical singularity.

<sup>1</sup> The modulation in the curve is an artifact of integration over the entire Gaussian pulse envelope.

In the spectral domain, the phenomena of SPM is responsible for the spectral broadening of the pulse via the creation of new frequency components. As the pulse propagates in the nonlinear medium, it accumulates a nonlinear phase distribution:

$$\phi_{NL}(t) = \int_0^L n_2 I(z, t) \frac{\omega_0}{c} dz \quad [1.7]$$

where  $L$  is the distance the pulse propagates in the medium,  $n_2$  is the nonlinear index of the medium,  $\omega_0$  is the central angular frequency of the pulse and  $c$  is the speed of light.

The instantaneous rate of change in the nonlinear phase function of the pulse,  $\frac{d\phi_{NL}(t)}{dt}$ , generates frequency components on the Stokes  $\omega_-$  (red) and anti-Stokes  $\omega_+$  (blue) sides of  $\omega_0$ . The rise time of the pulse, i.e. the instantaneous slopes of the leading edge, produces red-shifted (Stokes) frequencies and the decay time, i.e. the instantaneous slopes of the trailing edge, produces blue-shifted (Anti-Stokes) frequencies. The maximal extent of broadening due to SPM, i.e. the production of frequencies furthest from the pump is found at times  $t$  where the absolute slope of the phase-profile is at a maximum [2.8]:

$$\Delta\omega_{\mp} = \left( -\frac{d\phi_{NL}(t)}{dt} \right)_{\frac{min}{max}} \quad [1.8]$$

Figure 2.15, taken from [2.8], illustrates this frequency shift, where Figure 2.15(a) shows the time-dependant phase profile generated due to SPM in the pulse, while Figure 2.15(b) corresponds to the frequency-shifts associated with the slopes of the time-dependant phase profile.

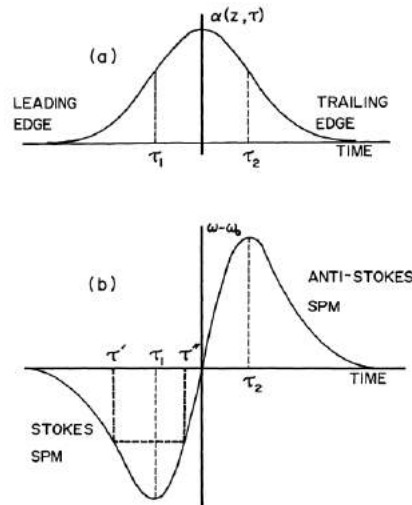


Fig. 2. — (a) Time-dependent phase  $\alpha(z, t)$  generated by self phase modulation (SPM). (b) Time distribution of SPM-shifted frequencies  $\partial\omega(z, t) = -\partial\alpha/\partial t$ .

Figure 2.15: Pulse SPM rise time, from [2.8]

SPM in the intense, ultrafast regime is very strong, with a rapid, “explosive” onset of broadening [2.22] due to the sharp increase in the intensity gradient of the pulse in both space and time as the pulse nears the Kerr focus. Considering only the Kerr nonlinearity, the rate of change of the temporal intensity gradient of the pulse (i.e. the steepness of the temporal intensity gradient) governs the maximal spectral extent of the broadening. It follows that the extent of spectral broadening is inversely proportional to temporal pulse-width (Figure 2.16). Further, the transverse focusing of the pulse as it undergoes SF generates very high peak intensities, even if the foot-to-foot temporal width of the pulse remains the same as it propagates, leading to a corresponding increase in spectral broadening (Figure 2.17).

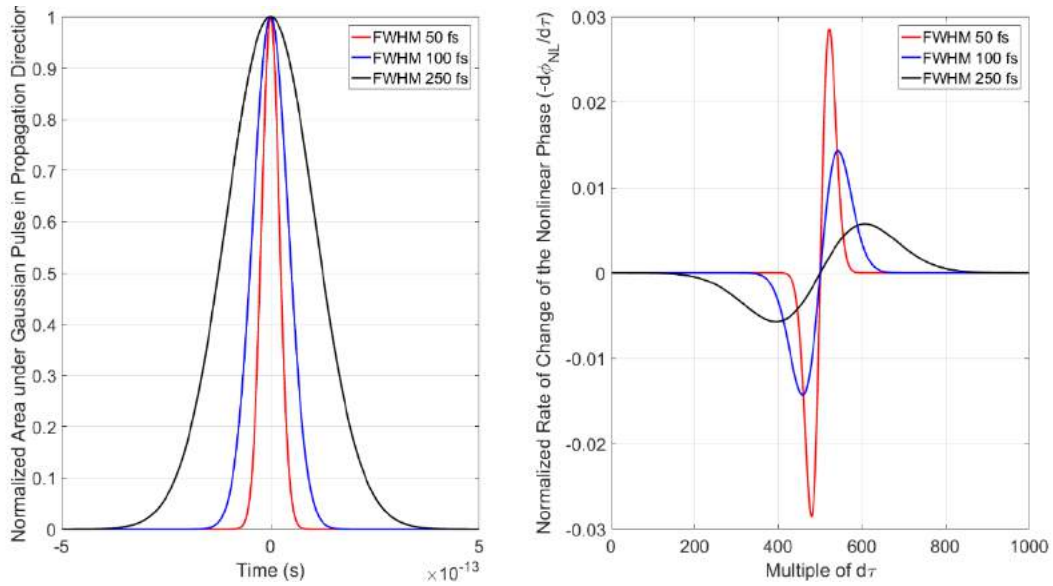


Figure 2.16: Constant intensity pulse rise time

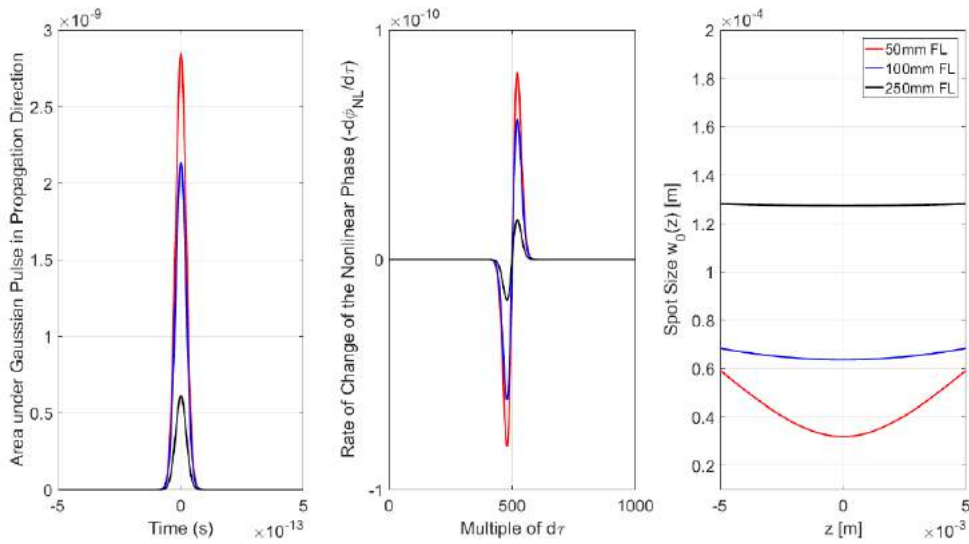


Figure 2.17: Constant pulse temporal width intensity spike

In the absence of other effects, the extent of spectral broadening in an intense ultrashort pulse undergoing SF in a nonlinear medium increases with the propagation length—longer propagation

distances lead to steeper intensity gradients in the transverse direction, associated with a greater rate of accumulation of nonlinear phase as the pulse nears the Kerr focus, as illustrated in Figure 2.18<sup>2</sup>.

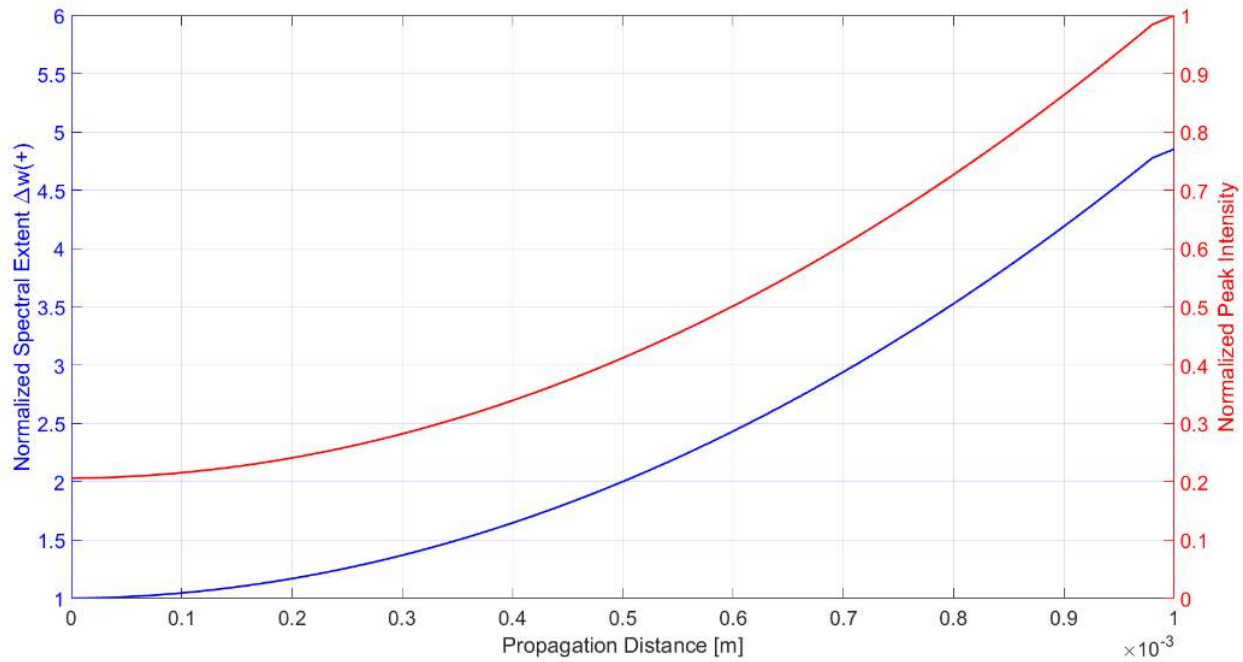


Figure 2.18: Spectral Extent

The interaction length of the pulse within the nonlinear medium (even if the intensity gradient does not change) contributes to an accumulation of spectral energy density at all frequencies created by the  $\frac{d\phi_{NL}(t)}{dt}$  function—the longer the pulse propagates, the more energy is shifted from the central driving frequency  $\omega_0$  into  $\omega_-$  and  $\omega_+$ . Identical slopes of the phase function, for example at  $\tau'$  and  $\tau''$  in Figure 2.15: Pulse SPM rise tim, generate the same frequency components, but appear at different times, leading to interference and modulation of the SPM spectrum<sup>3</sup>.

<sup>2</sup> As an aside, the propagation length/spectral extent dependence is what lies behind approaches that rely on filament suppression for extreme spectral broadening via the use of pure SPM in combination with other linear/nonlinear effects (See Chapter 4.2).

<sup>3</sup> It should also be noted that any other frequency generation process that creates overlapping frequencies with the “core” SCG process (for example stimulated Raman emission or the generation of higher harmonics) will result in further modulation of the

It should be noted that for the very intense fields associated with SF, the higher-order (odd orders for the most part, as the even orders will vanish or be negligible due to symmetries in many nonlinear crystals) nonlinear contributions to the polarization of the material become important. Marburger [2.21] terms these higher-order contributions “saturation terms” as they limit the magnitude of the response. The saturation of the nonlinear polarization can only occur with extremely short pulses [2.23]—the molecules attempt to rotate and reorient themselves in the presence of a strong driving field, but do not have time to relax during the pulse, leading to an effective saturation of the polarization at field strengths lower than those required to reorient unhindered molecules. Further, though the timescale of the Kerr response is far shorter than the pulse, the saturation of the polarization essentially acts to lengthen it, and for extremely short pulses on the order of a few fs (as may be formed even out of longer pump pulses due to multiple pulse-splitting at the height of the SC pulse’s evolution), the nonlinear response of the material cannot follow the pulse [2.21], leading to a lower-than-expected intensity gradient and an effective clamping of peak intensity.

### 2.2.2 Plasma Generation

The two ionization processes relevant to the production of plasma in bulk nonlinear media are multiphoton ionization and avalanche ionization (tunnel ionization is applicable to SC in gasses [2.4]). When the energy of the photons in the input pulse is below the energy required to ionize the medium, multiple photons can be absorbed simultaneously for ionization. The MPI order  $m$ , i.e. the number of photons required to ionize the medium is given by:

$$m = \text{floor} \left( 1 + \frac{E_{gap}}{\hbar\omega_0} \right) \quad [1.9]$$

---

spectrum through cross-phase modulation [2.24]. Cross-phase modulation can also result due to an induced polarization rotation of the driving pulse through a nonlinear medium (discussed in Chapter 3).

where  $E_{gap}$  is the bandgap energy of the medium,  $\hbar$  is the reduced Planck constant and  $\omega_0$  is the central frequency of the input pulse. The probability of absorbing  $m$  photons decreases with increasing wavelength (a reduction in photon energy), and requires extremely high pulse intensities in order to generate sufficient plasma to halt SF. The scaling of MPI order with wavelength for ZnSe, YAG and Diamond is given in Figure 2.19.

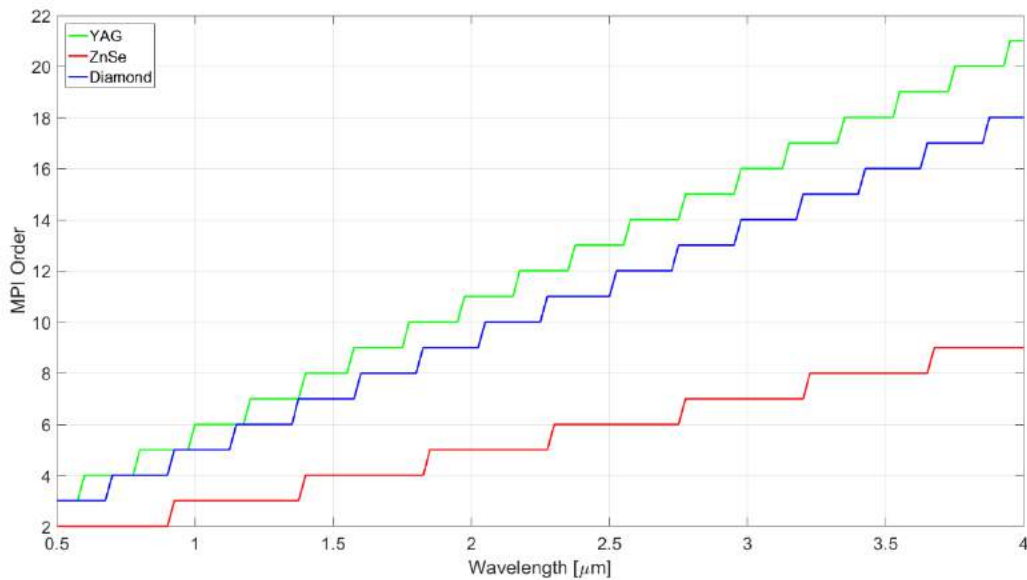


Figure 2.19: MPI order vs. wavelength for various materials

For avalanche ionization, a free electron in a medium is accelerated by the electric field of the laser pulse until it has sufficient energy to ionize an atom in the medium through collision (impact ionization), thereby generating an additional free electron that is then itself accelerated by the electric field of the optical pulse. A chain reaction—an “avalanche”—is initiated, and the population of free electrons grows exponentially [2.25].

The number of AI doubling events is related to the pulse duration. Based on dielectric breakdown measurements in NaCl, the time required for a doubling event has been estimated as  $\sim 50\text{fs}$  [2.25]. Given the number of doubling events required to reach the free-electron density necessary to balance SF (30

generations to reach a  $10^{18}$  [ $\text{cm}^{-3}$ ] electron density [2.8]), contributions from AI can be neglected for pulses shorter than 40fs [2.26], but at pulse durations longer than  $\sim 1.5\text{ps}$ , AI alone can generate sufficient free electrons to halt SF. Numerical estimates show that at pulse durations exceeding a picosecond, the intensity clamping contribution from AI generated plasma can dominate MPI [2.27,2.28].

Following the development of Brodeur and Chin [2.8], the critical intensity,  $I_{stop}$ , at which SF is arrested by plasma generation is the intensity at which the (positive) nonlinear change in refractive index due to the Kerr nonlinearity is balanced by the (negative) linear change in refractive index due to free electrons,  $\Delta n_e$ , i.e.:

$$n_2 I_{stop} + (-\Delta n_e) = 0 \quad [1.10]$$

$$n_2 I_{stop} = \Delta n_e \quad [1.11]$$

and

$$\Delta n_e = -\frac{2\pi e^2 N_e}{n_0 m_e (\omega_0^2 + \nu^2)} \quad [1.12]$$

Where  $N_e$  is the electron density,  $\nu$  is the electron collision frequency,  $m_e$  is electron mass and  $e$  is the electron charge.

In general, the free electron density,  $N_e$ , is modeled as a differential equation comprising of avalanche ionization, MPI and recombination. Kolesik et. al [2.29] give this model equation as:

$$\partial_t N_e(r, z, t) = \frac{\sigma}{n_0^2 E_{gap}} N_e I(r, z, t) + \frac{\beta^{(m)}}{m \hbar \omega_0} I(r, z, t)^m - a N_e^2 \quad [1.13]$$

where  $\sigma$  is the cross-section of inverse bremsstrahlung,  $n_0$  is the background refractive index,  $E_g$  is the bandgap energy,  $I$  is the field intensity (also a function of  $r, z, t$ ),  $\beta^{(m)}$  is the MPI coefficient for MPI order  $m$  and  $a$  is the plasma recombination rate.

For the sake of simplicity, AI can be neglected in the femtosecond regime. It is also assumed that  $\omega_0^2 \gg \nu^2$ . In this case, free electrons are generated by MPI alone. The MPI rate,  $W$ , required to generate  $N_e$  in one half-cycle of the pump pulse is given as [2.8]:

$$W = \frac{N_e}{\left(\frac{1\lambda_0}{2c}\right)} = \frac{2cN_e}{\lambda_0} \quad [1.14]$$

At a certain intensity,  $I_{stop}$ , the  $W$  will be high enough to generate sufficient free electrons to halt SF.

Therefore, combining Equations [1.14] and [1.12],

$$W = \frac{n_0 m_e \omega_0^2 n_2 I_{stop}}{2\pi e^2 \left(\frac{1\lambda_0}{2c}\right)} = \frac{cn_0 m_e \omega_0^2 n_2 I_{stop}}{\pi e^2 \lambda_0} \quad [1.15]$$

The rate of MPI can be obtained using Keldysh formulation [2.27]. While there has been some discussion regarding the accuracy of Keldysh-formulation obtained MPI rates [2.26], it is regarded as the more accurate model in literature [2.30]. The rate of MPI at  $I_{stop}$ , within the framework of the model developed by Kennedy [2.26], is:

$$W = A(BI_{stop})^m \quad [1.16]$$

Where  $m$  is the order of MPI, given by:

$$m = \text{floor} \left( 1 + \frac{E_{gap}}{\hbar\omega_0} \right) \quad [1.17]$$

and

$$A = \frac{2}{9\pi} \omega_0 \left( \frac{m\omega_0}{\hbar} \right)^{\frac{3}{2}} \exp \left( 2m\phi(z) \left( \frac{1}{16} \right)^m \right) \quad [1.18]$$

$$B = \frac{e^2}{m' E_{gap} \omega_0} \quad [1.19]$$

$m'$  is the effective mass ratio<sup>4</sup>,  $z \approx \sqrt{2m - \frac{2E_{gap}}{\hbar\omega}}$  is the residual energy, and  $\phi(z)$  is Dawson's Integral<sup>5</sup>.

Substituting equation [1.14] into [1.15], and solving for  $I_{stop}$ :

$$I_{stop} = \left(\frac{R}{A}\right)^{\frac{1}{m-1}} B^{\frac{m-1}{m}} \quad [1.20]$$

$$\text{where } R = \frac{cn_0 m_e \omega_0^2 n_2}{\pi e^2 \lambda_0} \quad [1.21]$$

Care is taken to avoid having the expression  $B^m$  directly in the calculation, as depending on the order of  $m$ ,  $B^m$  drops below the threshold for the smallest positive normalized floating-point number in most software packages. The major assumption in equation [1.15] must also be noted, i.e. the assumption that *all* free electrons are generated during the optical half-cycle of the central frequency at the peak of the pulse—in reality the number of free electrons due to MPI will always be larger because the leading (temporal) edge of the pulse is also generating free electrons. Properly, the MPI portion of the differential equation [1.13] must be integrated over the entire leading portion of the pulse envelope (with recombination added in the case of an extremely long pulse). Given the abrupt rise in intensity of the peak under SF, the assumption that all free electrons due to MPI are abruptly created at the peak of the pulse can still be used to give a roughly correct estimate of  $I_{stop}$ . Values for  $I_{stop}$  for three sample materials are plotted in Figure 2.20.

---

<sup>4</sup> Where  $\frac{1}{m'} = \frac{1}{m_e} + \frac{1}{m_h}$ ,  $m_e$  and  $m_h$  are the electron and hole mass respectively. Though the conduction band effective mass[2.31] should be used if complete harmonic mean calculations for the crystal structure in question can be carried out, this work uses the the density of states effective masses given in literature for various semiconductors.

<sup>5</sup>  $\phi(z)$  can be evaluated as  $\phi(z) = \exp(-z^2) \sum_0^\infty \frac{z^{2n+1}}{n!(2n+1)}$

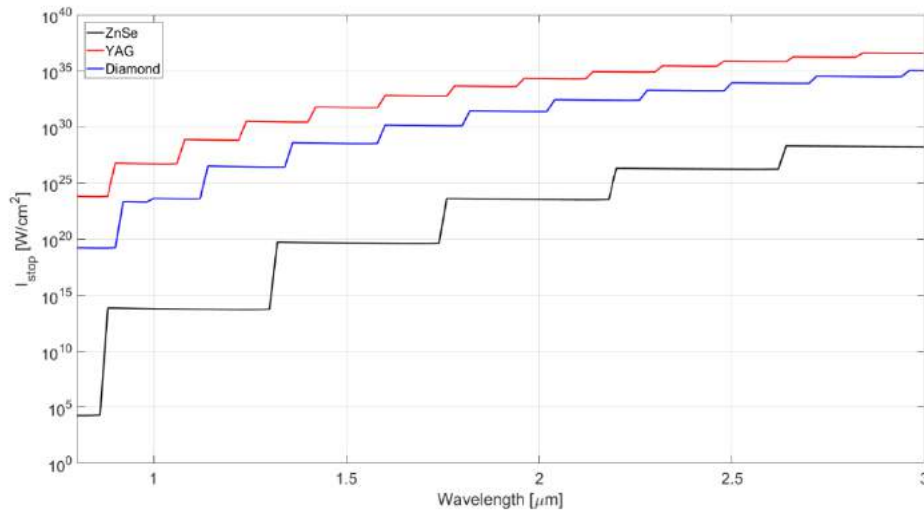


Figure 2.20: Clamping Intensity  $I_{stop}$  vs. wavelength for ZnSe, YAG and Diamond.

Given the value for  $I_{stop}$ , and the change in spot size due to Kerr focusing as a function of propagation distance (Equation 1.6), the propagation distance at which Kerr Self-Focusing is arrested due to MPI can be estimated as a “poor man’s” analytical tool to determine the suitability of nonlinear media for bulk SCG, propagation lengths and input powers required—sample values for YAG are plotted in Figure 2.21.

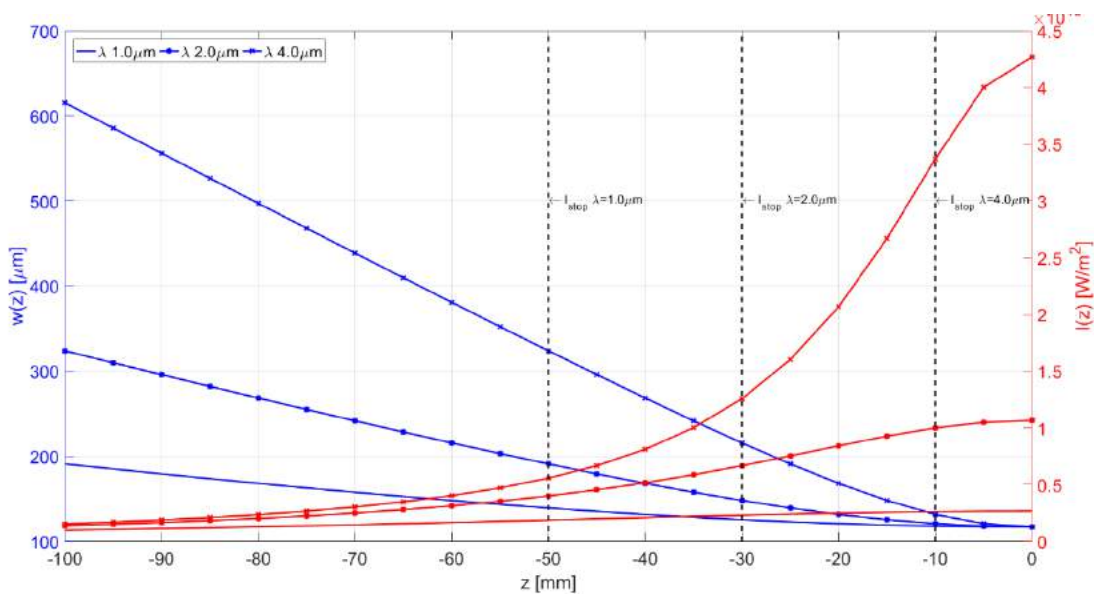


Figure 2.21: Spot-size and Intensity vs. propagation distance for YAG at different wavelengths— $I_{stop}$  for each case is shown as a dashed line.

So far, the effects of Avalanche Ionization have been neglected in favor of an MPI-only model. To understand the contribution of AI to the plasma evolution of the system, the inverse can now be considered—the effects of AI in the absence of MPI.

To model AI at the peak of the pulse, one can use the expression developed by Blombergen [2.32], where the number of free electrons generated by AI for a given pulse width  $\tau_p$  is:

$$N_e(\tau_p) = N_0 \exp\left[\int_0^{\tau_p} \eta(E(\tau)) d\tau\right] \quad [1.22]$$

$$\eta(E(\tau_p)) \approx \frac{\ln \frac{N_{th}}{N_0}}{\tau_p} \quad [1.23]$$

where  $N_0$  is the background initial density of free electrons in the medium (taken here as  $\sim 10^8 \text{cm}^{-3}$  as per [2.32]) and  $N_{th}$  is the threshold breakdown density of free electrons, developed by Yamada et. al [2.33] as:

$$N_{th} = \frac{\pi m_e c^2}{e^2 \lambda_0^2} \quad [1.24]$$

Using the above equations, the (proportional) growth of the number of free electrons in a medium due to AI over the evolution of the pulse can be estimated, as shown in Figure 2.22. Focusing on the peak of the pulse (Figure 2.23), it can be seen that the ionization rate per electron is retarded with respect to the optical peak of the pulse that occurs at  $\tau = 0$ . This leads to an AI-based growth in (normalized) plasma density that follows the peak of the pulse, with a delay—the majority of free-electrons generated due to AI are seen by the trailing portion of the pulse, though they have been generated by the passage of the pulse peak (Figure 2.25).

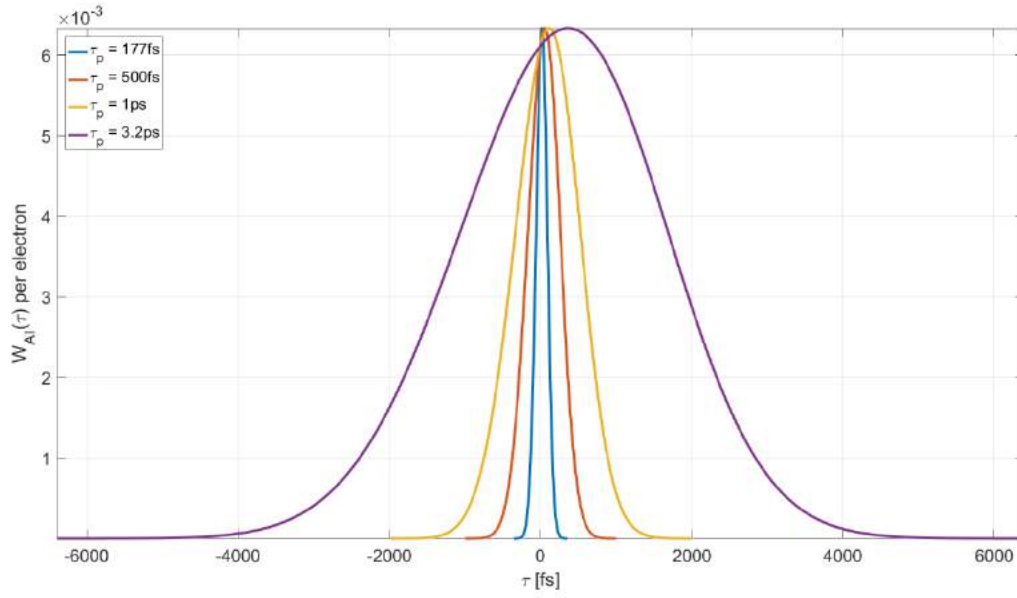


Figure 2.22: Ionization rate per electron due to AI

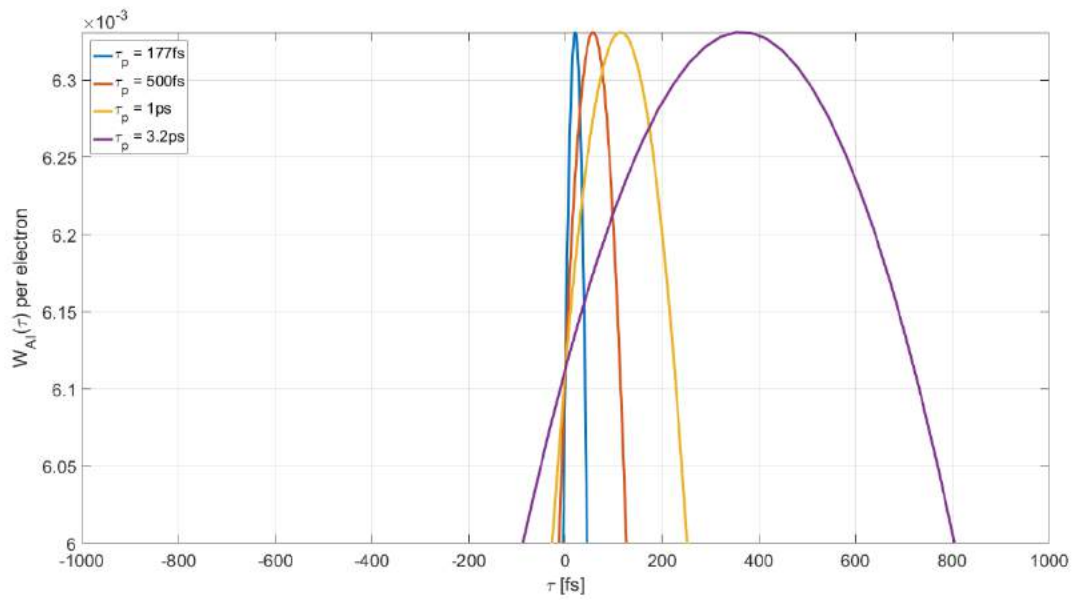


Figure 2.23: Ionization rate per electron (focus on peak)

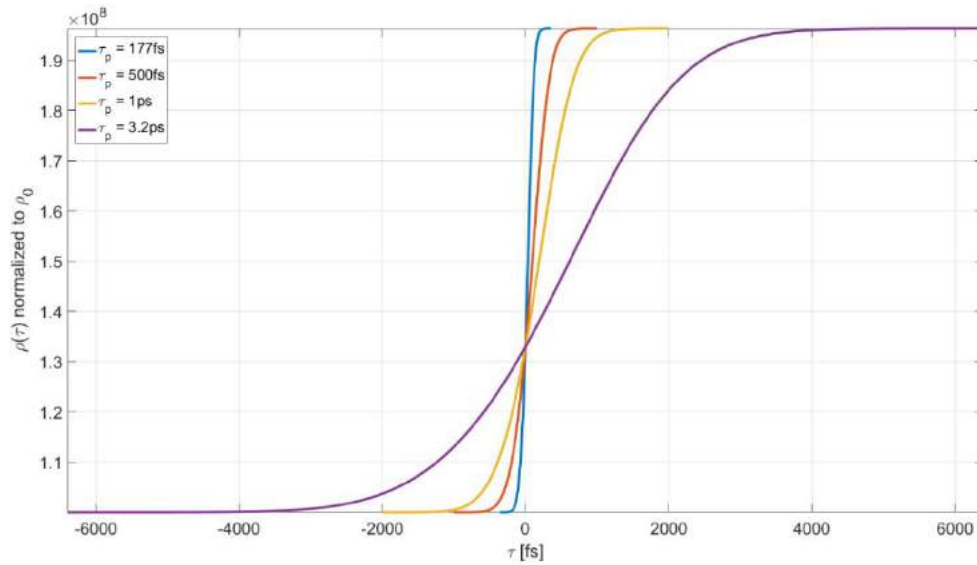


Figure 2.24: Normalized plasma density growth due to Al

In terms of pulse width, it is clear that though the ionization rate is highest for the shortest pulse (with the greatest peak intensity) as shown in Figure 2.25, and the normalized plasma density is “capped” at the plasma breakdown threshold of the material, the *total* number of free electrons created (the area under the curve of Figure 2.24, integrated over the 3D spatial profile of the pulse) is greatest for the long pulse.

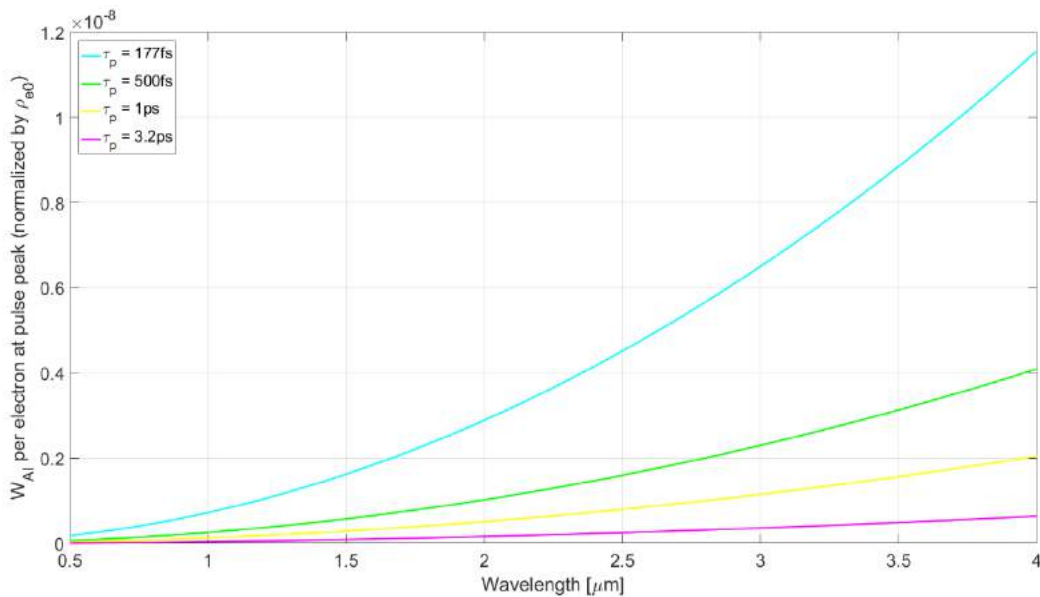


Figure 2.25: Ionization rate of Al as a function of pulse width

The competition between AI and MPI becomes a dominant factor in shaping the spectral profile of the pulse. As AI takes time to build up (on the order of multiple 100s of femtoseconds), the free electrons generated through this process act to gradually “quench” the peak powers of the trailing edges, leading to a slow defocusing of the trailing edge and therefore a shallow decay of the intensity gradient. As it is the slope of the intensity gradient of the trailing edge that determines the Anti-Stokes extent of spectral broadening in the pulse, AI effectively *reduces* the blueshift of the pulse[2.8].

MPI acts to increase spectral blue-shift [2.8, 2.34]. Because the rise-time for the MPI is on the order of half an optical cycle [2.8], the free electrons generated by the leading edge of the pulse act to defocus the middle of the pulse. The quenching of powers in the middle of the pulse is extremely abrupt and the reduction of peak intensities on the trailing edge happens far faster than the rise-time of the intensity gradient at the leading edge of the pulse. This steep gradient in the trailing edge generates a large Anti-Stokes broadening. For an MPI-dominated regime, the plasma-based maximal blue-side spectral extent  $\Delta\omega \propto I_{stop}^m$  where  $m$  is the order of MPI [2.29].

As In the phase-spectral domain, plasma formation also balances (to some extent) the positive chirp (positive nonlinear phase) accumulated by the pulse through SPM: since plasma generation effects the refractive index negatively as a function of the temporal intensity envelope, a negative chirp is imparted to the pulse as it defocuses. Also, at higher peak powers, the competition between SF and plasma generation causes a redshifting of the pulse [2.35]: while SF acts to push the peak of the pulse to the rear, creating a sharp trailing edge and therefore blueshifted frequency components, while, overall, the generation of free electrons due to all ionization processes acts to defocus the rear of the pulse [2.14].

The material bandgap,  $E_g$ , is a critical parameter that governs the generation of free electrons, and ultimately determines the  $I_{stop}$  in a given medium. The bandgap has also been implicated in determining the cut-off frequency for the Anti-Stokes spectral extent of an SC pulse, and whether or not

it is possible to generate SC in a material in the first place [2.8]. The mechanism at action here limiting SC generation is the order of MPI: in materials with small bandgaps, the pulse triggers two photon absorption and the corresponding  $I_{stop}$  is orders of magnitude lower than that for higher orders of MPI. This means the pulse does not propagate far enough in the nonlinear medium, nor does it self-focus to appreciable peak intensities (large  $w_{min}$ ). This mechanism of action is investigated by Brodeur and Chin, where they confirm that “...the jump of approximately an order of magnitude at  $m = 3$  is of particular interest inasmuch as it occurs at the measured  $E_{gap}^{th} \sim 4.7 \text{ eV}$ .”

However, the order of MPI is wavelength-based ( $m = \frac{E_{gap}}{\hbar\omega_0}$ ). There is no theoretical reason why a material like CaF<sub>2</sub> with above-threshold bandgap of 10.4eV can generate supercontinuum in the 4-photon regime (pump wavelength  $\lambda_0 = 500\text{nm}$ ) while a material like ZnSe with a below-threshold bandgap of 2.7eV cannot generate supercontinuum in a 4-photon regime as well (pump wavelength  $\lambda_0 = 1.5\mu\text{m}$ ).

Experimentally, SCG in materials with bandwidths lower than 4.7eV has been demonstrated repeatedly, when the SCG process is driven by longer pump wavelengths. Plasma generation at low intensities does, however, become a limiting factor for SCG when (a) the Anti-Stokes wing of the SC spectra broadens into lower MPI-order wavelength regions, especially when there is significant conversion from  $\lambda_0$  to blue frequencies due to the interplay of other processes like GVD, pulse-splitting and the MPI itself, and (b) when other nonlinear processes like harmonic generation, XPM, or stimulated Raman scattering create blue frequencies with good conversion efficiency. Incidentally, this blue-shift to lower MPI-order wavelength regions (and the consequent low-intensity arrest of SF through plasma generation) also accounts for the Anti-Stokes cutoff of spectral broadening that has been shown to be dependant on the bandgap of the material [2.36, 2.37].

The increased scaling of increased spectral extent with increasing bandgap observed, in experiment and theory [2.8, 2.4, 2.16], is also directly related to the maximum achievable intensities in larger bandgap materials before SF is arrested by MPI. The SF process itself is affected by the material bandgap. The material nonlinear index,  $n_2$ , scales inversely with bandgap [2.38]. Even considering only the effect of SF, light propagating through materials with lower nonlinear indices (higher bandgaps) exhibit weaker Kerr lensing, and (at powers above  $P_{cr}$ ) have a longer interaction length in the medium, a slower rate of growth of the intensity profile, and reach smaller diameters (and therefore higher intensity gradients, and a broader spectrum via SPM) before the self-focus.

When simulating spectra, especially with a focus on plasma generation, studies focus on tuning parameter sensitivity such as the plasma recombination rates, MPI rates, electron collision time, etc. [2.7, 2.29]. However, when comparing spectra at two different driving wavelengths, it is often the case that spectral extents and blue-side cut-off are compared and discussed with respect to the bandgap energies of the materials *without* taking into account the wavelength-based GVD or the wavelength-based change in  $\frac{P}{P_{cr}}$  ratio for the given input energies. For example, looking at Figure 4 in [2.29], reproduced below, it is clear that 6 $\mu$ J and 9 $\mu$ J at a driving wavelength of 400nm provide an entirely different  $\frac{P}{P_{cr}}$  ratio to 6 $\mu$ J and 9 $\mu$ J at a driving wavelength of 800nm, leading to different propagation lengths in the material, different accumulation of group delay due to GVD, and different dynamics for pulse-splitting and blueshift of the output spectra. Without analyzing these factors or taking care that they remain identical for all cases (even artificially), it is difficult to qualitatively compare or discuss SC spectra generated by two different driving wavelengths. Further, the authors show that the maximal plasma density value reached is entirely independent of the input pulse energy—the arrest of self-focusing occurs at the same intensity level for all input energies—and that the spectral content of the SC output is tied to the rate of change of plasma density, not the absolute plasma density attained. In

Section 2.2.1, it was demonstrated that this rate of change is intimately tied to the self-focusing parameters: wavelength, propagation length, and  $\frac{P}{P_{cr}}$  ratio (*not* simply the input energy), which in turn affect the length of the filament and the number of self-focusing cycles that can be sustained for a given propagation length.

### 2.2.3 Group Velocity Dispersion (GVD)

GVD causes a temporal “spreading” of the pulse, leading to a quenching of the peak power and the intensity gradient of the pulse within the nonlinear medium. In fact, for extremely broadband pulses (at sufficiently small ratios of  $\frac{P}{P_{cr}}$ ), it has been shown that GVD alone is sufficient to halt self-focusing before the pulse reaches collapse via plasma generation (i.e. the pulse stops self-focusing due to GVD before intensities equalling  $I_{stop}$  are reached) [2.39]. At sufficiently high input peak powers, GVD is not a dominating factor in the arrest of self-focusing, but the effects of peak-power quenching still affect the filament length—with the total peak power being quenched as the pulse propagates in the medium, less and less peak power is available to the pulse to “refocus” after each collapse cycle. Each subsequent cycle has a less steep intensity gradient, producing frequencies closer to the pump wavelength—the spectral energy density in the wings of the supercontinuum is greatly reduced.

GVD is directly proportional to the interaction length in the medium—as illustrated in Section 2.2.1, longer driving (pump) wavelengths require longer interaction lengths. Coupled with the generally increasing value of the GVD with increasing wavelength, IR and Mid-IR driven SCG processes require higher input peak powers to counter the quenching effects of GVD. For a simplified case for illustration purposes, the GVD-based Peak-Power equation from Agrawal [2.40] can be used:

$$P(z) = \frac{P_o}{\sqrt{\left[1 + \left(\frac{z}{L_D}\right)^2\right]}} \quad [1.25]$$

where  $L_D$  is the dispersion length,  $L_D = \frac{\tau_p}{|GVD(\lambda)|}$ ,  $\tau_p$  is the pulse width,  $GVD$  is the value of the group velocity dispersion at the pulse at the central pump wavelength  $\lambda$ ,  $z$  is the interaction length in the medium and  $P_0$  is the input peak power.

It has been shown that when the dispersion length  $L_D \gg z_f$  of the pulse, SF dominates the pulse dynamics, and GVD only comes into play at the onset of SCG and the explosive growth of bandwidth; for input parameters where  $L_D \ll z_f$  in the normal dispersion regime, GVD lowers the peak power of the pulse and can be a dominating mechanism to prevent collapse [2.18].

The effects of GVD are also inversely proportional to the spectral content of the pulse. Peak power is quenched much more rapidly for femtosecond driving pulses (Figure 2.26) than for the picosecond. But picosecond pulses with similar input energies require a greater interaction length in the nonlinear medium to reach collapse, leading to higher accumulated group delay and an additional reduction in peak power.

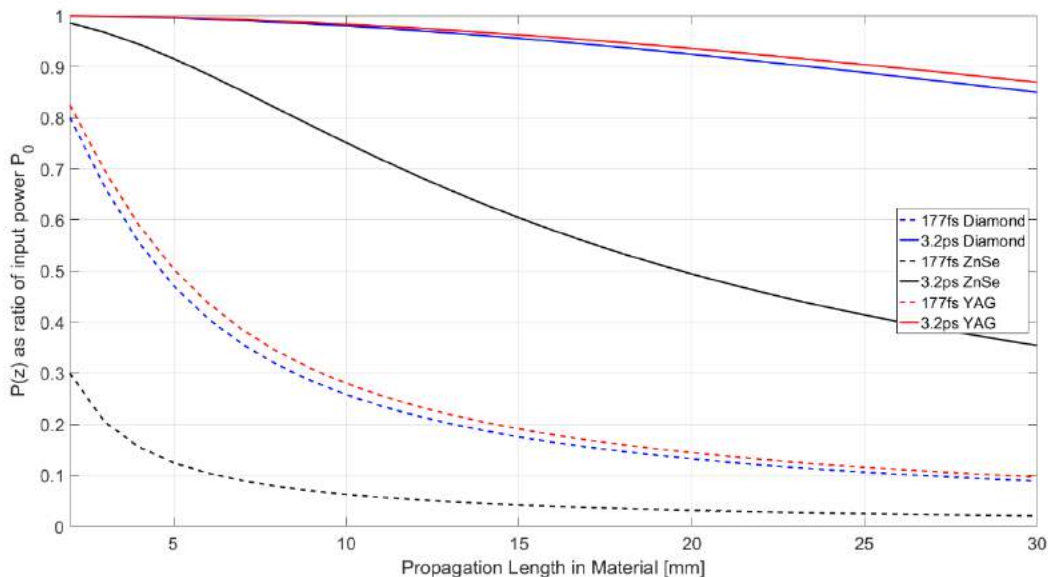


Figure 2.26: Reduction in peak powers vs. propagation length due to GVD for various materials at different pulse widths.

## 2.3 SPATIO-TEMPORAL EVOLUTION OF THE SC PULSE

The evolution of the pump pulse evolving into an SC can be divided into two “regimes”. The first is a slow-developing, SF-dominated process. The input intensity and spectral profile also starts changing, developing chirp and temporal broadening due to the GVD of the pulse, accumulating nonlinear phase and frequency components due to SPM, and developing the spatio-temporal profile that is a precursor to pulse-splitting due to the increasingly higher nonlinear index seen by the high-intensity peak of the pulse. Then, at some critical point in the pulse’s propagation, there is a very abrupt onset of self-steepening [2.41], rapid spectral broadening, the sudden appearance of conical emission (CE) in the output spatial profile of the pulse, followed by plasma generation, all within a few microns of propagation length.

### 2.3.1 The Moving Focus Model

So far, only the peak of the pulse has been considered—non peak regions of the pulse (both spatial and spectral) with peak powers in excess of  $P_{cr}$  also self-focus based on their individual  $\frac{P}{P_{cr}}$  ratios and the transverse profile of these components of the pulse evolves differently than the peak. Marburger et al. [2.19, 2.21] use the moving focus model to analyze the evolution of such a system—the pulse is modeled as longitudinal stack of infinitely thin transverse slices that propagate independently from each other at the pulse’s group velocity. Because the position of the self-focus depends on power, each slice will focus at a different  $z$  position and at different times  $t$ . Even in the absence of other linear/nonlinear effects, this model accounts for the reason why the onset of SCG always occurs at peak powers *greater* than  $1.0P_{cr}$ —each “slice” of the pulse only contains some percentage of the total energy of the pulse, i.e.  $E_{slice} = (1 - \gamma)E_{input}$  where  $\gamma$  is the fraction of energy contained in the rest of the pulse, with the value of  $\gamma$  dependant on the pulse shape. This means that  $P_{slice} = \frac{E_{slice}}{\tau_0} \ll P_{input} = \frac{E_{input}}{\tau_0}$ , where  $\tau_0$  is

the temporal pulse-width. If  $P_{input}$  is set to  $1.0P_{cr}$ , the power in the central (peak) slice of the pulse will always be less than  $P_{cr}$  and the pulse will not self-focus.

In the moving focus model, one expects that the highest-peak-power slice (i.e. the central slice of a pulse given a Gaussian input profile) will focus first along the propagation axis at some  $z_{f,peak}$ , followed by a region containing a continuous distribution of self-foci formed by slices of intermediate power. Finally, the slice with peak power  $1.0P_{cr}$  will focus furthest from the entrance face of the nonlinear medium, at some  $z_{f,cr}$ . As predicted by this model, experimental observations find that input pulses with higher peak powers trigger the formation of a filament closer to the entrance face of the crystal [2.8].

### 2.3.2 Pulse Splitting

The phenomena of temporal pulse-splitting has been reported experimentally [2.42, 2.43] and investigated theoretically [2.44, 2.45] for intense pulses propagating in a nonlinear medium.

Considering only the Kerr nonlinear effect, at the onset of SCG, the sudden spike in intensity of the central peak means it experiences a sharply different, high, refractive index and is retarded with respect to the wings of the pulse. This creates an asymmetrical temporal “split” within the pulse—a low-intensity leading sub-pulse and a high-intensity trailing sub-pulse, with an appreciable temporal separation between each pulse [2.44, 2.46] and temporal durations for each sub-pulse shorter than the original input pulse [2.46].

Considering only SF and GVD, multiple studies [2.47, 2.48] demonstrate that through four-wave mixing of the pulse, red and blueshifted wavepackets form within the pulse, and separate in the temporal domain due to normal GVD, eventually splitting the pulse. Figure 2.27, from [2.44], shows the evolution of the pulse-split.

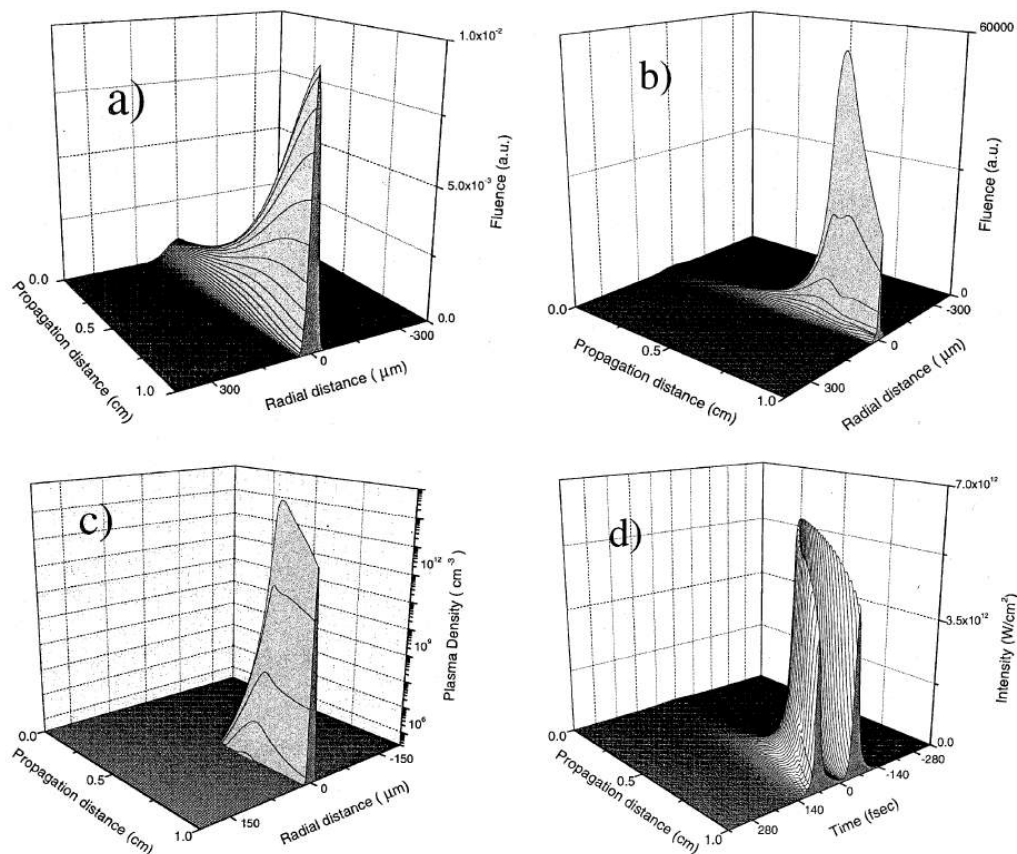


Figure 2.27: Split Pulse propagation from [2.44]

Spatially, plasma generation has also been implicated in the pulse-splitting process: the plasma defocuses and quenches the back of the pulse, effectively “pushing” the peak intensity to the front [2g-19]. This creates a steep leading edge and leaves a “tail” of smaller peaks. This tail can be caused by one (or many) of the formative process of SCG pulses—due to SF and the multi-focus model, where higher power portions of the pulse focus earlier in the medium [2.10], due to the higher order dispersion of the spectral components of the pulse [2.14] or self-steepening [2.10]. As the pulse propagates, the leading pulse decays and the trailing pulse re-focuses [2.49] as long as the trailing pulse remains above  $P_{cr}$ . Figure 2.28, taken from X. Chen et al. [2.14] illustrates the formation of this asymmetric split pulse as a function of input energy. Note that MPI itself also contributes to further pulse-splitting due to the abrupt defocusing of the *middle* of the pulse[2.29].

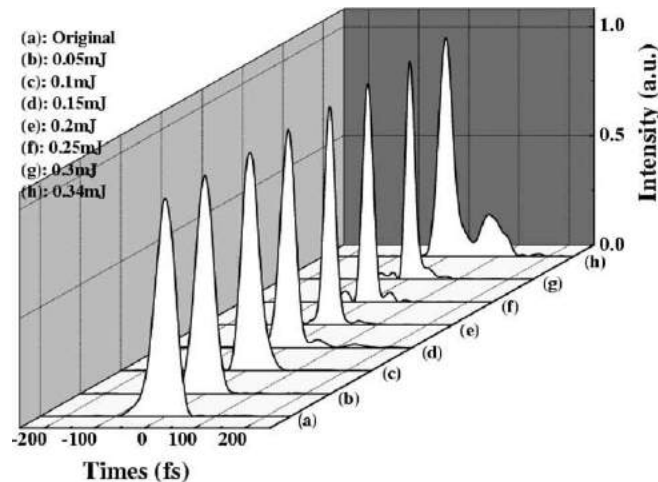


Figure 2.28: Temporal profiles of the output pulse at different input pulse energy, from X. Chen et al., [2.14].

GVD also plays a significant role in shaping the temporal asymmetry of the split pulse—by discarding the slowly varying envelope approximation and incorporating space-time focusing terms in the propagation equation, Rothenburg [2.30] shows that the group velocity variation of off-axis rays causes a dramatic shift of energy to the trailing edge of the input pulse, leading to a strongly asymmetric splitting of the pulse with a weak (almost pedestal-like) leading sub-pulse and a strong self-focusing trailing sub-pulse accompanied by a shock on the trailing edge of the delayed sub-pulse. These results (for the normal dispersion regime) are confirmed by Gaeta [2.10], and account for a portion of the blueshift of the SC output. Contradicting the simulations by Durand et al. [2.51], the study by Rothenburg [2.30] shows that the asymmetric splitting effect is found in both the anomalous and normal dispersion regimes and the dispersive wave is generated in both normal [2.29, 2.52] and anomalous [2.50, 2.53] regimes. Contradicting Rothenburg [2.30], Durand et al. [2.51] conclude via simulation that the intense input pulse undergoes filamentation in the anomalous dispersion regime but does not split. Given experimental observations of SC generated in the anomalous region [2.7], it is difficult to accept the study by Durand et al. in the absence of a mechanism that explains conical emission in the absence of pulse-splitting.

### 2.3.3 Conical Emission and X-Waves

The “ringed” output of the SC, termed the conical emission (CE) (as opposed to the WL—white light—core) arises out of the group velocity dispersion, phase-matching and four-wave mixing process during pulse-splitting [2.50].

Pulse splitting naturally emerges out of the X-wave four-wave mixing model [2.50] as the momentum-conservation mechanism for phase and group matching between the two localized pump waves and two (weak) amplifying X waves.

A study by Jarnac et al. [2.54] on pulse reshaping during filamentation shows the formation of a ring-like structure at the middle of the pulse during the splitting process. The two-sub pulses move away from the middle as the pulse propagates, while the ring refocuses and rebuilds the axial component of the pulse (Figure 2.29). Then, diffraction increases the dimension of the entire spatiotemporal profile of the pulse.

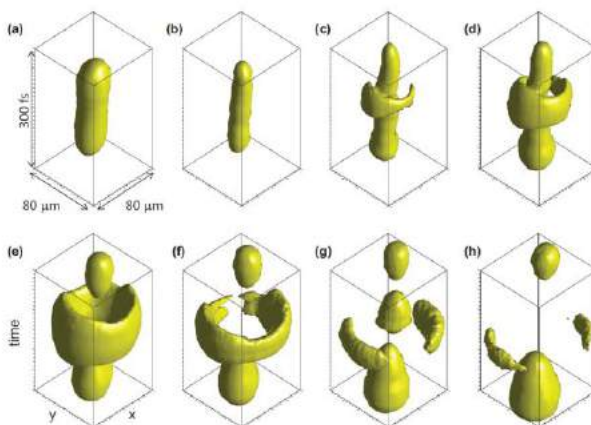


Figure 2.29: Ring-like structure in pulse from [2.29]

Studies [2.50, 2.54] confirm that the temporal splitting of the input pulse generates X-waves. Nonlinear X-Waves—nondiffracting and nondispersive spatially and temporally extended solutions to the NLSE [2.55]—have a characteristic X-shaped structure in the transverse momentum/spectral domain and the

space-time domain [2.56]. Created by a four-wave mixing process involving two highly localized pump waves and two X-waves [2.50], X-waves have been shown to replenish energy losses in the core of the pulse by drawing energy from the extended tails [2.57], and are part of the dispersive dynamics (the core-replenishing “ring structure” reported in [2.54]) that create CE during the pulse-splitting process. The CE portion of the SC output is the result of group and phase matching conditions between the generated X-waves and the pump pulse: if the group velocity of the X-wave is significantly different from the pulse group velocity, a strong blue-shifted peak appears in the spectrum [2.50]. Jarnac et al. [2.54] confirm that the “rings” of color seen in the CI are produced during the pulse-splitting event; successive pulse-splitting events lead to modulation of the central WL spectra *and* additional rings of color in the CI—the same colors that resulted from the first pulse-splitting event, but with different divergence angles. Further, multiple simulations [2.58-2.60] have found nonlinear X-Waves to be responsible for the mode self-cleaning found in the SC output.

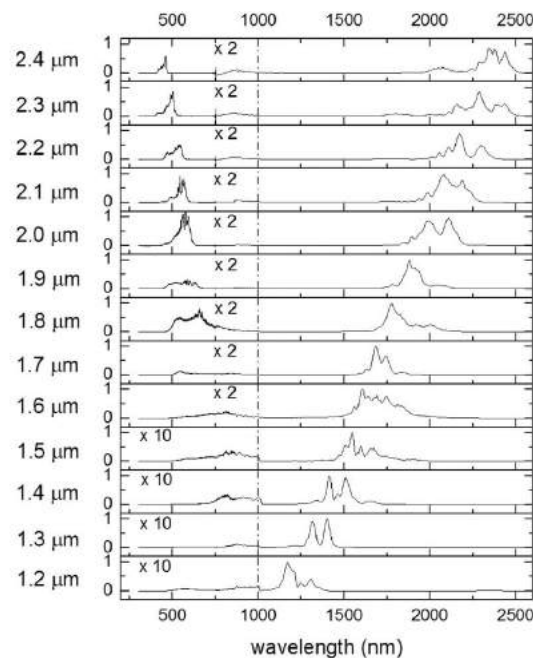


Figure 2.30: Blueshift of the dispersive wave, from [2.51]

The visible dispersive wave component of the SC output is increasingly blueshifted with increasing pump wavelength (Figure 2.30).

#### 2.3.4 Self Steepening

Self-steepening occurs when the leading component of the pulse experiences a greater degree of SF than the trailing portion as the pulse propagates through the medium; the leading component propagates slower than the trailing, resulting in a spatio-temporal compression of the pulse and the development of a sharp optical shock-like dropoff of intensity in the trailing part, as studied by [2.61] and [2.10]. Essentially, the peak of the pulse sees a higher refractive index than the wings—it travels slower than the leading and trailing edges. This leads to an intensity build-up in the trailing edge of the pulse as the peak shifts further and further back towards the trailing edge. Effectively, the “original” trailing edge moves faster within the co-moving frame of the pulse-peak, “catching up” to the peak. The intensity gradient of the pulse now has a sharpened trailing edge, leading to the favourable production of blue-shifted frequencies as the pulse propagates in the medium.

The onset of self-steepening is very abrupt and accompanied by a very large broadening on the Anti-Stokes side of the driving pulse as well as CI. Schroeder et al. [2.61] state, “*We emphasize that the steep jump in spectral broadening in {Fig. 4} corresponds to self-steepening*”. However, they study self-steepening as a phenomenon isolated from pulse-splitting and space-time focusing—the detailed study by Jarnac et al. [2.54] has already demonstrated that it is pulse-splitting that is directly responsible for the presence of CI and that asymmetry in the splitting process leads to large, fast-onset blueshifts. Space-time focusing [2.30] and MPI [2.8] also create intensity profiles and the formation of an optical shock at the trailing edge of the pulse [2.10]. It is simplistic to consider that self-steepening alone acts to shape the pulse profile in such a manner since all of the above processes can be termed “abrupt”, i.e.

they develop on the order of half an optical cycle of the driving frequency to a few femtoseconds when the critical intensity begins to approach  $\sim 10^{18}$  W/cm<sup>2</sup>.

Self-Steepening and Space-Time Focusing are largely responsible for the temporal pulse compression seen in the high-power, femtosecond regime in normally dispersive bulk nonlinear media [2.16, 2.62, 2.63] due to self-channeling of high-peak-power fs pulses [2.64], which leads to compression up to few-cycle pulses [2.49, 2.65].

## 2.4 ADDITIONAL NOTES ON THE ORIGIN OF SPECTRAL STRUCTURE IN THE SC PULSE

The asymmetric spectral broadening of the SC pulse (with greater spectral extent and energy densities towards the Anti-Stokes side of the driving wavelength) has been attributed to various phenomena: self-steepening of the pulse, leading to shockwave formation [2.10], intensity clamping and spectral blueshifting due to plasma generation [2.8,2.66], an asymmetry in the pulse-splitting dynamics due to CE [2.55], as well as the formation of blueshifted x-waves due to three and four wave mixing processes [2.36]. There is an inherent error in ascribing any one of these processes as the dominant or standard mechanism for the asymmetric broadening observed in experiment (or in numerical studies that model multiple effects to improve the accuracy of simulations), namely that each spectral region is *not* a monolithic block of frequencies with a single or combination source.

The author of this work proposes that the ASW region contains frequencies generated via multiple effects, and the spectral energy density at any given wavelength may be a combination of:

- a) The Anti-Stokes side spectral broadening of the central peak. This would include the “standard” blueshifted frequency components attributed to self-steepening and plasma generation, with the maximum spectral extent  $\Delta\omega_{+(max)} \propto \delta_t \rho$ , the rate of change of the plasma density [2.36].

- b) The axial component of the conical emission [2.51], X-waves and four (three) wave mixing formed due to momentum-conservation during the pulse-splitting process.
- c) Broadening of the third harmonic itself at extremely high input powers.
- d) Raman contributions, especially in materials with a strong Raman response, like diamond.

A qualitative assessment of the combined contributions of each of these effects goes a long way towards explaining the structure and spectral behavior of the ASW region.

As noted by Kolesik et al. [2.36], chromatic dispersion plays a large part in determining the limits of the SC spectral extent, and the ratio of material bandgap to pump photon energy implicated in the plasma blueshift/intensity clamping phenomena [2.67] is not sufficient to explain the total spectral extent of the ASW. Brodeur and Chin [2.8] note that with increasing shorter pump wavelength  $\lambda_0$ , the width of the continuum decreases but the blue-side cutoff frequency increases [2.67]. While the absolute cutoff is determined to be a bandgap/plasma related phenomena, the increasingly narrow width of the (total) spectrum can be entirely explained by the smaller phase-matched region available at shorter pump wavelengths due to stronger dispersion at these wavelengths [2.36] Also, while multiple studies have shown that the Anti-Stokes Peak (ASP) cannot be ascribed to third harmonic generation [2.68] and indeed, our studies show a distinct third harmonic peak as well as a well-defined ASP at 2 $\mu$ m pump wavelengths (See Chapter 3), the interaction of frequencies generated through the HHG process and their contribution to the ASW cannot be ignored.

Apart from the total spectral extent of the SC output, the behavior of the blueshifted peak in the ASW can be explained by considering that the total spectral energy density in this region is a combination of multiple factors. First, the *location* of the blueshifted peak can be predicted using the momentum conservation constraints placed upon the four-wave mixing process [2.53], and predictions are in good agreement with experimental observations [2.8].

Given that the change in susceptibility has slower time variations than the dominant phase-match between the optical carrier group velocity interacting with the transverse material excitation [2.36] mainly due to GVD (especially as the pulse broadens spectrally), there is a relaxation in phase-matching conditions that increases with increasing  $\lambda_0$  (as the group velocity offset between the blueshifted peak and the pump wavelength increases). This should lead to a broadening of the spectral region of the blueshifted peak, i.e. the blue-side dispersive wave component of the ASW. However, it was noticed [2.68] that the spectral band of this peak region *narrowed* with increasing pump wavelength. Looking at the angle-resolved study by Silva et al. [2.7], the similar extent and spectral energy density of the blue wing of the dispersive wave for all driving wavelengths (see Figure 2.30), it can be concluded that the narrowing spectral extent of the blue-side dispersive wave is illusory—it is merely that the spectral energy density contribution at these wavelengths from the *primary* pump broadening that has dropped in the ASW region *between* the blueshifted peak and the exponential Anti-Stokes side dropoff of the primary pump broadening. With increasingly redshifted pump wavelengths, the dispersive wave spectral region is further and further away from  $\lambda_0$ , and though the total *extent* of spectral broadening is greater for longer wavelengths, total spectral energy density available at these further wavelengths is much lower.

The cutoff wavelength of the Anti-Stokes side of the SC spectral output depends on the wavelength of the driving pulse [2.67], but does not increase with increasing input energy. Also, the appearance of the Anti-Stokes side broadening is abrupt, and it covers the entire blue-side spectral range immediately [2.69].

On the other hand, it has been observed that the Stokes side spectral extent increases with increasing input pulse energy, and progressively shifts towards longer wavelengths with longer input focusing geometry [2.69]. The difference in timing that generates the Stokes side wavelength (i.e. they originate in the intensity gradient of the leading edge of the pulse instead of the trailing edge, as for Anti-Stokes

wavelengths) means the intensity clamping, plasma generation and x-wave generation that determines the extent of the Anti-Stokes side of the pulse is not in play. A looser focusing geometry means that the power contained in the leading edge of the pulse is better localized in the filament-forming central region (better conversion efficiency), can propagate longer in the nonlinear medium and form longer filaments with increasing input powers without running into the shock-wave formation problems of the trailing edge.

It should be noted that given the origin of the dispersive wave, there should be a matching component on the Stokes side of  $\lambda_0$  as well, and in studies that do extend their spectral coverage deeper into the infrared region [2.7], this “red side” dispersive wave has been observed. Also, on the Stokes side, one would also expect  $\lambda_0$ -driven parametric amplification of the Stokes-side counterparts of (a) and (b) depending on the nature of the third-order and induced second-order susceptibility.

The effect of GVD on the spectral profile of the SC output is further studied by Junnarkar [2.44], where it is shown that a positive chirp on the input pulse blueshifts the SC-produced output spectrum, similar to the effect of MPI, whereas a negative chirp suppresses blue enhancement. The study [2.44] was carried out in the normal dispersion regime (fused silica,  $\lambda_0 = 800\text{nm}$ ), where due to GVD, the red frequencies travel to the leading edge of the pulse and blue to the trailing edge. As discussed in Section 2.3.2 and 2.2.2, the accumulated effect of SF and plasma generation serve to create an asymmetric split pulse with a sharp dropoff in the intensity gradient of the trailing edge of each sub-pulse, enhancing the blueshift of the output spectra. So, in the normal dispersion regime, a positive chirp will serve to shift the high frequency (high photon energy) components of the pulse(s) to the trailing edges, further enhancing the blueshift, while a negative chirp will (to some extent) balance the asymmetry in the pulse split and temporal intensity gradients, shifting the high frequency components towards the leading edge. Golubstov et al. [2.41] have also demonstrated the use of negative chirp to extend the length of a filament. The generation of Anti-Stokes wavelengths and the pump-to-red conversion efficiency of the

SC depends heavily on the spectral makeup of the pulse; Golubstov et al. [2.41] conclude a negative chirp increases the propagation length of the pulse in the medium before filamentation is triggered (i.e. before critical intensities are reached), and lengthens the filament itself. In the context of SCG in the anomalous dispersion regime, the negative chirp imposed upon the pulse by the material itself would account for the greater spectral widths observed in experiments [2.7]. Also, the separation between refocusing events is larger [2.70] in the anomalous dispersion regime, as more energy is transferred back into the collapse region from the energy reservoir after plasma defocusing—energy is drawn in from the dispersive waves to sustain the filament [2.70]. This means that the length of the filament is larger in the anomalous dispersion regime, length of filament is larger in anomalous [2.70]. There is also an enhancement of the Anti-Stokes broadening: the filament start distance is smaller for a given  $\frac{P}{P_{cr}}$  ratio due to anomalous GVD [2.71]. Also, the greater self-steepening due to anomalous GVD (i.e. intensity piles up in the tail of the pulse) leads to a larger intensity gradient and larger anti-Stokes broadening than in the zero or normal GVD [2.68] regime.

## 2.5 ADDITIONAL NOTES ON PRE-FOCUSING CONDITIONS OF THE INPUT PULSE

The central White Light (WL) portion of the SC output represents a small part of the total pulse energy [2.8], with an additional portion of the SC spectral energy contained in the highly divergent Conical Emission (CE) portion (Figure 2.31).

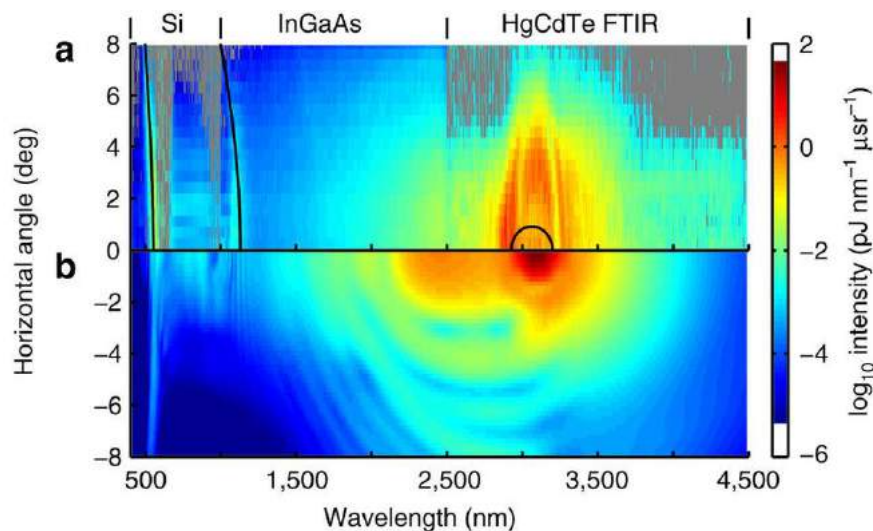


Figure 2.31: (a) Measurement and (b) simulation of the far field  $\{\vartheta, \lambda\}$  representation in absolute units, from [2.7].

The conversion efficiency of the SC process (shifting energy from the pump wavelength to the SC-generated Stokes and Anti-Stokes wavelengths) depends on the length of the filament and its transverse diameter over its evolution in the nonlinear medium. Apart from the nonlinear effects intrinsic to the SC process, pre-focusing conditions and the numerical aperture match of the input pump beam with the filament—the localization of the intense input pump along the length of the filament—are key players in determining the conversion efficiency, and have a large part in determining the residual pump fraction (portions of the pulse that will *not* undergo self-focusing). One can simulate the effects on self-focusing distance due to an external lens using Eq. (3) from the study by Brodeur and Chin [2.8] (Figure 2.32). Here, as the focus of the external lens is offset from the naturally-occurring Kerr-focus (of a collimated beam in a nonlinear medium), there is a drastic change in the equivalent focus based on the  $\frac{P}{P_{cr}}$  ratio of the beam. Different portions of the beam have very different divergence angles, and the “continuum of self-focal spots” for varying powers breaks down—parts of the beam (especially lower-power axial portions) may not self-focus strongly at all, leading to an artificially shortened filament size and a

residual pump portion whose divergence angle will be drastically different from the central WL portions of the SC pulse.

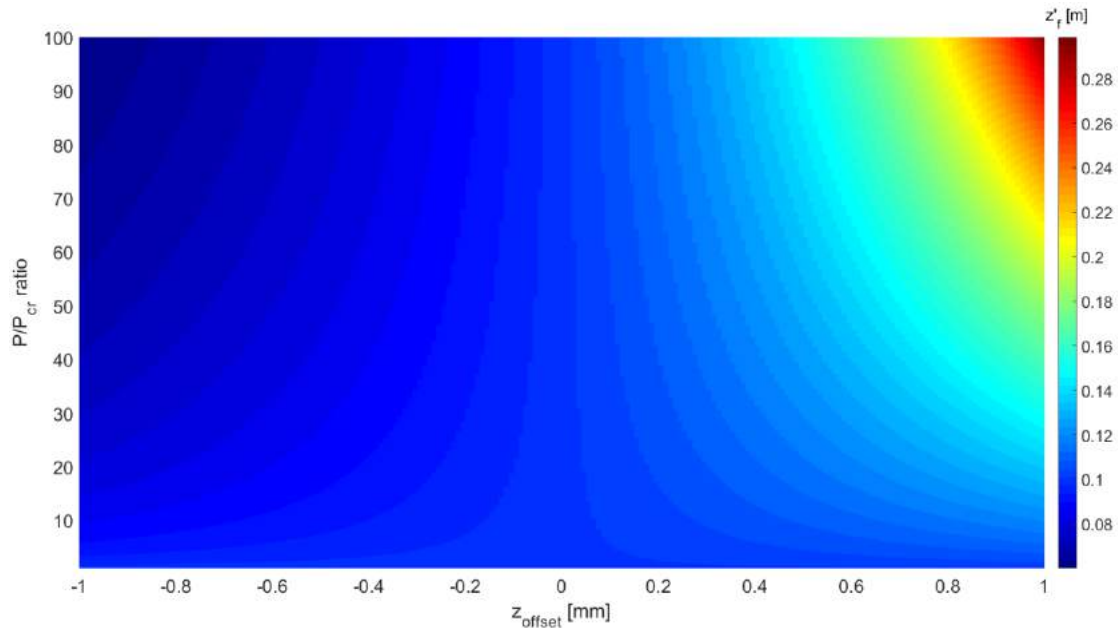


Figure 2.32: Effect of External Focusing on SF distance

It has been shown that loose focusing geometry in bulk materials results in the extension of the Stokes-side of SC output spectra [2.73 – 2.76]. A study by Jukna et al. [2.69] supports the interpretation of this work, i.e. that longer propagation length in the medium before the abrupt increase in self-focused intensity results in redshifted spectra.

Ref [2.72] notes that the femtosecond continuum will have a smaller beam divergence of the WL component than the picosecond continuum (in air). However, the divergence of the beam is based upon a number of interrelated factors including the nonlinear propagation length before collapse (different for femtosecond and picosecond regimes), the  $\frac{P}{P_{cr}}$  ratios, and the focusing geometry changes that may be required to “force” self-focusing for picosecond beams for a given length of nonlinear material— theoretically, the divergence of a femtosecond beam should be more sensitive to GVD, and it has been observed during the FLASH-WL study that the CE of shorter pulses diverges more than that of longer

pulses at similar input powers: a 500fs input pulse at 5 [W] average power generated a 6.8 [cm] diameter CE pattern on a screen 200mm away from the exit face of the crystal, whereas a 700fs input pulse under identical conditions produced a much smaller 4 [cm] diameter CE pattern.

Linear focusing by an external lens also results in a temporal distortion of the pulse, (a) due to the variation of the group delay of off-axis rays [2.77], and (b) due to the different on-axis positions of self-foci for off-axis pulse components with similar peak powers but different divergence angles. As per earlier discussion, the intensity gradient of each pulse component is roughly similar for components of similar peak power—the frequencies produced through SPM will be the same, but the variable time delay between the formation of each component's self-focus will result in a distorted phase profile that does not match that of the phase profile of the intense, on-axis component of the beam. The contribution to pulse temporal distortion from (a), the variation in group delay of the pulse components, is extremely pronounced for broadband (~femtosecond regime) pulses. To wit, the space-time, frequency-phase coupling of SC processes means that the temporal distortions introduced to the pulse due to strong external focusing translate into temporal distortions of the pulse and very high modulation instabilities in both spatial and temporal domains that are magnified as the pulse intensity increases drastically near the SF.

## 2.6 REFERENCES

- [2.1] Alfano, Robert R. "The supercontinuum laser source." (1989): 458.
- [2.2] Dudley, John M., and James Roy Taylor, eds. *Supercontinuum generation in optical fibers*. Cambridge University Press, 2010.
- [2.3] Corkum, P. B., Claude Rolland, and T. Srinivasan-Rao. "Supercontinuum generation in gases." *Physical review letters* 57.18 (1986): 2268.
- [2.4] Couairon, Arnaud, and André Mysyrowicz. "Femtosecond filamentation in transparent media." *Physics reports* 441.2 (2007): 47-189.
- [2.5] "White light continuum." Heriot Watt University Non-Linear Optics Group. 08/12/2017, retrieved 23/7/2017. <http://www.nlo.hw.ac.uk/node/8>
- [2.6] Liu, W., et al. "Intensity clamping of a femtosecond laser pulse in condensed matter." *Optics Communications* 202.1 (2002): 189-197.
- [2.7] Silva, F., et al. "Multi-octave supercontinuum generation from mid-infrared filamentation in a bulk crystal." *Nature communications* 3 (2012): 807.
- [2.8] Brodeur, A., and S. L. Chin. "Ultrafast white-light continuum generation and self-focusing in transparent condensed media." *JOSA B* 16.4 (1999): 637-650.
- [2.9] Yablonovitch, Eli. "Self-phase modulation of light in a laser-breakdown plasma." *Physical Review Letters* 32.20 (1974): 1101.
- [2.10] Gaeta, Alexander L. "Catastrophic collapse of ultrashort pulses." *Physical Review Letters* 84.16 (2000): 3582.
- [2.11] Kandidov, V. P., et al. "Self-transformation of a powerful femtosecond laser pulse into a white-light laser pulse in bulk optical media (or supercontinuum generation)." *Applied Physics B: Lasers and Optics* 77.2 (2003): 149-165.
- [2.12] Boyd, Robert W. *Nonlinear optics*. Academic press, 2003.
- [2.13] Butcher, Paul N., and David Cotter. *The elements of nonlinear optics*. Vol. 9. Cambridge university press, 1991.
- [2.14] Chen, Xiaowei, et al. "Pulse self-compression in normally dispersive bulk media." *Optics communications* 259.1 (2006): 331-335
- [2.15] Hauri, C. P., et al. "Generation of intense, carrier-envelope phase-locked few-cycle laser pulses through filamentation." *Applied Physics B: Lasers and Optics* 79.6 (2004): 673-677.

- [2.16] Diddams, Scott A., et al. "Characterizing the nonlinear propagation of femtosecond pulses in bulk media." *IEEE Journal of selected topics in quantum electronics* 4.2 (1998): 306-316.
- [2.17] Henz, S., and J. Herrmann. "Self-channeling and pulse shortening of femtosecond pulses in multiphoton-ionized dispersive dielectric solids." *Physical Review A* 59.3 (1999): 2528.
- [2.18] Luther, G. G., et al. "Self-focusing threshold in normally dispersive media." *Optics letters* 19.12 (1994): 862-864.
- [2.19] Marburger, J., and W. Wagner. "Self-focusing as a pulse sharpening mechanism." *IEEE Journal of Quantum Electronics* 3.10 (1967): 415-416.
- [2.20] Shen, Y. R., and Michael MT Loy. "Theoretical interpretation of small-scale filaments of light originating from moving focal spots." *Physical Review A* 3.6 (1971): 2099.
- [2.21] Marburger, J. H. "Self-focusing: theory." *Progress in Quantum Electronics* 4 (1975): 35-110.
- [2.22] Moloney, J. V., et al. "Femtosecond self-guided atmospheric light strings." *Chaos: An Interdisciplinary Journal of Nonlinear Science* 10.3 (2000): 559-569.
- [2.23] Gustafson, T., and C. Townes. "Influence of steric effects on nonlinear responses to laser pulses and the diameters of self-trapped filaments." *IEEE Journal of Quantum Electronics* 8.6 (1972): 587-588.
- [2.24] Baldeck, P. L., P. P. Ho, and R. R. Alfano. "Effects of self, induced and cross phase modulations on the generation of picosecond and femtosecond white light supercontinua." *revue de physique appliquée* 22.12 (1987): 1677-1694.
- [2.25] Yablonovitch, Eli, and N. Bloembergen. "Avalanche ionization and the limiting diameter of filaments induced by light pulses in transparent media." *Physical Review Letters* 29.14 (1972): 907.
- [2.26] Feng, Q., et al. "Theory and simulation on the threshold of water breakdown induced by focused ultrashort laser pulses." *IEEE Journal of Quantum Electronics* 33.2 (1997): 127-137.
- [2.27] Keldysh, L. V. "Ionization in the field of a strong electromagnetic wave." *Sov. Phys. JETP* 20.5 (1965): 1307-1314.
- [2.28] Slusher, R. E., W. Grijat, and S. R. J. Brueck. "Multiphoton-injected plasmas in InSb." *Physical Review* 183.3 (1969): 758.
- [2.29] Kolesik, M., et al. "Theory and simulation of supercontinuum generation in transparent bulk media." *Applied Physics B: Lasers and Optics* 77.2 (2003): 185-195.
- [2.30] Rothenberg, Joshua E. "Space-time focusing: breakdown of the slowly varying envelope approximation in the self-focusing of femtosecond pulses." *Optics Letters* 17.19 (1992): 1340-1342.

- [2.31] Chuang, Shun Lien, and Shun L. Chuang. "Physics of optoelectronic devices." (1995): 1-1.
- [2.32] Bloembergen, Nicolaas. "Laser-induced electric breakdown in solids." *IEEE Journal of Quantum Electronics* 10.3 (1974): 375-386.
- [2.33] Yamada, Kazuhiro, et al. "Volume grating induced by a self-trapped long filament of femtosecond laser pulses in silica glass." *Japanese journal of applied physics* 42.11R (2003): 6916.
- [2.34] Smith, W. Lee, P. Liu, and N. Bloembergen. "Superbroadening in H<sub>2</sub>O and D<sub>2</sub>O by self-focused picosecond pulses from a YAG: Nd laser." *physical Review A* 15.6 (1977): 2396.
- [2.35] Champeaux, Stéphanie, and Luc Bergé. "Femtosecond pulse compression in pressure-gas cells filled with argon." *Physical Review E* 68.6 (2003): 066603.
- [2.36] Kolesik, M., et al. "Physical factors limiting the spectral extent and band gap dependence of supercontinuum generation." *Physical review letters* 91.4 (2003): 043905.
- [2.37] Brodeur, A., and S. L. Chin. "Band-gap dependence of the ultrafast white-light continuum." *Physical review letters* 80.20 (1998): 4406.
- [2.38] Sheik-Bahae, M., David J. Hagan, and Eric W. Van Stryland. "Dispersion and band-gap scaling of the electronic Kerr effect in solids associated with two-photon absorption." *Physical review letters* 65.1 (1990): 96.
- [2.39] Potasek, M. J., Govind P. Agrawal, and Steven C. Pinault. "Analytic and numerical study of pulse broadening in nonlinear dispersive optical fibers." *JOSA B* 3.2 (1986): 205-211.
- [2.40] Agrawal, Govind P. *Nonlinear fiber optics*. Academic press, 2007.
- [2.41] Golubtsov, Il'ya Sergeevich, Valeriy Petrovich Kandidov, and Ol'ga Grigor'evna Kosareva. "Initial phase modulation of a high-power femtosecond laser pulse as a tool for controlling its filamentation and generation of a supercontinuum in air." *Quantum Electronics* 33.6 (2003): 525
- [2.42] Zozulya, Alex A., et al. "Propagation dynamics of intense femtosecond pulses: multiple splittings, coalescence, and continuum generation." *Physical review letters* 82.7 (1999): 1430.
- [2.43] Mlejnek, M., E. M. Wright, and J. V. Moloney. "Dynamic spatial replenishment of femtosecond pulses propagating in air." *Optics Letters* 23.5 (1998): 382-384.
- [2.44] Junnarkar, Mahesh R. "Short pulse propagation in tight focusing conditions." *Optics communications* 195.1 (2001): 273-292.
- [2.45] Zozulya, Alex A., et al. "Propagation dynamics of intense femtosecond pulses: multiple splittings, coalescence, and continuum generation." *Physical review letters* 82.7 (1999): 1430.

- [2.46] Ranka, Jinendra K., Robert W. Schirmer, and Alexander L. Gaeta. "Observation of pulse splitting in nonlinear dispersive media." *Physical Review Letters* 77.18 (1996): 3783.
- [2.47] Chernev, P., and V. Petrov. "Self-focusing of light pulses in the presence of normal group-velocity dispersion." *Optics letters* 17.3 (1992): 172-174.
- [2.48] Rothenberg, Joshua E. "Pulse splitting during self-focusing in normally dispersive media." *Optics letters* 17.8 (1992): 583-585.
- [2.49] Ward, H el ene, and Luc Berg e. "Temporal shaping of femtosecond solitary pulses in photoionized media." *Physical review letters* 90.5 (2003): 053901.
- [2.50] Faccio, Daniele, et al. "Conical emission, pulse splitting, and X-wave parametric amplification in nonlinear dynamics of ultrashort light pulses." *Physical review letters* 96.19 (2006): 193901.
- [2.51] Durand, Magali, et al. "Blueshifted continuum peaks from filamentation in the anomalous dispersion regime." *Physical Review A* 87.4 (2013): 043820.
- [2.52] Faccio, D., et al. "Generation and control of extreme blueshifted continuum peaks in optical Kerr media." *Physical Review A* 78.3 (2008): 033825.
- [2.53] Porras, Miguel A., et al. "From X-to O-shaped spatiotemporal spectra of light filaments in water." *Optics letters* 30.24 (2005): 3398-3400.
- [2.54] Jarnac, Am elie, et al. "Whole life cycle of femtosecond ultraviolet filaments in water." *Physical Review A* 89.3 (2014): 033809.
- [2.55] Prade, Bernard, et al. "Spatial mode cleaning by femtosecond filamentation in air." *Optics letters* 31.17 (2006): 2601-2603.
- [2.56] Conti, C., et al. "Nonlinear electromagnetic X waves." *Physical review letters* 90.17 (2003): 170406.
- [2.57] Dubietis, Audrius, et al. "Light filaments without self-channeling." *Physical review letters* 92.25 (2004): 253903.
- [2.58] Kolesik, M., E. M. Wright, and J. V. Moloney. "Dynamic nonlinear X waves for femtosecond pulse propagation in water." *Physical review letters* 92.25 (2004): 253901.
- [2.59] Couairon, A., et al. "Nonlinear X-wave formation by femtosecond filamentation in Kerr media." *Physical Review E* 73.1 (2006): 016608.
- [2.60] Kolesik, M., E. M. Wright, and J. V. Moloney. "Interpretation of the spectrally resolved far field of femtosecond pulses propagating in bulk nonlinear dispersive media." *Optics express* 13.26 (2005): 10729-10741.

- [2.61] Schröder, Hartmut, et al. "Self-steepening is an abrupt process." *Optics communications* 266.1 (2006): 302-306.
- [2.62] Ryan, Andrew T., and Govind P. Agrawal. "Pulse compression and spatial phase modulation in normally dispersive nonlinear Kerr media." *Optics letters* 20.3 (1995): 306-308.
- [2.63] Becker, A., et al. "Intensity clamping and re-focusing of intense femtosecond laser pulses in nitrogen molecular gas." *Applied physics B* 73.3 (2001): 287-290.
- [2.64] Henz, S., and J. Herrmann. "Self-channeling and pulse shortening of femtosecond pulses in multiphoton-ionized dispersive dielectric solids." *Physical Review A* 59.3 (1999): 2528.
- [2.65] Liu, Jun, et al. "Spectrum reshaping and pulse self-compression in normally dispersive media with negatively chirped femtosecond pulses." *Optics express* 14.2 (2006): 979-987.
- [2.66] Yuan-Dong, Qin, et al. "Spectral and temporal properties of femtosecond white-light continuum generated in H<sub>2</sub>O." *Chinese Physics Letters* 18.3 (2001): 390.
- [2.67] Nagura, Chihiro, et al. "Generation and characterization of ultrafast white-light continuum in condensed media." *Applied optics* 41.18 (2002): 3735-3742.
- [2.68] Smetanina, E. O., et al. "Anti-Stokes wing of femtosecond laser filament supercontinuum in fused silica." *Optics Letters* 38.1 (2013): 16-18.
- [2.69] Jukna, V., et al. "Infrared extension of femtosecond supercontinuum generated by filamentation in solid-state media." *Applied Physics B* 116.2 (2014): 477-483.
- [2.70] Moll, K. D., and Alexander L. Gaeta. "Role of dispersion in multiple-collapse dynamics." *Optics letters* 29.9 (2004): 995-997.
- [2.71] Dharmadhikari, Jayashree A., et al. "Effect of group velocity dispersion on supercontinuum generation and filamentation in transparent solids." *Applied Physics B* 117.1 (2014): 471-479.
- [2.72] Corkum, P. B., Claude Rolland, and T. Srinivasan-Rao. "Supercontinuum generation in gases." *Physical review letters* 57.18 (1986): 2268.
- [2.73] Bradler, Maximilian, Peter Baum, and Eberhard Riedle. "Femtosecond continuum generation in bulk laser host materials with sub- $\mu$  pump pulses." *Applied Physics B* 97.3 (2009): 561.
- [2.74] Ghotbi, M., V. Petrov, and F. Noack. "Broadly tunable, sub-30 fs near-infrared pulses from an optical parametric amplifier based on BiB<sub>3</sub>O<sub>6</sub>." *Optics letters* 35.13 (2010): 2139-2141.
- [2.75] Isaienko, Oleksandr, Eric Borguet, and Peter Vöhringer. "High-repetition-rate near-infrared noncollinear ultrabroadband optical parametric amplification in KTiOPO<sub>4</sub>." *Optics letters* 35.22 (2010): 3832-3834.

- [2.76] Andriukaitis, Giedrius, et al. "90 GW peak power few-cycle mid-infrared pulses from an optical parametric amplifier." *Optics letters* 36.15 (2011): 2755-2757.
- [2.77] Bor, Zsolt. "Distortion of femtosecond laser pulses in lenses." *Optics letters* 14.2 (1989): 119-121.
- [2.78] Liu, Jiansheng, et al. "Ultrafast control of multiple filamentation by ultrafast laser pulses." *Applied Physics Letters* 87.16 (2005): 161105.
- [2.79] Bergé, L., S. Mauger, and S. Skupin. "Multifilamentation of powerful optical pulses in silica." *Physical Review A* 81.1 (2010): 013817.
- [2.80] Hosseini, S. A., et al. "Competition of multiple filaments during the propagation of intense femtosecond laser pulses." *Physical review A* 70.3 (2004): 033802.
- [2.81] Corsi, C., A. Tortora, and M. Bellini. "Mutual coherence of supercontinuum pulses collinearly generated in bulk media." *Applied Physics B: Lasers and Optics* 77.2 (2003): 285-290.
- [2.82] Bellini, Marco, and Theodor W. Hänsch. "Phase-locked white-light continuum pulses: toward a universal optical frequency-comb synthesizer." *Optics letters* 25.14 (2000): 1049-1051.
- [2.83] Wilson, Kent R., and Vladislav V. Yakovlev. "Ultrafast rainbow: tunable ultrashort pulses from a solid-state kilohertz system." *JOSA B* 14.2 (1997): 444-448.
- [2.84] Watanabe, Wataru, et al. "Coherent array of white-light continuum generated by microlens array." *Optical review* 6.3 (1999): 167-172.

### 3 EXPERIMENTAL STUDIES IN SUPERCONTINUUM GENERATION

---

Bulk SCG in the  $2\mu\text{m}$ , high-energy, multi-picosecond regime has, to the best of the author's knowledge, not been investigated in published literature. The relative unknowability of parameters in the regime prompted the development of a (3+1)D simulation tool based on a slowly varying envelope approximation model developed by Gaeta [3.10] that could be used to experiment with pulse parameters and nonlinear crystals to maximize coherent, high energy-density SCG output on the Stokes (red) side of the pump wavelength. Experiments with  $1\mu\text{m}$ , 500-fs,  $5\mu\text{J}$  pumped Yttrium Aluminum Garnet (YAG) SCG were used to provide benchmarks and spectra to check the accuracy of the simulation, and fine-tune material parameters.

The experimental (in-vitro and in-silico) confirmation of exponential dropoff on the Stokes side of the pump pulse resulted in an attempt to determine whether the conical emission (CE) in the SCG output could be utilized to increase spectral energy density at far-from-pump wavelengths. This led to the first (to the best of the author's knowledge) spatio-spectral polarization analysis of SCG in a cubic crystal including the Conical Emission (CE), with an emphasis on studying induced nonlinear polarization rotation due to very high intensity pumps.

Based on the problems inherent in simulating SCG processes, the uncertainty in extrapolating parameters for  $2\mu\text{m}$  pump wavelengths from  $1\mu\text{m}$  data, and the computational cost in extending the simulation tool to picosecond pulses, a comparative study of the SCG performance of YAG, ZnSe, Sapphire and Diamond was carried out to in the  $\sim 2\mu\text{m}$ , sub 2-cycle pulse regime in the ICFO laser facility. SCG generated in Diamond at the ICFO facility raised the question of the impact of Stimulated Raman Scattering in increasing spectral energy density in SCG output. Simulations carried out in collaboration with the University of Warsaw prompted a Stimulated Raman Amplification (SRA) "proof of concept"

study to demonstrate that SCG-seeded Raman Amplification is (a) coherent as it is not noise-seeded, and (b) a viable approach for Stokes-Side amplification of SCG spectral energy density. With ZnSe identified as the leading candidate for picosecond,  $2\mu\text{m}$  SCG, the core IRDL nonlinear broadening experiment was carried out, and the creation of cascaded supercontinuum filaments from second and third harmonic conversion was investigated.

### 3.1 (3+1)D BULK SUPERCONTINUUM GENERATION SIMULATION DEVELOPMENT<sup>1</sup> & $1\mu\text{m}$ BASELINE SCG STUDY (FLASH-2, DESY)

Various models for Bulk-WLG use the nonlinear envelope equation under the slowly-varying-envelope approximation, which addresses self-phase modulation, diffraction, dispersion and self-steepening but is not sufficient to explain the SCG results seen experimentally. However, an approach by Gaeta [3.10] addresses this by considering plasma generation as well, and this approach forms the basis of the numerical simulations developed to support the IRDL supercontinuum generation efforts. In the NLSE considered (Equation [3.1]), the coupling between the  $\omega$  and  $\tau$  terms makes the textbook split-step implementation impossible. However, if the system is expressed in the Momentum-Frequency ( $k_x, k_y, \omega$ ) and Spatio-Temporal ( $x, y, \tau$ ) domains, they can be decoupled. Also, explicitly including the (3+1)D momentum propagation allows for more accurate solutions with respect to CE and X-wave generation.

The ubiquity of  $1\mu\text{m}$  supercontinua, pump pulse widths ranging from less than 100fs [3.5, 3.6, 3.9] to sub-picosecond [3.7] and up to 3 picosecond (1.8ps chirped) durations [3.8], makes such a wavelength range an useful choice to provide parameter inputs to simulations, and confirm the accuracy of the method. This  $1\mu\text{m}$  baseline SCG study was conducted in collaboration with the FS-LA group at DESY.

---

<sup>1</sup> The work in this subsection was presented at Europhoton 2014 by Choudhuri et al. [3.11] and CLEO 2015 by Zia et al. [3.12]. Further developments of the methodology and the code were carried out as part of the doctoral thesis work by Zia in [3.13].

### 3.1.1 Numerical Model

The formalism of the NLSE is given in Appendix B.

Each individual term in the equation corresponds to different physical effects, illustrated in Figure 3.1.

$$\frac{\partial u}{d\zeta} = \frac{i}{4} \left( 1 + \frac{i}{\omega_o \tau_p} \frac{\partial}{\partial \tau} \right)^{-1} \nabla_{\perp}^2 u - i \frac{L_{df}}{L_{ds}} \frac{\partial^2 u}{\partial \tau^2} + i \left( 1 + \frac{i}{\omega_o \tau_p} \frac{\partial}{\partial \tau} \right) \left[ \frac{L_{df}}{L_{nl}} |u|^2 u - \frac{L_{df}}{L_{pl}} \left( 1 - \frac{i}{\omega_o \tau_c} \right) \rho u + i \frac{L_{df}}{L_{mp}} |u|^{2(m-1)} u \right]$$

Figure 3.1: Physical breakdown of the Gaeta NLSE

### 3.1.2 Implementation

The NLSE can be divided into three operators, corresponding to the linear, nonlinear, and coupling (cross) terms as follows:

$$\hat{A} = \frac{i}{4} \left( 1 + \frac{i}{\mathbf{a}} \frac{\partial}{\partial \tau} \right)^{-1} \nabla_{\perp}^2 - i \mathbf{b} \frac{\partial^2}{\partial \tau^2} \quad \left. \vphantom{\hat{A}} \right\} \text{Linear Terms}$$

$$\hat{B} = i \left[ \mathbf{c} |u|^2 - \mathbf{d} \left( 1 - \frac{i}{\omega_o \tau_c} \right) \rho + i \mathbf{g} |u|^{2(m-1)} \right] + \left( \frac{-1}{\mathbf{a}} \right) \left[ \mathbf{c} \frac{\partial}{\partial \tau} |u|^2 - \mathbf{d} \left( 1 - \frac{i}{\omega_o \tau_c} \right) \frac{\partial}{\partial \tau} \rho + i \mathbf{g} \frac{\partial}{\partial \tau} |u|^{2(m-1)} \right] \quad \left. \vphantom{\hat{B}} \right\} \text{Nonlinear Terms}$$

$$\hat{C} = \left( \frac{-1}{\mathbf{a}} \right) \left[ \mathbf{c} |u|^2 \frac{\partial}{\partial \tau} - \mathbf{d} \left( 1 - \frac{i}{\omega_o \tau_c} \right) \rho \frac{\partial}{\partial \tau} + i \mathbf{g} |u|^{2(m-1)} \frac{\partial}{\partial \tau} \right] \quad \left. \vphantom{\hat{C}} \right\} \text{Nonlinear Cross Terms}$$

Given normalized amplitude  $\mathbf{u}$  for each “slice”  $\mathbf{z}_n$ , the split-step implementation can be broken down into the scheme outlined in Figure 3.2.

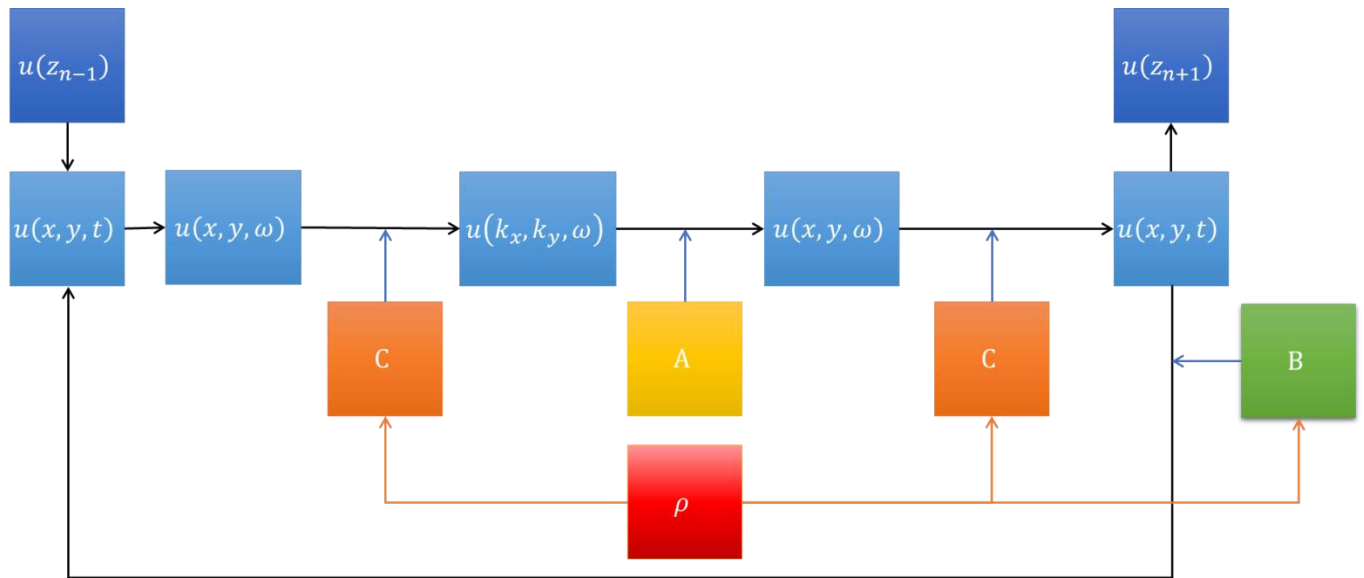


Figure 3.2: Split Step Implementation

The convention used for Fourier transforms is of the form:

$$f(t) = \int f(\omega) e^{i\omega t} d\omega$$

And

$$f(\omega) = \int f(t) e^{-i\omega t} dt$$

### 3.1.3 FLASH-2 Pump Source

The FLASH-2 seed laser is designed to serve a variety of experiments, some which require pulse energies in the hundreds of  $\mu\text{J}$ . Pulses at 1030nm from a commercial frontend oscillator (Origami, [3.77]) are amplified using a fiber amplifier to several hundred watts. The overall laser system setup is shown in Figure 3.3, but only the output of the fiber amplifier for the White Light Seeder stage is used in this specific study.

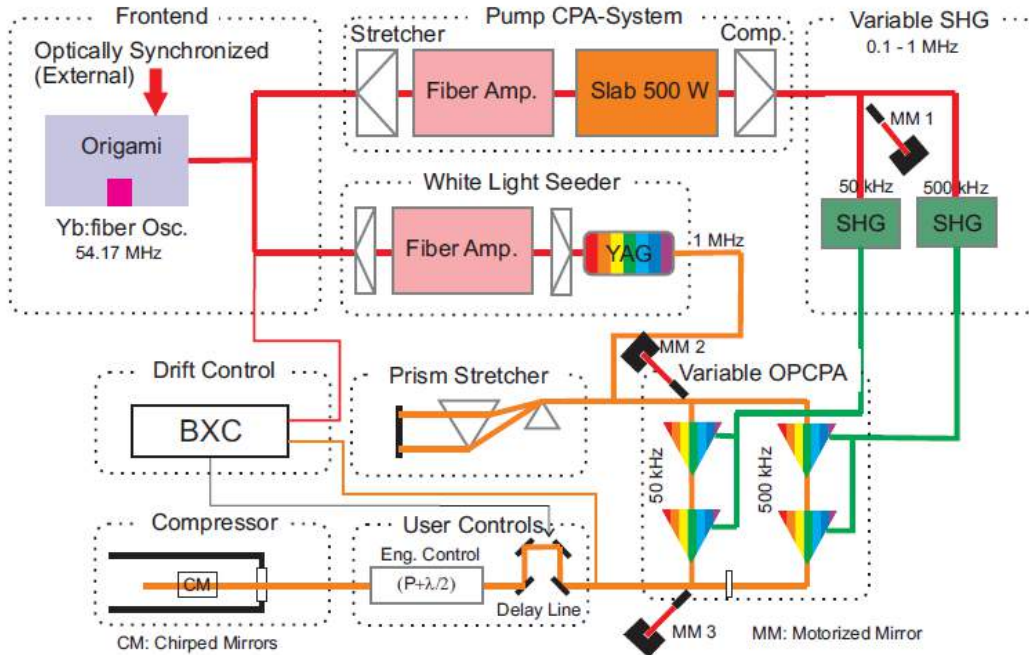


Figure 3.3: FLASH-2 Seed Laser System, from [3.73]

The fiber amplifier for the White Light Seeder stage (Figure 3.4) contains two pre-amplifiers (PA1, PA2), two main amplifiers (MA1, MA2), two AOMs to reduce the repetition rate, and a stretcher/compressor unit (fiber stretcher, Offner stretcher, mini compressor and main grating compressor).

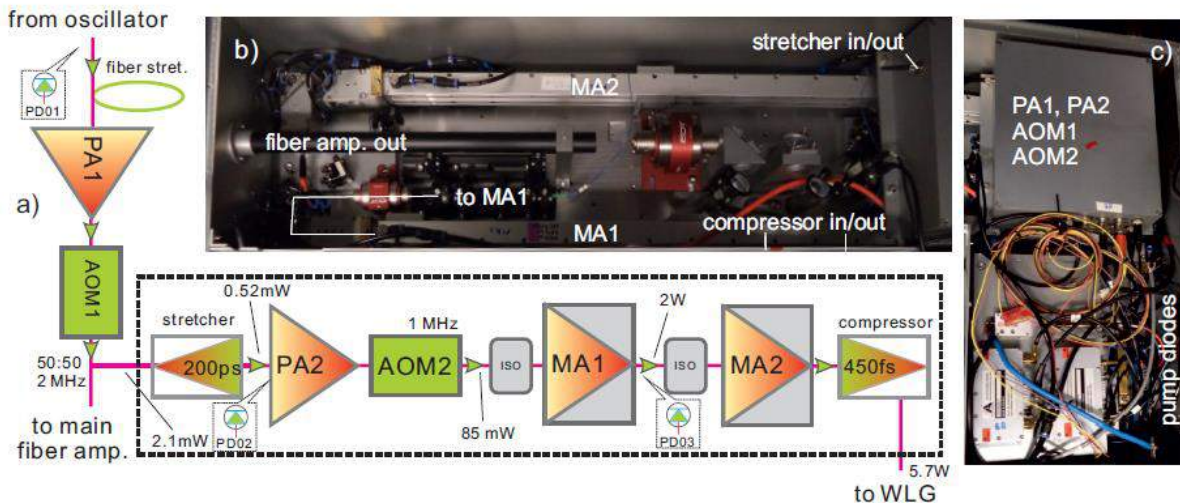
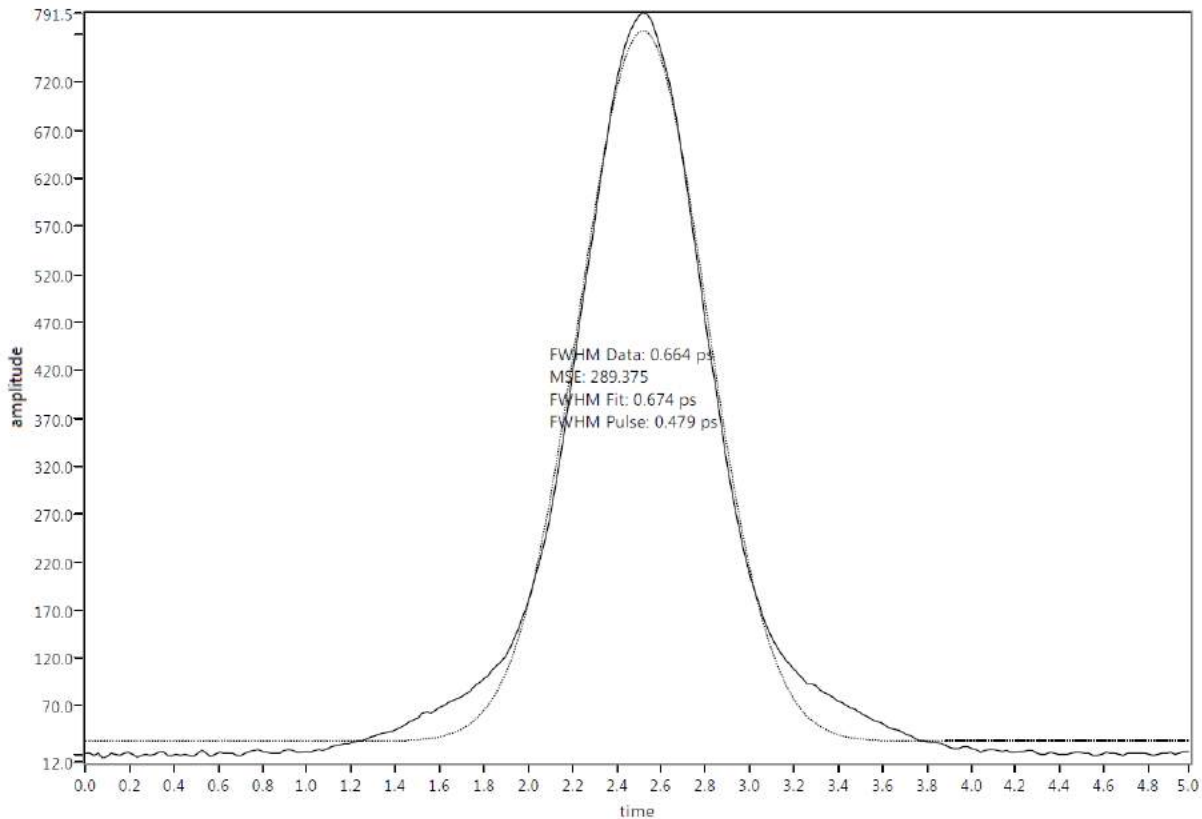


Figure 3.4: Fiber Amplifier System for the FLASH-2 White Light Seeder Stage, from [3.73]

The output power stability is 0.17% rms and the amplified spectral width is 3.4 nm at FWHM, with a compressed pulse duration is 456 fs. An autocorrelation measurement conducted during this study (Figure 3.5) shows a pulse width of  $\sim 479$  fs, assuming a Gaussian fit.



*Figure 3.5: FLASH-2 Autocorrelation Measurement*

The output of the fiber amplifier was passed through a thin-film polarizer (TFP), generating a linearly polarized pulse with an extinction ratio of  $\sim 1500:1$ —contrast was measured using a Glan-Taylor polarizer after the TFP (Figure 3.6). The polarizer showed some manufacturing/alignment defects when used to record the polarization vectors on the secondary lobe, leading to absorption of high input energies in a certain orientation. Therefore, only the positions of the polarizer corresponding to the maximal, well-behaved lobe and extinction angle were used for further analysis.

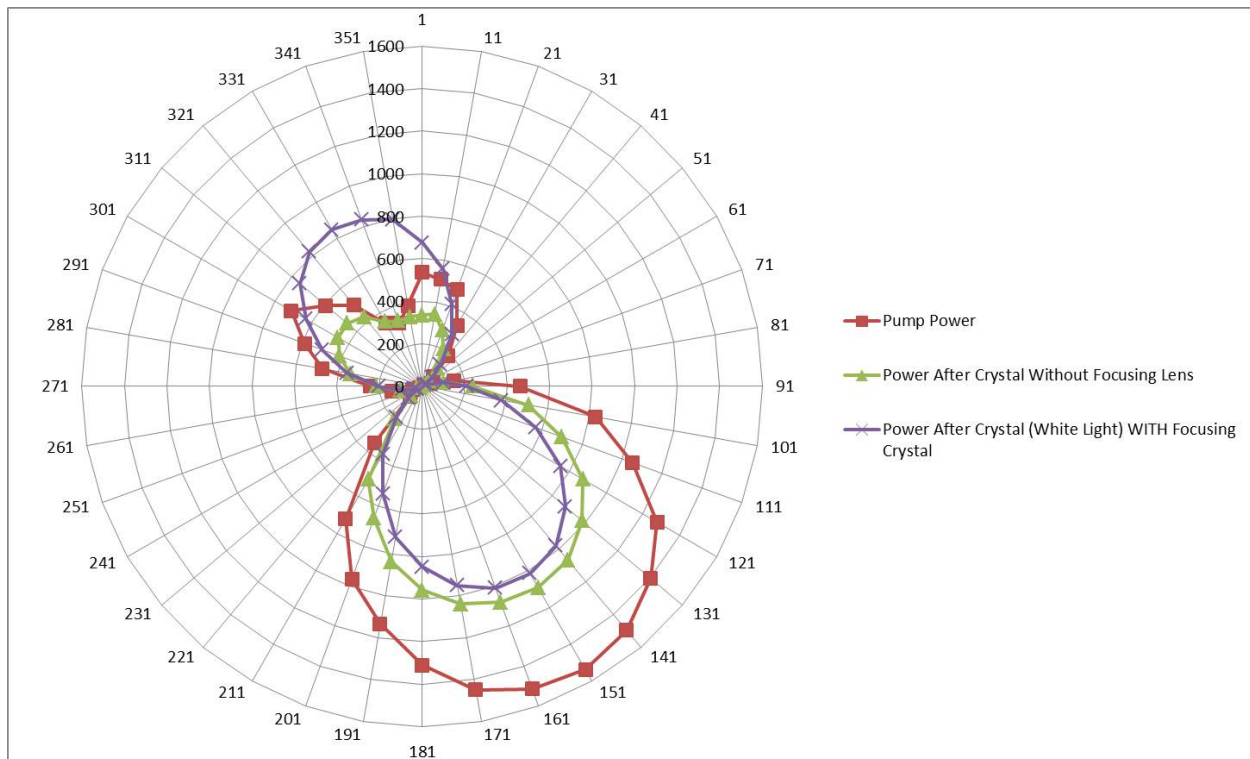


Figure 3.6: Polarization analysis of FLASH-2 SCG pulses

### 3.1.4 FLASH-2 Supercontinuum Setup

A 150mm fused silica (FS) plano-convex lens (PCX) was used to focus  $5\mu\text{J}$  of pump light into a 10-mm YAG crystal. An iris was placed before the YAG crystal to control the numerical aperture of the beam into the crystal, but was found to be unnecessary in this case. A 50mm FS PCX lens was used to collimate the SCG output. The output was further filtered using a 1000nm short-pass filter from Thorlabs (to cut out the intense pump wavelengths); the intensity of the remaining light was further reduced using an ND-NIR OD 2.0 filter (also from Thorlabs). A 50/50 polka-dot beamsplitter was used to divide the remaining SCG light for delivery to an Avantes VIS spectrometer and a Si CCD camera. Figure 3.7 (a) and (c) illustrate the SCG setup used, with Figure 3.7 (b) showing the direct visible portion of the SCG output on a screen.

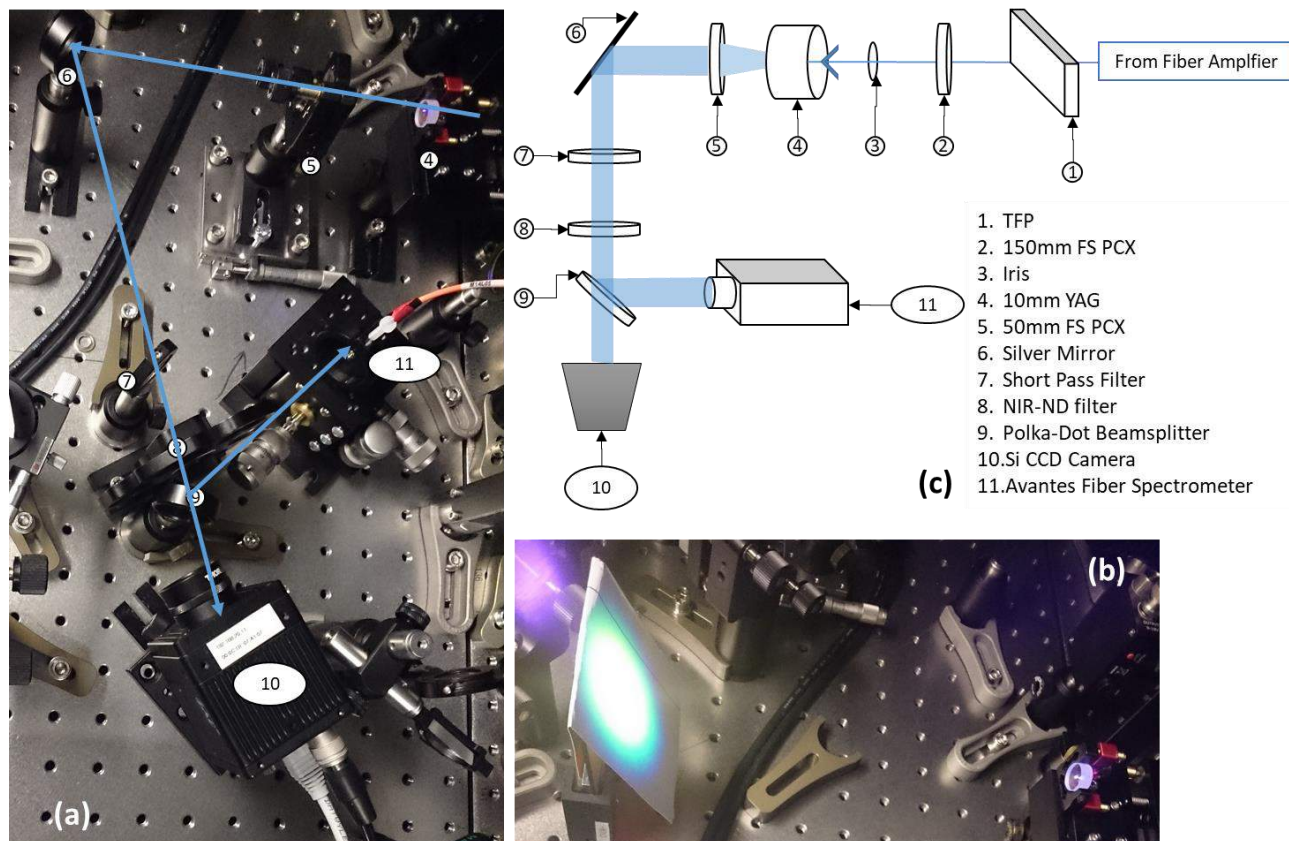


Figure 3.7: Experimental Setup and Table-top image for FLASH-2 SCG Study

### 3.1.5 Pertinent Experimental Results & Discussion

Spectra were measured at various transverse locations of the collimated output beam, with the central WL portion providing the highest intensity for all Anti-Stokes side wavelengths. Spectra with and without the Glan Taylor polarizer, at maximum and extinction angles, are shown in Figure 3.8.

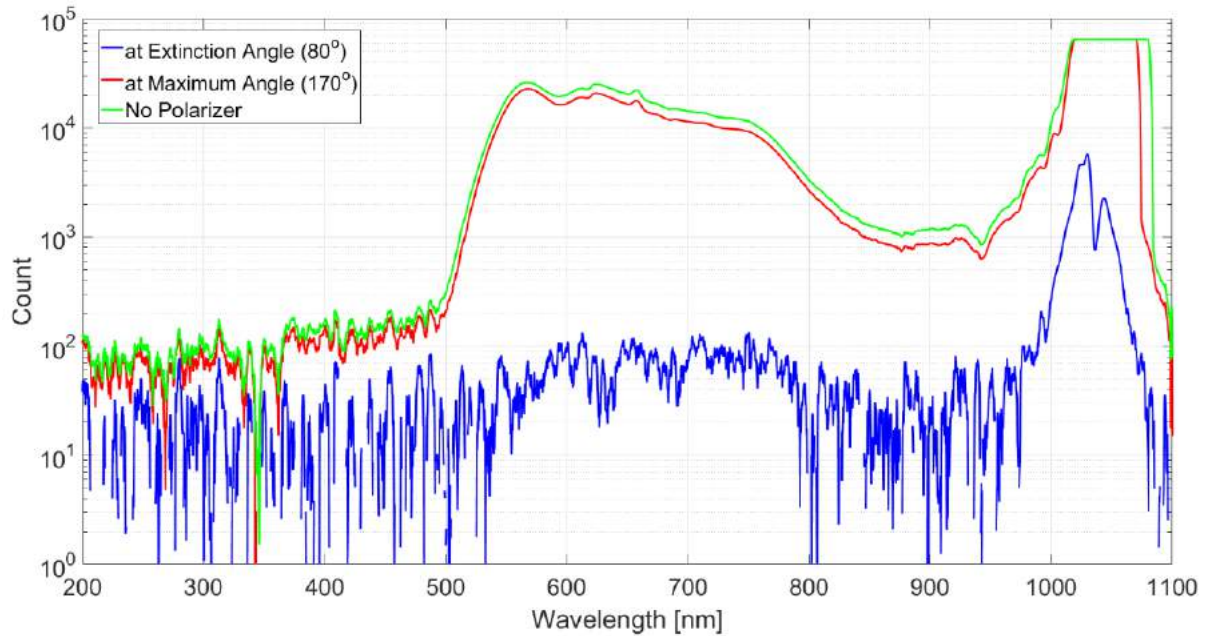


Figure 3.8: FLASH-2 SCG Spectra

Figure 3.9 shows the spectrometer output used to fine-tune the z-position of the YAG crystal in the focal region of the pump pulse. At the low energies used for z-position alignment (so as not to damage the crystal if its input face crosses the focus of the input focusing lens), the SC has not broadened to its maximal extent, but the broad AS peak is clearly visible. The onset of spectral conversion is abrupt, and the z-position coinciding with maximum pump depletion corresponds to the maximal spectral width of the AS peak—this will also be the position that, in general, delivers the maximal spectral energy density on the AS side with higher energies (note that the input position and numerical aperture for maximum conversion of pump energies to *Stokes* wavelengths may be different, as the Stokes side broadening is more sensitive to input focusing geometry—see Chapter 2).

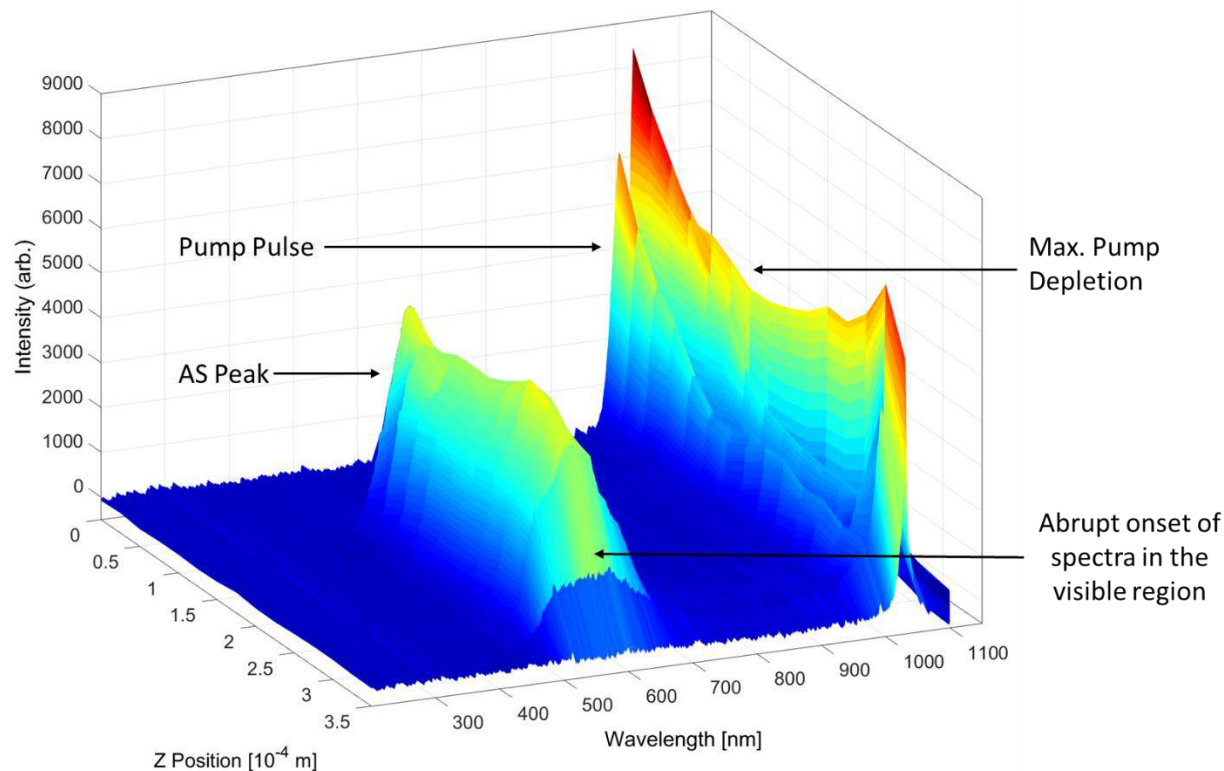
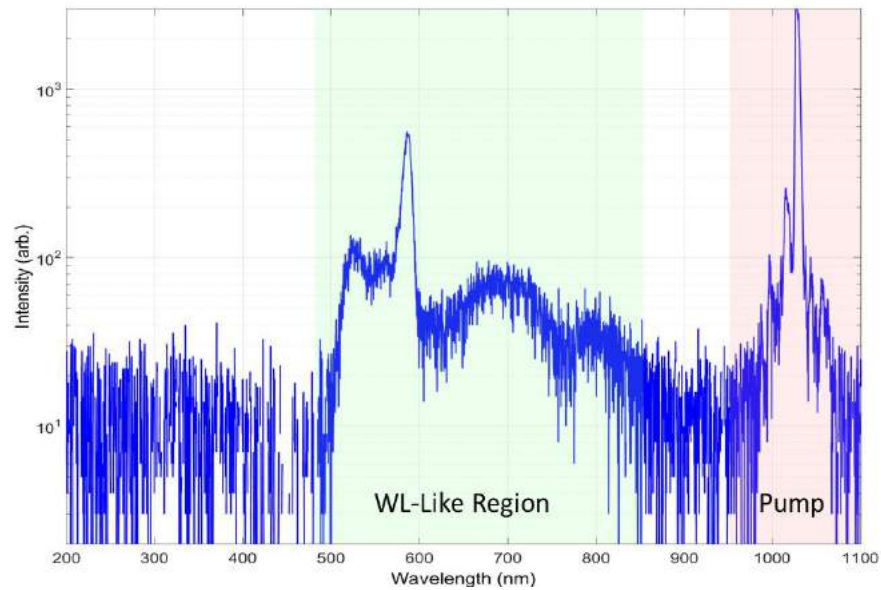


Figure 3.9: Z-Scan spectra for SCG alignment in the FLASH-2 study

It was also found that a fiber spectrometer is *not* suitable to record spectra from high-energy SCG setups without extensive characterization—the delivery fiber modulates the spectra and contributes to the generation of additional broadening/wavelengths due nonlinear fiber effects that come into play at high energies. In the absence of extensive and reliable delivery fiber characterization, a free-space input should be used at the spectrometer—spectra gathered in Figure 3.8 and Figure 3.9 are obtained with a direct free space coupling into the spectrometer.

One initial experiment conducted in the Kaertner group as a precursor to the studies outlined in [3.7] showed the spectra of a YAG-based SCG output (Figure 3.10) that was inconsistent with published results, i.e. a mostly unbroadened pump and a White Light (WL) like region with significant broadening around the 2<sup>nd</sup> harmonic of the pump (whereas there should be no 2<sup>nd</sup> harmonic effects in YAG). These results were later found to have been an artifact of small alignment errors in the initial SCG setup, but in

the interim they prompted further investigation regarding the formation of the visible portion of the SCG spectra.



*Figure 3.10: Preliminary SCG output of 1 $\mu$ m SCG in the Kaertner laboratory.*

No second harmonic or other polarization sensitive effects for found during this study, and there were preliminary indications that the spectra seen in Figure 3.10 were a result of a off-center sampling position of the SGC output beam—a sampling of spectra within a portion of the Conical Emission where the well-collimated wavelengths around the pump are not well-represented, but the Anti-Stokes dispersive wave is.

### 3.1.6 Numerical Simulation Results and Discussion

Simulations were carried out for YAG crystals pumped by a  $1\mu\text{m}$  input pulse with various input conditions. Additional experimental data was obtained from the Kaertner group's precursor SCG experiments that formed an earlier iteration of the sub-picosecond study [3.7].

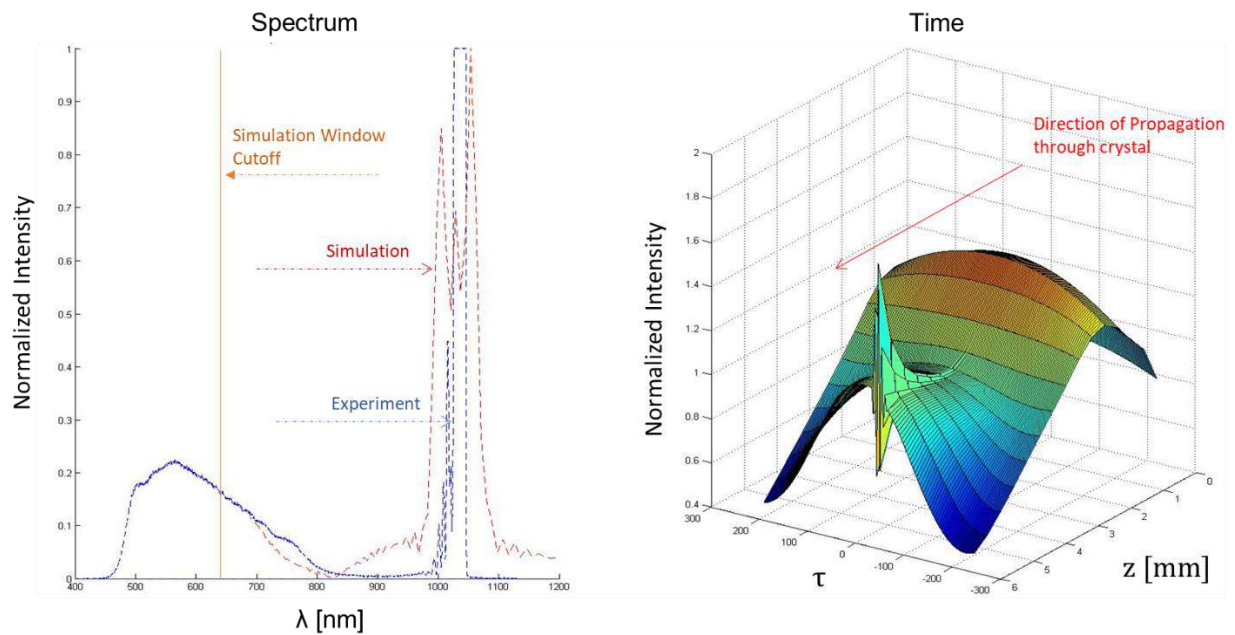


Figure 3.11: Preliminary comparison to experimental data

As can be seen from the preliminary comparison in Figure 3.11, there are (a) discrepancies between simulation and experimental results, most strikingly the broadening of the pump predicted by the simulation that is not borne out by the experimental data, and (b) a breakdown of the simulation method due to explosive growth of instability after  $\sim 5\text{mm}$  of propagation in the crystal, and a cutoff of the simulation window within the Anti-Stokes wing of the pulse spectra.

The breakdown of the slowly-varying envelope formation of the femtosecond supercontinuum problem is well appreciated [3.75]. A number of computational factors also limit the simulation tool, including (a), the physical implications of catastrophic focusing – a sudden rise in the intensity gradient during propagation requires extremely small step sizes or adaptive step-size control, and (b) that ultra-

broadband pulses require extremely large simulation windows in all (3+1)D, leading to extremely high computational requirements. A comprehensive review by [3.14] provides a list of methods that may be better suited to (3+1)D supercontinuum generation simulations, including the use of conical forms of the propagation.

Despite failing to (convincingly) reproduce experimental observations, the numerical simulation developed can be used as a learning tool to gain a better understanding of the SCG phenomena. For example, when an absorbing “bumper” is placed at the edges of the simulation windows in all domains in order to prevent aliasing effects, a model 500fs,  $1\mu\text{m}$ ,  $1\mu\text{J}$  pulse collimated to an input beam size of  $100\mu\text{m}$  into a 3mm YAG crystal can be used to observe the development of pulse splitting, multiple self-focusing cycles and intensity quenching as the pulse propagates through the material (Figure 3.12). While it is unlikely that the final spectral or temporal profile of the pulse will be accurate, input parameters can be changed to observe the effects on the dynamics of the pulse.

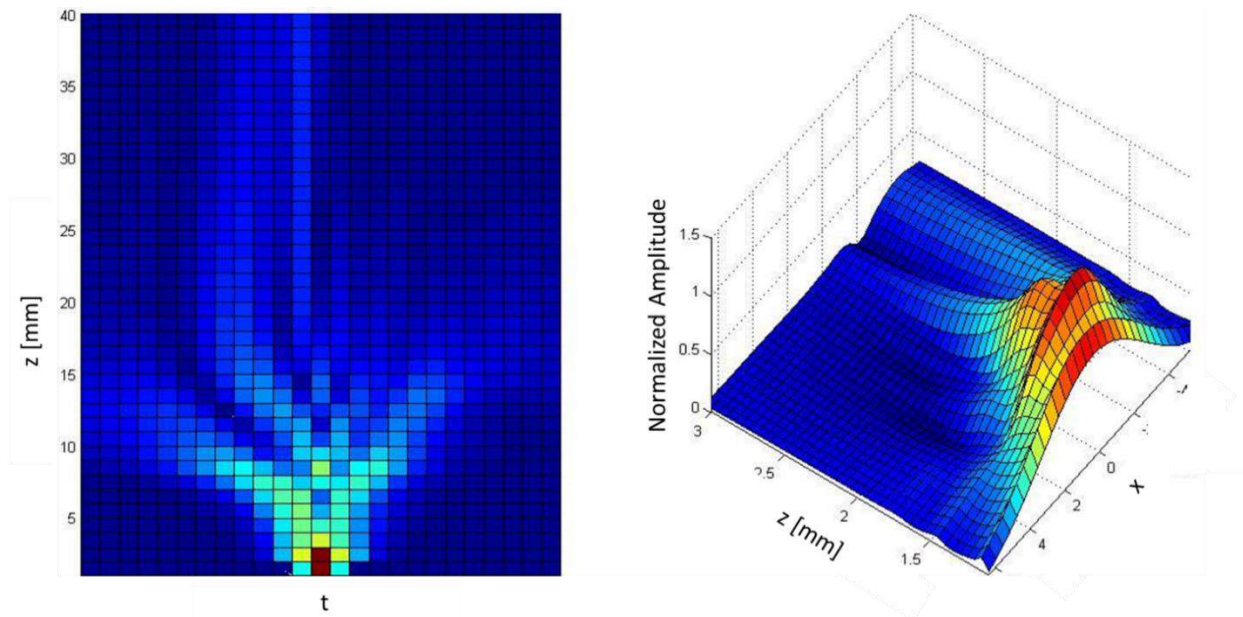
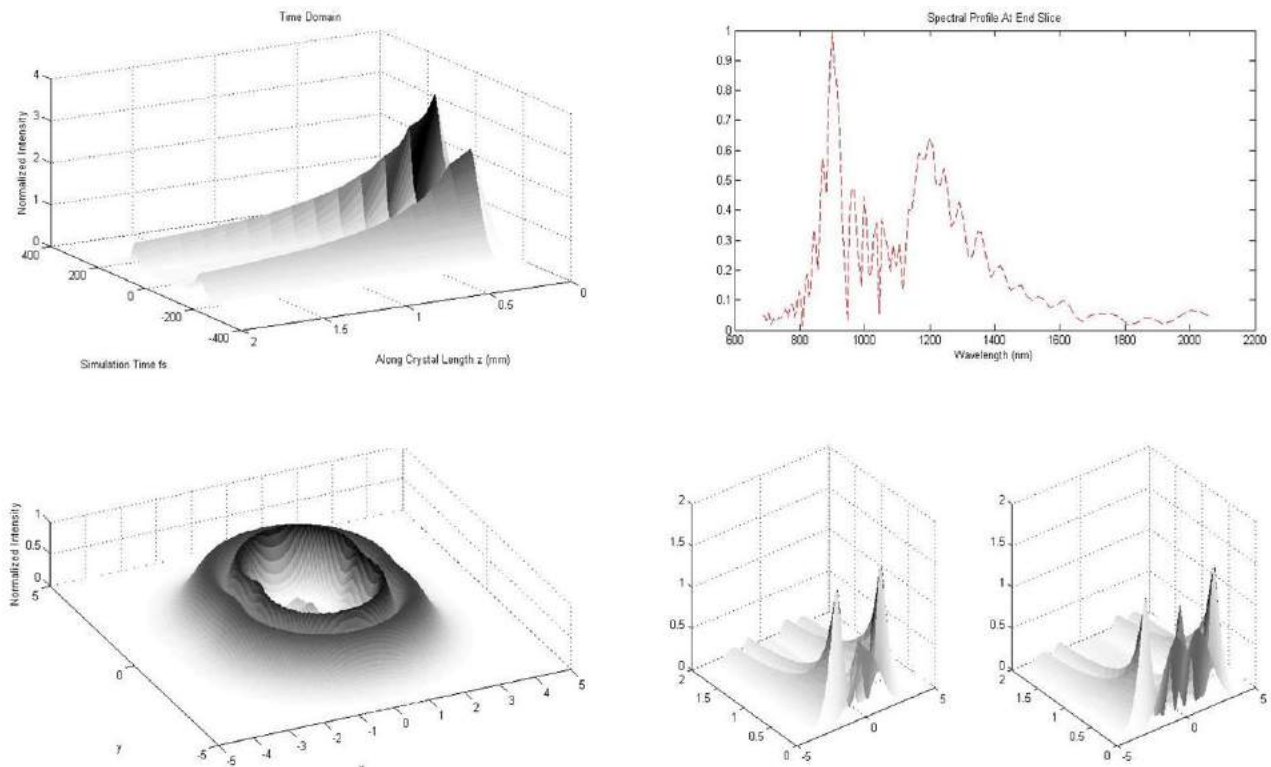


Figure 3.12: Simulation results for 500fs,  $1\mu\text{m}$ ,  $1\mu\text{J}$  pulse

Another example is the propagation of a spatio-temporal asymmetric pulse through the medium (Figure 3.13) which resembles a split pulse. Further splitting, the formation of conical structures and strong modulation in the spectral profile can be observed—all physical effects that do occur in real pulses.



*Figure 3.13: Split-Pulse Propagation*

The method, is, however, not suitable for further analysis. If energy conservation is strictly implemented and the absorptive “bumpers” in the edges are removed, the spectrum quickly overruns the simulation window due to aliasing and wraparound. Figure 3.14 is a very exaggerated case of this effect—the same non-zero spectral intensity at the edges of the window that lead to aliasing can be seen in much subtler form in other spectral comparisons that use variants or advancements of this method [3.12].

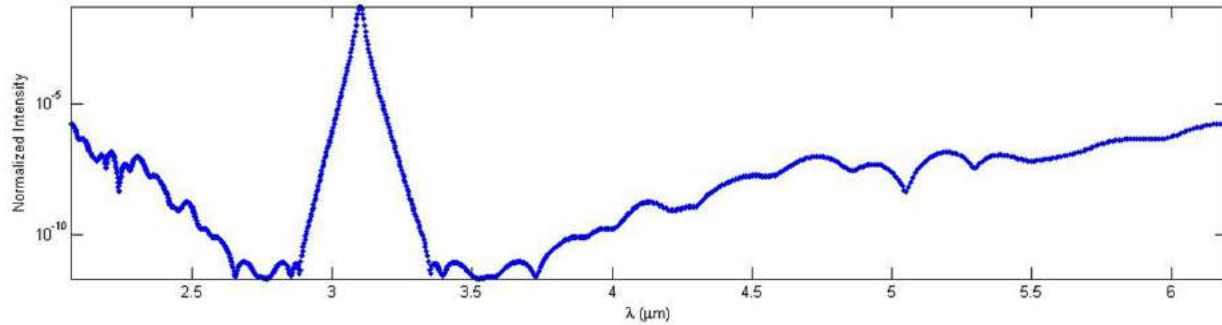


*Figure 3.14: Spectral problems due to wrap-around*

In the end it was determined that the simulation tool could not be used for understanding unknown parameter ranges in the IRDL operating regime in the absence of experimental data. Full simulations in long crystals were also not possible—the multi-octave spectrum targeted required a high-resolution grid in frequency domain, whereas the use of multi-picosecond pulses required a large grid in time-domain—making computation prohibitive.

### 3.2 SPATIO-SPECTRAL POLARIZATION ANALYSIS IN A CUBIC CRYSTAL (PHAROS, MPSD)<sup>2</sup>

The seed wavelength requirements for the parametric color conversion into deeper MIR regions requires high spectral energy density in the Stokes side of the pump wavelength. Additionally, the anti-Stokes portion of the SCG output is aimed towards a probe for shorter wavelength experiments in the NIR region. However, the characteristic drop in energy density at far-from pump wavelengths and low energy conversion between the pump and ASW wavelengths prompted the need to study whether additional spectral energies could be recovered from the non-core WL portion of the SCG output.

A significant portion of the spectral energy of the SC output lies in the frequencies found in the CE [15]—the presence of the same frequencies in the WL core, especially the far-from-pump Anti-Stokes peak, has been identified as the axial portion of the CE [3.16], implying a good phase relationship between identical frequency components in the CE and the WL. Also, in the case of polarization-sensitive processes like OPAs and DFGs seeded with specific wavelengths in the low energy-density region of the SC output, careful management of depolarization and beamline losses is required to efficiently generate the desired high-energy output [3.18, 3.19].

If the CE has a well-behaved polarization state, it opens the possibility of utilizing the CE energies in addition to the WL core itself. However, many of the bulk crystals commonly used for high-energy ultra-broadband SC generation (SCG), including CaF<sub>2</sub>, BaF<sub>2</sub> and YAG, exhibit a cubic crystal structure. Studies have reported cross-polarized wave generation and polarization rotation of the intense pump pulse during propagation in cubic crystals, leading to a depolarization of the SC output [3.20, 3.21]. This effect has been demonstrated in various crystals, including CaF<sub>2</sub> [3.22-3.27]. In contrast, SC generated in YAG shows little or no depolarization [28]. This creates a puzzling discrepancy between theoretical

---

<sup>2</sup> This sub-section is derived from the contents of a paper by Choudhuri et al., currently in review [3.30].

predictions [3.26, 3.27] for polarization rotation in cubic crystals, versus the experimental findings of polarization-maintenance in YAG. Given the induced polarization rotation of intense pump pulses in cubic crystals and the wavelength-dependent depolarization of bulk SC [3.22], a significant portion of seed energy may be lost due if the desired wavelength(s) lie in the high depolarization spectral region of the SC output.

Buchvarov et al. [3.29] proposed that different wavelengths of light are produced at different positions along the propagation path of the intense pump pulse. Based on this interpretation, one expects that a polarization modulation/rotation of the intense input pulse should be imprinted upon the polarization properties of the ringed structure of the SC output. Should SC generated in YAG exhibit depolarization due to YAG's crystal structure and the anisotropy of its  $\chi^{(3)}$  tensor, the proposed mechanism of action for depolarization [3.26] would be most clearly evident in a spatio-spectral depolarization analysis of the CE.

This study analyzes the polarization properties of the entire spatio-spectral structure of the output of a bulk SC process in YAG, and present the first spatio-spectral study of SCG in a cubic crystal, including its ring structure. It also highlights the possibility of utilizing the CE as well as the WL of the SC to seed subsequent parametric amplification stages.

While there is a lot of debate regarding the exact mechanisms giving rise to SC characteristics [3.17], the general consensus is that the process is heavily reliant upon the third-order susceptibility tensor  $\chi^{(3)}$ . Input (pump) field intensity affects many critical nonlinearities via the mediation of the  $\chi^{(3)}$  tensor. Also, cross-polarized wave generation of intense incident light in cubic crystals is dependent upon the orientation of the crystal planes with respect to the pulse propagation direction [3.21].

### 3.2.1 PHAROS Pump Source

The PHAROS specifications are derived directly from the internal PHAROS user manual for the specific laser system in question [3.30]. PHAROS is a direct-diode-pumped Yb:KGW (Ytterbium doped potassium

gadolinium tungstate) femtosecond laser system based on the chirped pulse amplification technique. It consists of a Kerr lens mode-locked Oscillator (OSC), Regenerative Amplifier (RA), Stretcher-Compressor (S-C), power supply and other support sub-systems. Figure 3.15 shows the positions of each of the modules that make up the PHAROS laser system.

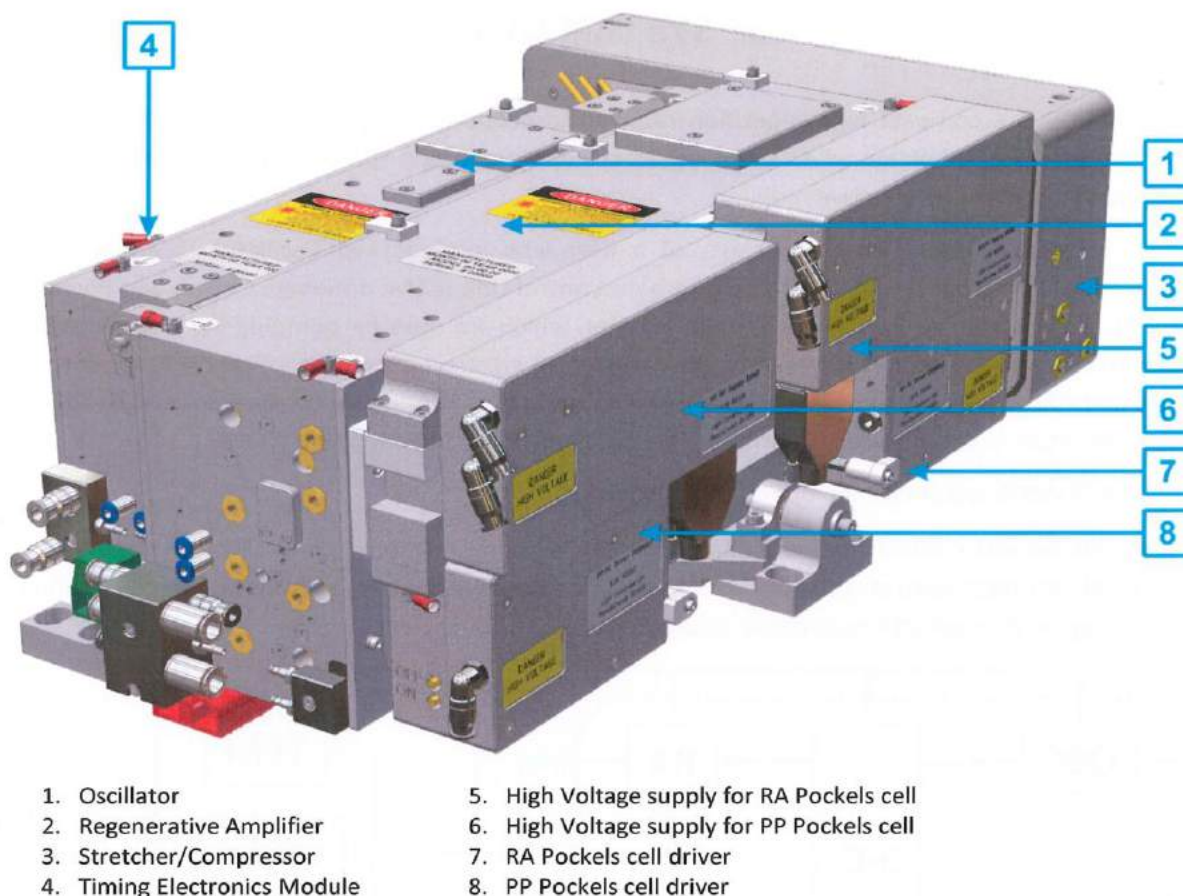


Figure 3.15: External View of the PHAROS Laser System, from [3.30]

The PHAROS SP system used is designed for a target maximum average power of 6W, with a greater than 1.0mJ pulse energy. Figure 3.16 shows the power calibration curve for the (relatively) lower energies used for the experiment; the curve was used to accurately determine pulse energies throughout the experiment without having to interrupt the beam during long-term SCG stability measurements.

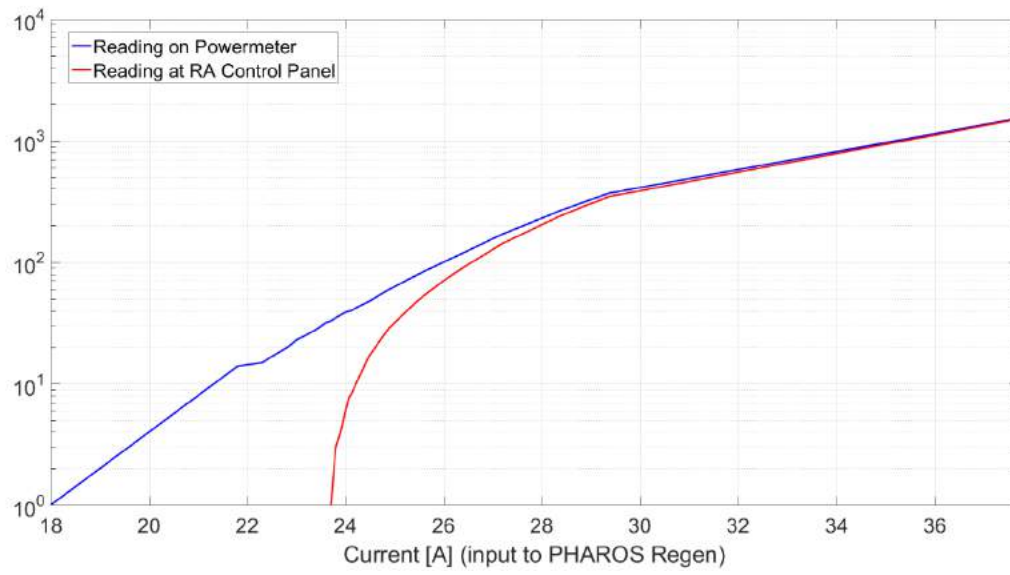


Figure 3.16: Power output as a function of input current, measured and displayed on PHAROS control panel

Figure 3.17 shows the measured spectrum of the PHAROS pulse. The autocorrelator-measured pulse width was  $\sim 177$ fs (assuming a Gaussian fit).

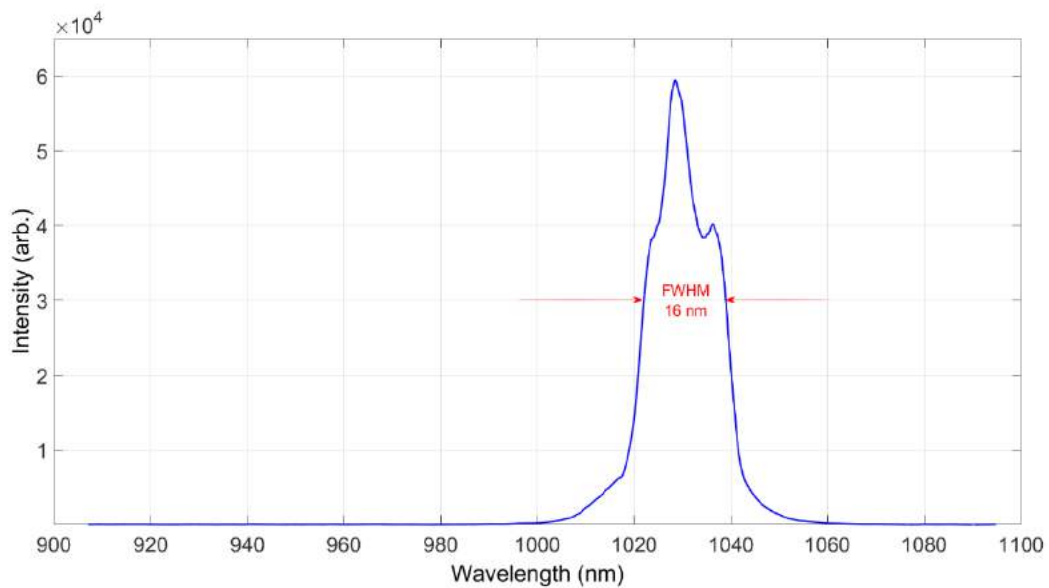


Figure 3.17: Measured spectrum of PHAROS pulse

### 3.2.2 Experimental Setup

For this study, pump pulse energy and intensity were chosen to maximize the probability of observing depolarization and cross-polarized wave generation, without pushing the SC output into an unstable or multi-filament regime. Pump peak power and intensity fall within the range covered by similar studies in literature, e.g. [3.22-3.24, 3.29]. As the growth direction of the YAG crystal with respect to its crystallographic plane orientation can be a factor contributing to crystal anisotropy, a [1,1,1] cut was chosen, as this is the only cut where the thermally induced birefringence is independent of the original growth direction [3.31]. Furthermore, the [1,1,1] cut has theoretically a high anisotropy of the  $\chi^{(3)}$  tensor under various orientations of incident pump polarization [3.20]. Should this anisotropy be a factor for SCG, choosing such a crystal cut would maximize the depolarization dependence on incident pump polarization angle.

A schematic of the optical setup is shown in Figure 3.18. The 180 fs, 10 kHz, 1032 nm output of the PHAROS system, linearly polarized at 600:1, was attenuated to 10  $\mu$ J and focused to a Gaussian waist diameter of approximately 30  $\mu$ m into the 5 mm long YAG crystal using a 100 mm Fused Silica (FS) lens. An iris before the focusing optics was used to optimize the numerical aperture of the beam for SCG. The pump laser has a pulse-to-pulse stability of < 0.5 % rms and power stability of < 0.5% rms over 24 hours. Environmental vibrations produce a beam-pointing jitter of approximately +/- 1 mm over 24 hours at the input lens.

The highly divergent and broadband SCG output beam was roughly collimated with a 2" 150 mm FS lens. A 1-mm pinhole on a motorized translation stage allowed sampling of the beam at various transverse positions. Due to the ultra-broadband nature of the SC output, a thin-film polarizer scheme (required for a full analysis of the Stokes vectors of the SC output) could not be used. Instead, a Glan-Taylor Polarizer on a rotation stage was mounted behind the pinhole to quantify the linear component of the polarization state sufficient to determine the degree of polarization rotation. A broadband, multimode

fiber (non polarization-maintaining, as only the total flux transmitted by the fiber was relevant) was used to sample the output of the polarizer and deliver the light to a spectrometer. The presence of widely different divergence angles and the inability to focus all of them equally upon the fiber-tip resulted in a modulation structure of the fiber sampled spectra, which disappeared when the full output was focused on the fiber tip, or collected using an integrating sphere. The setup was also sensitive to input beam-pointing spatial instabilities over the course of the measurement period as seen by the standard deviations of the measurements (Figure 3.19). While bulk SCG processes are relatively alignment insensitive, the shape of the focused spot-size was not—vibrations and displacements of the optical table resulted in changes in focused spot size and position over the course of the long-term spectral stability measurement.

Maximum depolarization during SCG is often reported on the Anti-Stokes (AS) side of the SCG output [3.25], and there is an exponential dropoff of spectral energy density on the red side leading to small changes in polarization being lost in background noise. Therefore, only the AS portion of the SCG output was used for this study.

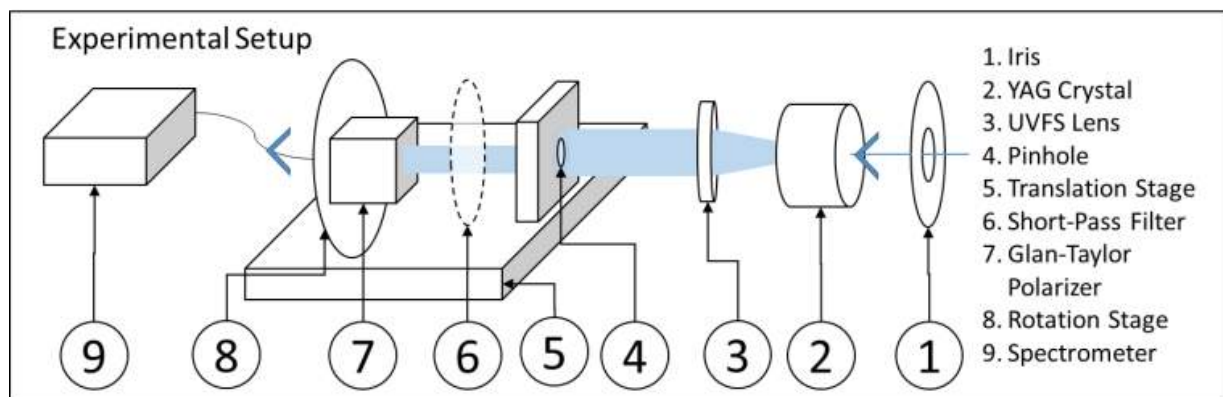


Figure 3.18: Polarization Study Experimental Setup

### 3.2.3 Results and Discussion

Spectra taken over the course of a day using an integrating sphere were compared to the integrated spectral intensity  $I_\lambda$  derived from the pinhole-sampled data using:

$$I_\lambda = \frac{\sum_x I_{\lambda,x} \pi(x^2 - (x-d)^2)}{A} \quad [3.2]$$

where  $I_{\lambda,x}$  is the spectral intensity recorded at radius  $x$  from the center of the beam with a pinhole diameter  $d$  and  $A$  is the total sampled area of the output. This comparison is shown in Figure 3.19. Both datasets were normalized using the pump intensity measured for each technique (input pulse without SC crystal) at 1  $\mu\text{m}$ , just below the short-pass filter (Thorlabs FESH1000) cutoff. The pinhole-derived data fall within  $1\sigma$  of the mean of the integrating sphere data and shows good general agreement in terms of spectral shape, highlighting the validity of our spatial sampling technique.

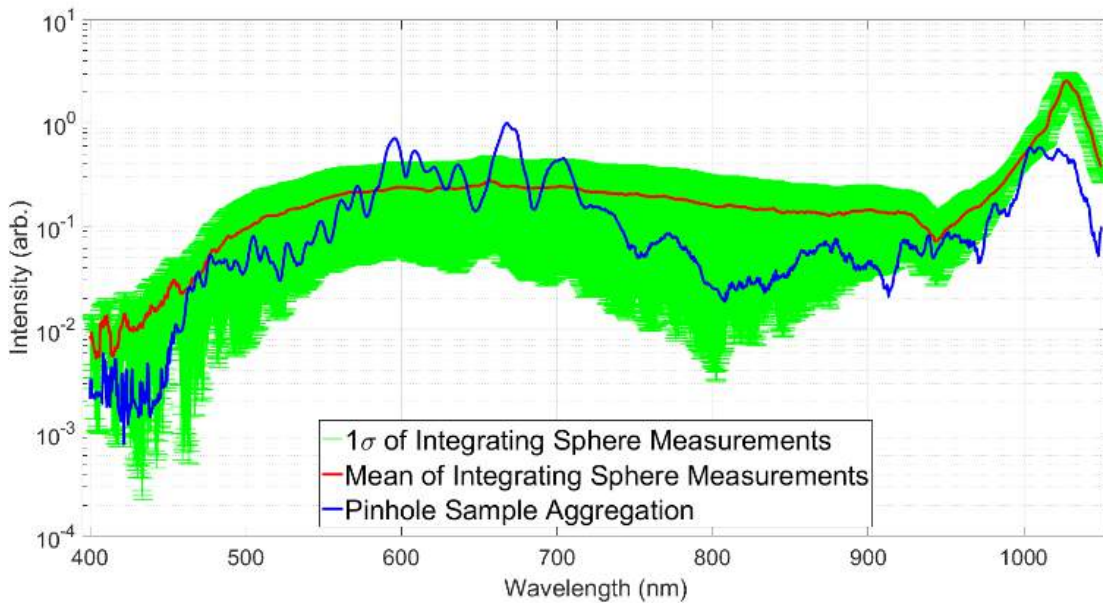


Figure 3.19: Comparison of SC output spectra—integrated values extrapolated from pinhole-sampled spectra (blue), and integrating sphere values over 1 day—mean (red),  $1\sigma$  extent (green).

The SC output was scanned in the transverse direction in 0.5 mm intervals over a beam radius of 10 mm (2 mm WL core radius, 10 mm maximal CE radius). At each spatial position, the polarizer was rotated by

360°, in 5° increments, and spectral data were recorded. Spatial symmetry of the output was verified via spectra taken at radially symmetric positions around the center of the beam (Figure 3.20). There is good agreement in spectral shape for identical radii. Working with a radially symmetric beam allows us to reduce the spatial analysis of the polarization to a single dimension.

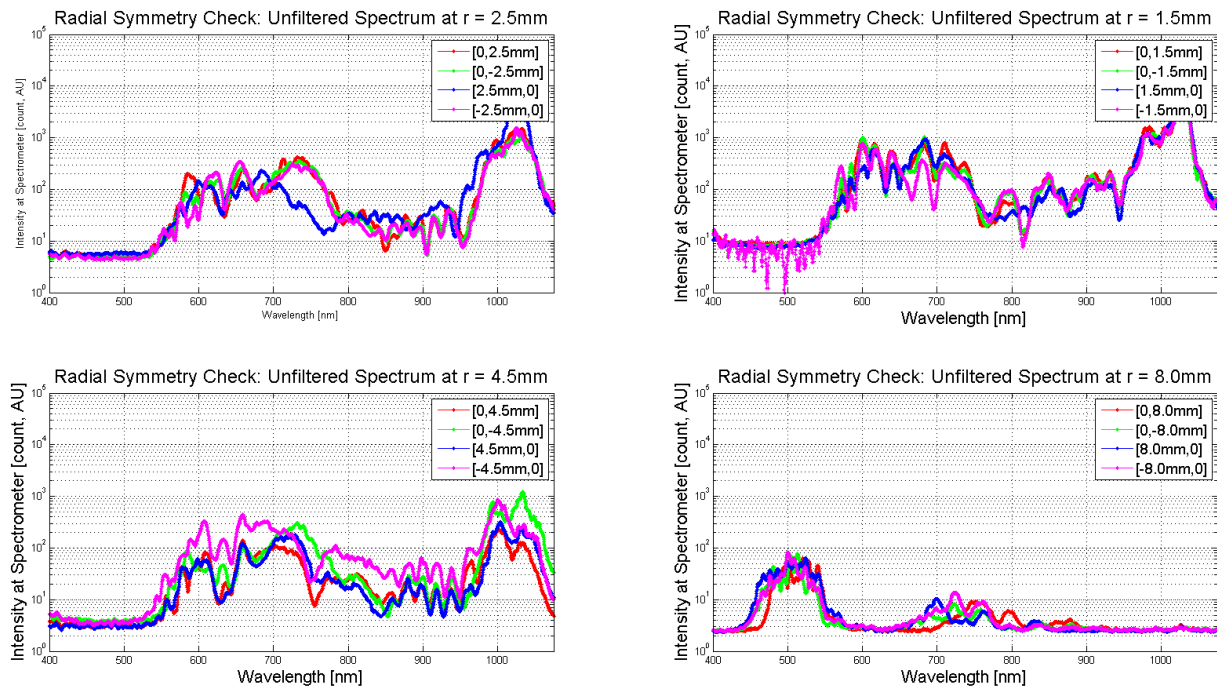


Figure 3.20: Optical spectrum at four sampling positions with a radial distance of (a)  $r = 8$  mm and (b)  $r = 1.5$  mm.

Figure 3.21 shows the spectral dependence of the polarization contrast, which follows the spectral energy density, suggesting a wavelength dependency of the polarization ratio, as reported in [3.28]. This is merely a measurement artifact due to the different spectral power available at each wavelength. For example, if 10  $\mu$ J are available near pump wavelengths with a noise floor of 100 nJ, it leads to a maximum possible polarization ratio of 100:1, whereas if only 1  $\mu$ J is available at 800 nm, it leads to a maximum possible polarization ratio of 10:1. The maximum polarization ratio is the decisive parameter and can be calculated as:

$$\rho_{max,\lambda} = \sum_x \rho_{max,\lambda,x} = \left( \frac{\frac{\sum_x I_{\lambda,x,\parallel}}{\sum_x I_{\lambda,x,\perp}}}{\frac{\sum_x I_{\lambda,x,\parallel}}{\sum_x I_{\lambda,noise}}} \right) \times 100 \%, \quad [3.3]$$

where  $I_{\lambda,x,\parallel}$  and  $I_{\lambda,x,\perp}$  are the intensities for a wavelength  $\lambda$  measured in the plane parallel and perpendicular, respectively, to the linear polarization of the incident pulse at a specific sampling location  $x$ . When plotting the  $\rho_{max,\lambda}$  trend as done in Figure 3.22, it is seen that the SC output is highly polarized, with a moving average of 99.8 %. The intense pump pulse itself does show a slight degree of depolarization, but the polarization-preservation in the SC output confirms the findings of Silva *et al.* [3.27], namely that the SC generated in YAG is not depolarized, and follows the polarization of the pump pulse.

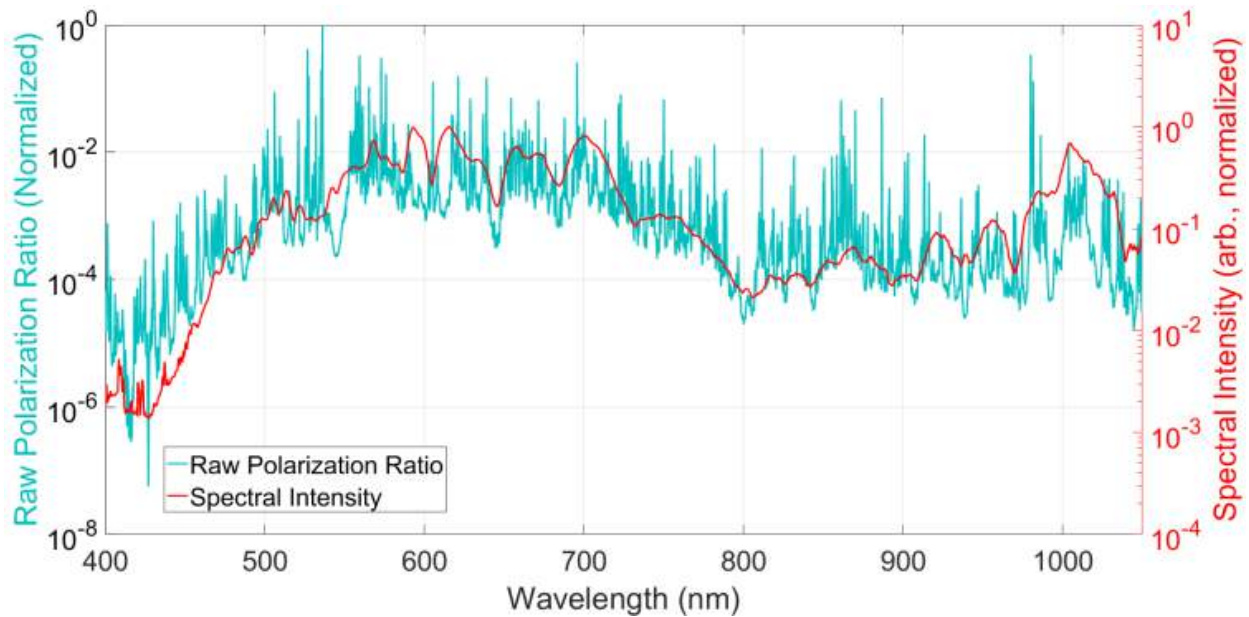


Figure 3.21: Spectral intensity (integrated over all sampling positions) vs. wavelength (red) and polarization ratio vs. wavelength (blue).

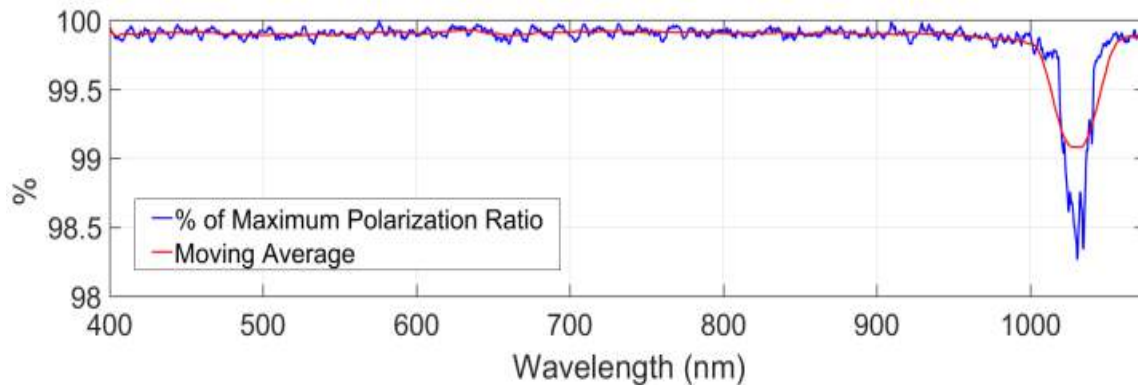


Figure 3.22: Percentage of maximum polarization ratio vs. wavelength (integrated over all sampling positions) (blue) and moving average (red).

The SC output exhibits multiple rings containing the same color but with different divergence angles, and it is assumed that regardless of the relative retardation of red frequency generation during a single cycle, each distinct spatial ring of a specific wavelength is created in a different focusing/defocusing cycle of the SC process. This guarantees multiple points of origin for each color along the evolution of the pump pulse in the nonlinear medium and allows evaluation of the impact of spatial pump / SC overlap on the polarization state of the SC output. The maximum polarization ratio in respect to the transverse position is shown in Figure 3.23 for selected wavelengths. A high degree of polarization (similar to the spatially integrated measurement shown in Figure 3.22) is present at any transverse position at any wavelength, despite the drastically different spectral contents at different transverse positions (see Figure 3.21). This highlights that under the experimental conditions used here, the spatial overlap between the pump beam and the SC does not lead to a polarization rotation via cross-phase modulation or any other nonlinear effect as suggested in Ref. [3.28].

The experimental results are puzzling given the anisotropy of the  $\chi^{(3)}$  tensor in YAG [3.32], which has a form identical to that of  $\text{CaF}_2$ , where a strong wavelength-dependent depolarization has been observed in previous studies, for example in [3.28]. The nonlinear index is, at its root, a function of the hyperpolarizability of the electron distribution forming the bonds in crystals. [3.27]. The

hyperpolarizability of oxygen in YAG varies up to a factor of 10, that of fluorine in  $\text{CaF}_2$  varies by a factor 7 [3.33], whereas the value of the nonlinear indices for  $\text{CaF}_2$  and YAG are also very similar,  $1.9 \times 10^{-16} \text{ cm}^2/\text{W}$  [3.27] and  $2.9 \times 10^{-16} \text{ cm}^2/\text{W}$  [3.23] respectively;  $\text{CaF}_2$  has even a *lower* nonlinear index than YAG. This should lead to an experimentally observable depolarization of the SC output in YAG that is greater than, or at least comparable, to  $\text{CaF}_2$ . Yet the SC-generated broadband portion of the output pulse in YAG demonstrates a distinct *lack* of depolarization—increasing input energies in the hopes of seeing depolarization results in multifilamentation and a destruction of the spatial structure of the output one wishes to study. In the operating regime, the minor polarization rotation of the intense pump, consistent with theory [3.20, 3.25], is not imprinted onto the SC output. It is proposed that the marginally depolarized portion of the pump is not sufficient to contribute to the nonlinear processes that create the SC output.

It should be noted that it is difficult to compare the true extent of depolarization of SC output vs. intense pump pulse polarization rotation. Studies that focus on wavelength-based depolarization effects of SCG in  $\text{CaF}_2$  use the raw polarization ratio and not a function of the maximum-possible polarization ratio as a metric.

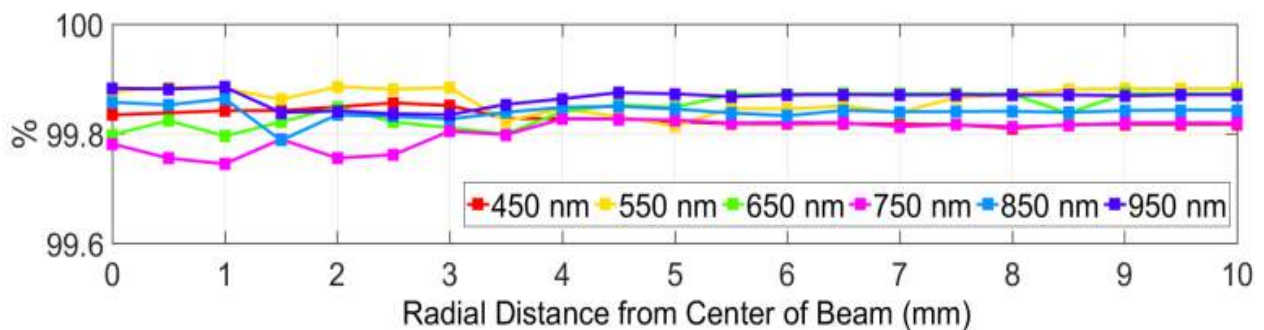


Figure 3.23: Percentage of maximum polarization ratio of SC output in respect to the radial position for various wavelengths.

Nagura *et al.* generated SC in  $\text{CaF}_2$  and various other media far in excess of  $P_{cr}$  in the materials, and found depolarization of the SC output only in the cubic crystals  $\text{CaF}_2$  and  $\text{LiF}$ , concluding that the SC is

polarized in the direction of the incident light in an isotropic material, but not cubic materials [3.26]. Kartzaev *et al.* generated SC in CaF<sub>2</sub> and reported a crystal-plane-orientation dependent, self-induced polarization rotation of the pump, with a direct influence on the polarization properties of the AS wing of the SC output spectra [3.23]. Johnson *et al.* [3.34] discovered polarization modulation in the SC output of CaF<sub>2</sub> pumped with linearly-polarized light vs. a very high degree of polarization preservation for the circularly-polarized pump case (which would mask any induced polarization rotation). As cross-polarized wave generation in cubic crystals is well established, there is no intrinsic reason that the mechanisms behind self-induced polarization of intense pulses should be readily apparent in CaF<sub>2</sub> but not in YAG. It is imperative that the crystallographic quality of nonlinear media used for SCG must be taken into account to explain this discrepancy, and the degree of depolarization of SC output demonstrated in fluoride crystals CaF<sub>2</sub>, BaF<sub>2</sub> and LiF has origins beyond the anisotropy of the  $\chi^{(3)}$  tensor. For example, Huber *et al.* detail a CaF<sub>2</sub> SC-seeded BBO OPA *without* the use of polarization-correction optics--by stringently controlling crystal quality, the authors could demonstrate a well polarized SC for OPA seeding [3.35]. Kumar *et al.* studied SC depolarization as a function of pump intensity [3.24] and demonstrated the role of crystallographic orientation—even in a non-centrosymmetric crystal like KDP, the authors found that if the crystal is oriented correctly, SC output preserves the input-polarization state.

Thus, the problem with using CaF<sub>2</sub> as a benchmark crystal for studying depolarization becomes one of crystallographic quality: CaF<sub>2</sub> exhibits an intrinsic birefringence [3.36], strong UV-absorption at the blue edge of the SC output leading to damage [3.38]. CaF<sub>2</sub> is easily damaged, and requires continual rotation of the CaF<sub>2</sub> plate for SC applications [3.34]. The crystal also has a tendency to grow in the  $\langle 1\ 1\ 0 \rangle$  direction [3.37] with implications of the crystal plane orientation rotating and introducing defects throughout the length of the rod as growth proceeds, which may account for the polarization modulation of SC output reported in [3.34] for a rotated  $[0\ 0\ 1]$  CaF<sub>2</sub> sample. Depolarization due to

damage caused by the intense incident pulses has been reported, not only in the case of  $\text{CaF}_2$ , but also for other nonlinear media. Inhomogeneities in electron density of the induced plasma would invariably arise in a damaged bulk crystal. The polarization state of the generated SC can also differ from pump even in isotropic amorphous media due to inhomogeneity in the electron density, and subsequent scattering as reported in Ref. [3.24]. Furthermore, Dharmadhikari *et al.* reported a 100-fold polarization degradation at the onset of multi-photon ionization occurring well below the damage threshold [3.22]. All of the above factors may contribute significantly to observed depolarization (to an extent not expected to arise solely from  $\chi^{(3)}$ -based polarization-rotation of intense pump pulses) of SC generated in  $\text{CaF}_2$ . But, to the best of our knowledge, there are no reports of YAG plates used for SC requiring rotation to prevent damage or any of the other issues (intrinsic birefringence, crystal-plane rotation during growth) of  $\text{CaF}_2$ . Structural studies of YAG show excellent crystal hardness, with low creep and stress-induced birefringence [3.39]. Consistent with the theory on polarization-rotation in cubic crystals, YAG shows polarization rotation of the high-intensity pump, but this small fraction of the intense input pump does not contribute to SCG, and the superior crystal quality of YAG allows us to observe the intrinsic polarization of the SC output itself, which arises from the un-rotated portion of the pump.

Given the highly polarized nature of the SC output beam across the entire spectral *and* spatial domains (even in the presence of some minor depolarization of the intense pump), the conclusion of this study is that while analyses of self-induced polarization rotation during highly nonlinear processes like SCG are fundamentally correct, the *extent* of depolarization of SC output studied in crystals like  $\text{CaF}_2$  is highly influenced by crystallographic quality and bulk damage, and is not intrinsic to SCG in cubic nonlinear crystals.

### 3.3 CRYSTAL PERFORMANCE COMPARISON FOR 2 $\mu$ M, SUB-2-CYCLE SCG (ICFO)<sup>3</sup>

The spatio-spectral polarization study highlights that the suitability of certain crystals like CaF<sub>2</sub> for operation in the high-energy regime is questionable, despite the broad spectra that can be obtained. There is also a wavelength dependence on damage thresholds, and high peak power experiments at 2 $\mu$  wavelengths were required to determine the suitability and spectral output characteristics of various candidate crystals. To date, there are only a handful of studies [3.40] that use 2 $\mu$ m radiation for supercontinuum generation, and there is a dearth of simulation results for the regime that can be used for crystal selection. Therefore, a study funded by Laserlab Europe was initiated at the ICFO facility in Barcelona, Spain. The goal was to (a) compare SCG generation in multiple candidate crystals, and (b) determine if additional nonlinear color conversion effects (like third harmonic generation and stimulated Raman scattering) could make an impact on spectral energy densities of the SCG output. Crystals studied were YAG, Diamond, Sapphire and ZnS<sub>2</sub>. Material parameters for the crystals used can be found in Appendix A.

Multioctave SCG in CaF<sub>2</sub> and BaF<sub>2</sub>, spanning from 340nm to beyond 3 $\mu$ m have been reported for 2 $\mu$ m, 15fs pulses [3.40 - 3.42]. However, given the spectral discontinuity reported in CaF<sub>2</sub> and BaF<sub>2</sub> with longer pulses [3.43, 3.44], the potentially poor crystallographic quality of these materials, damage under continuous usage, and the high degree of induced polarization rotation present with high input energies covered in Section 3, both were discarded as candidate SCG crystals for further study.

Sapphire has traditionally been used as an SCG crystal in the VIS range, and produces extremely broadband SCG [3.45 - 3.47]. SCG in Sapphire has also shown excellent spectral output in the long wavelength regime when pumped near the zero dispersion wavelength at 1.3 $\mu$ m [3.48, 3.49]. Pumped

---

<sup>3</sup> This study was funded via a Laserlab Europe grant, in collaboration with the Institute for... (ICFO).

at  $2\mu\text{m}$ , a three-octave SCG output in Sapphire was demonstrated using two-cycle pulses [3.40], but with a spectral discontinuity in the NIR spectral region. YAG is often the crystal of choice for MIR SCG studies—stable, multioctave SCG has been reported for YAG with  $\sim 2\mu\text{m}$  [3.40, 3.50, 3.51] and  $3\mu\text{m}$  [3.27] pulses. Both YAG and Sapphire were chosen as promising candidates for this study due to their high damage thresholds and high nonlinearity.

The extremely high nonlinearity of ZnSe (two orders of magnitude higher than YAG and Sapphire), along with its MIR transparency window, makes it an intriguing candidate for SCG generation. However, the low bandgap of the material has traditionally made it a poor choice for short-wavelength SCG, with very little spectral broadening at  $\sim 1\mu\text{m}$ , and no formation of an SCG filament at 800nm [3.52]. However, at long wavelengths (corresponding to higher orders of MPI), multi-octave spectra in ZnSe have been reported with  $\sim 5\mu\text{m}$  [3.53] and  $\sim 3\mu\text{m}$  [3.54, 3.55] pumped pulses. The extremely efficient production of higher harmonics in ZnSe [3.53] and second and third harmonic contributions to the SCG are addressed in Section 0. The gap between the poor-to-little spectral broadening produced by NIR pump pulses and the multi-octave SCG output with  $3\mu\text{m}$  pump pulses makes ZnSe a good candidate for further study.

Diamond, with its high transparency, high nonlinearity and high damage threshold should be an ideal candidate for SCG. But so far it has only been studied as an SCG material due to its strong Raman response, with the use of 800nm pump pulses [3.56, 3.57], perhaps due to its material expense and the difficulty in obtaining longer crystals. For short pulses such as those this study is based on, 2 – 3mm lengths of Diamond are suitable SCG nonlinear crystal candidates.

As derived in Chapter 2, for a given nonlinear material and input pulse parameters, one can calculate the critical intensity at which Kerr Self-Focusing is halted. Based on the propagation distance at which this critical intensity is reached, one can then estimate an approximate diameter for the filament (or obtain the “typical” size of a filament via experimental measurements in published literature). Combining these

values, one can obtain the minimum critical power required to trigger MPI. Figure 3.24 plots the minimum power thresholds for MPI and SF at MIR wavelengths for materials used in this study.

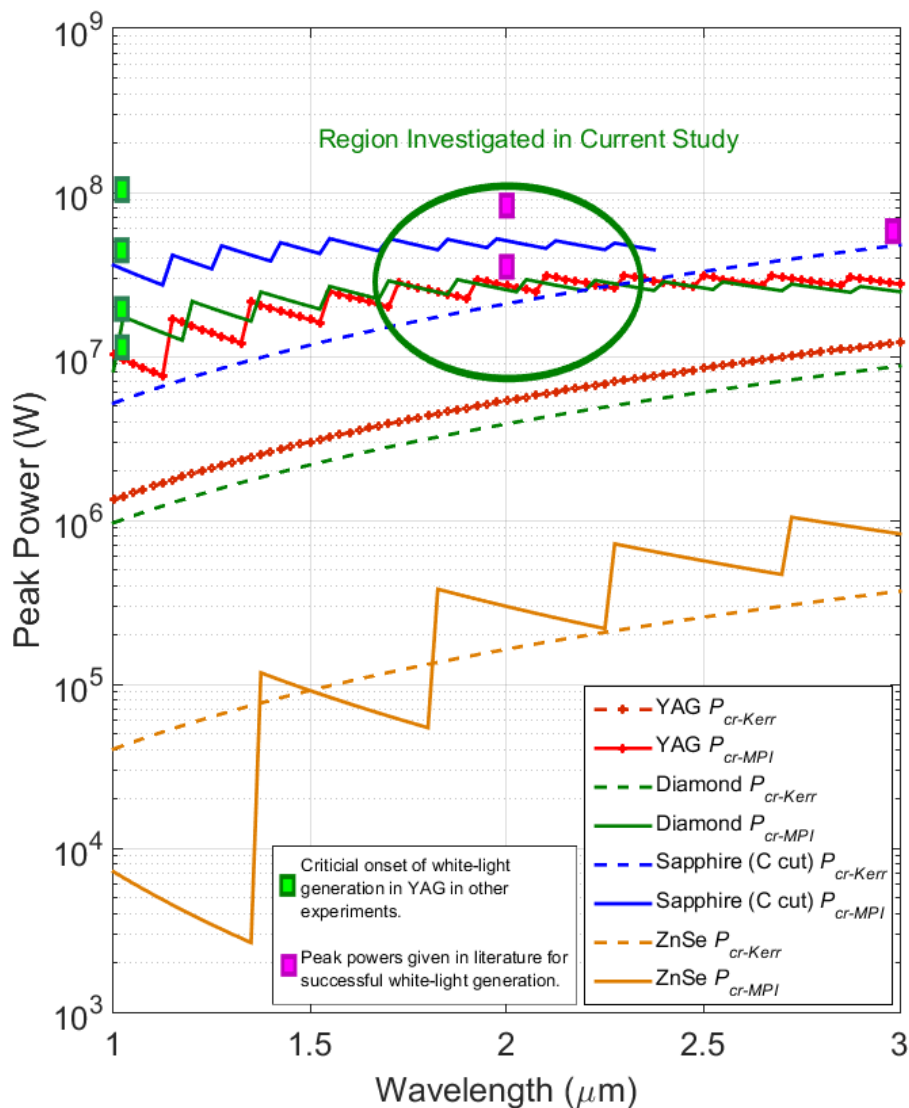


Figure 3.24: Critical Power Thresholds for Materials in Crystal Comparison Study

In order to trigger filamentation, the input pulse power needs to be above both minimum power thresholds (the upper bound for input powers would arise due to multifilamentation and the damage threshold of the material). As can be seen for YAG, all experimental studies that demonstrate SCG fall in a region that is above both power thresholds. Incidentally, this plot also demonstrates the problem with triggering filamentation in ZnSe with pump wavelengths in the NIR and 1 $\mu$ m regimes—the minimum

threshold for MPI is lower than the threshold for SF, i.e. the crystal undergoes two and three photon absorption at powers less than those required for SF, effectively preventing the formation of a filament.

### 3.3.1 Pump Source

The ICFO pump source is a Cryogenic Ti:Sa system that provides 1kHz, 7mJ, 40fs pulses at 800nm. These pulses are then shifted to NIR wavelengths and broadened using a commercial HE-TOPAS [3.76]/Hollow-Core Fiber/Bulk compressor system that outputs 1kHz, >200 $\mu$ J, 11fs (9fs Fourier limit) pulses with a central wavelength of 1.85 $\mu$ m. Figure 3.25 and Figure 3.26 (courtesy of ICFO and Laserlab Europe) show a schematic of the ICFO pump source. Figure 3.27 (courtesy of ICFO) is a picture of the hollow-core fiber broadening stage. Further system details can be found in [3.58, 3.59].

## Cryogenic Ti:Sa laser system

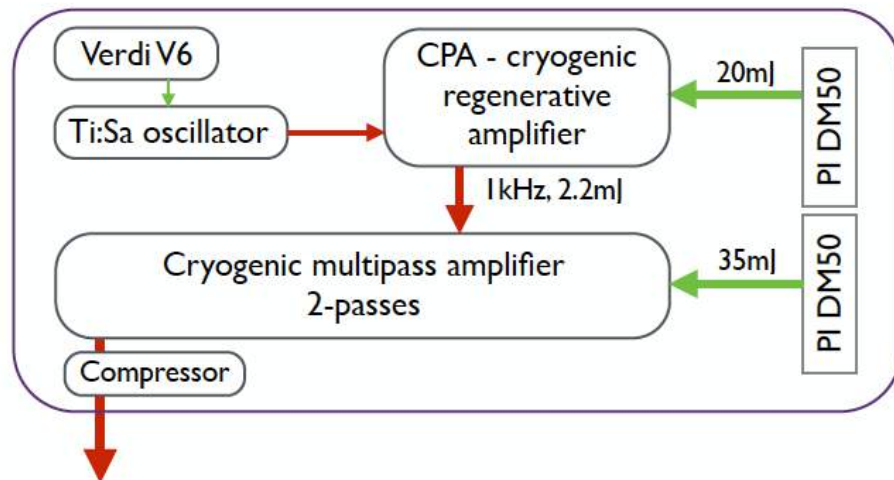


Figure 3.25: Cryogenic Ti:Sa system

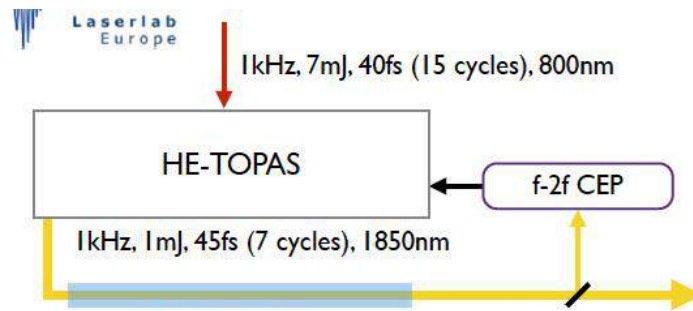


Figure 3.26: Nonlinear Broadening System

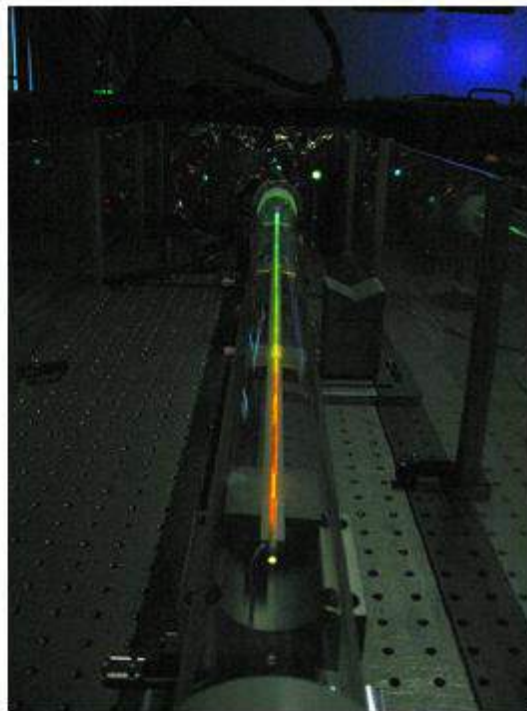


Figure 3.27: Hollow-Core Fiber Stage

Measured pump spectra (Figure 3.28) during the course of this study showed some spectral contamination at  $\sim 1450\text{nm}$  within the edges of the beam. The source of this contamination could not be isolated.

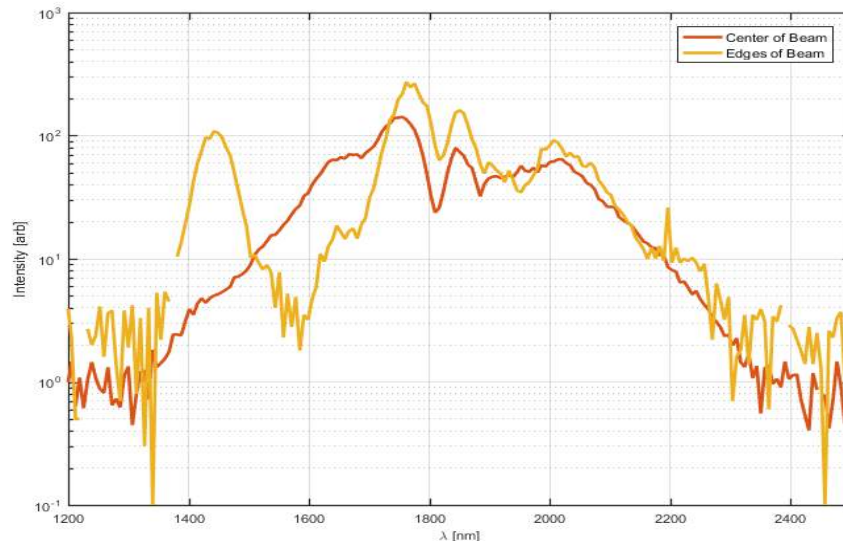


Figure 3.28: ICFO Pump Spectra

### 3.3.2 Experimental Setup

For the benchmarking experiment, all nonlinear bulk crystals were compared with identical input conditions to derive parameter ranges for stable single-filament WLG. The input pulse was attenuated to  $1\mu\text{J}$  using a Pellicle and a ZnSe wedge, then focused into the various crystals using a 150mm FL gold-coated off-axis-paraboloid. The core of the white-light output was collimated using a 40mm  $\text{CaF}_2$  PCX lens, and delivered to different spectrometers with mid-IR or visible optical fibers. The nonlinear response of the delivery fibers was analyzed in comparison to the free-space input—no nonlinear broadening or artifacts were observed in the fibers at the low energy level used for the comparison. Figure 3.29 and Figure 3.30 illustrate the setup. Note that the Sapphire sample was chosen to be a C-Cut to avoid birefringence effects (verified experimentally, even in the multi-filamentation regime).

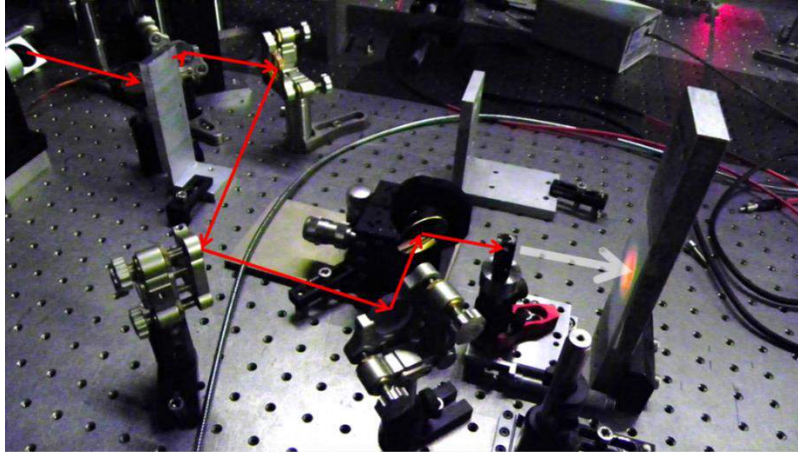


Figure 3.29: Image of ICFO Setup

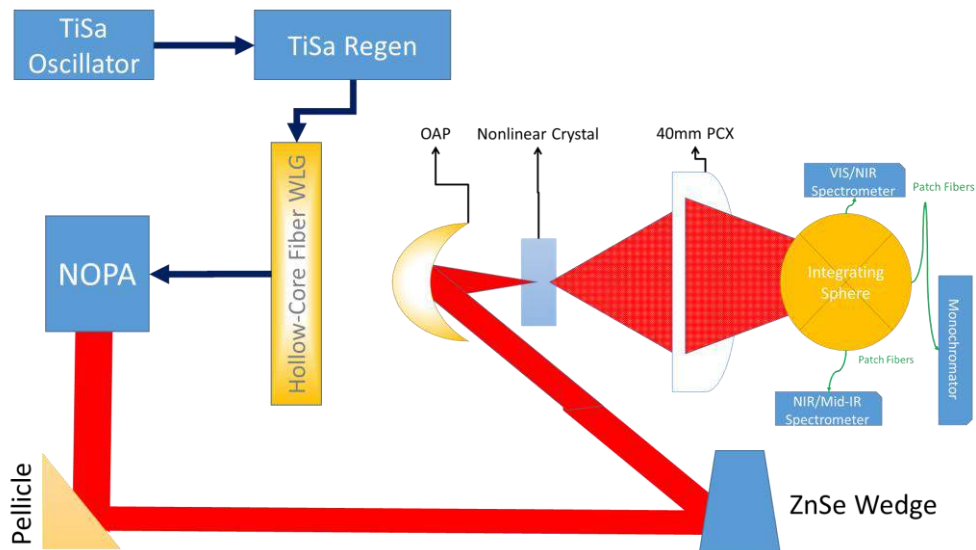


Figure 3.30: ICFO Supercontinuum Setup

Spectra from the two different (VIS and NIR) spectrometers were stitched using the overlap region between 950 and 1100nm (Figure 3.31).

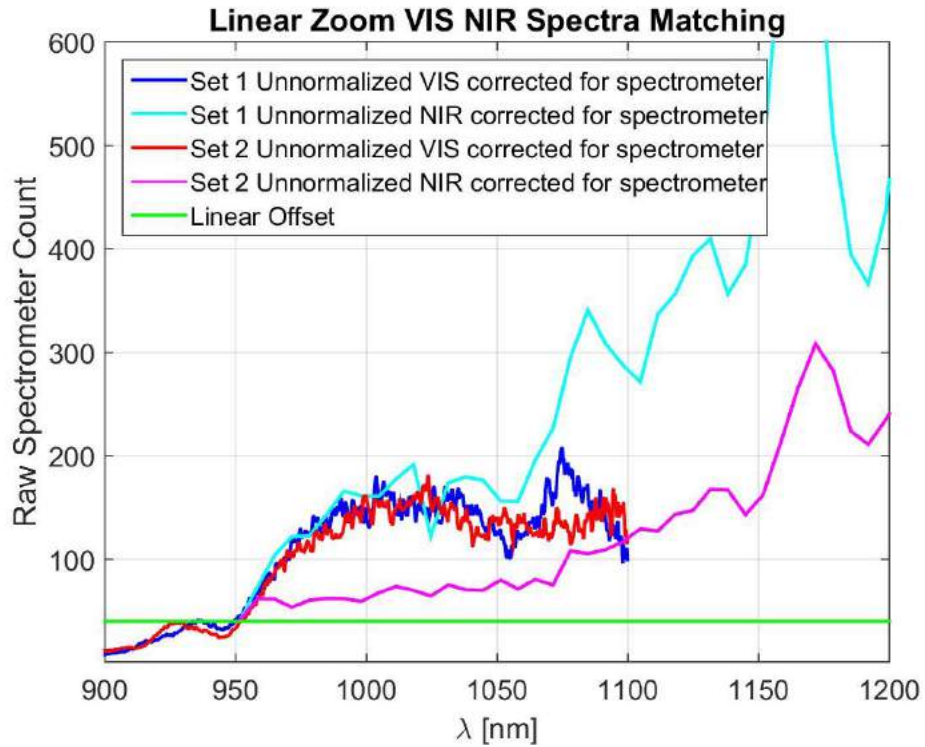


Figure 3.31: Spectrometer Stitching

Single versus multi-filament operation was verified by directly observing the output plane of the crystal with an IR micro-bolometer camera (Figure 3.32), and by checking the white-light output for interference fringes and speckle characteristic for multiple filaments.

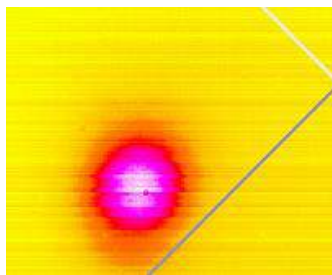


Figure 3.32: Micro-Bolometer Camera Image of Single Filament Operation

A gold integrating sphere was used for initially used for light-collection, but due to high absorption, was later removed from the setup. Readings for the wavelength region beyond the spectral coverage of the spectrometers were taken with a cryo-cooled monochromator coupled to a mercury-cadmium-telluride

detector. However, it was later observed that higher order ghosts of the pump were imprinted onto the spectral data, and it was difficult to separate the ghosting from real light at low spectral energy densities from the SCG output at the longer wavelengths. The spectral ghosts of the pump are shown in Figure 3.33. The monochromator data was therefore disregarded and not used for final spectral analysis.

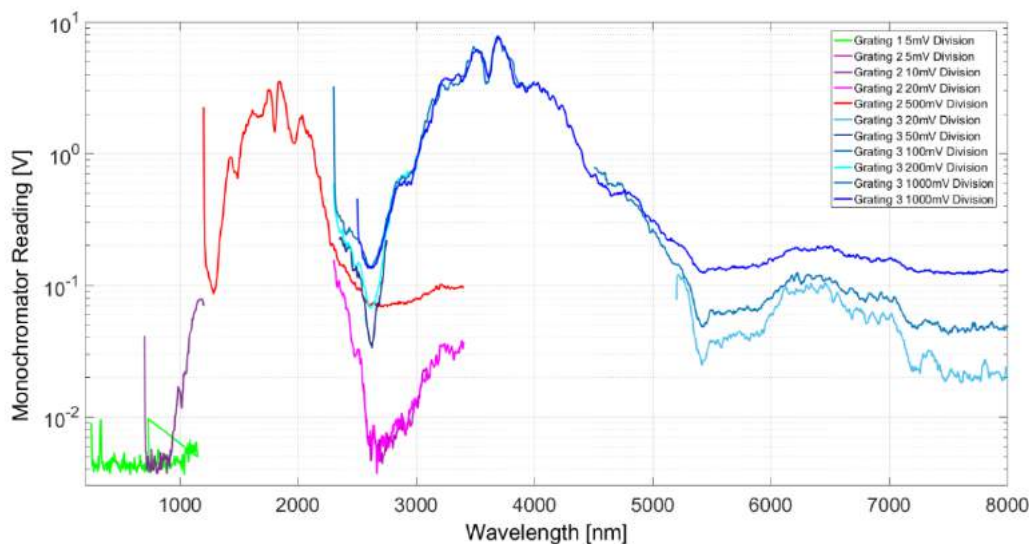


Figure 3.33: Monochromator Ghosting from Pump Pulse

### 3.3.3 Results and Discussion

The spectral output of SCG in 2mm YAG, 2mm C-Cut Sapphire and 2mm Diamond with identical input conditions for single-filament operation is shown in Figure 3.34 and Figure 3.35. Here, the 3<sup>rd</sup> harmonic of the pump is clearly visible at ~670nm, and separated from the ASW peak at ~550nm for each of the crystals. While the highly structured nature of the pump makes the spectral difficult to analyze, we can see that YAG offers high spectral energy density, and a flat spectral profile in the Stokes region. This makes YAG a good choice if seed wavelengths in the 2000 – 2500nm range are desired.

Sapphire has a much flatter spectral response in the NIR portion of the spectra, with a dramatic reduction in energy-transfer to the VIS—this makes Sapphire a good choice if seed wavelengths in the 1000-1500nm region are desired.

ZnSe has a more structured output, with spectral discontinuity between the broadened 3<sup>rd</sup> harmonic region in the VIS/NIR and the MIR portions of the output. However, the spectral energy density in the MIR is appreciable, making ZnSe a viable alternative in cases where very high nonlinearity is desirable.

SCG in diamond shows the most consistent spectral output with no spectral discontinuities or appreciable modulation, with spectral energy densities comparable to (or greater than) both YAG and Sapphire. This makes diamond the ideal SCG crystal for the entire range of wavelengths (or input pulse regimes that allow the use of a short crystal—the expense of procuring longer crystals makes Diamond unattractive for longer pulsewidths).

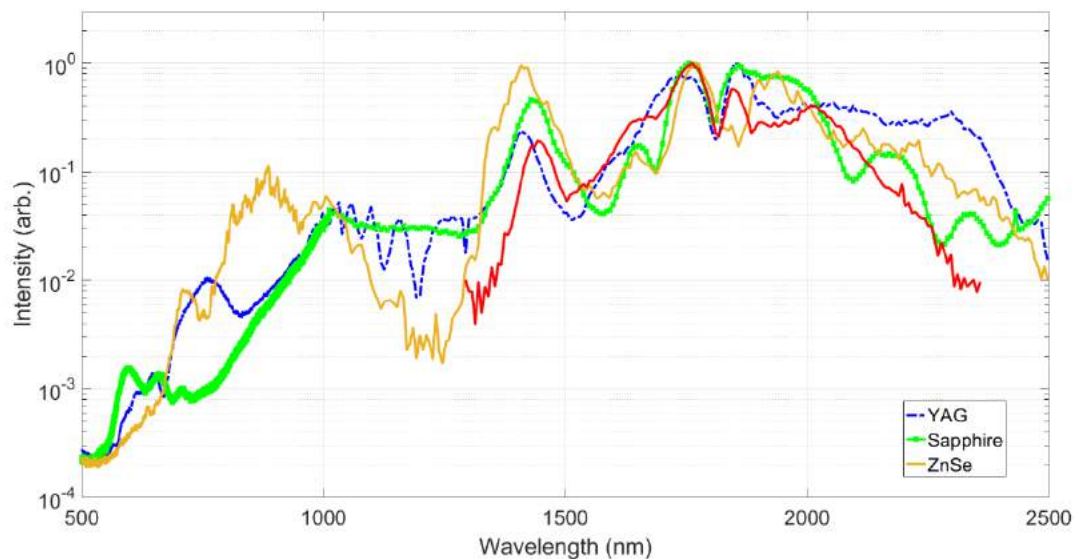


Figure 3.34: ICFO SCG Spectral Comparison, pump pulse is shown in red.

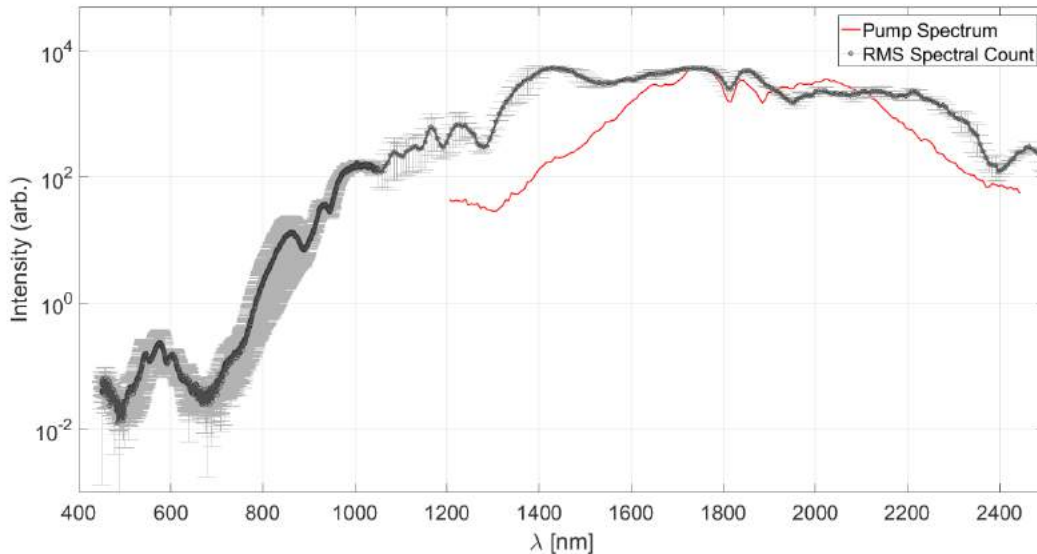


Figure 3.35: ICFO SCG Spectra for 2mm Diamond

The Raman response of diamond is orders of magnitude stronger than that of the other solids [3.60], thus its use in Raman lasers [3.61, 3.62] and in four wave mixing sources [3.63]. The transient nature of the SRS effect means optimal time delay of the seed vs. the pump pulse is a key factor in determining the efficiency of the process [3.74]. With short pulses with peak intensities (i.e. pulses capable of SCG in a suitable material), competing nonlinear processes arising from SF (like SPM and self-steepening) limit the conversion efficiency [3.64]. But while it has been argued that SRS effects during SCG is negligible, at least for short pulses [3.10], T. M. Kardas has studied the role of SRS in supercontinuum generation in bulk diamond with an 800nm pump pulse [3.56] and found it to be significant.

In collaboration with the University of Warsaw and T. M. Kardas, a similar approach was used to analyze the data from the ICFO study (Section 1.4). The HUSSAR [3.65] nonlinear pulse-propagation simulation package was used to carry out simulations regarding the role of SRS in bulk-diamond supercontinuum at 2 $\mu$ m wavelengths—the comparison to ICFO experimental data is shown in Figure 3.36. The inclusion of Raman terms within the simulation allowed a very close match with experimental spectra, and it was seen that the presence of Raman scattering increased spectral energy density of SC output by three

orders of magnitude over the case where only 3<sup>rd</sup> harmonic and SF effects were utilized. This raises the question of (a) coherence, as the SRS process is noise-seeded, and (b) how the effect of intense, competing nonlinear processes utilized in SCG allow for such significant SRS contribution at ultrashort timescales.

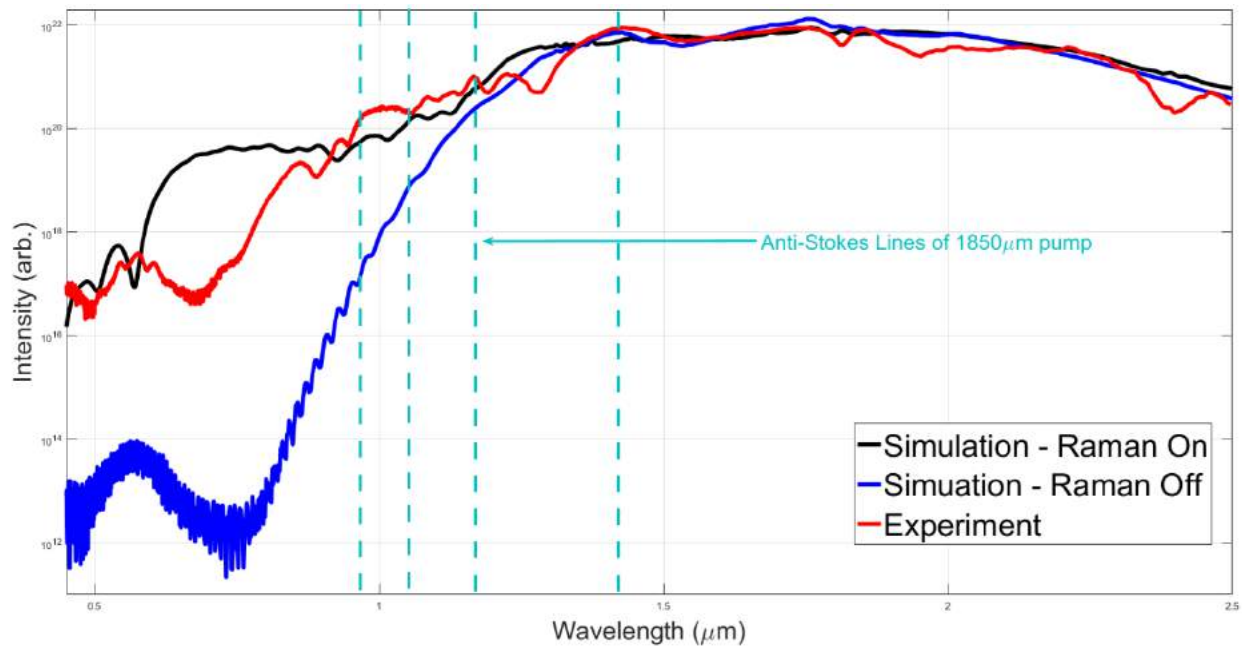
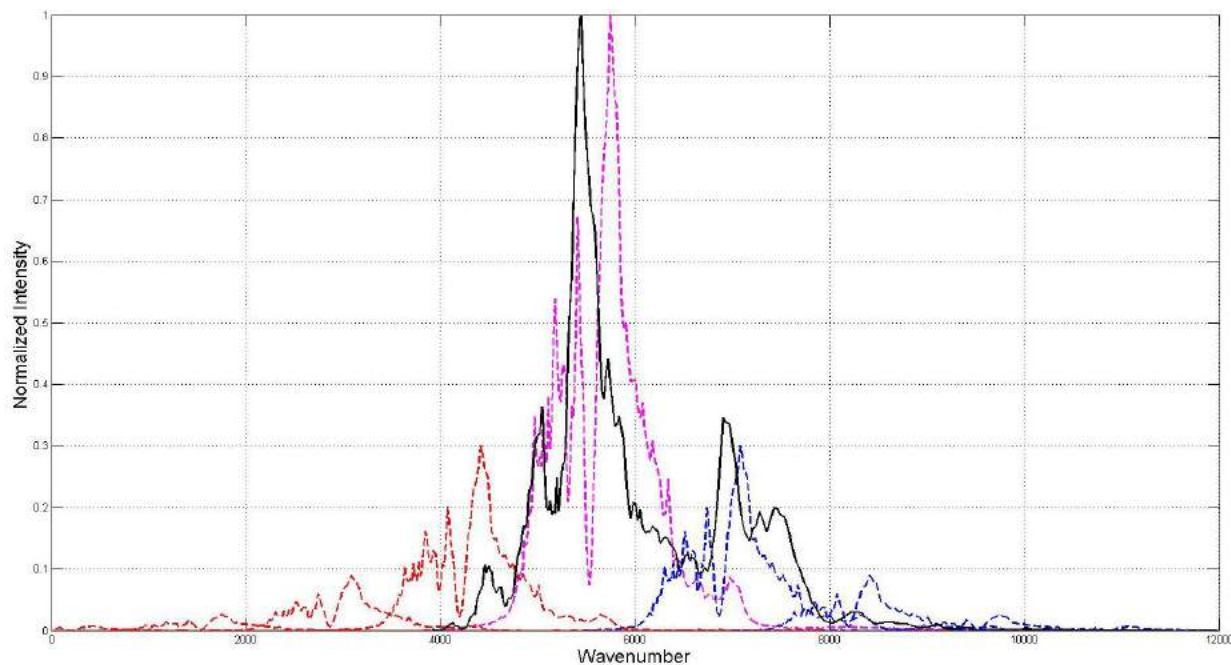


Figure 3.36: HUSSAR Simulations for Diamond SCG vs. Experiment. Simulations courtesy of T. M. Kardas, University of Warsaw.

Raman-assisted SGC in diamond at very short timescales has also been investigated by Lu et al. [3.57] using a chirped 7.7fs pulse. The supercontinuum obtained in this study is not a direct supercontinuum processes as it is “classically” understood—it is essentially a cascaded process, where anti-Stokes Raman orders are generated by four-wave mixing of two chirped input pulses with a variable time-delay between them. Similarly, differential two-phonon excitation [3.66] was used for Stokes suppression and SGC with an 800nm pump.

A weaker version of the same type of output (may, perhaps) be observable in the ICFO Diamond spectra—Figure 3.37 shows the superimposition of the pump (magenta) and its first few Stokes and Anti-

Stokes Raman bands (red and blue, respectively) with the SCG spectra (solid black). The structured nature of the pump makes it difficult to comment on this with any degree of certainty, but peaks in the SCG spectrum seem to coincide with the first few Raman bands.



*Figure 3.37: SCG Spectra in Diamond (Black), Pump (Magenta), Stokes Raman Shift of Pump (red), Anti-Stokes Raman Shift of Pump (Blue)*

In terms of perturbative higher harmonics like contributions from the 3<sup>rd</sup> harmonic to the energy density of the SCG, and 2<sup>nd</sup> harmonic (for ZnSe), indications were seen of 3<sup>rd</sup> harmonic peaks, but the input pump pulse was too structured to make definitive statements regarding the respective contributions of these processes.

Optical damage was not seen on any crystal during the benchmarking stage. Therefore, the input pump energy was increased by removing attenuators until a clear two-filament operation point was reached at  $\sim 5 \mu\text{J}$ , and then a stable multi-filament regime at  $\sim 10 \mu\text{J}$ , with no visible damage to the crystals. Caution must be taken in applying the results of an 11fs input pulse to the picosecond regime, however, the lack of damage to the crystals in this specific study is promising.

The increase in input energy allowed for a brief study of the multi-filamentation (MF) region. The MF WL and CE output was projected onto a screen and its visible component was imaged using a photographic camera (Figure 3.38: Fringe Contrast). The measured fringe-contrast was calculated to be  $\sim 70\%$ , though this value is not entirely reliable given the nature of the measurement equipment.

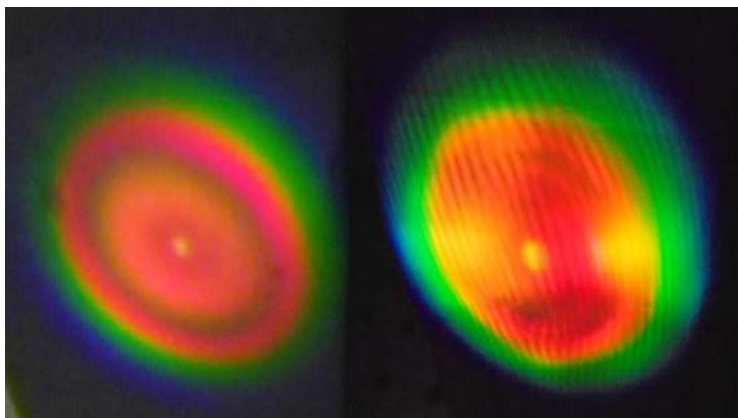


*Figure 3.38: Fringe Contrast*

It was verified that MF could be triggered even at the previous “stable” input energy point of  $1\mu\text{J}$  simply by offsetting the input focusing lens—given the broadband nature of the pump beam, even a minor offset introduced large chromatic aberrations at the focus within the YAG plate. As spatio-spectral hotspots in the wavefront of the input beam trigger of MF even at low powers, this finding is not remarkable. Material inhomogeneities in the SC-crystal, beam instability and the transverse modes of the beam have been further proposed as triggers for MF. Redefining these triggers as “filament nucleation events”, this work proposes that they are *not* an inevitable consequence of high input power ratios, but can be controlled to a certain extent by ensuring the transverse beam quality of the pump at its focus and the quality of the nonlinear crystal used for SCG.

Increasing the input pulse energy increased the number of filaments nucleated within the crystal, until a large number ( $>20$ ) filaments were observed at input powers of  $\sim 10\mu\text{J}$ , accompanied by the characteristic speckle pattern of the output WL and CE. The multiple filaments were stable in position

and the overall spectral energy density of the output was as stable as that of a single filament (with the same spectral extent) but with a 10x increase in intensity to match the increase in input pump energy. Figure 3.39 illustrates the transition of the visible portion of the SC output from a single-filament to a multi-filament regime.

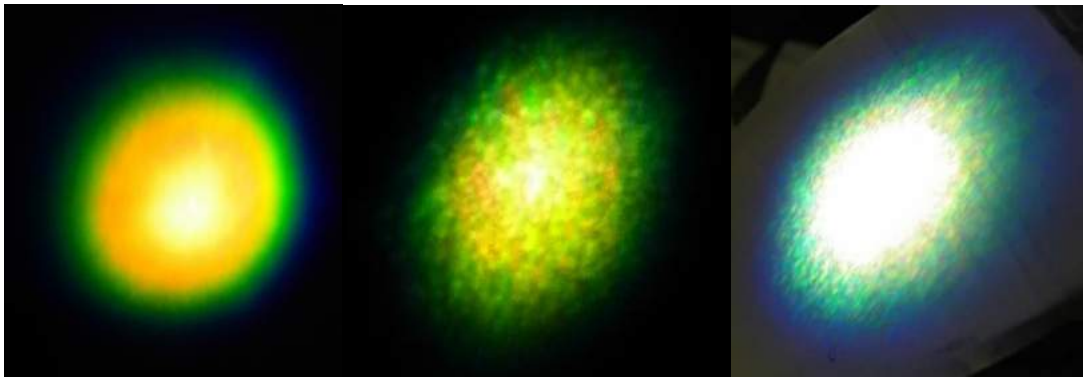


Figure 3.39: Sapphire Multi Filamentation Progression

Given the lack of visible surface damage to the crystals, questions of bulk damage and long-term stability were addressed by looking at the spectral output of MF SC generated in a 6mm C-Cut Sapphire plate. Damage in the Sapphire would result in a drop of the spectral energy density in the visible region and a distortion of the output spectral profile. As seen in Figure 3.40, the spectral output remains identical in shape and structure after 90 minutes of high-energy MF operation.

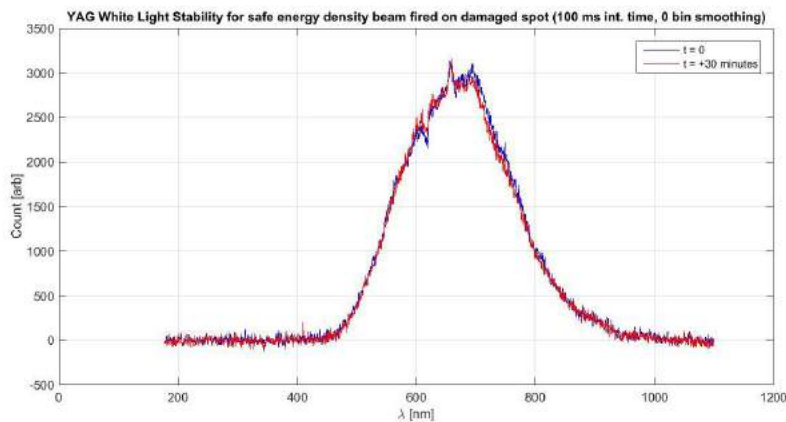
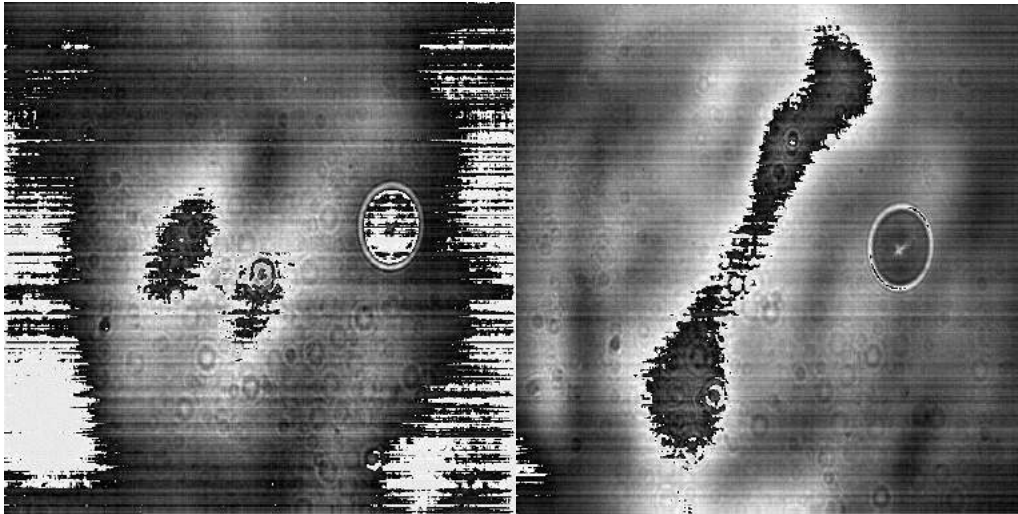


Figure 3.40: Sapphire MF VIS spectra changes under long-term operation

The end-face of the MF in the YAG plate was also imaged onto a Thermocam bolometer, and the two filaments were clearly visible (Figure 3.41).



*Figure 3.41: Two filament structures in YAG, recorded ~10 seconds apart*

The two-filament configuration was not spatially or energetically stable, with evidence of filament competition. The regular “breathing” and energy-exchange pattern between the two filaments (visible on the ThermoCam on the scale of seconds) raised intriguing questions regarding coupling a the pseudo-evanescent-wave like behavior of the plasma channel, the presence of a THz channel, or a shared energy reservoir outside the hot core of the filament acting as a coupling mechanism. These remain open areas of investigation—the scope and beamtime constraints of the ICFO-1.8 $\mu\text{m}$  study made further study unfeasible.

### 3.4 STIMULATED RAMAN AMPLIFICATION (SRA) IN DIAMOND OF YAG SUPERCONTINUUM (PHAROS, MPSD)

Given the results of the ICFO study for supercontinuum generated in diamond, i.e. that Raman processes could significantly alter the supercontinuum output spectra, it was determined that since (a) the SCG output of YAG was comparable in spectral energy density to diamond in the MIR, and (b) the SRS would, intra-crystal or externally, be of use in amplifying the energy at those wavelengths, Stimulated Raman *Amplification* of a supercontinuum would side-step the question of coherence by pre-seeding the Raman lines with coherent radiation.

The only known SRA of a supercontinuum was carried out by Krylov [3.72] in 1996, where a 780nm, 200fs pulse was used to generate supercontinuum in glass, then Raman amplified in a pressurized hydrogen-gas chamber.

Stimulated Raman Scattering (SRS) is a useful frequency-conversion process behind multiple laser setups [3.67, 3.68], but as it is seeded via quantum noise fluctuations, the coherence of the generated radiation and stability is poor. The first convincing study of Raman amplification of a Stokes signal was conducted by Duncan et al. in 1987 [3.69] where a 532nm, 40ps pulse was spectrally broadened in a hydrogen-gas cell, then raman amplified, also in a hydrogen cell, by a matched pump pulse. Many other experiments have used Stimulated Raman Amplification of a pump in the picosecond regime [3.70, 3.71]; one observation in literature is that seeding the SRS/SRA process produces much better results in terms of beam quality and coherence.

This proof-of-concept experiment is the first (to the best of our knowledge) study of Stimulated Raman Amplification of a supercontinuum in Diamond, and the first study of SRA in Diamond at long wavelengths.

### 3.4.1 SRA Setup

The SRA Setup is illustrated in Figure 3.42. Pulse of  $0.5\mu\text{J}$  energy,  $\sim 177\text{fs}$ ,  $1030\text{ nm}$  light from the PHAROS laser system (See Section 3.3.1) was split via a 50/50 TFP into a pump arm and a seed arm. The light in the seed arm was focused using a  $150\text{mm}$  FS PCX lens into a  $5\text{mm}$ , [1,1,1]-cut YAG crystal; the broadband SCG output was then collimated with another  $150\text{mm}$ ,  $2''$  PCX lens.

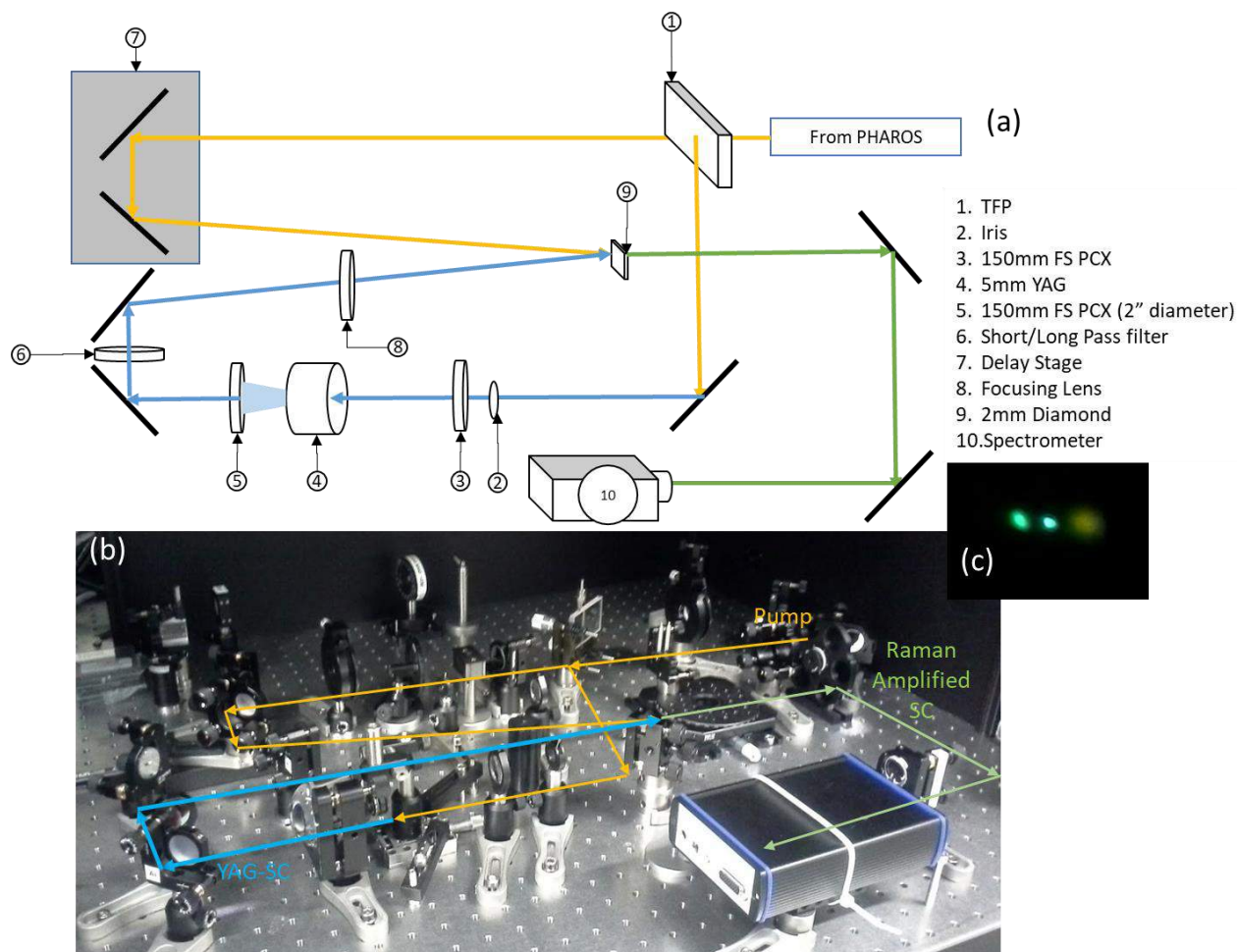


Figure 3.42: SRA Setup (a), Tabletop Photograph (b), Output of DFG in BBO (c)

In order to work with only the spectra produced by SCG on the Anti-Stokes side of the pump, a shortpass filter (Thorlabs FESH1000, cut-off wavelength of  $1000\text{nm}$ ) was used to remove the pump and longer wavelengths from the beam before directing it through a  $250\text{mm}$  PCX  $\text{CaF}_2$  focusing lens into a  $3\text{mm}$  CVD

single-crystal Diamond. A Thorlabs FEL1100 long-pass filter was used to work with the Anti-Stokes region of the pump.

On the pump side, the collimated light was sent through a delay stage before being focused through the diamond. A BBO crystal was used in place of the diamond to achieve spatial/temporal overlap of the pump and seed pulse through DFG—the mixing output of the 2<sup>nd</sup> harmonic of the pump, seed, and the DFG wavelength is seen in Figure 3.42 (c). The delay setting was different for both Stokes and Anti-Stokes side because of the difference thickness between the long and short pass filters.

An NIR –ND filter (OD 2.0) was used in the pump arm when it was noticed that even the low intensity light was generating spectral broadening and SCG in the Diamond. Subsequently, care was taken to ensure that there was no spectral broadening in the diamond due to the pump before recording each family of spectra.

### 3.4.2 Results and Discussion

The broadband, single-filament SC generated by the YAG showed a delay-based difference in the spectra after passing through the Diamond, on both the anti-Stokes (Figure 3.46) and Stokes (Figure 3.45) side of the pump. Without the pump, the diamond absorbed portions of the light, reducing the overall spectral energy density; there was no peak amplification or suppression. Similarly, for delays far from the optimal pump/seed overlap, no shape changes in the spectra were seen. However, as seen in Figure 3.44, there is a delay-based suppression/amplification as expected for SRA. On the Stokes-Side (Figure 3.43), the delay-based effect shows an amplification of all peaks in the spectra. Further analysis and simulations are required to determine whether the amplification seen is consistent with theory.

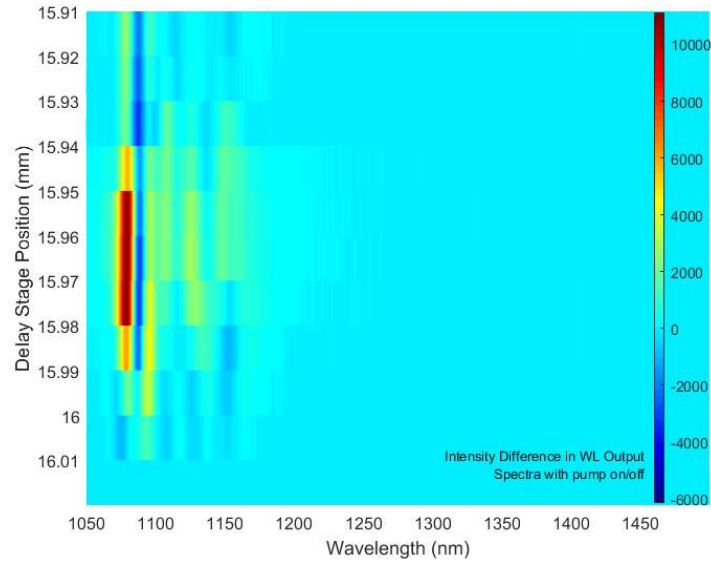


Figure 3.43: Delay-Based Amplification of Stokes-Side SCG Output. Color bar indicates normalized difference in amplified and unamplified SCG spectra (arb. Units).

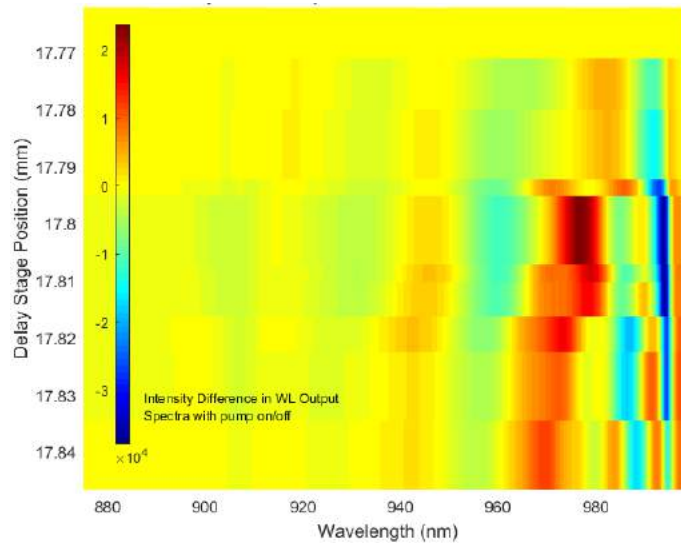


Figure 3.44: Delay-Based Differences of Anti-Stokes Raman Lines. Color bar indicates normalized difference in amplified and unamplified SCG spectra (arb. Units).

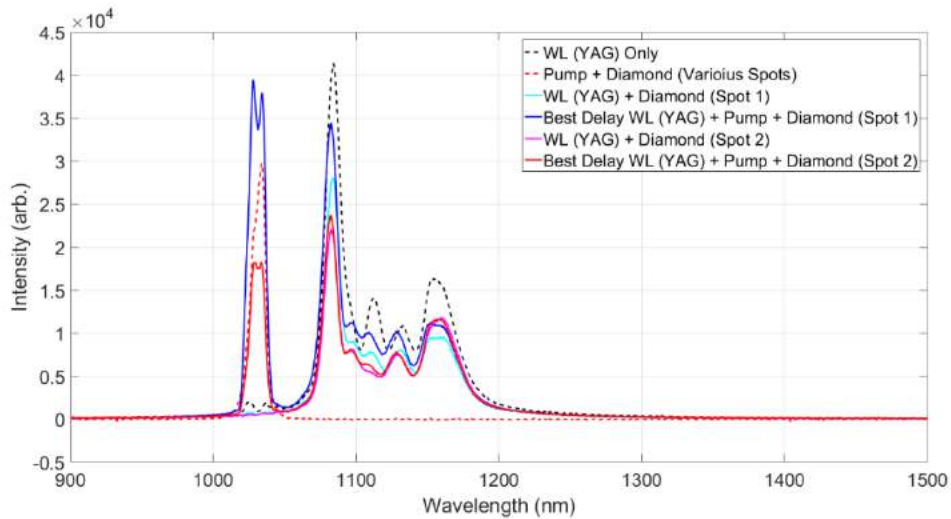


Figure 3.45: Stokes Spectral Output of FSRS Experiment

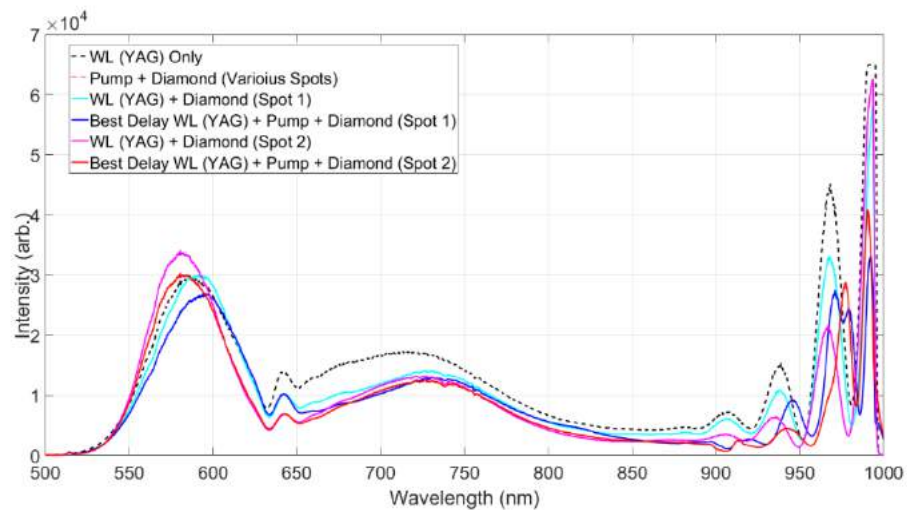


Figure 3.46: Anti-Stokes Spectral Output of FSRS Experiment

It should be noted that the spatial overlap between pump and seed was on a proof-of-concept, “best effort” basis—though the amplification gains are noticeable, they are not as substantial as those reported for SRA in gasses. A comparative study would require a more developed setup and better alignment between pump and seed to achieve optimal gains.

### 3.5 SPECTRAL BROADENING AND HIGH HARMONIC CASCADED FILAMENTS IN ZNSE (MPSD)

The objective of all the experiments carried out so far is to study SCG processes in the MIR, and develop methods to increase spectral energy densities in the SCG output. With the IRDL pump source operative at the MPSD, the final study required was SCG generation in the  $2\mu\text{m}$ , 3.2ps regime.

High energy SCG in bulk materials is normally the domain of femtosecond pulses. Work in the 1980s and 1990s demonstrated the feasibility of picosecond pulses for SCG [a5], but these studies were carried out at shorter, sub- $\mu\text{m}$  pulses. Lately, there has been renewed interest in picosecond SCG for seeding  $1\mu\text{m}$  OPCA systems [3.83, 3.84], but again, these studies focus on a shorter wavelength regime, or at 1ps pulses that are generally frequency-doubled [bathuska]. One recent study [3.85] on the use of chirped 3ps pulses in a 13mm YAG crystal for stable SCG at  $3\mu\text{m}$  does demonstrate that  $>1\text{ps}$  pulses can be used to generate SCG. However, the spectral content in the chirped 3ps pulses is almost double that available to the IRDL system.

As can be seen from Chapter 2 (Figures 2.9 and 2.10), the damage thresholds for YAG and Sapphire (Appendix A) and the cost of procuring Diamond crystals with greater than 10mm lengths, ZnSe is the only viable candidate that can generate SCG with a reasonable crystal/propagation length (sub 20mm) due to its high nonlinearity.

#### 3.5.1 IRDL Pump Source

The passively mode-locked, tunable, soliton Ho: fiber ring oscillator provides 1ps, 800nJ pulses at  $\sim 2054\text{nm}$  [3.78] shown in Figure 47 provides seed pulses to the Ho:Ylf regenerative amplifier (schematic shown in Figure 48) [3.78 – 3.80].

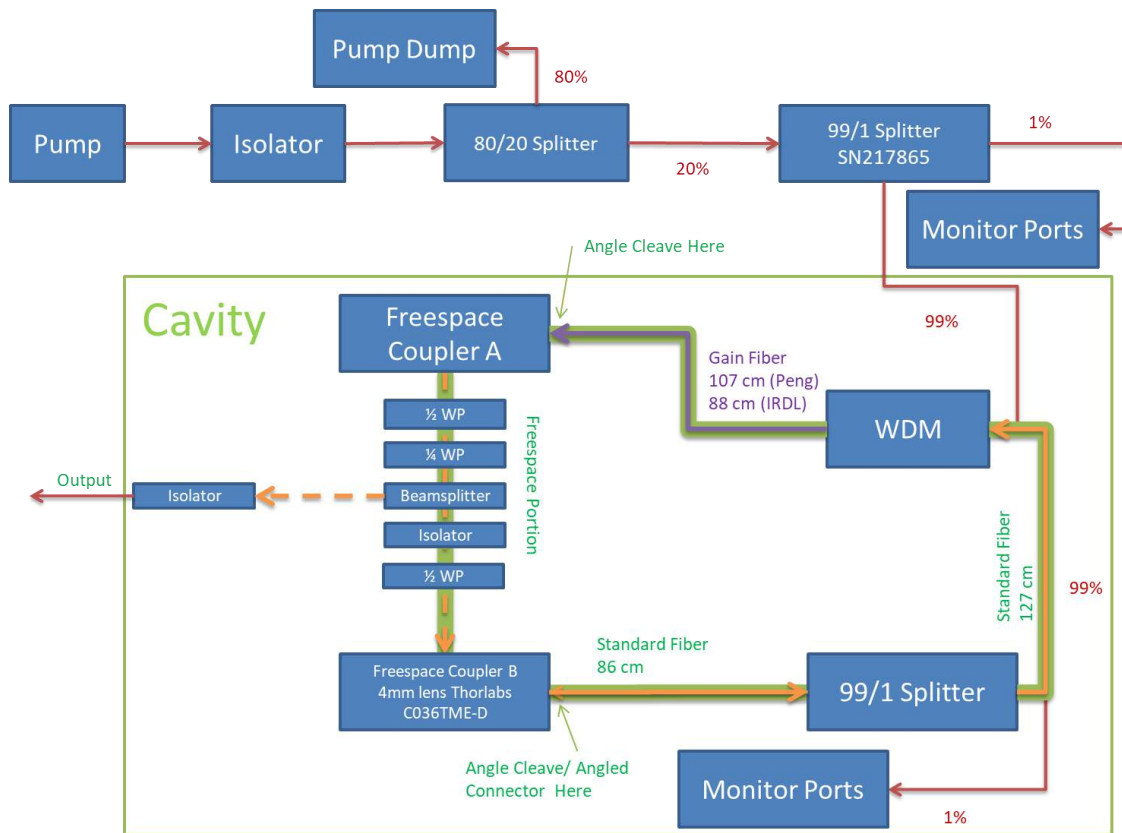


Figure 47: Fiber Oscillator

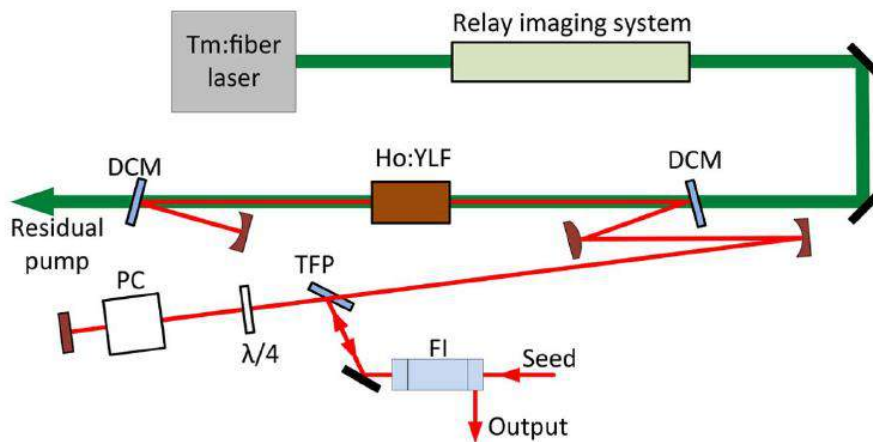


Figure 48: Schematic of the Ho:YLF Regenerative Amplifier, from [ref].

3.2ps, Fourier-Limited, 150μJ pulses centered at 2052nm, with a repetition rate of 1kHz, were available from the Regenerative Amplifier for the supercontinuum generation process.

### 3.5.2 Supercontinuum Setup

The output of the IRDL pump source was attenuated using a TFP and a  $\frac{1}{2}$  waveplate, then focused into various lengths of ZnSe crystal using different focusing configurations that included collimated beams, loose focusing ( $\sim 750\text{mm}$  FL) and tight focusing ( $\sim 50\text{mm}$  FL) conditions. The output of the nonlinearly broadened spectra generated in the ZnSe crystals was then either collimated or focused (depending on the desired measurement) onto an Avantes VIS spectrometer, or one of three Ocean Optics NIR/IR spectrometers with customized wavelength detection ranges and resolutions. Suitable ND filters for the VIS, NIR and IR ranges were used to prevent saturation on the spectrometer, and edgepass filters were used to selectively block spectral regions corresponding to the pump or 2<sup>nd</sup> harmonic, depending on the values being measured.

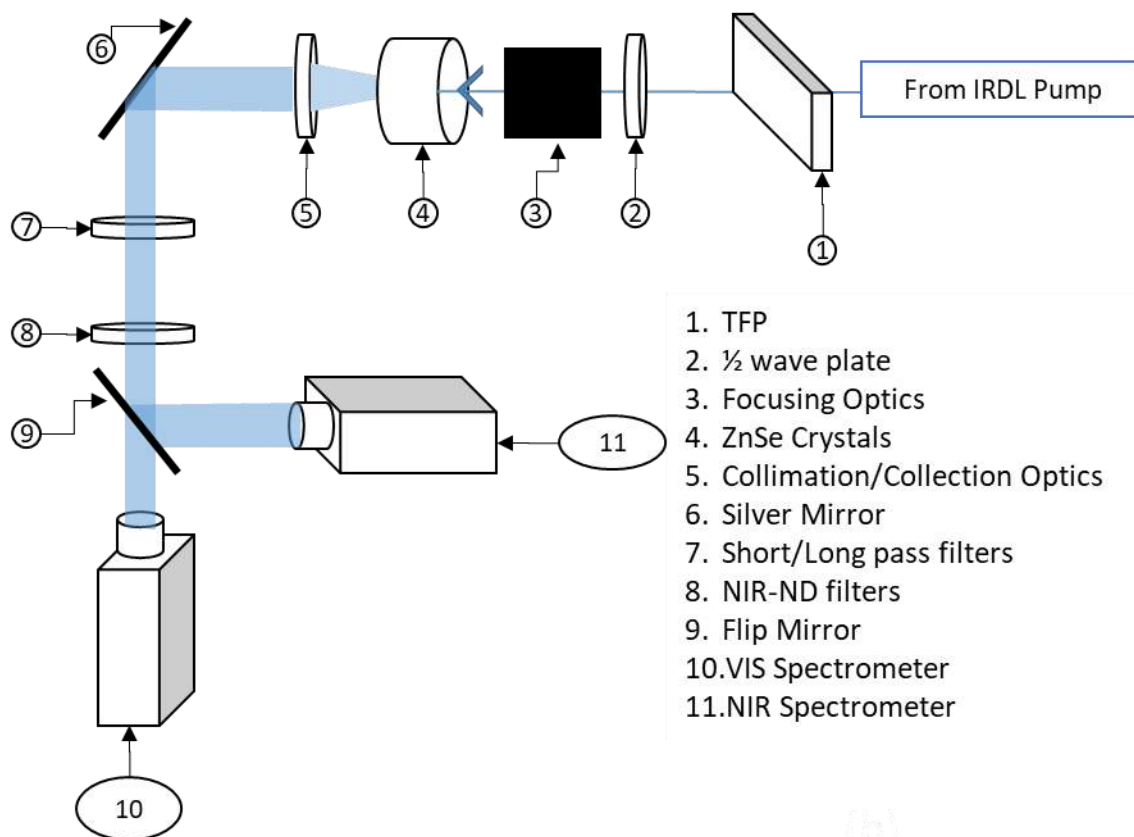


Figure 49: ZnSe SCG Setup

### 3.5.3 Nonlinear Broadening of the Fundamental: Results and Discussion

As a precursor to this ZnSe study, nonlinear broadening using the IRDL Ho:YLF pump was attempted in 10mm YAG and C-cut Sapphire crystals, with 150 $\mu$ J of input energy per pulse, in various loose and tight pre-focusing conditions. Approximately 4 – 6nm of pure-SPM based broadening was observed at these power levels for a loose focusing condition; reducing the focal spot size at the entrance of the crystals resulted in catastrophic damage (large, transverse cracks) originating in the heart of the crystal, though no surface damage was observed. Subsequently, an etalon was introduced within the IRDL regenerative amplifier for intra-cavity nonlinear broadening. This reduced the autocorrelator-measured pulse width to  $\sim$ 2ps, but also introduced spectral chirp in the pulse at the input to the nonlinear broadening stage, and failed to produce appreciable broadening in 10mm YAG or Sapphire crystals before damage. No attempt was made to introduce the 3mm Diamond samples to the setup.

Preliminary calculations using the analytic expressions from Chapter 2 indicated that a propagation distance of 15 – 20mm in the ZnSe crystal, coupled with external focusing via a 150mm PCX lens might yield the most appreciable broadening for pulse energies of  $\sim$ 50 $\mu$ J. A 20mm ZnSe crystal was then introduced into the experimental setup, and the input pulse energy was increased until the spectral broadening exceeded the wavelength range of the high resolution MIR spectrometer (1990 – 2110nm). Results are shown in Figure 50 (linear scale) and Figure 51 (log scale). The peak intensities were not normalized—it was important to consider total energy conversion as well as spectral bandwidth at each of the different input powers. For example, it can be seen that the 175 $\mu$ J pulse has the highest peak intensity at the pump, but the spectral energy density and flatness are not ideal, and may lead to problems in the subsequent compression stage. However, the 75 $\mu$ J pulse, though spectrally far narrower than the higher energy pulse, shows a very good spectral shape and possible eventual compressibility to close to its Fourier limit.

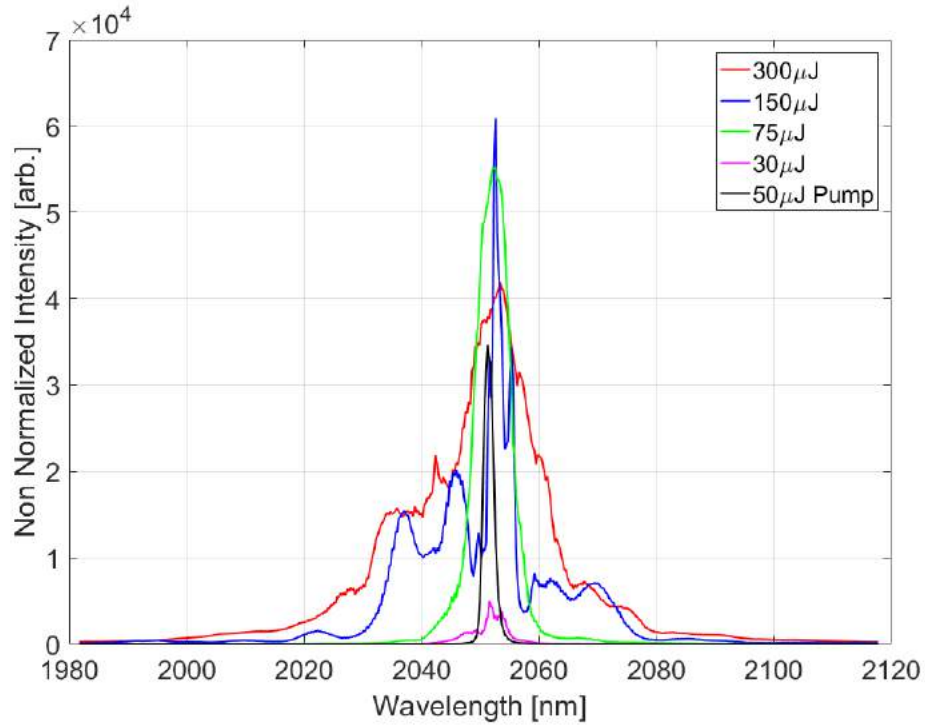


Figure 50: Nonlinear Broadening in ZnSe--energy scaling (linear scale)

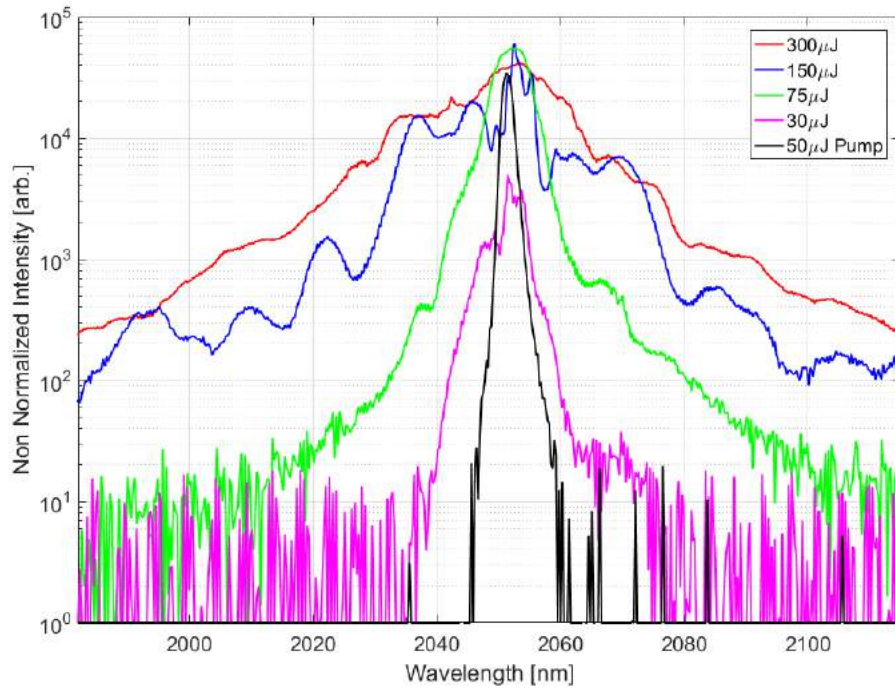


Figure 51: Nonlinear Broadening in ZnSe--energy scaling (log scale)

A fully developed supercontinuum emerged at pulse energies above  $300\mu\text{J}$ , leading to a visible, bright white spot in the SCG output. Table 1 summarizes the results obtained from this portion of the study. Note that compressibility over the entire foot-to-foot spectrum is not assumed—the complex structure of the spectrum makes estimations of pulse duration difficult, and FROG measurements are required.

*Table 1: Summary comparison of input pulse energies for spectral broadening in a 20mm ZnSe Crystal*

Pump Input Energy [ $\mu\text{J}$ ]	Output Energy [ $\mu\text{J}$ ]	Foot-To-Foot Spectrum [nm]	FWHM of central "peak" [nm]
30	22	30	6
75	40	90	10
150	70	135	12
300	120	>140	60

The input focusing conditions, especially at high energies, have a very large impact on the SCG spatio-spectral output. Small aberrations in the focus led to the formation of multiple filaments and significant asymmetry in the output beam. Care was taken to ensure single filament operation at all energy levels by monitoring the output beam on a Pyrocam detector (Figure 52) sensitive to wavelengths around and above  $2\mu\text{m}$ . The classic "ringed" structure of the SCG is visible.

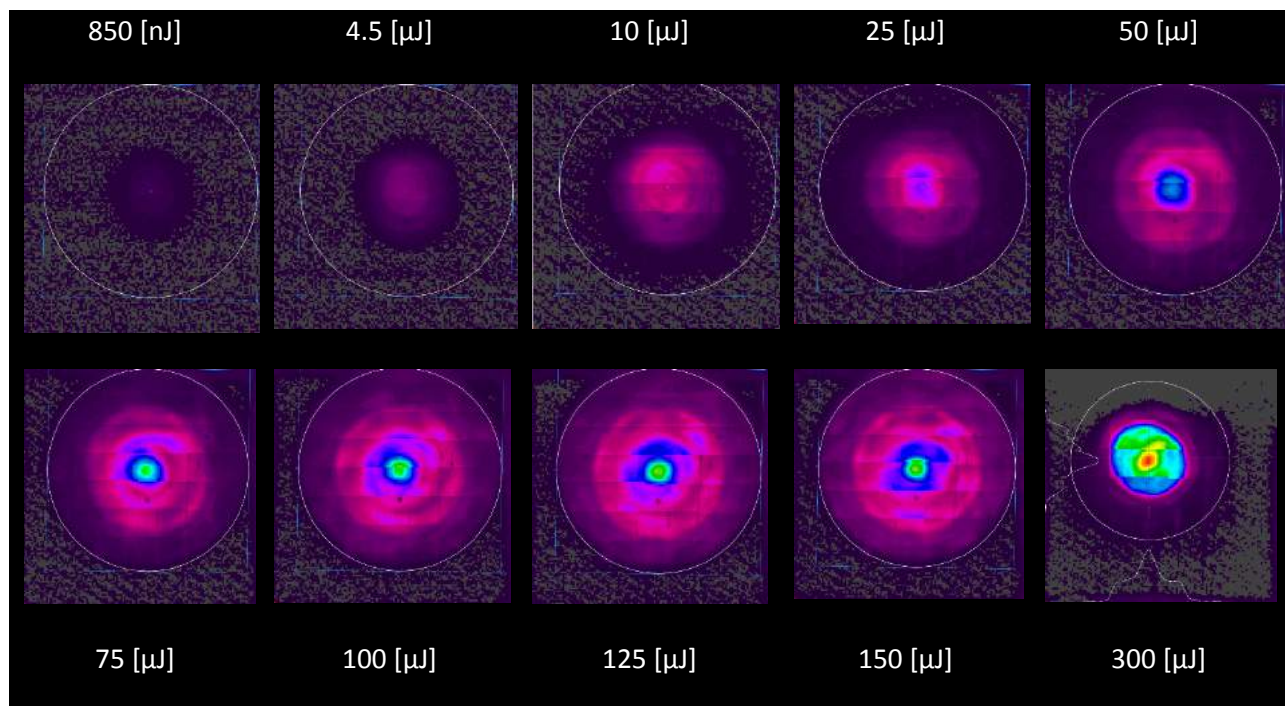


*Figure 52: Beam profiles in Pyrocam detector for SCG output at multiple input energy levels*

Figure 53 highlights the effect of focusing geometry on the spectral output of the pulse—the onset of spectral broadening is abrupt, and requires a specified NA and input spot size to be triggered. The most optimal configuration was found to be a loose focusing condition that yielded a spot-size of  $\sim 150\mu\text{m}$  in the focus, with the input face of the crystal displaced 1mm in front of the focal plane.

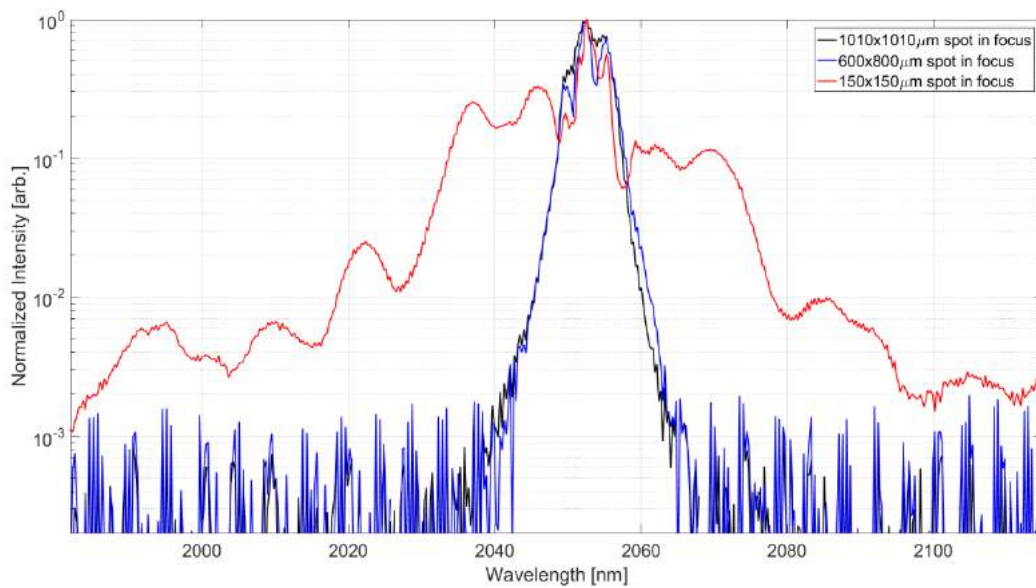


*Figure 53: Impact of focusing geometry on SCG output: three focusing conditions for a  $150\mu\text{J}$  beam.*

The energy-scaling study was carried out using a collimation beam after the ZnSe crystal to deliver energies in the WL core to the spectrometer. This setup is also ideal for beam delivery to the compression gratings or OPA stages, as the extremely high divergence of the CE and its broadband structure makes collimation over the entire beam unfeasible. However, there is appreciable energy in the CE of the pulse, even at wavelengths around the pump at  $150\mu\text{J}$  of input energy, as can be seen from Figure 54, where the CE was focused using a 2", 75mm FL  $\text{CaF}_2$  PCX lens, directly into the free-space output of the spectrometers. Given the high divergence of the pump beam after the ZnSe, as well as its long pulse duration, it was unlikely that there would be any contribution to the spectral broadening due

to the lenses after the ZnSe crystal, nevertheless, spectral comparisons were made with and without the collimation/focusing optics to rule out the possibility.

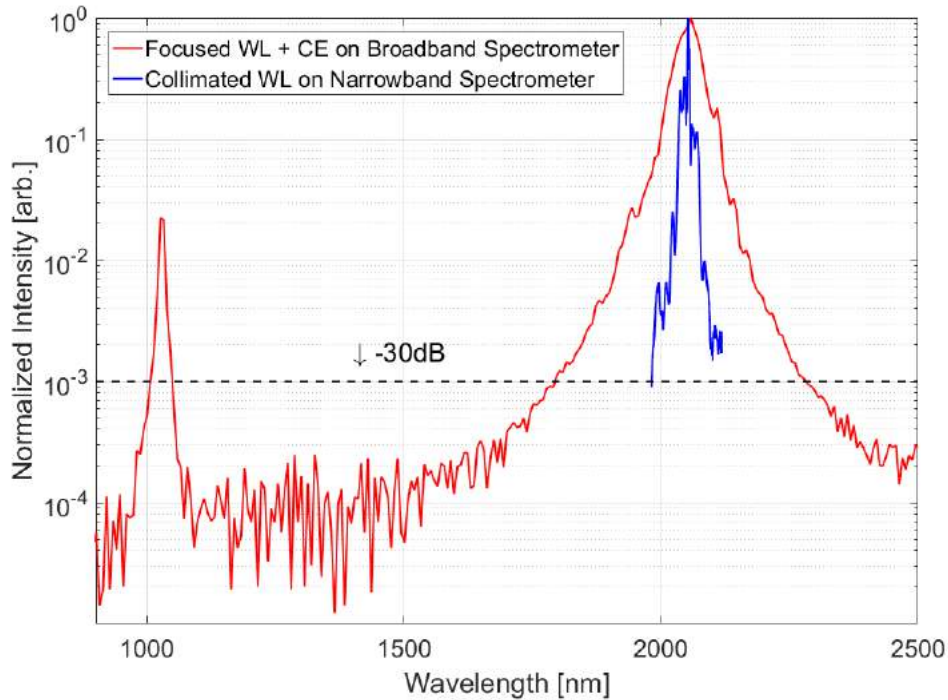
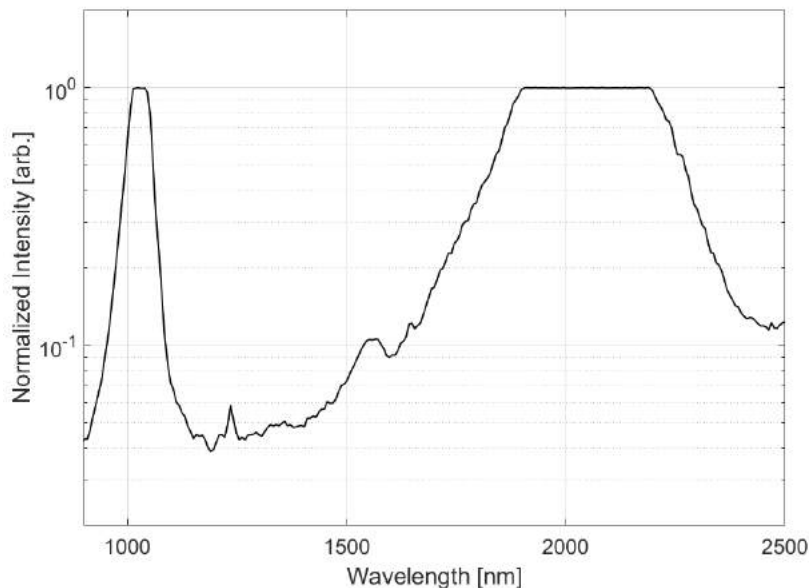


Figure 54: Central WL core (blue) in a collimated detection setup vs. WL + CE energy in a focused collection setup (red).

A large portion of the low-spectral-density light in the region between the pump fundamental and its 2<sup>nd</sup> harmonic was undetectable due to the presence of the ND filters required to prevent saturation in the spectrometer. Figure 55 shows spectra taken with fewer filters (OD 2.0 and OD 1.0) at a 1ms integration time—the detector is not saturated at this level, but the intensity count exceeds the limits of the detection software. Here, a broad pedestal to the fundamental and structure towards the 2<sup>nd</sup> harmonic can clearly be seen.



*Figure 55: Detail of pedestal spectra*

An input energy of  $150\mu\text{J}$  lies at the threshold of explosive, full-blown SCG in ZnSe in this setup. However, higher energies were no longer available from the pump source due to sustained and successive equipment malfunctions—a further studies were conducted with a maximum input energy of  $150\mu\text{J}$ , and the bright white-light core of a multi-octave supercontinuum was never seen again in the SCG output.

Studies were carried out to determine optimal crystal lengths for nonlinear broadening (Figure 56). Each crystal length required a re-adjustment of the collimation setup in order to deliver correctly focused pulses to the spectrometer input. Each length of crystal also showed different absorption values for peak energies, ranging from 30% (2mm crystal) to 60% (20mm crystal). The 6 and 8 mm crystals showed slightly higher spectral energy density around the pump, but far less conversion into shorter wavelengths. The 10mm crystal showed very little broadening, even around the pump region; a transverse shift of the input spot on the crystal showed as-yet unseen modulation of the spectra, leading to the conclusion that the specific sample has bulk defects, and is therefore unusable in the setup.

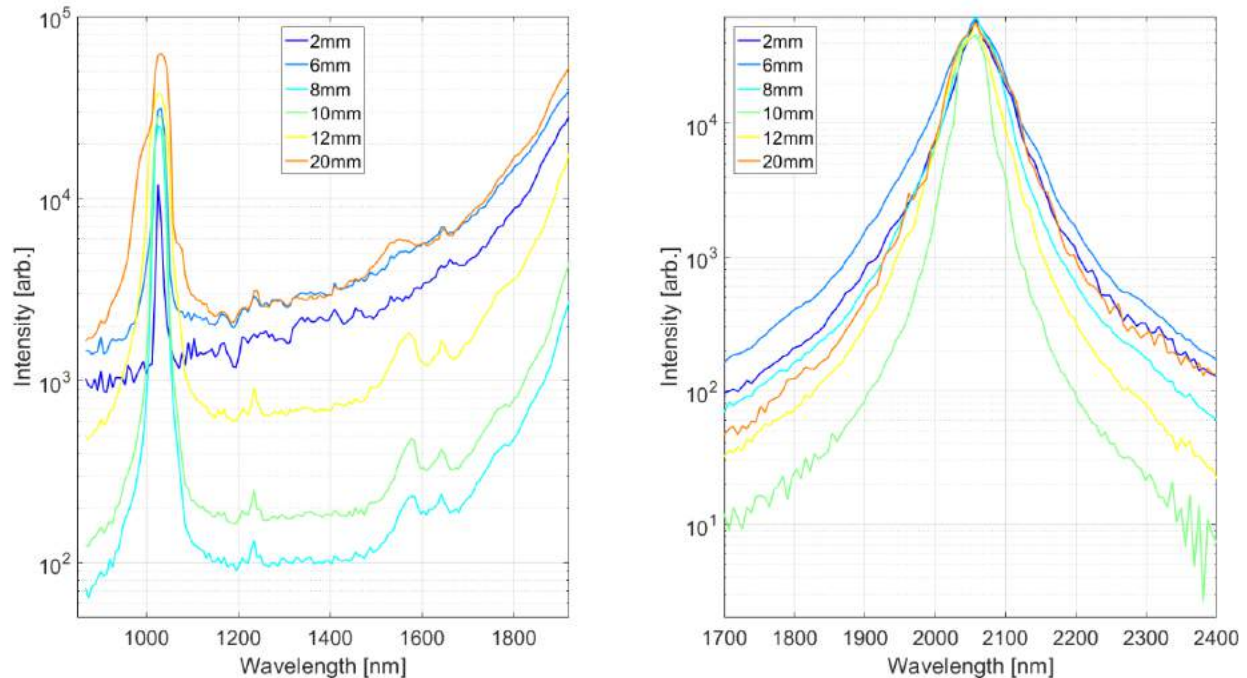


Figure 56: Effect of various crystal lengths on the broadened spectra near the pump (right) and between the pump and its 2<sup>nd</sup> harmonic (left).

With only 150 $\mu$ J of energy available to the SCG stage, a sub 100fs Fourier limit cannot be reached. Nevertheless, a sub 500fs pulse duration is most definitely supported.

Without specific information regarding the phase or pulse duration of the SCG output (some self-compression is expected, even in the normal regime), and the coherence between different parts of the spectra, a simple grating scheme was implemented. Figure 57 shows the analysis used to baseline grating selection—as the compressible output of the SCG stage may vary, the grating had to support a wide range of spectral widths with reasonable grating separation (i.e. greater than 8cm to accommodate mounting constraints and less than 60cm for a single pass, as the best collimation of the SCG WL core is only sustainable over a 120cm range). Three gratings at 35 grooves/mm, 70 groves/mm and 150 groves/mm were chosen, the last in the case that repairs to the support equipment for the pump would enable full SCG in the ZnSe crystal again, and therefore make pulses that support sub-100fs Fourier-limits available for compression.

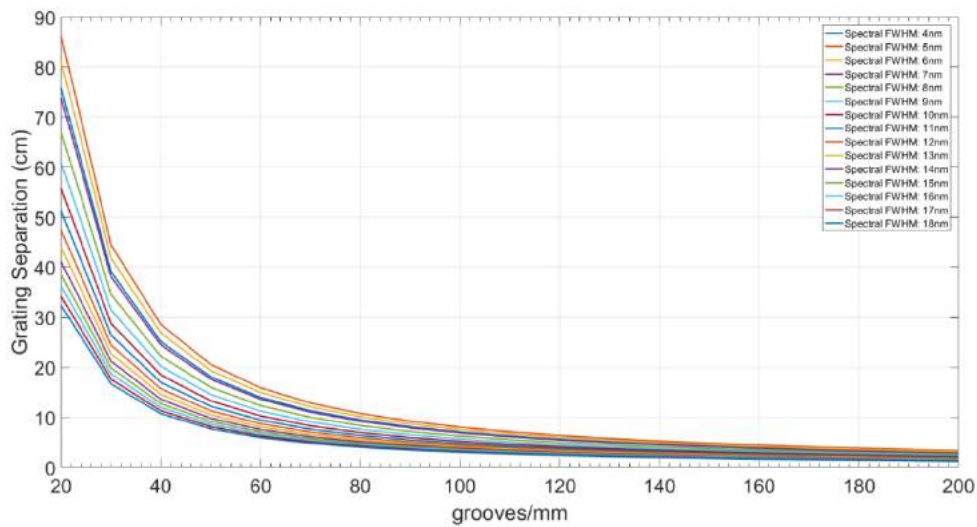


Figure 57: Grating separation vs. groove density for various spectral widths

Further analysis was used to configure the compression scheme, for example, Figure 58 shows the physical size required for the 35 groove/mm grating, based on the spectral width to be compressed and the grating separation.

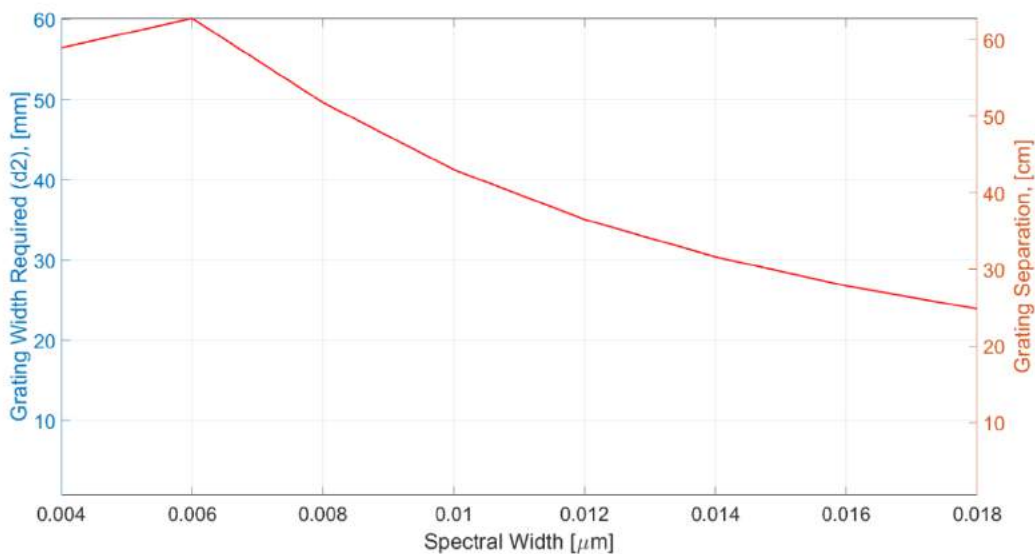


Figure 58: Physical grating width vs. spectral width for a 35 groove/mm grating.

Compression and characterization of the SCG output are ongoing as of the writing of this thesis.

### 3.5.4 Cascaded WL Generation in VIS/NIR region

The presence of the bright WL core in the ZnSe output prompted the study of broadening, and even filamentation, of the 2<sup>nd</sup> and 3<sup>rd</sup> harmonics. Though the extent of broadening will be limited due to the two-photon absorption of the ZnSe which starts at ~800nm, the low peak powers of the 2<sup>nd</sup> and 3<sup>rd</sup> harmonic, as well as the induced change to the two-photon absorption cross-section due to the high energy pump pulse, explain the presence of broadband energies in the VIS/NIR region--Alfano et al. [3.86] reported filamentation due to 2<sup>nd</sup> harmonic generation in a ZnSe crystal, and the results of the ICFO study demonstrate that there can be appreciable spectral energy density in the region of the 3<sup>rd</sup> harmonic as well.

Though limited by the input pulse energy, the start of filamentation was studied using three spectrometers spanning the VIS, NIR and IR regions. Figure 59 shows the spectra obtained over the entire wavelength range—the overlap region around 1000nm was used to calibrate and stitch the output of the three spectrometers, after correction of each family of spectra for the respective ND filters used to prevent saturation in each spectrometer.

Due to the different divergence angles for the dominating colors, the focusing conditions were optimized for collection of the “middle ground”, i.e the wavelengths around the 2<sup>nd</sup> harmonic. Therefore, though the same portion of the beam was sampled in all three spectrometers, the highly divergent VIS output is somewhat underrepresented. Also, the sensitivity of both the IR and VIS spectrometer falls off around the overlap region, leading to some uncertainty regarding the relative scale of the very large spectral width measured from the 2<sup>nd</sup> harmonic on the NIR spectrometer.

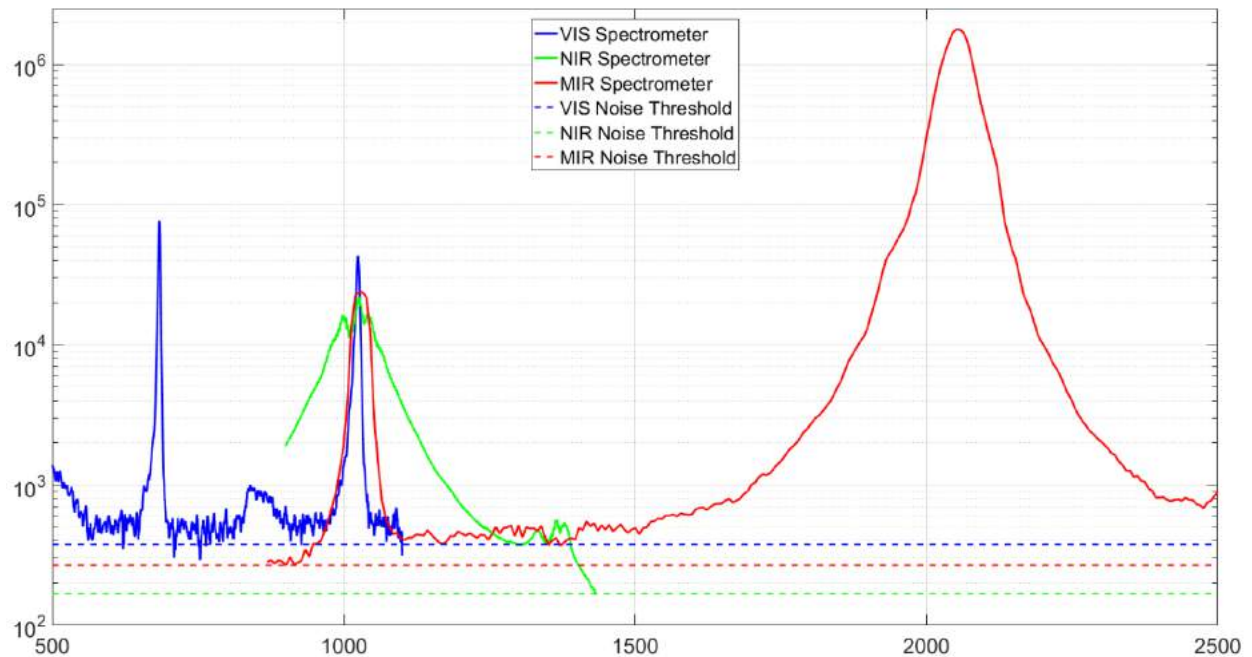


Figure 59: Full spectrum at 150 $\mu$ J

Curiously, the 4<sup>th</sup> harmonic of the pump is clearly seen in all VIS measurements, and it shows some degree of broadening (i.e. a wide pedestal at the base of the spike) for higher energies. A transparency scan was carried out for the 8mm ZnSe sample (curve shown in Figure 60) using a Perkins Elmer Lambda Spectrometer [3.87]. The 4<sup>th</sup> harmonic of the pump falls right at the edge of ZnSe's optical transparency.

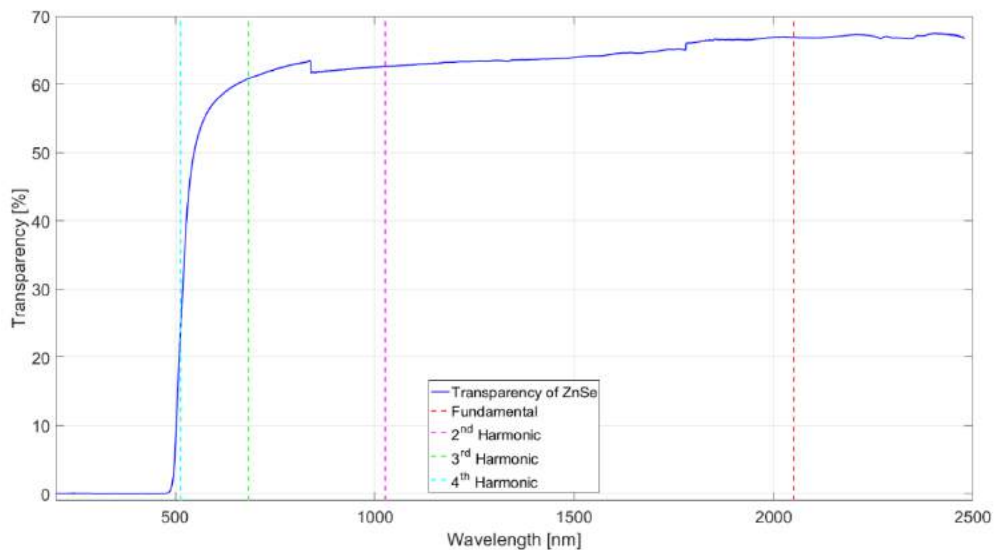


Figure 60: Measured Transparency Curve of ZnSe

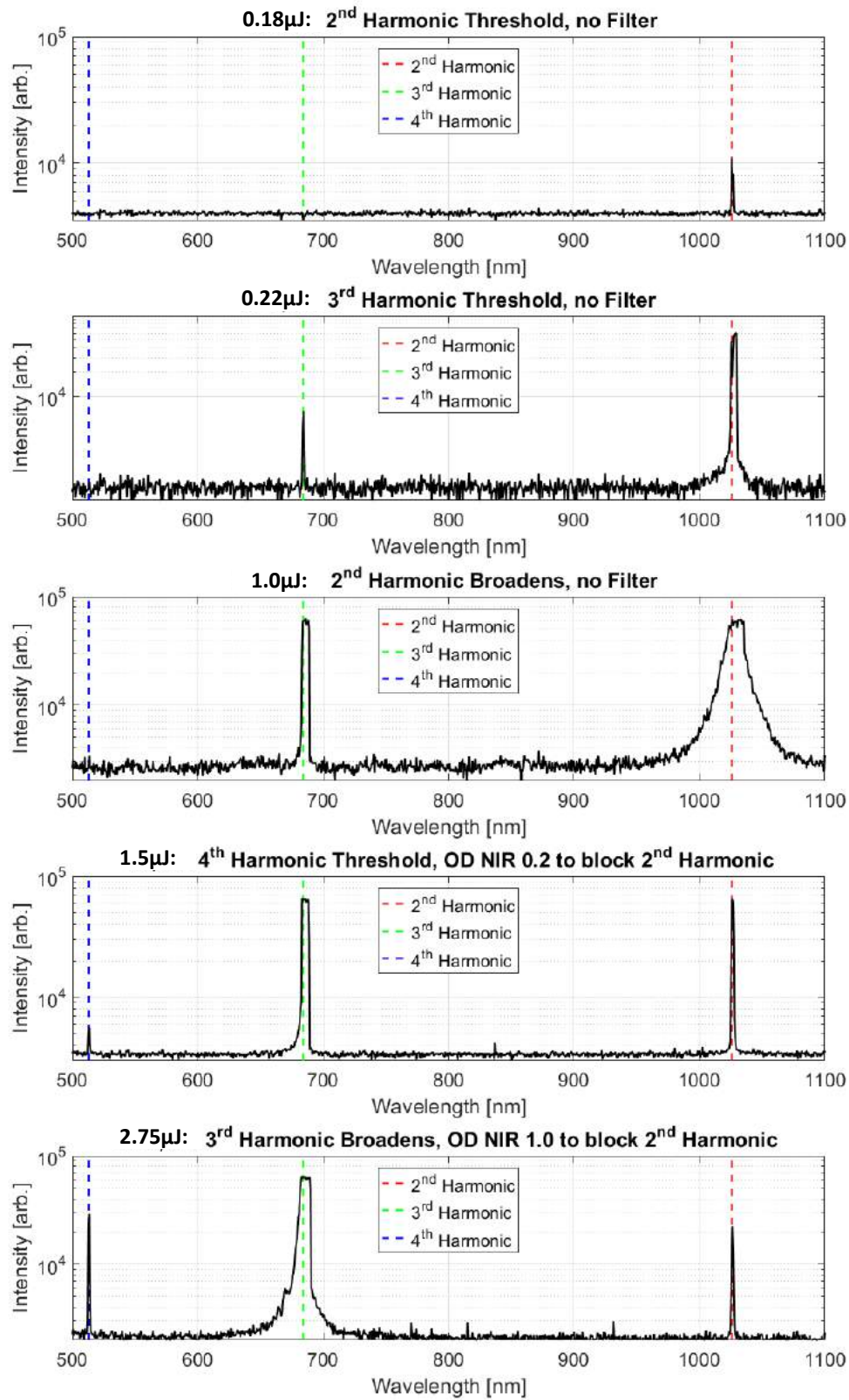


Figure 61: Threshold measurements for cascade broadening

Significant theory inputs are required to fully explain the experimental observations, especially in the presence of absorption bands and color centers in the ZnSe crystal. The input pump energy threshold for the onset of each of the nonlinear conversion processes was measured (Figure 61) as one of the inputs to theoretical simulations. Simulation work is being carried out in collaboration with the Couarion group at the Ecole Polytechnique, and the Biegert group at ICFO—work continuous at the time of the writing of this thesis.

### 3.6 REFERENCES

- [3.1] Augst, Steven J., et al. "Tunneling ionization and harmonic generation in krypton gas using a high-intensity, 1- $\mu$ m, 1-ps laser." *OE/LASE'90, 14-19 Jan., Los Angeles, CA*. International Society for Optics and Photonics, 1990.
- [3.2] Branlard, Julien, et al. "The european XFEL LLRF system." *IPAC 12 (2012)*: 55-57.
- [3.3] Mathew, Jose, et al. "Parametric studies on pulsed Nd: YAG laser cutting of carbon fibre reinforced plastic composites." *Journal of Materials Processing Technology* 89 (1999): 198-203.
- [3.4] Sattmann, Ralph, Volker Sturm, and Reinhard Noll. "Laser-induced breakdown spectroscopy of steel samples using multiple Q-switch Nd: YAG laser pulses." *Journal of Physics D: Applied Physics* 28.10 (1995): 2181.
- [3.5] Brodeur, A., and S. L. Chin. "Ultrafast white-light continuum generation and self-focusing in transparent condensed media." *JOSA B* 16.4 (1999): 637-650.
- [3.6] Van de Walle, Aymeric, et al. "Spectral and spatial shot-to-shot correlation analysis of bulk supercontinuum in the mid-infrared." *The European Conference on Lasers and Electro-Optics*. Optical Society of America, 2015.
- [3.7] Calendron, Anne-Laure, et al. "White-light generation with sub-ps pulses." *Optics express* 23.11 (2015): 13866-13879.
- [3.8] Indra, Lukáš, et al. "Stable Supercontinuum Generation in YAG with Picosecond Pulses." *CLEO: Applications and Technology*. Optical Society of America, 2017.
- [3.9] Dubietis, Audrius, et al. "Ultrafast supercontinuum generation in bulk condensed media (Invited Review)." *arXiv preprint arXiv:1706.04356* (2017).
- [3.10] Gaeta, Alexander L. "Catastrophic collapse of ultrashort pulses." *Physical Review Letters* 84.16 (2000): 3582.
- [3.11] Choudhuri, Aradhana, et. al. "Full 3D Simulation of White-Light Generation in Bulk Materials." *Proc. Europhoton 2014, Neuchatel, Switzerland*.
- [3.12] Zia, Haider, et al. "Full (3+ 1) D split-step technique for spatial mode analysis of white light generation in bulk Kerr-media." *CLEO: Science and Innovations*. Optical Society of America, 2015.
- [3.13] Zia, Haider. "Experimental and theoretical studies in non-linear optical applications. Fiber oscillators, regenerative amplifiers, simulations on white-light generation." (2015).
- [3.14] Kolesik, Miroslav, and JeromeV Moloney. "Modeling and simulation techniques in extreme nonlinear optics of gaseous and condensed media." *Reports on Progress in Physics* 77.1 (2013): 016401.

- [3.15] Jarnac, Amélie, et al. "Spatiotemporal cleaning of a femtosecond laser pulse through interaction with counterpropagating filaments in air." *Physical Review A* 89.2 (2014): 023844.
- [3.16] Durand, Magali, et al. "Blueshifted continuum peaks from filamentation in the anomalous dispersion regime." *Physical Review A* 87.4 (2013): 043820.
- [3.17] Couairon, Arnaud, and André Mysyrowicz. "Femtosecond filamentation in transparent media." *Physics reports* 441.2 (2007): 47-189.
- [3.18] Huber, Robert, et al. "Noncollinear optical parametric amplifiers with output parameters improved by the application of a white light continuum generated in CaF<sub>2</sub>." *Optics communications* 194.4 (2001): 443-448.
- [3.19] Fattahi, Hanieh, et al. "Third-generation femtosecond technology." *Optica* 1.1 (2014): 45-63.
- [3.20] Kourtev, S., et al. "Improved nonlinear cross-polarized wave generation in cubic crystals by optimization of the crystal orientation." *JOSA B* 26.7 (2009): 1269-1275.
- [3.21] Minkovski, N., et al. "Nonlinear optical transformation of the polarization state of circularly polarized light with holographic-cut cubic crystals." *Optics letters* 36.2 (2011): 301-303.
- [3.22] Dharmadhikari, A. K., F. A. Rajgara, and D. Mathur. "Depolarization of white light generated by ultrashort laser pulses in optical media." *Optics letters* 31.14 (2006): 2184-2186.
- [3.23] Kartazayev, V., and R. R. Alfano. "Polarization properties of SC generated in CaF<sub>2</sub>." *Optics Communications* 281.3 (2008): 463-468.
- [3.24] Kumar, R. Sai Santosh, K. L. N. Deepak, and D. Narayana Rao. "Control of the polarization properties of the supercontinuum generation in a noncentrosymmetric crystal." *Optics letters* 33.11 (2008): 1198-1200.
- [3.25] Midorikawa, Katsumi, et al. "Polarization properties of ultrafast white-light continuum generated in condensed media." *Applied physics letters* 80.6 (2002): 923-925.
- [3.26] Nagura, Chihiro, et al. "Generation and characterization of ultrafast white-light continuum in condensed media." *Applied optics* 41.18 (2002): 3735-3742. Yu, Jing, et al. "Mechanism of depolarization of white light generated by femtosecond laser pulse in water." *Optics express* 18.12 (2010): 12581-12586.
- [3.27] Silva, F., et al. "Multi-octave supercontinuum generation from mid-infrared filamentation in a bulk crystal." *Nature communications* 3 (2012): 807.
- [3.28] Buchvarov, Ivan, Anton Trifonov, and Torsten Fiebig. "Toward an understanding of white-light generation in cubic media—polarization properties across the entire spectral range." *Optics letters* 32.11 (2007): 1539-1541.

- [3.29] Choudhuri et al., "Spatio-Spectral Polarization Study of a 1 $\mu$ m-pumped Cubic Crystal (YAG)", *in review*.
- [3.30] Light Conversion Ltd., "Pharos Light Conversion User's Manual", January 2012.
- [3.31] Koechner, Walter, and Dennis K. Rice. "Birefringence of YAG: Nd laser rods as a function of growth direction." *JOSA* 61.6 (1971): 758-766.
- [3.32] Butcher, Paul N., and David Cotter. *The elements of nonlinear optics*. Vol. 9. Cambridge university press, 1991.
- [3.33] Adair, Robert, L. L. Chase, and Stephen A. Payne. "Nonlinear refractive index of optical crystals." *Physical Review B* 39.5 (1989): 3337.
- [3.34] Johnson, Philip JM, Valentyn I. Prokhorenko, and RJ Dwayne Miller. "Stable UV to IR supercontinuum generation in calcium fluoride with conserved circular polarization states." *Optics express* 17.24 (2009): 21488-21496.
- [3.35] Huber, Robert, et al. "Noncollinear optical parametric amplifiers with output parameters improved by the application of a white light continuum generated in CaF<sub>2</sub>." *Optics communications* 194.4 (2001): 443-448.
- [3.36] Burnett, John H., Zachary H. Levine, and Eric L. Shirley. "Intrinsic birefringence in calcium fluoride and barium fluoride." *Physical Review B* 64.24 (2001): 241102.
- [3.37] Senguttuvan, N., et al. "Oriented growth of large size calcium fluoride single crystals for optical lithography." *Journal of crystal growth* 280.3 (2005): 462-466.
- [3.38] Brodeur, A., and S. L. Chin. "Band-gap dependence of the ultrafast white-light continuum." *Physical review letters* 80.20 (1998): 4406.
- [3.39] Nie, Ying, et al. "Microstructure and mechanical properties of Al<sub>2</sub>O<sub>3</sub>/YAG eutectic ceramic grown by horizontal directional solidification method." *Journal of Alloys and Compounds* 657 (2016): 184-191.
- [3.40] Darginavičius, Julius, et al. "Ultrabroadband supercontinuum and third-harmonic generation in bulk solids with two optical-cycle carrier-envelope phase-stable pulses at 2  $\mu$ m." *Optics express* 21.21 (2013): 25210-25220.
- [3.41] Dharmadhikari, Jayashree A., et al. "Effect of group velocity dispersion on supercontinuum generation and filamentation in transparent solids." *Applied Physics B* 117.1 (2014): 471-479.
- [3.42] Liang, Houkun, et al. "Three-octave-spanning supercontinuum generation and sub-two-cycle self-compression of mid-infrared filaments in dielectrics." *Optics letters* 40.6 (2015): 1069-1072.
- [3.43] Dormidonov, A. E., et al. "Giantly blue-shifted visible light in femtosecond mid-IR filament in fluorides." *Optics express* 23.22 (2015): 29202-29210.

- [3.44] Chekalin, Sergei Vasil'evich, et al. "Supercontinuum spectrum upon filamentation of laser pulses under conditions of strong and weak anomalous group velocity dispersion in transparent dielectrics." *Quantum Electronics* 47.3 (2017): 252.
- [3.45] Bradler, Maximilian, Peter Baum, and Eberhard Riedle. "Femtosecond continuum generation in bulk laser host materials with sub- $\mu$ J pump pulses." *Applied Physics B* 97.3 (2009): 561.
- [3.46] Majus, D., et al. "Rogue-wave-like statistics in ultrafast white-light continuum generation in sapphire." *Optics express* 19.17 (2011): 16317-16323.
- [3.47] Majus, Donatas, and Audrius Dubietis. "Statistical properties of ultrafast supercontinuum generated by femtosecond Gaussian and Bessel beams: a comparative study." *JOSA B* 30.4 (2013): 994-999.
- [3.48] Budriūnas, Rimantas, et al. "53 W average power CEP-stabilized OPCPA system delivering 5.5 TW few cycle pulses at 1 kHz repetition rate." *Optics Express* 25.5 (2017): 5797-5806.
- [3.49] Budriūnas, Rimantas, Tomas Stanislaukas, and Arūnas Varanavičius. "Passively CEP-stabilized frontend for few cycle terawatt OPCPA system." *Journal of Optics* 17.9 (2015): 094008.
- [3.50] Garejev, Nail, Gintaras Tamošauskas, and Audrius Dubietis. "Comparative study of multioctave supercontinuum generation in fused silica, YAG, and LiF in the range of anomalous group velocity dispersion." *JOSA B* 34.1 (2017): 88-94.
- [3.51] Fattahi, Hanieh, et al. "Near-PHz-bandwidth, phase-stable continua generated from a Yb: YAG thin-disk amplifier." *Optics express* 24.21 (2016): 24337-24346.
- [3.52] Durand, Magali, et al. "Study of filamentation threshold in zinc selenide." *Optics express* 22.5 (2014): 5852-5858.
- [3.53] Mouawad, O., et al. "Filament-induced visible-to-mid-IR supercontinuum in a ZnSe crystal: towards multi-octave supercontinuum absorption spectroscopy." *Optical Materials* 60 (2016): 355-358.
- [3.54] Kanai, Tsuneto, et al. "Parametric amplification of 100 fs mid-infrared pulses in ZnGeP<sub>2</sub> driven by a Ho: YAG chirped-pulse amplifier." *Optics Letters* 42.4 (2017): 683-686.
- [3.55] Archipovaite, Giedre Marija, et al. "100 kHz Yb-fiber laser pumped 3  $\mu$ m optical parametric amplifier for probing solid-state systems in the strong field regime." *Optics Letters* 42.5 (2017): 891-894.
- [3.56] Kardaś, T. M., et al. "The role of stimulated Raman scattering in supercontinuum generation in bulk diamond." *Optics express* 21.20 (2013): 24201-24209.
- [3.57] Lu, Chih-Hsuan, et al. "Generation of octave-spanning supercontinuum by Raman-assisted four-wave mixing in single-crystal diamond." *Optics express* 22.4 (2014): 4075-4082.

- [3.58] Schmidt, Bruno E., et al. "CEP stable 1.6 cycle laser pulses at 1.8  $\mu\text{m}$ ." *Optics express* 19.7 (2011): 6858-6864.
- [3.59] Cousin, S. L., et al. "High-flux table-top soft x-ray source driven by sub-2-cycle, CEP stable, 1.85- $\mu\text{m}$  1-kHz pulses for carbon K-edge spectroscopy." *Optics letters* 39.18 (2014): 5383-5386.
- [3.60] Stolen, R. H., and E. P. Ippen. "Raman gain in glass optical waveguides." *Applied Physics Letters* 22.6 (1973): 276-278.
- [3.61] Feve, Jean-Philippe M., et al. "High average power diamond Raman laser." *Optics express* 19.2 (2011): 913-922.
- [3.62] Murtagh, Michelle, et al. "Efficient diamond Raman laser generating 65 fs pulses." *Optics express* 23.12 (2015): 15504-15513.
- [3.63] Zhi, MiaoChan, Xi Wang, and Alexei V. Sokolov. "Broadband coherent light generation in diamond driven by femtosecond pulses." *Optics express* 16.16 (2008): 12139-12147.
- [3.64] Krylov, Vitaly, et al. "Femtosecond stimulated Raman scattering in pressurized gases in the ultraviolet and visible spectral ranges." *JOSA B* 15.12 (1998): 2910-2916.
- [3.65] Kardaś, Tomasz M., et al. "Full 3D modelling of pulse propagation enables efficient nonlinear frequency conversion with low energy laser pulses in a single-element tripler." *Scientific Reports* 7 (2017).
- [3.66] Nishioka, Hajime. "Stokes suppression and supercontinuum generation by differential two-phonon excitation." *Optics express* 22.22 (2014): 26457-26461.
- [3.67] Krylov, V., et al. "Stimulated Raman scattering in hydrogen by frequency-doubled amplified femtosecond Ti: sapphire laser pulses." *Optics letters* 21.6 (1996): 381-383.
- [3.68] Irie, Yoshiya, and Totaro Imasaka. "Generation of vibrational and rotational emissions by four-wave Raman mixing using an ultraviolet femtosecond pump beam." *Optics letters* 20.20 (1995): 2072-2074.
- [3.69] Duncan, Michael D., et al. "Transient stimulated Raman amplification in hydrogen." *JOSA B* 5.1 (1988): 37-52.
- [3.70] Duncan, Michael D., et al. "Transient stimulated Raman amplification in hydrogen." *JOSA B* 5.1 (1988): 37-52.
- [3.71] Moon, J. A., et al. "Three-dimensional reflective image reconstruction through a scattering medium based on time-gated Raman amplification." *Optics letters* 19.16 (1994): 1234-1236.
- [3.72] Krylov, V., et al. "Stimulated Raman amplification of femtosecond pulses in hydrogen gas." *Optics letters* 21.24 (1996): 2005-2007.

- [3.73] Tavella, F., et al. "Pump-probe burst mode laser amplifier: operation manual and implementation in FLASH-2 experimental hall (28k)", Hemholtz-Institute Jena, Jena & DESY
- [3.74] Duncan, Michael D., et al. "Transient stimulated Raman amplification in hydrogen." *JOSA B* 5.1 (1988): 37-52.
- [3.75] Rothenberg, Joshua E. "Space-time focusing: breakdown of the slowly varying envelope approximation in the self-focusing of femtosecond pulses." *Optics Letters* 17.19 (1992): 1340-1342.
- [3.76] "He-TOPAS Prime High Energy Optical Parametric Amplifier", Light Conversion Pvt. Ltd., Last retrieved July 30<sup>th</sup> 2017. < <http://lightcon.com/Product/HE-TOPAS-Prime.html> >
- [3.77] "Origami Ultra-Low Noise, Femtosecond Laser Module", OneFive GmbH., Last retrieved July 30<sup>th</sup> 2017. < <http://www.onefive.com/products/origami> >
- [3.78] Li, Peng, et al. "Low noise, tunable Ho: fiber soliton oscillator for Ho: YLF amplifier seeding." *Laser Physics Letters* 13.6 (2016): 065104.
- [3.79] Kroetz, Peter, et al. "High energetic and highly stable pulses from a Ho: YLF regenerative amplifier." *Proc. SPIE*. Vol. 9726. 2016.
- [3.80] Kroetz, Peter, et al. "Numerical study of spectral shaping in high energy Ho: YLF amplifiers." *Optics express* 24.9 (2016): 9905-9921.
- [3.81] Kroetz, Peter, et al. "Overcoming bifurcation instability in high-repetition-rate Ho: YLF regenerative amplifiers." *Optics letters* 40.23 (2015): 5427-5430.
- [3.82] Baldeck, P. L., P. P. Ho, and R. R. Alfano. "Effects of self, induced and cross phase modulations on the generation of picosecond and femtosecond white light supercontinua." *revue de physique appliquée* 22.12 (1987): 1677-1694.
- [3.83] Galinis, J., et al. "Filamentation and supercontinuum generation in solid-state dielectric media with picosecond laser pulses." *Physical Review A* 92.3 (2015): 033857.
- [3.84] Gražulevičiūtė, Ieva, et al. "Supercontinuum generation in YAG and sapphire with picosecond laser pulses." *Lithuanian Journal of Physics* 55.2 (2015).
- [3.85] Indra, Lukáš, et al. "Picosecond pulse generated supercontinuum as a stable seed for OPCPA." *Optics Letters* 42.4 (2017): 843-846.
- [3.86] Alfano, R. R., et al. "Induced spectral broadening about a second harmonic generated by an intense primary ultrashort laser pulse in ZnSe crystals." *Physical Review A* 35.1 (1987): 459.
- [3.87] "Perkins Elmer Spectroscopy Instruments", Perkins Elmer Inc., Retrieved July 30<sup>th</sup> 2017. <<http://www.perkinelmer.com/category/molecular-spectroscopy-instruments>>

## 4 CONCLUSION

---

The research and development carried out during the course of this work was focused on generating high-energy, ultra-broadband supercontinua in the MIR in order to seed OPA/OPCPA stages for applications in fundamental chemistry. Due to the pump operating regime (picosecond,  $2\mu\text{m}$ , high energy pulses), research efforts were required to determine (a) the feasibility of bulk supercontinuum generation/nonlinear broadening in the regime, and suitable bulk media/setup parameters to realize such, and (b) methods to increase spectral energy density at far-from-pump wavelengths. Apart from feasibility and benchmarking studies, scientific studies were carried out to probe the complex interplay of nonlinear processes involved in bulk SCG, and the effects they have on the SCG output. The achieved outcome of these studies is as follows:

1. Generation of high-energy SCG in bulk ZnSe at 3.2ps,  $2\mu\text{m}$  pulses. The spectral content of the SCG output supports sub-100fs pulses at  $300\mu\text{J}$  input pump energy, with minimum sub-picosecond pulses for lower input energies.
2. Development of an analytical estimation tool for SCG generation parameters (minimum threshold powers, bulk material selection, propagation lengths) using the balance of Kerr Self-Focusing and Plasma Generation. The parameters obtained via this tool were used, successfully, to find starting parameters for bulk SCG for both ultrashort (11fs) and longer (3.2ps) pulses in the  $2\mu\text{m}$  pump wavelength region.
3. The first (to the best of the author's knowledge) study of Stimulated Raman Amplification of a supercontinuum in condensed media. The proof-of-concept study at  $1\mu\text{m}$  demonstrated the ability to increase spectral energy density on the Stokes (red) side of the SCG pump wavelength.
4. The first (to the best of the author's knowledge) study of the full spatio-spectral polarization properties of SCG produced in a bulk crystal. This study served to confirm the discrepancy

between lack of depolarization in YAG observed previously in literature, and the signification, wavelength-based depolarization observed in CaF<sub>2</sub>, despite both cubic crystals having the same form/symmetries of the  $\chi^{(3)}$  tensor and similar levels of nonlinearity. The poor crystallographic quality of CaF<sub>2</sub> was put forward as an explanation for the discrepancy.

5. Experiments were conducted to determine the effects of other nonlinear processes like 3<sup>rd</sup> harmonic generation and Stimulated Raman Scattering (SRS) on the SCG output. The formation of filaments from light converted to the 2<sup>nd</sup> and 3<sup>rd</sup> harmonic frequencies of the pump pulse was confirmed, as well as the substitution role that SRS plays in shaping the spectral output of SCG, even for very short pulses.
6. A (3+1)D numerical simulation tool was developed to model SCG propagation, and despite fundamental and computational issues limiting the use of the tool for modeling experimental data, the tool can be re-deployed as a learning mechanism to understand SCG pulse dynamics.

Substantial theoretical inputs are required to fully understand and explain the experimental observations from the SRS and cascaded filament studies. However, the experimental observations and background theory can be used to provide some insight (Section 4.1) into desirable qualities for hereto unexplored candidate media such as highly nonlinear glasses.

Further development of the IRDL requires characterization of the beam with respect to compressibility and mutual coherence of different spectral regions of the SCG output. The specific beamline configuration to be used depends upon the outcome of the simulation and scientific studies for DFG/OPA development—options are presented in Section 4.2.

## 4.1 SCG FOR LONG PULSE, LONG WAVELENGTH, HIGH ENERGY REGIONS

Bulk SCG has not been used to directly generate SCG in the deeper MIR region ( $>5\mu\text{m}$  pumping wavelengths) for seeding OPAs, and currently other, much more complicated techniques are used to reach long MIR wavelengths. The lack of SCG studies on this can be partially attributed to the use of standard VIS/NIR nonlinear materials for SCG generation, simply because the transparency window of these classical, high-bandwidth materials (like  $\text{CaF}_2$ ) extends into the MIR. However, semiconductors and highly nonlinear glasses, dismissed in the VIS/NIR regime as “unsuitable for supercontinuum generation” because of their low bandgap, enable the possibility of low-cost, low complexity, ultrabroadband seed sources in the deep MIR when combined with OPA-based pumps at  $4\mu\text{m}$ ,  $5\mu\text{m}$ , or even longer wavelengths—with the development of OPA sources that can act as mid-MIR, high-energy pump sources, bulk SCG becomes a feasible option to generate seed energies at longer wavelengths.

Apart from the standard parameters (critical power for self-focusing, numerical aperture and focus position optimization) covered elsewhere in published literature, additional factors must be included in a generic “recipe” for the generation of long-pulse, long-wavelength SCG in bulk materials:

1. High nonlinearity (determined by the critical power required for to self focusing—the pulse duration and the pulse energy available from the pump source provide the lower limit for material nonlinearity). For  $\sim 1\text{ps}$  systems, for example, the nonlinearity of a material like YAG would be sufficient; this is not the case for longer pulses. Note that low bandgap materials, including GaAs, can be used in the MIR region for supercontinuum generation as long as the material exhibits 3+ orders of multi-photon ionization at the pump pulse wavelength, *and* the production of high harmonics does not become efficient enough for two-photon absorption to take place at shorter, higher order harmonic wavelengths. Alternatively, one can ensure that the cross-section for two-photon absorption is small enough that any pump energy converted to shorter wavelengths is not sufficient for intensity clamping.

2. A zero dispersion wavelength that is much longer than the pump material (i.e. operation in the normal dispersion regime of the material)—while pumping SCG in the anomalous and zero dispersion regimes can yield soliton-like self-compression and ultrabroad pulses, this is the case for femtosecond pulses *only*. Picosecond pulses exhibit far more pronounced (and noise-seeded) modulational instabilities and phase mismatches between spectral components, making the output of SCG in the anomalous/zero dispersion regimes incompressible over a long spectral width, or at worse, entirely incoherent.
3. High dispersion at pump pulse wavelength—this is required because long pulses require long crystal lengths for SF, or, alternatively, tighter pre-focusing. The tighter pre-focusing results in a shortening of the propagation length of the pulse in the nonlinear material before the onset of filamentation, leading to shorter filaments and a smaller total spectral extent. However, in the normal regime, high dispersion means the redder frequencies travel faster than the blue, leading to a buildup of intensities in the rear of the pulse. This prevents the redshifted frequencies at the front of the pulse from “seeing” the avalanche ionization and high-intensity plasma formation seen by the blue frequencies at the rear of the pulse. Therefore, the redshifted portions of the pulse (that are also most sensitive to input focusing conditions) will be intensity-clamped at longer propagation lengths, which can then be better controlled by varying input focusing conditions or input numerical aperture. A high dispersion ensures enough separation between the red and blue shifted frequency components of the pulse such that during the pulse-splitting process, there is large spatial and temporal separation between these components. Also, the high dispersion is related to more energy “leaking” into the Conical Emission, but as the Conical Emission “ring” functions as the energy reservoir during pulse-splitting, the high dispersion will serve to replenish the core of the split pulse and elongate the filament. Note that care has to be taken to compensate for the peak power quenching effect of high dispersion by increasing input power.

4. Crystal structure of the nonlinear material that permits alternative color-conversion processes in the spectral region of interest (e.g. nonvanishing  $\chi^{(2)}$  susceptibility if wavelengths near the second harmonic of the pump are desirable, appropriate raman response, etc.) in order to (a) increase the overall spectral energy density in the region, and (b) provide a cascaded back-and-forth energy transfer/conversion process during pulse propagation that serves to sustain and elongate the primary filament.
5. Ensuring a sustained linear input polarization of the pump pulse—circular polarization can suppress filamentation at lower input powers by preventing the phase/momentum matching conditions required to replenish the core of the split pulse if the rotating (propagating) pulse evolution does not match the length of the pulse splitting/replenishing region at each “breathing” cycle of the filament. Induced polarization rotation of linear input pump polarizations will have a similar effect, and lead to depolarization of the pump pulse.

The analytic model used in Chapter 2 to show the minimum power thresholds required for MPI and Self-Focusing can be used to determine suitability of materials at a target wavelength. Further, given the phase coherence and spatial/energetic stability of certain regimes of multi-filamentation operation, this raises the possibility of using multifilament SCG as a tool to increase the spectral energy density of the SC output where beam quality may not be of much importance as the complex spatio-spectral structure of the output rules out the use of a zoneplate (such as that suggested for single-filament CE collimation), though spatial mode cleaning in a fiber may be a viable solution. Further research inputs are required.

## 4.2 IRDL BEAMLINE OPTIONS

Implementation, or even refined design, of the parametric amplification system is not possible without full temporal, spectral, and noise characterization of the seed pulse. Spectral portions of the pulse that are of interest need to be:

1. Selected using a grating monochromator (preferable) or bandpass filter (not ideal due to the not-quite-zero extinction/passthrough observed for the extremely intense pump pulse).
2. Delivered to a FROG (preferable), or an autocorrelator, for the wavelength in question in order to determine the pulse duration and chirp
3. Monitored for intensity and phase noise fluctuations in relation to the input pump source

Alternatively, an XFROG can be used to check the characteristics of portions of the SC output against the known, referenced pump.

Once the output of the SCG stage has been characterized, the pulse needs to be compressed. Given that the broadening is produced in the normal dispersion regime (ZnSe) without crossover of the zero dispersion wavelength, it is assumed that the induced positive chirp can be sufficiently removed using a grating pair to get sub-picosecond pulse-widths.

There is some doubt at the moment as to whether (a) the seed needs to be compressed for the parametric amplification stage, or whether the uncompressed seed would be better matched to the 3.2ps pump, and (b) whether the residual pump itself should be compressed for the first color conversion (DFG) stage. The results from simulations out of the parametric amplification group will inform the compression choice.

1. In the case that it is determined that an uncompressed seed (FWHM approximately on the order of the pump pulse duration) is optimal for the first DFG stage, and sufficient seed energy in the deep MIR is detected, the direct output of the ZnSe SGC setup (outlined in Chapter 3) can be used.
2. In the case that it is determined that an uncompressed seed can be utilized for the first DFG stage, but that the system would benefit from higher spectral energy densities in the deep MIR, a multi-SCG stage approach can be implemented. Stable SCG-based seed generation from a chirped 3ps pulse has already been demonstrated recently in literature—the spectral content of

the ZnSe SCG output enables the use of subsequent, lower nonlinearity materials (e.g. YAG) to directly generate SCG. Beam quality and spectral interference will need to be managed via the use of spatial and spectral filters to ensure a clean output. Preliminary simulations using HUSSAR (out of scope of this thesis) also suggest that a multi-plate approach (Figure 4.1: Multi-Plate Nonlinear Broadening for Seed Generation) can be implemented, where bulk nonlinear broadening (not SCG) in the normal dispersion regime in ZnSe is followed by bulk self-compression in long sapphire plates (anomalous dispersion regime). This more “gentle” nonlinear broadening approach means that beam management and beam quality are far less of an issue than in the ZnSe SCG + YAG SCG approach. However, the multi-plate approach requires pulse phase and temporal characterization after every plate/external focusing step which necessitates the development or purchase of a working FROG, XFROG or Autocorrelator in the spectral region of interest.

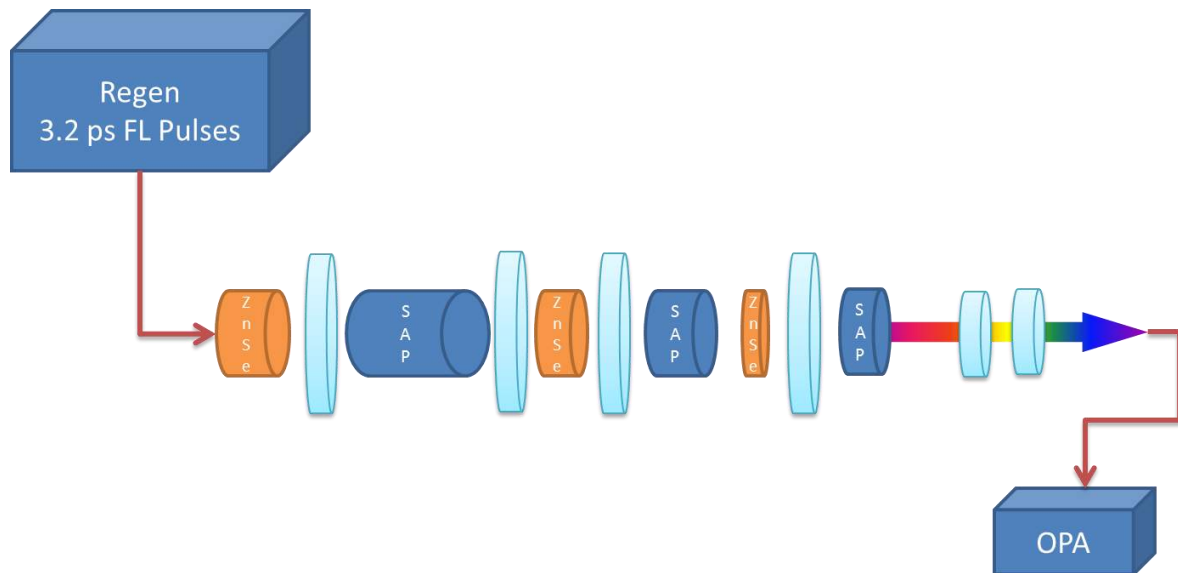


*Figure 4.1: Multi-Plate Nonlinear Broadening for Seed Generation*

3. Finally, in the case that a fully compressed seed is required, and there is not enough spectral energy density in the MIR for appreciable suppression of parametric superfluorescence, an approach can be used that consists of, in sequence (Figure 4.2):

- a. Nonlinear broadening in ZnSe
- b. Grating compression to sub-200fs pulse width
- c. Supercontinuum generation in YAG
- d. Femtosecond Stimulated Raman Amplification of the YAG supercontinuum in 3mm Diamond. This is pumped by the residual (unconverted) 2 $\mu$ m pump that remains in the center of the WL portion of the beam.

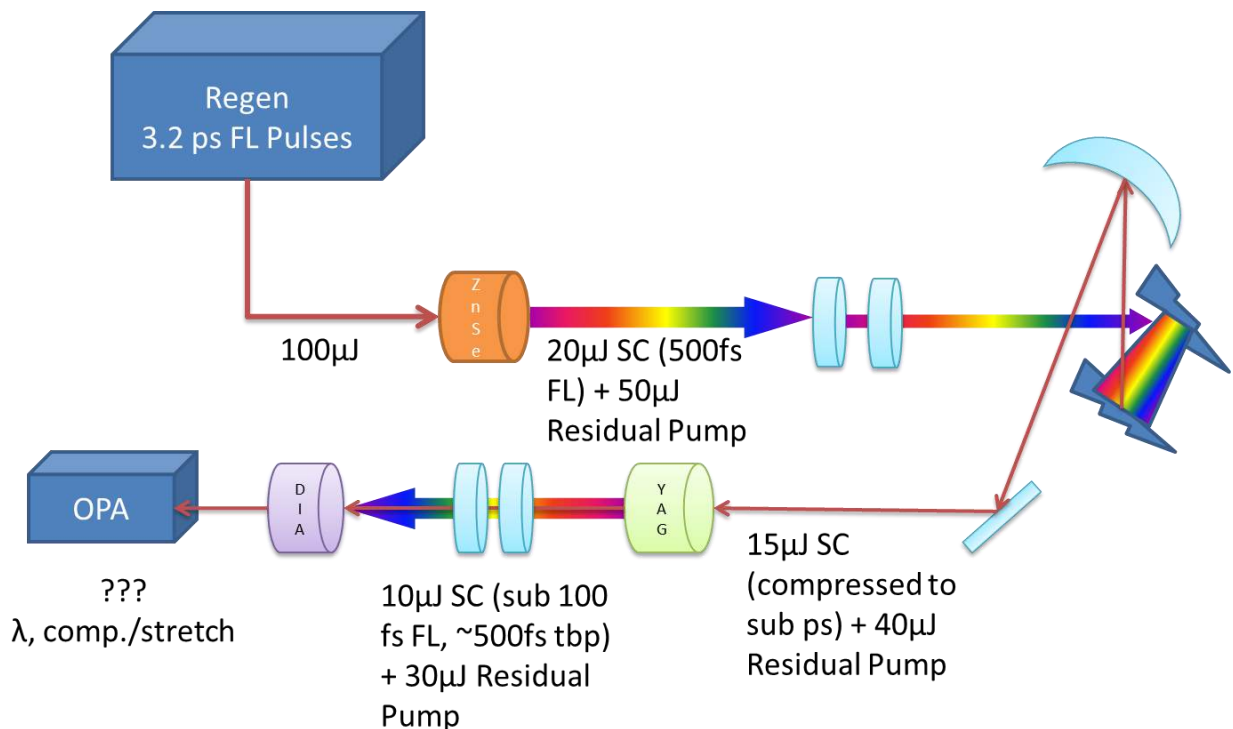


Figure 4.2: Sub 100fs, High Stokes Spectral Energy Density Beamline

In the case that the physical chemistry theory group determines that the output of the first color conversion stage is energetic enough to begin scientific experiments, a multi-channel, AOM (Acousto-Optic-Modulator) based pulse shaper has been designed and can be integrated into the beamline to directly use the output of the ZnSe SCG output spectra for the OPA.

### 4.3 SUMMARY

To summarize, in order to support the scientific objectives of the IRDL project (Laser Selective Chemistry), the final “design-to” system parameters for the IRDL system were baselined as three, 100fs, phase-locked pulses at 3, 6 and 8 $\mu$ m, with each wavelength carrying 1mJ of energy. A 2 $\mu$ m pump capable of multiple mJ pulses of 3.2ps duration had to be used as the pump-source for ultrabroadband seed generation; the temporal duration of the pump pulses made them unsuitable for “traditional” supercontinuum generation due to the inevitable rise of incoherence and modulational instabilities seen in the long-pulse regime in fiber-based systems. Therefore, an alternative—bulk supercontinuum generation—was identified as a key technology for broadband seed generation in this region.

The roles of Kerr Self-Focusing, Multi Photon Ionization, Avalanche Ionization and Group Velocity Dispersion in shaping the spatio-temporal and spectral characteristics of bulk supercontinua were studied through literature and application of various numerical relations/models to the long-pulse, MIR regime.

Experiments were used to further investigate the physics of supercontinuum generation, as well as to confirm feasibility of the approach and discover methods to increase spectral energy density at far-from-pump wavelengths.

Finally, the IRDL pump pulses system was used to drive supercontinuum generation in ZnSe, demonstrating bulk nonlinear broadening, cascaded supercontinuum generation, and the tantalizing possibility that a multi-octave supercontinuum *could* be generated directly from 3.2ps pulses.

*This work was funded by the Max Planck Institute for the Structure and Dynamics of Matter, with material or personnel support from the University of Hamburg, the FS-LA group at DESY, Laserlab Europe, The Institute for Photonic Sciences (ICFO), and Warsaw University.*

## APPENDIX A: MATERIAL PARAMETERS OF RELEVANT CRYSTALS

Crystal	YAG	ZnSe	Diamond, CVD Type IIa	Sapphire (ordinary ray, C-cut)
<b>Optical Properties</b>				
Transparency Window [ $\mu\text{m}$ ]	0.21 – 5.5 [A.1]	0.6 – 21 [A.9]	0.3 - >100 [A.10]	0.17 – 5.5 [A.11]
Sellmeier Equation	$n^2 - 1 = \frac{2.28200 \lambda^2}{\lambda^2 - 0.01185} + \frac{3.27644 \lambda^2}{\lambda^2 - 282.734}$ [A.5]	$n^2 - 1 = 3.00 + \frac{1.90 \lambda^2}{\lambda^2 - 0.113}$ [A.8]	$n^2 - 1 = \frac{0.3306 \lambda^2}{\lambda^2 - 0.1750^2} + \frac{4.3356 \lambda^2}{\lambda^2 - 0.1060^2}$ [A.13]	$n^2 - 1 = \frac{1.023798 \lambda^2}{\lambda^2 - 0.06144821^2} + \frac{1.058264 \lambda^2}{\lambda^2 - 0.1106997^2} + \frac{5.280792 \lambda^2}{\lambda^2 - 17.92656^2}$ [A.12]
n (at 2.052 $\mu\text{m}$ )	1.7997 <sup>1</sup>	2.4398 <sup>1</sup>	2.4022 <sup>1</sup>	1.7367 <sup>1</sup>
GVD (at 2.052 $\mu\text{m}$ ) [fs <sup>2</sup> /mm]	-70.4 <sup>1</sup>	248.68 <sup>1</sup>	185.52 <sup>1</sup>	-135.15 <sup>1</sup>
$n_2$ [cm <sup>2</sup> /W]	2.9x10 <sup>-16</sup> [A.3]	3x10 <sup>-14</sup> [A.3]	1.3x10 <sup>-15</sup> [A.3]	3x10 <sup>-16</sup> [A.3]
Optical Damage Threshold, [J/cm <sup>2</sup> ]	100 (ns pulses at 1.064 $\mu\text{m}$ ) [A.4]	5 (100 ns pulses at 10 $\mu\text{m}$ ) [A.14]	1.2 (200 ps pulses at 10 $\mu\text{m}$ ) [A.17]	11 (100 fs pulses at 0.6 $\mu\text{m}$ ) [A.16]
<b>Electronic Properties</b>				
Band Gap (at 300K) [eV]	10 [A.21]	2.82 [A.19]	5.47 [A.20]	13 [A.18]
Electron/Hole Effective mass ( $m_e/m_h$ )	0.5 [A.7]	0.35 [A.22]	0.22 [A.23]	0.21 [A.24]
<b>Crystal Properties</b>				
Manufacturing Method	Czochralski Growth Process [A.2]	Vapor Synthesis [A.9]	Chemical Vapor Deposition (CVD) [A.10]	Czochralski Growth Process [A.11]
Chemical Formula	Y <sub>3</sub> Al <sub>5</sub> O <sub>12</sub> [A.2]	ZnSe [A.9]	C <sub>60</sub> [A.10]	Al <sub>2</sub> O <sub>3</sub> [A.11]
Crystal Structure	Cubic, m3m [A.2]	HIP Polycrystalline cubic (Zinc blende) [A.9]	Diamond [A.10]	Trigonal [A.11]
Space Group	m3m [A.2]	f43m [A.9]	fd3m [A.10]	r3c [A.11]

<sup>1</sup> Derived from Sellmeier Equation

## APPENDIX B: THE GAETA NLSE

The NLSE developed by Gaeta [A.25] is of the form:

$$\frac{\partial u}{d\zeta} = \frac{i}{4} \left( 1 + \frac{i}{\omega_o \tau_p} \frac{\partial}{\partial \tau} \right)^{-1} \nabla_{\perp}^2 u - i \frac{L_{df}}{L_{ds}} \frac{\partial^2 u}{\partial \tau^2} + i \left( 1 + \frac{i}{\omega_o \tau_p} \frac{\partial}{\partial \tau} \right) \left[ \frac{L_{df}}{L_{nl}} |u|^2 u - \frac{L_{df}}{L_{pl}} \left( 1 - \frac{i}{\omega_o \tau_c} \right) \rho u + i \frac{L_{df}}{L_{mp}} |u|^{2(m-1)} u \right] \quad [\text{B.1}]$$

Where:

$u(r, z, t)$  is the normalized Amplitude  $\frac{A}{A_0}$ : the input pulse at  $z = 0$  is taken to be Gaussian in space and time such that:

$$A(r, z = 0, t) = A_0 e^{\left[ \frac{-r^2}{2w_0^2} - \frac{t^2}{2\tau_p^2} \right]}$$

$\omega$  is the central frequency of the pulse

$\tau_p$  is the pulse duration

$$\nabla_{\perp}^2 u = \frac{\partial^2}{\partial x^2} + \frac{\partial^2}{\partial y^2}$$

$L_{df} = \frac{kw_0^2}{2}$  is the diffraction length

$k = \frac{n_0 \omega}{c}$  is the vector wave amplitude

$n_0$  is the linear refractive index of the material

$c$  is the speed of light

$w_0$  is the Full Width At Half Maximum for the input beam (spot size)

$\zeta = \frac{z}{L_{df}}$  is the normalized distance

$L_{ds} = \frac{\tau_p^2}{\beta_2}$  is the dispersion length

$\beta_2$  is the group-velocity dispersion

$\tau = \left( t - \frac{z}{v_g} \right) / \tau_p$  is the normalized retarded time for the pulse traveling at the group velocity

$v_g$  is the group velocity

$L_{nl} = \frac{c}{\omega n_2 I_0}$  is the nonlinear length

$L_{pl} = \frac{2\rho_0}{\sigma \omega \tau_c}$  is the plasma length

$L_{mp} = \frac{1}{\beta^{(m)} I_0^{(m-1)}}$  is the  $m$  photon absorption length

$\beta^{(m)}$  is the  $m$  photon absorption coefficient

$n_2$  is the nonlinear refractive index of the material

$\sigma$  is the cross-section for inverse bremsstrahlung

$\tau_c$  is the electron collision time

$I_0 = \frac{n_0 c |A_0|^2}{2\pi}$  is the peak input intensity

$\rho = \frac{\rho_e}{\rho_0}$  is the electron density normalized to the total density

$\rho_0 = \frac{\beta^{(m)} I_0^m \tau_p}{n \hbar \omega}$  is the total density of electrons that would be produced by the input pulse through multiphoton absorption.

$\rho$  satisfies the equation  $\frac{\partial \rho}{\partial \tau} = \alpha \rho |u|^2 + |u|^{2m}$

Where  $\alpha = \frac{\sigma I_0 \tau_p}{n_0^2 E_g}$

And  $E_g$  is the band-gap energy of the material.

Solving for nonlinear polarization, as per Gaeta [A.25],

$\rho$  satisfies the equation  $\frac{\partial \rho}{\partial \tau} = \rho \alpha |u(\tau)|^2 + |u(\tau)|^{2m}$

This is a first-order linear ordinary differential equation with the solution:

$$\begin{aligned} \rho(\tau) = & e^{\int_1^\tau \alpha |u(\xi)|^2 d\xi} \\ & - e^{\int_1^0 \alpha |u(\xi)|^2 d\xi} \left( e^{\int_1^0 \alpha |u(\xi)|^2 d\xi} \int_1^\tau |u(\zeta)|^{2m} e^{-\int_1^\zeta \alpha |u(\xi)|^2 d\xi} d\zeta \right. \\ & \left. - e^{\int_1^0 \alpha |u(\xi)|^2 d\xi} \int_1^0 |u(\zeta)|^{2m} e^{-\int_1^\zeta \alpha |u(\xi)|^2 d\xi} d\zeta + \rho_0 \right) \end{aligned}$$

With  $\rho(\tau = 0) = \rho_0$

Simplifying,

$$\begin{aligned} \rho(\tau) = & e^{-\alpha \int_\tau^{t_{max}} |u(\xi)|^2 d\xi} \\ & + e^{-2\alpha \int_{-t_{max}}^{t_{max}} |u(\xi)|^2 d\xi} \left( \int_\tau^{t_{max}} |u(\zeta)|^{2m} e^{-\alpha \int_\zeta^{t_{max}} |u(\xi)|^2 d\xi} d\zeta \right. \\ & \left. - \int_{-t_{max}}^{t_{max}} |u(\zeta)|^{2m} e^{\alpha \int_\zeta^{t_{max}} |u(\xi)|^2 d\xi} d\zeta + \rho_0 \right) \end{aligned}$$

## REFERENCES

- [A.1] Yttrium Aluminium Garnet (YAG) Datasheet. 2014. Crystran Ltd., UK, retrieved July 23<sup>rd</sup> 2017. <<https://www.crystran.co.uk/optical-materials/yttrium-aluminium-garnet-yag>>
- [A.2] Xiao, Qiang, and Jeffrey J. Derby. "Heat transfer and interface inversion during the Czochralski growth of yttrium aluminum garnet and gadolinium gallium garnet." *Journal of Crystal Growth* 139.1-2 (1994): 147-157.
- [A.3] Glass, Alexander J., and Arthur H. Guenther. "Laser induced damage of optical elements—a status report." *Applied Optics* 12.4 (1973): 637-649.
- [A.4] Bisson, Jean-François, et al. "Laser damage threshold of ceramic YAG." *Japanese journal of applied physics* 42.8B (2003): L1025.
- [A.5] Zelmon, David E., David L. Small, and Ralph Page. "Refractive-index measurements of undoped yttrium aluminum garnet from 0.4 to 5.0  $\mu\text{m}$ ." *Applied optics* 37.21 (1998): 4933-4935.
- [A.6] Xu, Yong-Nian, and W. Y. Ching. "Electronic structure of yttrium aluminum garnet ( $\text{Y}_3\text{Al}_5\text{O}_{12}$ )." *Physical Review B* 59.16 (1999): 10530.
- [A.7] Xu, Yong-Nian, W. Y. Ching, and B. K. Briceken. "Electronic structure and bonding in garnet crystals  $\text{Gd}_3\text{Sc}_2\text{Ga}_3\text{O}_{12}$ ,  $\text{Gd}_3\text{Sc}_2\text{Al}_3\text{O}_{12}$ , and  $\text{Gd}_3\text{Ga}_3\text{O}_{12}$  compared to  $\text{Y}_3\text{Al}_5\text{O}_{12}$ ." *Physical Review B* 61.3 (2000): 1817.
- [A.8] Marple, D. T. F. "Refractive index of ZnSe, ZnTe, and CdTe." *Journal of Applied Physics* 35.3 (1964): 539-542.
- [A.9] Zinc Selenide (ZnSe) Datasheet. 2014. Crystran Ltd., UK, retrieved July 23<sup>rd</sup> 2017. <<https://www.crystran.co.uk/optical-materials/zinc-selenide-znse>>
- [A.10] Diamond Datasheet. 2014. Crystran Ltd., UK, retrieved July 23<sup>rd</sup> 2017. <<https://www.crystran.co.uk/optical-materials/diamond-cubic-carbon-c>>
- [A.11] Sapphire Datasheet. 2014. Crystran Ltd., UK, retrieved July 23<sup>rd</sup> 2017. <<https://www.crystran.co.uk/optical-materials/sapphire-al2o3>>
- [A.12] Malitson, Irving H. "Refraction and dispersion of synthetic sapphire." *JOSA* 52.12 (1962): 1377-1379.
- [A.13] Peter, Fritz. "Über Brechungsindizes und Absorptionskonstanten des Diamanten zwischen 644 und 226  $\mu\text{m}$ ." *Zeitschrift für Physik A Hadrons and Nuclei* 15.1 (1923): 358-368.
- [A.14] Zinc Selenide (ZnSe Windows). Throlabs GmbH. 2017. Retrieved July 23<sup>rd</sup> 2017. <[https://www.thorlabs.com/NewGroupPage9\\_PF.cfm?Guide=10&Category\\_ID=185&ObjectGroup\\_ID=3981](https://www.thorlabs.com/NewGroupPage9_PF.cfm?Guide=10&Category_ID=185&ObjectGroup_ID=3981)>
- [A.15] Diamond
- [A.16] Uteza, Olivier, et al. "Laser-induced damage threshold of sapphire in nanosecond, picosecond and femtosecond regimes." *Applied Surface Science* 254.4 (2007): 799-803.
- [A.17] Chiang, A. C., et al. "Laser-induced damage threshold at chemical vapor deposition-grown diamond surfaces for 200-ps  $\text{CO}_2$  laser pulses." *Optics letters* 27.3 (2002): 164-166.

- [A.18] Dobrovinskaya, Elena R., Leonid A. Lytvynov, and Valerian Pishchik. *Sapphire: material, manufacturing, applications*. Springer Science & Business Media, 2009.
- [A.19] Shan, W., et al. "Pressure dependence of the fundamental band-gap energy of CdSe." *Applied physics letters* 84.1 (2004): 67-69.
- [A.20] Koizumi, S., et al. "Growth and characterization of phosphorous doped {111} homoepitaxial diamond thin films." *Applied physics letters* 71.8 (1997): 1065-1067.
- [A.21] Xu, Yong-Nian, and W. Y. Ching. "Electronic structure of yttrium aluminum garnet (Y<sub>3</sub>Al<sub>5</sub>O<sub>12</sub>)." *Physical Review B* 59.16 (1999): 10530.
- [A.22] Singh, Jasprit. *Physics of Semiconductors and their Heterostructures*. McGraw-Hill College, 1993.
- [A.23] Löfås, Henrik, et al. "Effective masses and electronic structure of diamond including electron correlation effects in first principles calculations using the GW-approximation." *AIP Advances* 1.3 (2011): 032139.
- [A.24] Morkoç, Hadis. *Handbook of nitride semiconductors and devices, Materials Properties, Physics and Growth*. Vol. 1. John Wiley & Sons, 2009.
- [A.25] Gaeta, Alexander L. "Catastrophic collapse of ultrashort pulses." *Physical Review Letters* 84.16 (2000): 3582.